

**Making it Work:
Second Generation Interferometry
in GEO 600 !**

Vom Fachbereich Physik
der Universität Hannover
zur Erlangung des Grades

**Doktor der Naturwissenschaften
– Dr. rer. nat. –**

genehmigte Dissertation von

Dipl.-Phys. Hartmut Grote

geboren am 19. Februar 1967 in Hemer

2003

Referent: Prof. K. Danzmann
Korreferent: Prof. M. Kock
Tag der Promotion: 2. Juli 2003
Druckdatum: 15. Oktober 2003

Zusammenfassung

Die erste Generation laserinterferometrischer Gravitationswellendetektoren mit Armlängen im Kilometerbereich beginnt derzeit mit der Datenaufnahme, wodurch der direkte Nachweis von Gravitationswellen in greifbare Nähe rückt. Der deutsch-britische Gravitationswellendetektor GEO 600 bei Hannover ist ein Teil dieses internationalen Netzwerks mit dem Ziel, ein neues Fenster zum Universum zu öffnen.

Das Kernstück von GEO 600 ist ein Michelson-Interferometer für die Messung von durch Gravitationswellen hervorgerufenen Längenänderungen entlang zweier rechtwinkliger Messstrecken. Mittels einer Technik zur resonanten Überhöhung der im Interferometer gespeicherten Lichtenergie (*Power Recycling*) wird die schrotrauschbegrenzte Empfindlichkeit des Interferometers erhöht. GEO 600 ist weltweit das erste der großen Interferometer, in welchem elektrostatische Aktuatoren zur Längenregelung benutzt werden. Zudem sind die vier Endspiegel und der Strahlteiler mit Quarzfäden als Endstufe dreifacher Pendel aufgehängt.

Diese Arbeit beschreibt die Implementierung und den erfolgreichen stabilen Betrieb des Michelson-Interferometers mit Power Recycling (Kapitel 1). Es wurde ein computergestütztes System entwickelt, welches den vollautomatischen Betrieb von GEO 600 nahezu ohne menschlichen Eingriff gestattet.

Für den stabilen Langzeitbetrieb „aufgehängter“ Interferometer ist ein automatisches System zur Winkeljustierung (kurz *Autoalignment*) der Spiegel unentbehrlich. Basierend auf früheren Experimenten der Forschungsgruppe in Glasgow und am 30-m-Prototypen in Garching wurde ein Autoalignmentsystem basierend auf differentieller Wellenfrontabtastung entwickelt und erfolgreich für alle aufgehängten Spiegel von GEO 600 implementiert. Insgesamt werden 34 Winkelfreiheitsgrade von 17 aufgehängten Spiegeln mit diesem System automatisch justiert (Kapitel 3). In einem 17 Tage dauernden Testlauf im Sommer 2002 war das Michelson-Interferometer mit Power Recycling für fast 99 % der Zeit in Betrieb, wobei die längste ununterbrochene Messphase länger als 120 Stunden andauerte.

Im Gegensatz zu den Gravitationswellendetektoren LIGO, VIRGO und TAMA 300 ist bei GEO 600 die *Dual-Recycling-Technik* vorgesehen, um die angestrebte Empfindlichkeit zu erreichen. Dual Recycling ist die Kombination von *Signal Recycling* und Power Recycling. Durch die Benutzung eines Signal-Recycling-Spiegels im Ausgang des Michelson-Interferometers kann das Gravitationswellensignal resonant verstärkt werden. Mit der Spiegelposition ist das Frequenzverhalten des Detektors einstellbar, wodurch verschiedenen erwünschten Messanforderungen genügt werden kann. Dual Recycling ist eine fortgeschrittene Interferometertechnik, die zum Beispiel in der zweiten Generation der LIGO-Interferometer zum Einsatz kommen wird.

Während Dual Recycling für aufgehängte Interferometer am Garchinger 30-m-Prototypen demonstriert wurde, ist die Implementierung von Dual Recycling für GEO 600 aus verschiedenen Gründen eine neue Herausforderung. Ein Schema für den Betrieb von GEO 600 mit Dual Recycling in einem sogenannten verstimzten Modus wurde entwickelt und erfolgreich getestet (Kapitel 2).

Stichworte: Gravitationswellendetektor, Dual Recycling, Autoalignment . . .

Abstract

The first generation of kilometer-scale laser-interferometric gravitational wave detectors recently started collecting data and the direct detection of gravitational waves may be excitingly close. The British-German gravitational wave detector GEO 600 near Hannover in Germany is part of this international effort to open a new window on the universe.

The core instrument of GEO 600 is a Michelson interferometer which is used for the detection of differential length changes along two orthogonal arms that may arise from gravitational waves. The power recycling technique is used in order to resonantly enhance the light power stored inside the interferometer and thus increase the shot-noise limited sensitivity of the detector. The Michelson interferometer of GEO 600 is the first of the large-scale detectors that uses electrostatic drives as displacement actuators for two of the Michelson end mirrors. The four mirrors of the folded interferometer arms and the beamsplitter are monolithically suspended by triple pendulum chains.

This work describes the implementation and subsequently successful stable operation of the power-recycled Michelson configuration (chapter 1). A computer-controlled locking scheme has been developed and was implemented in order to operate the power-recycled Michelson almost without human interaction.

For long-term stable operation of suspended interferometers an automatic alignment (short *autoalignment*) system is indispensable. Based on earlier experiments carried out on the Garching 30 m prototype and by the Glasgow group, an autoalignment system based on the differential wavefront sensing technique has been developed and successfully implemented for all suspended mirrors of GEO 600. A total of 34 angular degrees of freedom of 17 suspended mirrors are automatically aligned with this system (chapter 3). In a 17 day long test run in the summer of 2002, the power-recycled Michelson operated for nearly 99 % of the time with the longest continuous-lock stretch lasting more than 120 hours.

In contrast to the gravitational wave detectors LIGO, VIRGO and TAMA 300, GEO 600 was designed to use *dual recycling* from the beginning in order to reach the design sensitivity. Dual recycling is the combination of signal recycling and power recycling. By using a signal-recycling mirror at the output of the Michelson interferometer, the gravitational wave signal can be resonantly enhanced and the detector's frequency response can be shaped for specific observational requirements. Dual recycling is an advanced interferometer technique that will also be implemented in the second generation of, for example, the LIGO detectors.

While dual recycling on a suspended interferometer was demonstrated with the Garching 30 m prototype, its implementation for GEO 600 is a new challenge for various reasons. A scheme capable of locking GEO 600 in a dual recycling mode (the so-called *detuned* state) was developed and tested successfully (chapter 2).

Keywords: Gravitational wave detector, Dual recycling, Autoalignment ...

Contents

Zusammenfassung	iii
Abstract	v
Contents	vii
List of figures	xiii
List of tables	xix
Glossary	xxi
1 The Power-Recycled Michelson Interferometer	1
1.1 Introduction	1
1.2 Power-recycling cavity and lock	2
1.2.1 Frequency stabilisation	2
1.2.2 Feedback control loop design	5
1.2.2.1 Actuators	5
1.2.2.2 Loop filters	5
1.2.3 Lock acquisition of the power-recycling cavity	6
1.2.4 The loop in operation	7
1.2.4.1 Frequency noise	7
1.2.4.2 Stability problems due to suspension resonances	9
1.2.5 Low frequency length control	10
1.3 The electrostatic drive	12
1.3.1 Overview	12

1.3.2	Driving the ESD	13
1.3.3	ESD induced damping	16
1.3.4	Calibration and drift	17
1.4	Michelson lock	19
1.4.1	Determining the Schnupp frequency	20
1.4.2	Feedback design	21
1.4.2.1	Actuators	21
1.4.2.2	Loop filters	23
1.4.2.3	Locking performance	24
1.4.3	Lock acquisition	25
1.4.4	Longitudinal calibration	29
1.4.5	The evolution of lock	30
1.4.5.1	Mid fringe lock	30
1.4.5.2	Test PRMI	30
1.4.5.3	Final PRMI	31
1.5	Problems with scattered light	33
1.6	Lock automation	35
1.6.1	LabView	35
1.6.2	Microcontroller	36
1.6.3	Locking sequence	37
1.6.4	Long time locking during the S1 run	37
2	The Dual Recycling Lock	41
2.1	Introduction	41
2.2	Experimental setup	44
2.3	Locking strategy	45
2.3.1	Power-recycling control	45
2.3.2	Michelson control	49
2.3.3	Signal-recycling control	50
2.3.3.1	Signal-recycling demodulation phase	52
2.3.3.2	Michelson deviation from dark fringe	52
2.3.3.3	PR resonance deviation from laser frequency	53

2.3.3.4	Michelson differential alignment	54
2.3.4	Summary	55
2.4	Feedback design	56
2.4.1	Actuators	56
2.4.2	Loop filters	56
2.5	Towards locking dual recycling	58
2.5.1	Finding the proper SR demodulation phase	58
2.5.2	Normalizing the Michelson gain	59
2.6	Experimental results	61
2.6.1	Acquisition	61
2.6.2	Sensitivity	63
3	The GEO 600 Autoalignment	65
3.1	Introduction	65
3.1.1	Differential wavefront sensing	66
3.2	Alignment requirements	68
3.2.1	Michelson light power	69
3.2.2	Michelson error signal gain	71
3.2.3	Power noise coupling	73
3.2.4	Frequency noise coupling	75
3.2.5	Summary	76
3.3	Modecleaner alignment	76
3.3.1	Overview	76
3.3.2	Control signals	77
3.3.3	Experimental setup	79
3.3.3.1	Setup schematic	79
3.3.3.2	Breadboard optical setup	81
3.3.4	Beam centering scanners	81
3.3.4.1	Scanner design	83
3.3.5	Photodetector design	83
3.3.5.1	Which bias voltage to use?	85

3.3.6	Lens system and linear combination	85
3.3.7	Control topology	87
3.3.7.1	LabView control	88
3.3.8	Feedback design and performance	90
3.3.8.1	Actuators	90
3.3.8.2	Loop filters	91
3.3.8.3	Performance	92
3.4	Power-recycling cavity alignment	93
3.4.1	Introduction	93
3.4.2	Experimental setup	95
3.4.2.1	Beam rotating periscope	95
3.4.2.2	Breadboard optical setup	95
3.4.3	Lens system and linear combination	97
3.4.4	Control topology	97
3.4.4.1	Computation of control signals	99
3.4.4.2	LabView control	100
3.4.5	Feedback design and performance	101
3.4.5.1	Actuators	101
3.4.5.2	Loop filters	102
3.4.5.3	Performance	103
3.5	Michelson alignment	104
3.5.1	Overview	104
3.5.2	Experimental setup	104
3.5.2.1	Detection bench layout	105
3.5.3	Lens system and control topology	106
3.5.3.1	LabView control	107
3.5.4	Feedback design and performance	109
3.5.4.1	Actuators	109
3.5.4.2	Loop filters	112
3.5.4.3	Performance	114
3.6	Michelson spot position control	118

3.6.1	How individual mirror misalignments affect the eigenmode	118
3.6.2	Control signals for n-dimensional problems	120
3.6.3	Formal approach to obtain control signals	121
3.6.4	Spot position sensors	123
3.6.5	Spot position fluctuations	125
3.6.5.1	Spot position measurements	126
3.6.5.2	DWS feedback measurement	127
3.6.6	Faster alignment control for MCE and MCn common mode	129
3.6.7	Long term drifts	129
3.7	Alignment calibrations	130
3.7.1	Analog feedback	130
3.7.2	Digital feedback	130
Appendix		133
A Optical layout of GEO 600		133
B Electronics		136
B.1	Resonant quadrant cameras	136
B.2	Orthogonal current driver	138
B.3	ESD alignment driver	140
B.4	Microcontroller and spot positions	143
C Software		145
C.1	Microcontroller code	145
C.1.1	Flow diagrams	145
C.1.2	C code	148
C.1.2.1	Main loop	148
C.1.2.2	Power-recycled Michelson lock	150
C.1.2.3	Dual Recycling lock	152
C.1.2.4	Fringe damping	155
C.1.2.5	Input / output routines	156
C.1.2.6	Interrupts	158

C.2	LabView code	160
C.2.1	Modecleaner alignment	160
C.2.2	Michelson alignment	160
D	ESD Design Drawing	166
E	Timetable	168
	Bibliography	169
	Acknowledgements	173
	Curriculum vitae	175
	List of publications	177

List of figures

1.1	Overview of GEO 600 optics.	2
1.2	Schematic overview of the power recycling lock.	4
1.3	Open loop gain and phase of the power recycling lock.	6
1.4	Spectral density of the feedback signal to the master laser.	8
1.5	Spectral density of the power-recycling cavity errorpoint.	9
1.6	Modecleaner resonance of MMC2b suspension.	10
1.7	Electrode pattern of the electrostatic drive (ESD).	12
1.8	Signal chain from Michelson feedback point to ESD.	14
1.9	HV amplifier and sqrt-circuit noise.	15
1.10	Calibration factor of the east electrostatic drive over one month.	18
1.11	Michelson length control scheme.	20
1.12	Triple pendulum suspension.	22
1.13	Open loop gain and phase of the Michelson lock.	23
1.14	Longitudinal feedback to the Michelson intermediate mass.	25
1.15	Simulated Michelson error signal.	25
1.16	The free moving Michelson interferometer.	27
1.17	A successful lock acquisition of the Michelson interferometer.	28
1.18	Heater setup for mirror MFe.	32
1.19	Sensitivity development due to scattered light investigations.	34

1.20	Typical sensitivity to gravitational waves during the S1 run.	35
1.21	Light power levels during a fully automated locking sequence.	37
1.22	Time series and spectral density of Michelson feedback.	39
2.1	Principle distribution of light fields for dual recycling.	42
2.2	Simulated strain sensitivities for dual recycling.	43
2.3	Dual-recycling lock control scheme.	46
2.4	Power-recycling error signal for 6 different tunings of MSR.	47
2.5	Michelson error signal versus the signal-recycling mirror tuning.	50
2.6	Slope of the Michelson and signal-recycling error signals.	51
2.7	Optimal demodulation phase of the Michelson and signal-recycling error signals.	51
2.8	Simulated signal recycling error signal.	52
2.9	Signal recycling error signal for Michelson deviations.	53
2.10	Signal-recycling error signal for different deviations of the power-recycling mirror.	54
2.11	Signal-recycling error signal for Michelson alignment deviations.	55
2.12	Open loop gain and phase of the signal recycling lock for two different states.	57
2.13	Coupling of a laser frequency test signal to the signal-recycling errorpoint.	58
2.14	Simulation of the Michelson gain.	60
2.15	Acquisition of the largely detuned dual-recycling lock.	62
2.16	Equivalent MCE displacement sensitivity for largely detuned dual recycled lock.	63
3.1	Schematic of a triangular ring cavity.	66
3.2	Influence of individual mirror rotation misalignments onto the power buildup.	69
3.3	Influence of beamsplitter rotation misalignment onto power buildup.	70
3.4	Influence of mirror rotation misalignments on the Michelson error signal gain.	72
3.5	Influence of beamsplitter rotation misalignment on power noise coupling.	74
3.6	Optical setup of the two GEO 600 modecleaner cavities.	76

3.7	Aligned and misaligned modecleaner.	78
3.8	Schematic overview of the alignment control for one modecleaner.	80
3.9	Optical layout of the breadboard east of TCMA.	82
3.10	Equivalent schematic of the resonant circuit of a photodiode.	84
3.11	Lens system in beam path to quadrant detector.	86
3.12	How the LabView system works together with the analog DWS feedback.	89
3.13	Alignment transfer function for MMC1b intermediate mass input.	91
3.14	Time series of reflected light power from MC1.	93
3.15	Schematic overview of the main interferometer alignment control.	94
3.16	Arrangement of optical components around the beam extracting Faraday rotator.	95
3.17	Optical layout of the breadboard west of TCMB.	96
3.18	Lens system in beam path to PR quadrant detector.	97
3.19	Schematic diagram of the GEO 600 PR cavity.	99
3.20	Integration of the LabView control for the power-recycling cavity alignment.	100
3.21	Open loop transfer function of power-recycling mirror alignment.	102
3.22	Amplitude spectral density of mirror MPR rotation.	103
3.23	Michelson misalignment caused by the end mirrors.	105
3.24	Preliminary optical layout of the detection bench.	106
3.25	Integration of the LabView control for the Michelson alignment.	108
3.26	Transfer function of MCE intermediate mass current driver tilt input.	109
3.27	Transfer function of MCE tilt for monolithic suspension.	110
3.28	MCE current driver transfer function for different LC gains.	111
3.29	Electrostatic drive with high and low voltage amplifiers.	112
3.30	Open loop gain and phase of the Michelson fast autoalignment for tilt.	113
3.31	Open loop gain and phase of the Michelson fast autoalignment with ESD.	114

3.32	Amplitude spectral density of DWS signal for MCE and MCn rotation.	116
3.33	Time series of Michelson interferometer power levels.	117
3.34	Relative amplitude spectral density of light power at dark port.	117
3.35	Eigenmode position shift of the Michelson interferometer east arm.	119
3.36	Misalignment of MCE can be compensated by aligning MPR.	120
3.37	Actuators (A,...,D) and sensors (S1,...,S4) for the spot position control.	122
3.38	Optical layout of the breadboards in the two far end stations.	124
3.39	Spot position deviations from the center of rotation of a mirror.	125
3.40	Vertical spot position fluctuations on end mirrors MCE and MCn.	127
3.41	Coherence of the spot positions on MCE and MCn.	128
3.42	Differential Michelson length noise introduced by the DWS alignment feedback.	128
3.43	Beamsplitter alignment feedback and central cluster temperature.	130
A.1	Complete optical layout of GEO 600.	134
A.2	Optical layout of the central interferometer area.	135
B.1	Electronics around resonant quadrant photodiode.	137
B.2	Demodulation electronics for one quadrant of a resonant photodiode.	137
B.3	Arrangement of coils on 6 suspensions.	138
B.4	'Orthogonal' current driver unit.	139
B.5	Filter electronics for ESD alignment feedback.	141
B.6	Orthogonalization electronics for ESD alignment feedback.	142
B.7	Processing sums and differences from quadrant diode signals.	143
B.8	Infineon C 167 microcontroller with periphery.	144
C.1	Flow diagram of the acquisition DC lock and power recycling lock control.	146
C.2	Flow diagram of the subroutine controlling the dual recycled lock.	147

C.3	Modecleaner 1 alignment supervising VI panel.	161
C.4	Modecleaner 1 alignment supervising VI diagram.	162
C.5	Modecleaner spot position control VI panel.	163
C.6	Michelson drift control VI diagram.	164
C.7	Main interferometer spot position control VI panel.	165
D.1	Electrostatic drive design drawing.	167

List of tables

1.1	Capture range and slope of the Michelson error signal.	29
1.2	Radii of curvature of the four final Michelson mirrors.	32
1.3	Input signals connected to the microcontroller unit.	36
1.4	Duty cycle of the optical systems of GEO 600 during the S1 run.	38
1.5	Losses of lock over two weeks of the S1 run.	38
2.1	Filter parameters for the signal-recycling mirror feedback loop.	57
3.1	Beam displacements caused by small horizontal misalignments of mirrors.	78
3.2	Beam displacements caused by small vertical misalignments of mirrors.	79
3.3	Properties of the three feedback loop types of the automatic alignment system.	88
3.4	Alignment control signals for all suspended modecleaner mirrors.	90
3.5	Spot positions on all suspended modecleaner mirrors.	90
3.6	Alignment transfer function for modecleaner IM input.	91
3.7	Filter parameters for fast modecleaner alignment feedback.	92
3.8	Results of the ray-tracing program for the GEO 600 PR cavity.	99
3.9	Fitted parameters for BDIPR and MPR alignment transfer functions.	101
3.10	Filter parameters of the power-recycling cavity DWS loops.	102
3.11	Alignment control signals for each mirror of the main interferometer.	108
3.12	Fitted parameters for MCE and MCN alignment transfer functions.	110

3.13 Filter parameters for the Michelson DWS feedback. 113

3.14 Spot positions on all suspended main interferometer mirrors. 124

3.15 Alignment feedback calibration factors for the main optics digital control. 131

Glossary

autoalignment: automatic beam alignment system, subject of chapter 3.

broadband: the state of a signal recycled interferometer when the SR cavity is resonant for the carrier frequency (see section 2.1).

BS: a beamsplitter, usually the main beamsplitter of a Michelson interferometer.

camera: term used for a photodiode in an assembly together with preamplifiers etc.

CCD: charge-coupled device, used in a videocamera.

DC: average of a fluctuating signal; also used to indicate the limit of some function for low frequencies.

detuned: the state of a signal recycled interferometer when the carrier frequency is *not* resonant in the SR cavity (see Section 2.1).

DR: dual recycling (the combination of power and signal recycling).

EOM: an electro-optic modulator (used for modulating or shifting the phase of a light beam); see also 'Pockels cell'.

ESD: electrostatic drive (see section 1.3).

FSR: the Free Spectral Range of a cavity.

HPD: high power detector, a photodiode or array of photodiodes capable of detecting up to 2 W light power (see page 34).

HV: high voltage, maximally 1000 V are used to drive the ESDs.

local control: feedback system installed for each suspended mirror that damps the pendulum resonances.

longitudinal: in the direction of the beam axis.

LISO: program for 'Linear Simulation and Optimization' of analog electronic circuits [Hei99b].

M: a mirror.

MPR: power recycling mirror.

MSR: signal recycling mirror.

Michelson: the Michelson interferometer formed by the beamsplitter BS and the four mirrors **MFe**, **MCE**, **MF_n**, and **MC_n**, often used to specifically indicate this part of a more complex interferometer.

opamp: operational amplifier.

PD: a photodetector (usually a photodiode).

Piezo: a piezo-electric transducer, used to control the master laser frequency; see also 'PZT'.

Pockels cell: used as synonym for EOM.

PR: Power recycling.

PSD: power spectral density or a position sensitive device (used for beam spot position measurements).

PZT: used as a synonym for a piezo-electric transducer.

QD: a quadrant photodiode, used for the DWS technique and determining spot positions.

rotation: a movement of a suspended component that causes a *horizontal* movement of the affected beam (cf. 'tilt').

RF: radio frequency (in GEO 600 usually between 9 and 38 MHz).

rms: root mean square.

ROC: radius of curvature of a mirror.

SNR: signal-to-noise ratio.

SR: Signal recycling.

tilt: a movement of a suspended component that causes a *vertical* movement of the affected beam (cf. 'rotation').

tuning: the microscopic position of a mirror that determines the resonance condition of an interferometer (see Section 2.1).

c: the speed of light in vacuum, 299792458 m/s.

C: a capacitor, also used for its capacitance (in Farad).

d: a distance.

d_c: capture range (see section 1.4.3).

E : the electric field. Also used to denote beams in chapter 3.

f : a frequency with the unit Hz.

f_{MI} : Schnupp modulation frequency for the Michelson interferometer.

f_{SR} : Schnupp modulation frequency for the signal-recycling cavity.

I : a current, in particular a photocurrent.

i : $\sqrt{-1}$.

L : a physical armlength or distance in the interferometer.

Q : the quality factor of a resonant system.

q : a complex parameter describing a Gaussian beam.

R : a resistor or its resistance (in Ohms).

U : a voltage.

w : the radius (half-width) of a laser beam.

w_0 : the radius of a laser beam at its waist.

x, y, z : the three spatial dimensions, with z usually indicating the beam axis or the direction of propagation.

Z : an impedance (usually complex).

z_r : the Rayleigh range of a laser beam ($\lambda z_r = \pi w_0^2$).

α : the angle by which a component is misaligned.

β : the angle corresponding to α in the other dimension.

γ : the angle between two wavefronts or beam axes.

δ : the angle corresponding to γ in the other dimension.

ΔL : a length difference.

ϵ : dielectric constant.

ϵ_r : relative dielectric constant for a specific material.

η : the Guoy phase shift.

θ : an angle describing the ‘character’ of a misalignment.

θ^w : an angle describing the ‘character’ of a misalignment at the beam waist (see Section 3.1.1).

θ^d : an angle describing the ‘character’ of a misalignment at a detector (see Section 3.1.1).

λ : the wavelength of the light, 1064 nm in GEO 600.

ϕ : a tuning (i.e. microscopic position of one or several mirrors) of one degree of freedom of the interferometer.

ϕ_{MI} : the tuning of the Michelson interferometerpower recycling mirror.

ϕ_{SR} : the tuning of the signal recycling mirror (which has no influence at a perfect Michelson dark fringe, but influences the gain and frequency response in dual recycling).

Chapter 1

The Power-Recycled Michelson Interferometer

1.1 Introduction

GEO 600 is the British-German laser-interferometric gravitational wave detector. GEO's core instrument is a Michelson (for short *MI*) interferometer with an armlength of 600 m which is sensitive to differential length changes induced, for example, by gravitational waves. The light paths in the arms are folded once, yielding an effective arm length of 1200 m and a round trip arm length of 2400 m. The sensitivity of this instrument to differential arm length changes can be increased by enhancing the circulating light power with the power-recycling (*PR*) technique [DC83, Sch81, SMH⁺97]. The installation of the GEO 600 power-recycled Michelson was finished in 2001.

The operation of complex interferometers requires many control loops to work simultaneously. Often the process of activating these control loops (the *lock acquisition*), requires special care and techniques. Experiments on the lock acquisition and control of the power-recycled Michelson interferometer of GEO 600 are described in chapter 1.

The sensitivity of the power-recycled Michelson can be increased further with the signal recycling (*SR*) technique. This involves the installation of an additional mirror at the detector output port. The resulting configuration is called *dual recycling* and we will have a look at the dual recycling experiments on GEO 600 in chapter 2. A major part of the work at hand deals with the automatic alignment system (often called *autoalignment*), which is responsible for automatically adjusting the two relevant angular degrees of freedom of each suspended mirror within GEO 600. This system is described in chapter 3.

Although GEO 600 in its final configuration will use dual recycling to reach the design-sensitivity, the power-recycled Michelson without signal recycling is still an important configuration used to characterize and validate the involved subsystems.

Figure 1.1 gives a simplified schematic overview of GEO 600 including the light source, two mode-cleaners, and the power-recycled Michelson. Additional beam steering mirrors are omitted for clarity. (The *physical* arrangement of GEO's optical components is shown in Figures A.1 and A.2 in appendix A.)

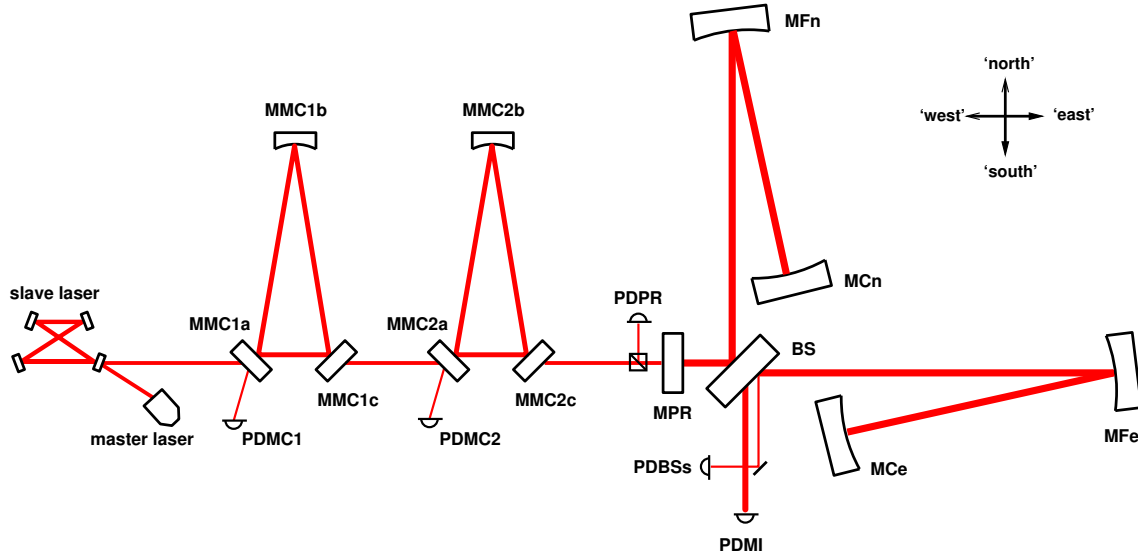


Figure 1.1: Schematic overview of GEO 600 optics in the power-recycled Michelson configuration. The light source is an injection-locked master-slave system. Two sequential suspended modecleaners are used before the light enters the power-recycled Michelson interferometer.

The light source of GEO 600 comprises an injection locked master-slave system with 14 W output power¹ [ZBk⁺02, Bro99, Nag01]. The laser output light passes two sequential modecleaners which filter the light with respect to beam geometry fluctuations, frequency and amplitude noise. The light leaving the second modecleaner is the input light to the power-recycling cavity consisting of the power recycling mirror and the Michelson interferometer operating at the dark fringe. The modecleaners and their longitudinal control are described in detail by A. Freise [Fre03b], together with a complete overview of GEO 600. Hence the discussion in the current chapter starts with the power-recycling cavity, while the modecleaners are referred to as required along the way.

1.2 Power-recycling cavity and lock

1.2.1 Frequency stabilisation

The frequency stabilisation of the laser system for an interferometric gravitational wave detector has two main goals:

- Minimizing couplings of light frequency noise into the Michelson output signal in the measurement band of a gravitational wave detector (e.g. 50 – 5000 Hz).

¹To date, the light power injected to the first modecleaner is attenuated to 2 W. Later it will be increased to the full available power in order to reach the design-sensitivity when required.

- Minimizing the rms frequency noise over all frequencies, such that a sufficiently easy lock acquisition of the power-recycling cavity is possible.

The Michelson length control system uses the Schnupp modulation technique (see chapter 1.4) which requires an asymmetry in the length of the interferometer arms. Due to this asymmetry, the interferometer becomes sensitive to frequency fluctuations of the incident laser light. To minimize this technical noise source, the light frequency has to be stabilized to a reference, as the frequency noise of the free running laser system exceeds the required limits.

The power-recycling cavity is a good frequency reference in the gravitational wave measurement band (50 – 5000 Hz) for this purpose. As the power-recycling mirror, **MPR**, is suspended as a double pendulum (in contrast to all other mirrors that are a part of the PR cavity being suspended as triple pendulums), its motion dominates the frequency stability of the power-recycling cavity. Due to the simpler vertical isolation, the longitudinal mirror displacement is likely being dominated by coupling of vertical mirror motion to longitudinal displacement. For a rough estimate of the frequency stability of the power-recycling cavity at 50 Hz, we assume a ground displacement noise of $5 \times 10^{-11} \text{ m}/\sqrt{\text{Hz}}$ and an isolation of this displacement noise by the suspension of **MPR** by a factor of 2×10^8 [Pli03]². This yields a displacement noise of **MPR** of about $\Delta l \approx 1 \times 10^{-19} \text{ m}/\sqrt{\text{Hz}}$ at 50 Hz. Using $\Delta f/f = \Delta l/l$ we get $\Delta f \approx 0.2 \mu\text{Hz}/\sqrt{\text{Hz}}$, with $f = 282 \text{ THz}$ as light frequency and $l = 1200 \text{ m}$ as cavity length. With this, the frequency stability of the power-recycling cavity is about 500 times better than the GEO 600 requirement of about $100 \mu\text{Hz}/\sqrt{\text{Hz}}$ [Bro99] (however the readout system required to reach this sensitivity is not trivial). Recent calculations of the required laser frequency noise give different numbers of 5 to $100 \mu\text{Hz}/\sqrt{\text{Hz}}$, depending on the interferometer configuration (e.g. broadband / narrowband signal recycling, or deviation from the dark fringe) [Fre03a].

The power-recycling cavity is the frequency reference for the laser light and locking of this cavity can be done by adjusting the input light frequency to resonate within the free (i.e. longitudinally uncontrolled) power-recycling cavity. The resulting concept in GEO 600 forms a frequency stabilisation chain. Figure 1.2 gives an overview of the power-recycling lock and the associated frequency stabilisation chain of GEO 600.

The first modecleaner (MC1) is locked with the reflection locking (Pound-Drever-Hall [DHK⁺83]) technique. Light incident onto MC1 is modulated in phase with the electro-optic modulator EOM1 and the light being reflected at the input mirror of MC1 is demodulated at the modulation frequency. The resulting signal (also called *error signal* when emphasizing its use in a feedback loop) is a measure for the match between the frequency of an eigenmode of the cavity and the incident laser frequency.

The resonance condition (‘lock’) is maintained by continuously feeding back the error signal to the laser frequency through an appropriate electronic filter (‘servo’). A control bandwidth of about 100 kHz has been achieved. If only MC1 is locked, it serves as the frequency reference for the laser.

²This estimate assumes a coupling factor of vertical to horizontal displacement of 0.1%. The coupling factor depends on how horizontal the beam is with respect to the center of gravity of the earth [Sau94].

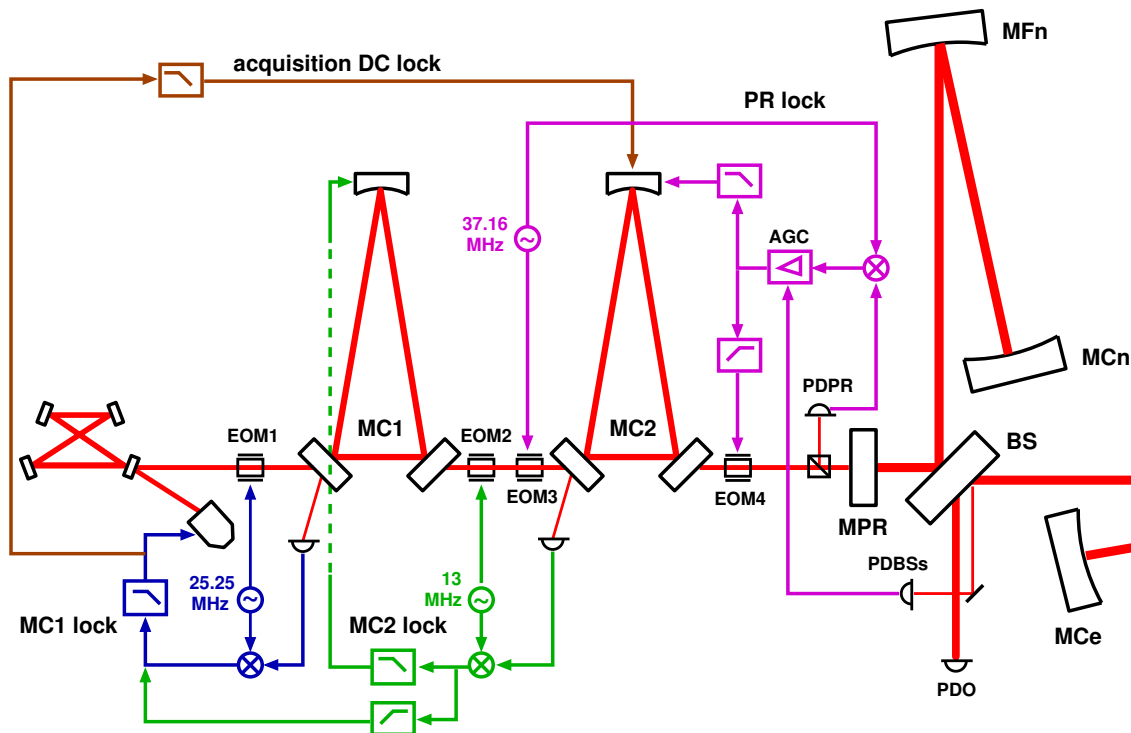


Figure 1.2: Schematic overview of the power-recycling lock and the associated frequency stabilisation chain of GEO 600.

For the locking of modecleaner MC2, the reflection locking technique is also used, with phase modulation sidebands being applied to the incident light by EOM2. MC2 is locked by feeding back the error signal information to the length of MC1 in the frequency band from DC to 1 kHz. Above 1 kHz feedback is added to the error signal of MC1 (and thus to the laser servo input directly) with a unity gain frequency of about 20 kHz. With this split feedback, the light frequency is adjusted to match a resonance of MC2, and if MC2 is locked in this way, it serves as the frequency reference for the laser. Finally the light leaving MC2 is the light source for the power-recycling cavity. See [Fre03b] for more details about the modecleaners and modecleaner locking.

Control sidebands for the reflection locking technique used for the power-recycling cavity are applied by EOM3 in the light path before MC2. The modulation frequency $f_{PR} = 37.16\text{ MHz}$ is chosen to match the free spectral range of MC2, such that the sidebands are transmitted through MC2. When MC2 is locked, the frequency of the light incident on MPR can be adjusted by changing the length of MC2. Fast frequency fluctuations (which can also be considered as phase fluctuations) can also be corrected by EOM4 in the light path behind MC2. Both corrections are done for locking of the power-recycling cavity (see Figure 3.16 on page 95 for details of the beam extraction on reflection from MPR).

The power-recycling cavity is not a simple Fabry-Perot cavity, but it can be approximated as a Fabry-Perot cavity with variable reflectivity of the rear mirror (the virtual mirror opposing MPR consisting of the Michelson interferometer). The transmittance of this virtual mirror depends on the interference condition of the Michelson interferometer.

The incident laser light can be locked to the power-recycling cavity even when the Michelson interferometer is not in the dark fringe condition. If the Michelson is uncontrolled, all mirrors move freely and the fraction of light being reflected from the Michelson towards **MPR** varies with time. Hence the finesse of the power-recycling cavity is variable as well, depending on the tuning (the microscopic pathlength difference) of the Michelson. With the changing finesse of the power-recycling cavity the optical gain (the error signal slope) of the cavity is altered proportionally to the light power available in the power-recycling cavity [Bon95]. The power-recycling error signal is divided by the light power in order to make the PR control loop more stable.

In order to obtain proper signals for locking of the Michelson interferometer, the power-recycling cavity has to be locked first. Otherwise the light level available for the Michelson in an anti-resonant power-recycling cavity is 10000 times smaller than with a locked power-recycling cavity (provided **MPR** has a transmittance of 1 %). It is not necessary to lock the power-recycling cavity and Michelson simultaneously. This would be harder, since, a coincidence of a Michelson dark fringe and the incident light being resonant within the power-recycling cavity is rather rare.

The feedback path labelled ‘acquisition DC lock’ is only required for a proper lock acquisition of the power-recycling cavity. It reduces the rms frequency noise of the light leaving MC2 as explained in section 1.2.3.

1.2.2 Feedback control loop design

1.2.2.1 Actuators

As we have seen, the power-recycling cavity is locked by adjusting the frequency of the light incident on the power-recycling cavity such that it matches an integer multiple of the cavity’s free spectral range. This is done by changing the length of the second modecleaner, which in turn changes the laser frequency by the described frequency stabilisation chain. The additional phase modulator, EOM4, in the path behind MC2, is used in order to increase the bandwidth of the power recycling lock independently of feedback to the modecleaners.

1.2.2.2 Loop filters

The crossover frequency between the two actuators (the longitudinal feedback to MC2 and EOM4 after MC2) is at 1 kHz and the unity gain frequency of the whole loop is at about 20 kHz. Figure 1.3 shows the open loop gain and phase of the designed servo for the two actuators individually, as well as for the combined loop. The loop is unconditionally stable, making it very robust during the lock acquisition phase of the Michelson, where the optical gain (the slope of the error signal) varies significantly ³. With two additional transient integrator stages, the gain can be increased below 2 kHz and 30 Hz, once the Michelson is locked. As there is plenty of phase margin around

³If an automatic gain control (AGC) for the power-recycling cavity lock is used, the gain variations are compensated over a fairly wide range. However it is still desirable to make the power-recycling cavity lock as stable as possible even without AGC.

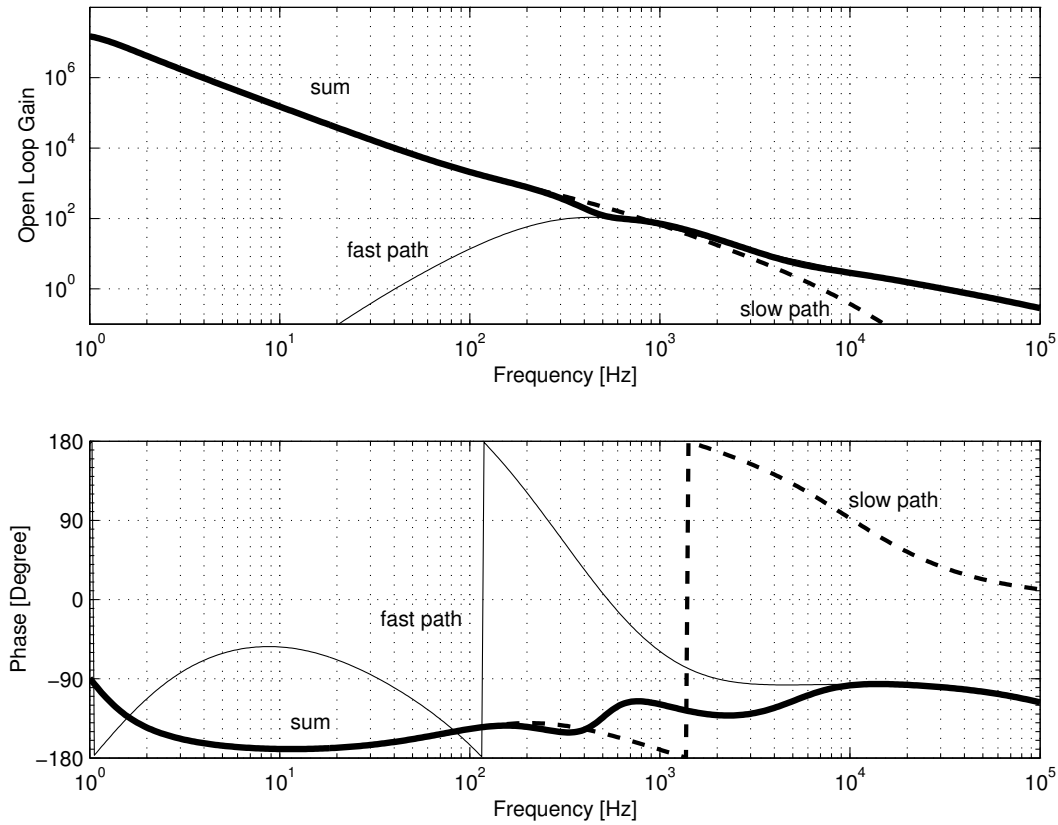


Figure 1.3: Open loop gain and phase of the power recycling loop. The ‘sum’ plot shows the (complex) sum of the slow and fast actuator paths. The crossover frequency is at 1 kHz, the overall unity-gain frequency is at about 20 kHz.

the unity gain point, further integrators may be added, if required for further frequency noise suppression.

1.2.3 Lock acquisition of the power-recycling cavity

One goal of the laser frequency stabilisation is to enable a fairly easy lock acquisition of the power-recycling cavity. For this purpose, the rms frequency noise of the laser light with respect to the power-recycling cavity is important. In the case of GEO 600, the laser is not locked to a rigid referency cavity, but to the modecleaners, such that the rms frequency noise is dominated by the main resonances of the modecleaner pendulums. The modecleaner mirror displacement noise can be as large as $1\mu\text{m}_{\text{rms}}$, giving a frequency noise of $\Delta f = 70\text{MHz}_{\text{rms}}$.

As the power-recycling cavity is 300 times longer than the modecleaners (1200 m versus 4 m), its rms frequency noise is 300 times smaller (assuming the same mirror displacement noise around 1 Hz). However the larger modecleaner length noise (which determines the light frequency noise of the light incident to the power recycling cavity when the PR cavity is not yet locked) leads to a more difficult lock acquisition of the power-recycling cavity, as several 100 fringes per second are

observed at the power-recycling cavity ⁴.

Of course it is possible to lock such a system on a turning point of a modecleaner pendulum, where relative frequency changes are small. But the crucial point is that the power-recycling servo has to be in the locked condition for a large fraction of time. The power-recycling cavity must be locked *before* the Michelson can attempt to lock, such that lock acquisition times for the full system can be drastically decreased if the power-recycling cavity acquires lock as fast and as often as possible. For this purpose we stabilize the frequency (and thus the length) of the second modecleaner to the frequency of the (virtually) *free* running master laser in a frequency band from DC up to roughly 10 Hz ⁵. This is done by feeding back the information contained in the *feedback* signal of the master laser to the longitudinal position of modecleaner mirror MMC2b, as shown in Figure 1.2. This control loop is called *acquisition DC lock*.

Above approximately 4 Hz the frequency noise of the modecleaners is smaller than the master laser's frequency noise, such that for frequencies above 4 Hz the modecleaners are the 'quieter' frequency reference. However, a bandwidth of about 10 Hz for the feedback to MC2 length is used in order to provide sufficient loop gain around 1 Hz. Note that in this kind of feedback the master laser is locked to the modecleaners with a feedback loop of high bandwidth (DC – 100 kHz), while in turn the modecleaners are locked to the master laser's feedback signal with a low-bandwidth loop (DC – 10 Hz). The result is a laser frequency noise which has the smallest possible noise of the two references used in combination. This stabilisation scheme is sufficient for reducing the rms frequency noise of the laser for acquisition purposes. However, after lock acquisition of the Michelson, the acquisition DC lock is switched off to give full control of the laser frequency to the power-recycling lock and avoid any contamination with noise from the (virtually) free running laser.

Figure 1.4 shows the amplitude spectral density of the feedback signal to the master laser, calibrated as laser frequency noise. It can be seen that the uncontrolled second modecleaner dominates the laser frequency noise below 4 Hz. With the acquisition DC lock active, the rms frequency noise is sufficiently reduced to enable the lock acquisition of the power-recycling cavity. Nevertheless the laser frequency noise is still dominated by the modecleaner from about 1 to 4 Hz. If the power-recycling cavity is locked, the feedback signal to the laser is (except for the small peak around 0.6 Hz) determined by the frequency noise of the (virtually) uncontrolled master laser. The peak around 0.6 Hz is caused by the free longitudinal motion of the power-recycling cavity.

1.2.4 The loop in operation

1.2.4.1 Frequency noise

Figure 1.5 shows the measured spectral density of the power-recycling cavity errorpoint with the PR loop in operation (this is an in-loop measurement). Also shown is the feedback applied to the

⁴A *fringe* denotes the transition of the incident light frequency across a resonance frequency of the power-recycling cavity.

⁵The Nd:YAG crystal of the master laser can be seen as the reference 'cavity' in the band from DC to 10 Hz, as long as the power-recycling cavity is not locked.

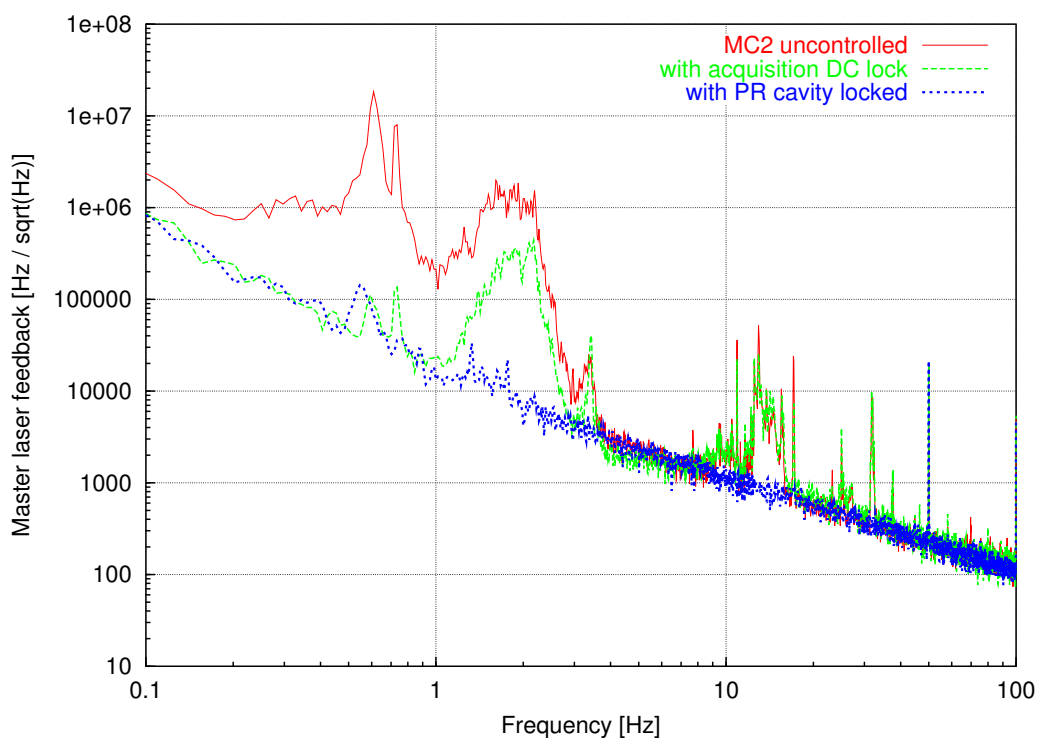


Figure 1.4: Spectral density of the feedback signal to the master laser, calibrated as laser frequency noise.

length of MC2 in the frequency band up to 1 kHz, where it represents the noise of the free mode-cleaner against the power-recycling cavity. The difference between the two curves is a measure for the suppression of the free mode-cleaner noise that is achieved by the PR lock.

The power recycling errorpoint frequency noise does not yet reach the required level of at most $100 \mu\text{Hz}/\sqrt{\text{Hz}}$. However this is expected to be reached in the final GEO 600 configuration, as the optical gain of the PR lock will be increased by a factor of 10 then, by increasing the finesse of the power-recycling cavity. Furthermore, it has to be noted that the photodetector currently in use for the power-recycling cavity longitudinal lock (which is used for automatic alignment as well) can detect the error signal of a full fringe without saturation. To enable this, the light power detected has to be largely attenuated. In the final setup it might be required to use the current detector only for acquisition and then switch to another detector running with larger light level. Another possibility could be to increase the light level on the existing photodetector in lock.

It should be noted that the above measurement of the power recycling errorpoint is an in-loop estimation of the frequency noise. It remains to be seen whether the frequency noise contribution to the main detector output signal indicates a larger frequency noise than estimated by the errorpoint measurement.

The calibration of the frequency noise was done by injecting a signal into the power recycling loop and determining its size in the feedback to MC2 mirror MMC2b. MMC2b is then calibrated by injecting a larger signal to MMC2b (with the power-recycling cavity unlocked) such that it can be observed in the signal applied to the master laser frequency actuator, for example the piezo

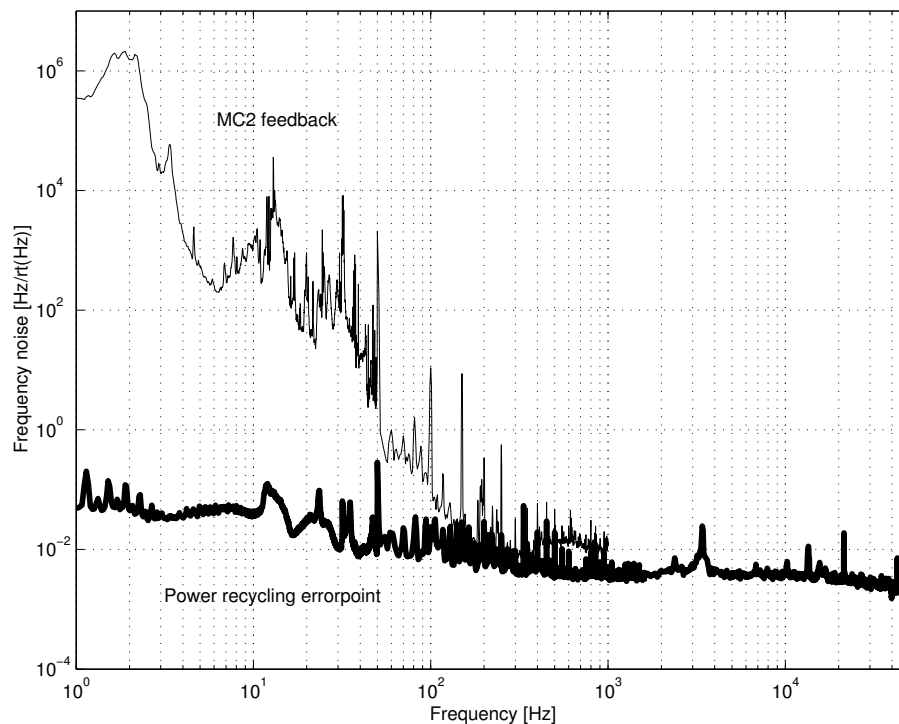


Figure 1.5: Spectral density of the power-recycling cavity errorpoint with the PR loop in operation. Also shown is the feedback applied to the length of MC2. The MC2 feedback is only shown in the frequency band up to 1 kHz, where it displays the noise of the free modecleaner against the power-recycling cavity.

mounted onto the master oscillator crystal. In a final step, the master laser piezo actuator is calibrated by driving it with a ramp and observing the sideband resonances (of the phase modulation applied by EOM1) at the first modecleaner. (See [Fre03b], section 2.5.3 for further details about the calibration of the master laser.)

1.2.4.2 Stability problems due to suspension resonances

At a point in time when locking of the power-recycled Michelson had become more and more stable, it turned out that continuous lock stretches were not longer than about 2-3 hours. Observing the error- and feedback signals of the involved loops, it became obvious that the feedback to the phase modulator EOM4 (which acts on the frequency of the light incident to the power-recycling cavity) was saturating at a frequency around 197.3 Hz. Observing the spectrum of this feedback in lock revealed that the line at 197.3 Hz was growing exponentially with time and needed some time to decay after excitation. The measurement of the transfer function from the MMC2b actuator to the laser frequency shows a resonance around 197.3 Hz, which is a violin mode of the steel wire slings that suspend MMC2b.

Figure 1.6 shows this resonances structure which has a particularly large phase lead of about 40° at 197.335 Hz. The measurement shows the transfer function from MMC2b longitudinal input to the master laser frequency feedback (measured at the PZT actuator of the master laser). The power-recycling cavity was not locked for this measurement.

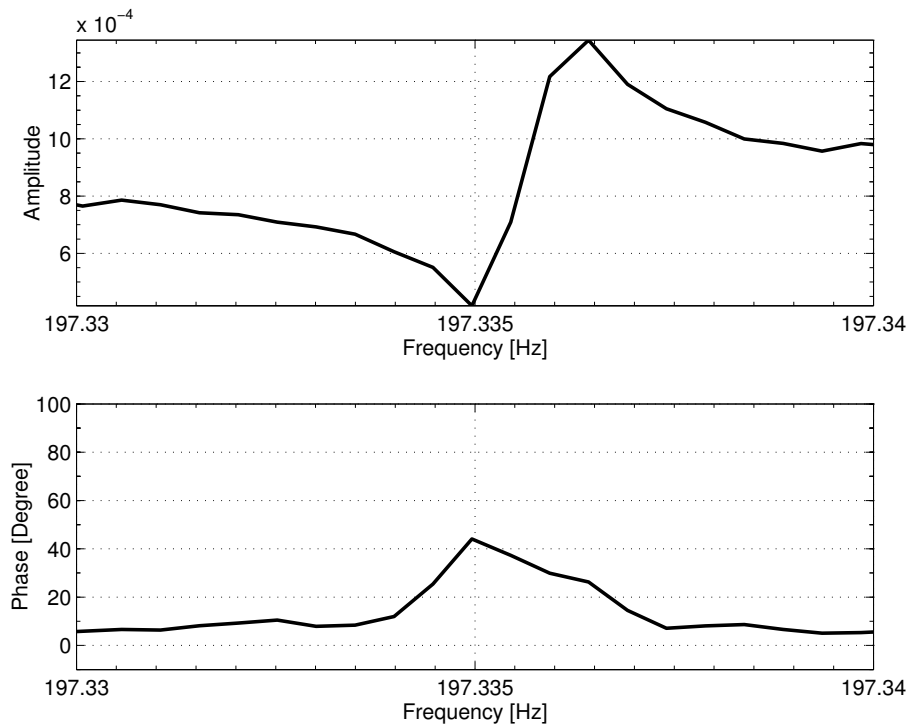


Figure 1.6: Modecleaner resonance of MMC2b suspension, visible in the transfer function from MMC2b longitudinal input to the master laser frequency feedback.

As the crossover frequency between the coil-magnet actuator and the EOM is around 1 kHz, the resonance at 197.335 Hz causes an additional crossing of the gain curves of the two actuators at this frequency (see Figure 1.3 for reference). To make such a system stable, it is required that the phase difference between the two actuators is below 180° at the frequencies of equal gain. Due to the relatively large phase lead of the resonance shown, the system was just unstable at this frequency. An additional phase lead in the electronic feedback filter of the EOM path of about 20° around 200 Hz removed the oscillation at 197 Hz. The additional phase lead was introduced by shifting one of the pole frequencies in the EOM path servo design to a lower frequency.

1.2.5 Low frequency length control

In general, the low-frequency stabilisation of the laser frequency is called *DC lock* in GEO 600. We have two different types of DC lock:

- The *acquisition* DC lock described above in section 1.2.3, using the length of the master laser's YAG ring resonator as frequency reference.
- The DC lock stabilizing the laser frequency to a GPS-locked rubidium clock standard after the power-recycling cavity is locked. This DC lock is described below.

We have seen above that when the power-recycling cavity is locked, it serves as the frequency reference for the master laser up to 1 kHz (the bandwidth up to which feedback is applied to the length of MC2). This implies that absolute length drifts of the power-recycling cavity in lock will lead to absolute frequency changes of the laser. While this does not affect experiments in principle (concerning the carrier light), an absolute length change of the power-recycling cavity leads to an imperfectly resonant Schnupp frequency within the power-recycling cavity, which can increase the frequency noise coupling as a consequence. Furthermore, it is undesirable to have a change in MC2 length at low frequencies, as this slightly affects the phase of the transmitted sidebands, although this effect is very small due to the length difference of the modecleaners and the power-recycling cavity.

In the final GEO 600 setup, there will be a low-frequency length stabilisation of the power-recycling cavity. A preliminary version of such a length control is set up at MC2, detecting the light in reflection of the MC2 input mirror. A dedicated photodiode ⁶ measures the beat signal of the phase modulation at 13 MHz (used for obtaining the locking signal for MC2) and the phase modulation at f_{PR} . If the free spectral range (which is determined by the length) of MC2 deviates from f_{PR} , a small fraction of the power-recycling control sidebands is reflected and beats with the 13 MHz sidebands, yielding a length control signal, which could be applied to the length of the power-recycling cavity. Preliminary experiments showed that the length resolution obtainable with this setup is of the order $1\ \mu\text{m}$, which corresponds to a relative accuracy of order 1×10^{-6} .

A similar possibility is to demodulate the reflected light at **MPR** with the difference frequency of f_{PR} and the Michelson Schnupp frequency f_{MI} . This signal will be zero when the Michelson Schnupp sidebands are exactly resonant within the power-recycling cavity. As the integer multiple of the FSR of the power-recycling cavity that matches f_{MI} is known, this kind of measurement is also a measure of the absolute length of the power-recycling cavity.

Finally, another way of determining the absolute power-recycling cavity length, is from the coupling of a laser frequency test peak into the Michelson output signal, which is at a local minimum if f_{MI} matches an integer multiple of the FSR of the power-recycling cavity. This effect is enhanced by imperfect optics and is described in [Fre03b]. However, this signal does not contain suitable sign information, such that a control system would have to implement a modulation of the power-recycling cavity length or the Michelson Schnupp frequency. The resolution achieved with this measurement is currently of the order $10\ \mu\text{m}$. Compared to the length of the power-recycling cavity this is a relative accuracy of the order 1×10^{-8} .

All oscillators used for the various phase modulators within GEO 600 are phase locked to a GPS-locked clock which uses a rubidium oscillator to enhance the clock stability at intermediate frequencies. This time reference provides a relative accuracy of approximately 1×10^{-12} over a very wide range of frequencies, such that the accuracy of the absolute length measurement is dominated by the limited accuracy of the measurement techniques described above.

⁶labelled ‘DC lock camera’ in Figure 3.9 on page 82.

1.3 The electrostatic drive

Before going on with the Michelson interferometer, its main displacement actuator, the *electrostatic drive*, is explained in this chapter.

1.3.1 Overview

GEO 600 is the first of the large-scale interferometers that uses electrostatic drives as displacement actuators. The electrostatic drive (ESD) is an actuator capable of applying force to testmasses (which are the Michelson end mirrors in our case) by means of an electric field. By using this actuator instead of a standard coil/magnet system, it can be avoided to attach magnets to the testmass, which might degrade the thermal noise properties of the mirror.

The chosen ESD actuator design consists of thin gold electrodes ⁷ coated in a comb-like pattern onto the surface of a fused silica [Bea02] mass, which acts as a reaction body to the force applied. Figure 1.7 shows the electrode arrangement.

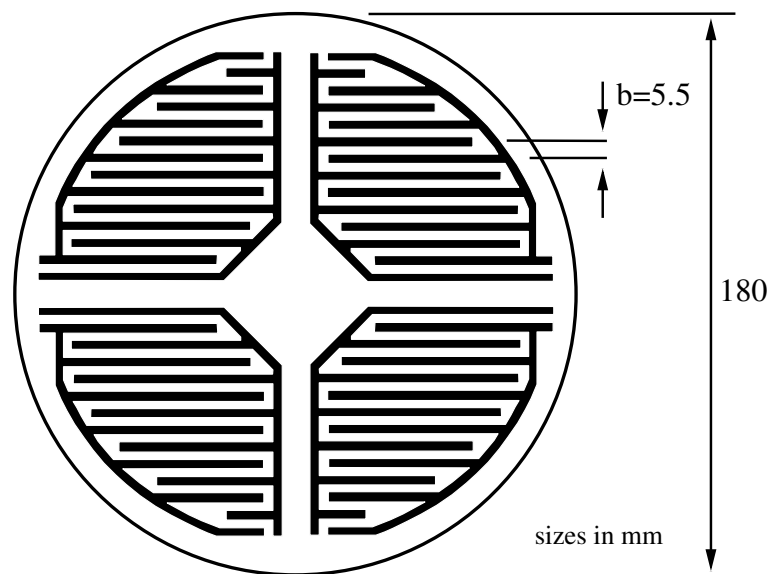


Figure 1.7: Electrode pattern of the electrostatic drive (ESD). The electrodes consist of gold stripes coated onto a fused silica mass of equal size to the testmass. The distance b between two adjacent electrodes is $b = 5.5$ mm. Four pairs of electrodes allow for a balancing of the applied force, as well as for the application of mirror alignment forces.

The distance b between two adjacent electrodes is 5.5 mm, suitable for a distance between the reaction mass and the mirror of $d = 1 \dots 3$ mm. Four pairs of electrodes allow for a balancing of the applied force (to minimize undesired force couplings into other degrees of freedom), as well as for the application of mirror alignment forces.

⁷Gold as electrode material has a smaller damping influence onto the testmass than, for example, aluminium [MST02].

The electrodes form a capacitor which partly ‘sees’ the mirror’s substrate as a dielectric. Applying a voltage to the electrodes pulls the dielectric into the electric field, hence the ESD can only apply pulling forces to a mirror.

Another important difference to coil-magnet displacement actuators is the fact that the force between the reaction mass and the mirror substrate is proportional to the square of the applied electric field (and thus to the square of the voltage applied). This is true because the electric field induces a polarization of the dielectric proportional to the field, while the force applied to the induced dipoles is again proportional to the external electric field.

Equation 1.1 gives a general form of the force F obtained.

$$F = U^2 * \epsilon \epsilon_r d^x a \quad (1.1)$$

U is the voltage applied, ϵ and ϵ_r are the dielectric constant and relative dielectric constant of the testmass substrate ($\epsilon_r = 3.77$ for fused silica), d (with exponent x) is the distance between the testmass and reaction mass, and a is a constant geometry factor depending on the electrode pattern design. Calculating F (which means calculating x and a) exactly from the known geometry is complicated, as the electric field is very inhomogenous at the distance used. Experiments with a drive of similar geometry (K. Strain: [Str02]) yielded $x \approx 1.5$ for $d < b$. The parameter a can be determined experimentally by measuring the f as a function of U .

1.3.2 Driving the ESD

In order to use the ESD as a bipolar displacement actuator, a constant bias force has to be applied by the ESD. Different configurations of distributing a bias voltage and the main signal (containing the information about the variable force to be applied) to the electrodes are possible:

1. A constant high voltage can be applied to one electrode (of each quadrant) while the symmetric signal is applied to the respective other electrode. To obtain a close to linear dependence of the force from the signal voltage, the bias voltage has to be significantly larger than the maximal signal voltage. The advantage of this solution is that the high bias voltage can be constant (and thus have particularly low noise for example) while the signal may be provided by standard operational amplifiers. The drawback of this method is the limited force range due to the fact that the signal voltage has to be smaller than the bias voltage to maintain the linearity. A slight variation of this approach is to add the (low voltage) signal to the (high voltage) bias, apply the sum of both to one electrode and the inverted sum to the other electrode. This can make the response more independent of any conductive material in the vicinity of the electrodes.
2. If a maximum force range is to be obtained while maintaining the linearity, the signal voltage can be pre-processed by computing its square root. The drawback of processing the square root is the noise introduced by this process (see text below). Using a square root only makes

sense if high voltage amplifiers are used to amplify the square-rooted signal. Otherwise the above method (1) would be more appropriate, since it yields a linear response without the necessity of a square-root circuit with its additional noise contribution. If a square-root circuit is used, the signal has to be biased before processing the root, such that the use of a separate constant bias voltage becomes obsolete in this case. The square-rooted and amplified signal can be applied to one electrode, while the respective other electrode of a quadrant is held to zero potential. Again it would also be possible to apply the inverted square-rooted signal to the other electrode, which requires another high voltage amplifier.

Currently a combination of both above possibilities is used in GEO 600. Using the ‘sqrt-circuit’ is mainly useful for the lock acquisition process, as here the full force range of the ESD is required. The square-rooted and amplified signal is applied to one electrode of each ESD quadrant. All adjacent electrodes are held to zero (or close to zero) electrical potential by the output of an individual operational amplifier for each quadrant (see the details on this setup in Figure 3.29 on page 112). If the signal is small with respect to the possible signal range (in the stable locked interferometer), the ESD force will be closer to a linear dependence on the drive voltage without processing the square root. As a future option, the signal without square-rooting can be applied to the operational amplifiers driving the opposite electrodes *after* the lock acquisition succeeded. The high voltage could then be made constant and filtered in order to reach a lower noise level.

Figure 1.8 shows the steps of processing the ESD voltage in the current setup. Names for the intermediate voltages are defined as required.

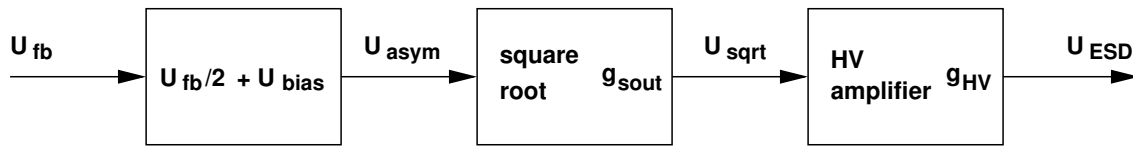


Figure 1.8: Signal chain from Michelson feedback point to ESD. The voltage at the Michelson feedback point U_{fb} is divided by two and then biased by adding voltage U_{bias} . The resulting asymmetric voltage U_{asym} is passed to the sqrt-circuit, multiplied with gain g_{sout} and then amplified by a high voltage amplifier with gain g_{HV} to yield U_{ESD} driving the ESD.

The voltage at the Michelson feedback point U_{fb} is divided by a factor of two, in order to fit within standard operational amplifier voltages after adding the voltage U_{bias} . The resulting asymmetric voltage U_{asym} is passed to the sqrt-circuit and its range is adjusted by multiplying gain g_{sout} to match the high voltage amplifiers input range⁸. The HV amplifier then multiplies by the gain factor g_{HV} to yield U_{ESD} driving one electrode of each ESD quadrant. Equation 1.2 shows how a symmetric voltage U_{fb} is translated to the asymmetric, square-rooted and amplified output voltage U_{ESD} .

$$U_{ESD} = \sqrt{(U_{fb}/2 + U_{bias}) \times 2U_{bias}} \times g_{sout} \times g_{HV} , \quad (1.2)$$

⁸Using the amplifier or attenuator stage g_{sout} allows the use of the full dynamic range of the sqrt-circuit, which is important for an optimal noise performance.

using $U_{\text{bias}} = 6\text{V}$, $g_{\text{sout}} = 0.8$ and $g_{\text{HV}} = 100$, we obtain

$$U_{\text{ESD}} = 679\text{V}, \quad (1.3)$$

resulting as ESD bias voltage for a zero input $U_{\text{fb}} = 0$.

The disadvantage of the sqrt-circuit is a large voltage noise level of $3\mu\text{V}/\sqrt{\text{Hz}}$ (in the band from 10 Hz to 10 kHz) at its output, which is about 1000 times larger than the input voltage noise of a standard low noise opamp. Figure 1.9 shows the displacement noise caused by the sqrt-circuit and the high voltage amplifier independently. The graph contains the measured electronic noise levels which are multiplied with the respective ESD's transfer function from drive voltage to displacement.

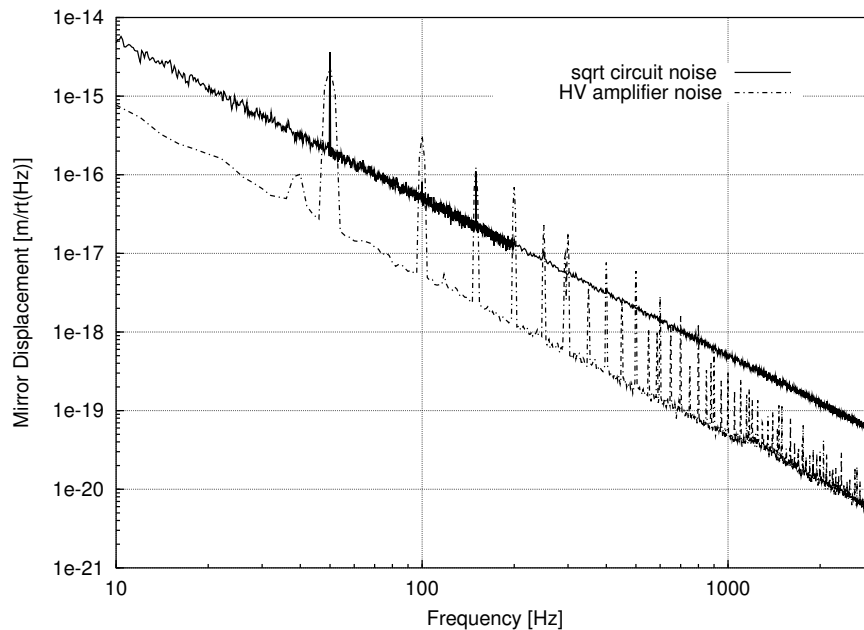


Figure 1.9: Main mirror displacement caused by HV amplifier noise and the square-root circuit preceding the HV amplifier input. The amplifier's DC output voltage was 500 V for this measurement.

The displacement noise of the sqrt-circuit is a factor of 10 larger than the displacement noise caused by the HV amplifier. In the final setup for GEO 600, no larger displacement noise than $2 \times 10^{-20} \text{m}/\sqrt{\text{Hz}}$ above 50 Hz can be tolerated. To achieve this goal, the sqrt-circuit has to be bypassed after the detector has acquired lock. This will likely be possible, as the maximum dynamic range of the ESD is only required during the lock acquisition process.

The HV amplifier's noise can be reduced if they are used in a closed loop system. The amplifiers feature a built-in monitor output, sampling the HV-output of the device. This output can be fed back to the amplifiers input, thus reducing the HV amplifier's output voltage noise. As the bandwidth of the amplifier is about 30 kHz, the noise suppression feedback can easily have a bandwidth of 5 kHz. With a simple $1/f$ gain rolloff, a gain of 100 at 50 Hz can be obtained, reducing the HV amplifier caused displacement noise to $3 \times 10^{-19} \text{m}/\sqrt{\text{Hz}}$. A further reduction of the effective noise level may be obtained by lowering the bias voltage applied after a stable lock is achieved.

1.3.3 ESD induced damping

As the ESD force depends on the distance d between drive and testmass, damping of the testmass has to be considered. A motion of the testmass around the nominal distance changes the capacity of the electrode pattern. Damping will take place if the change of capacity leads to energy dissipation in any real impedance of the high voltage amplifier output and the leads between the amplifier and electrodes. The dissipation loss can be translated to a quality factor Q of the pendulum damping if the dissipated energy per cycle is related to the total pendulum energy for a cycle with frequency ω . According to [Str02] we obtain

$$Q = \frac{4m\omega d^3}{C^2 R U^2} \quad (1.4)$$

with m being the equivalent mass of a mirror and the substrate carrying the ESD electrodes. C is the ESD capacity around the operation distance, R is the real part of the voltage source impedance, and U is the bias voltage permanently applied⁹. For GEO 600 we obtain:

$$Q = 7.5 \times 10^8 \left[\frac{m}{14 \text{ kg}} \right] \left[\frac{\omega}{5 \text{ s}^{-1}} \right] \left[\frac{d}{1 \text{ mm}} \right]^3 \left[\frac{C}{10 \text{ pF}} \right]^{-2} \left[\frac{R}{10 \Omega} \right]^{-1} \left[\frac{U}{600 \text{ V}} \right]^{-2}, \quad (1.5)$$

which should be sufficiently large compared to the pendulums inherent quality factor. Note that the damping according to (1.5) gets smaller with increasing frequency ω .

When the high voltage amplifiers which drive the electrostatic drives were first installed, output resistors of 40 k Ω were inserted to limit the possible output current. With $R = 40 \text{ k}\Omega$ and the other parameters as above, we get

$$Q \approx 2 \times 10^5, \quad (1.6)$$

which is probably unacceptable for the final design sensitivity, such that these resistors have to be removed at some point in time. On the other hand it might be possible to leave the resistors in, but use the noise suppression circuit described above, sampling the voltage to be controlled as close as possible to the vacuum feedthrough. The maximal possible current would still be limited with $R = 40 \text{ k}\Omega$, but the effective resistance would be reduced by the loop gain of the voltage regulating circuit.

⁹Equation 1.5 is valid under the assumption that the amplitude of the pendulum oscillation is smaller than the distance d . Furthermore, the voltage U at the ESD is assumed to be constant during the damping process. This is the case if $1/RC \gg \omega$.

1.3.4 Calibration and drift

An important value to measure is the calibration factor of the ESD and its variation over time. The calibration factor relates the frequency dependent test mass displacement or the force applied to the testmass to the voltage applied to the input of the sqrt-circuit or to the ESD's electrodes directly. In the usual experimental situation of testing feedback loops, the calibration factor giving displacement as a function of voltage input to the sqrt-circuit is most appropriate. Possible calibration methods are given in section 1.4.4.

The complex force applied by the ESD can be calculated by the displacement caused, which can be measured in the given interferometer setup. The force F computes to

$$F = 2x_{\omega}m((\omega_0^2 - \omega^2) + i\gamma\omega), \quad (1.7)$$

where x_{ω} is the displacement of the testmass at angular frequency ω , m is the mass of the testmass, ω_0 is the resonance frequency of the mirror pendulum stage, and γ is a damping factor. The factor of two is caused by the fact that the force is applied to the mirror *and* reaction mass, which is suspended similar to the mirror and has equal mass. Thus a force applied between the two masses results in an equally sized absolute displacement of mirror and reaction mass.

For $\omega \gg \omega_0$ Equation (1.7) simplifies to

$$F = -2x_{\omega}m\omega^2, \quad (1.8)$$

however it should be noted that internal mirror modes are not taken into account here. For $\omega \ll \omega_0$ (in particular for ω close to zero: at DC) we have

$$F = 2x_{\omega}m\omega_0^2. \quad (1.9)$$

In the first implementation of the ESDs in GEO 600, the testmasses were suspended with steel wires. A slightly higher calibration factor than expected sustained the assumption that a part of the force resulted from actuation of the ESD onto the suspension wires. In the standard setup, one electrode is biased with a positive voltage, while the other one is grounded, such that the biased electrode might have applied a direct force onto the grounded suspension wire. This is confirmed by the fact that symmetrically driving the electrodes (with a double voltage difference between the electrodes compared to the asymmetric case) did not show a significant increase of the calibration factor. In this case, forces on the wire from both electrodes cancel each other.

After the mirrors were suspended monolithically with fused silica wires, the calibration factor became slightly smaller. However, the calibration factors on the two different suspension types are hard to compare, as the gap between the ESD and the mirror has a large influence onto the

calibration factor (see equation 1.1), and can not be adjusted exactly to the same distance after changing the suspension.

With a mirror mass of $m = 5.6\text{ kg}$ the corresponding force according to equation 1.8 is ¹⁰

$$F = 47 \times 10^{-6} \left[\frac{\text{N}}{\text{V}_{\text{rt.in}}} \right]. \quad (1.10)$$

With the maximum possible voltage range $-12\text{ V} < \text{V}_{\text{rt.in}} < +12\text{ V}$ we get an ESD force range of $F \approx 1\text{ mN}_{\text{pp}}$. The usable one sided peak force F_p is half of this value, and is used in section 1.4.3 to calculate the lock acquisition performance with the ESD.

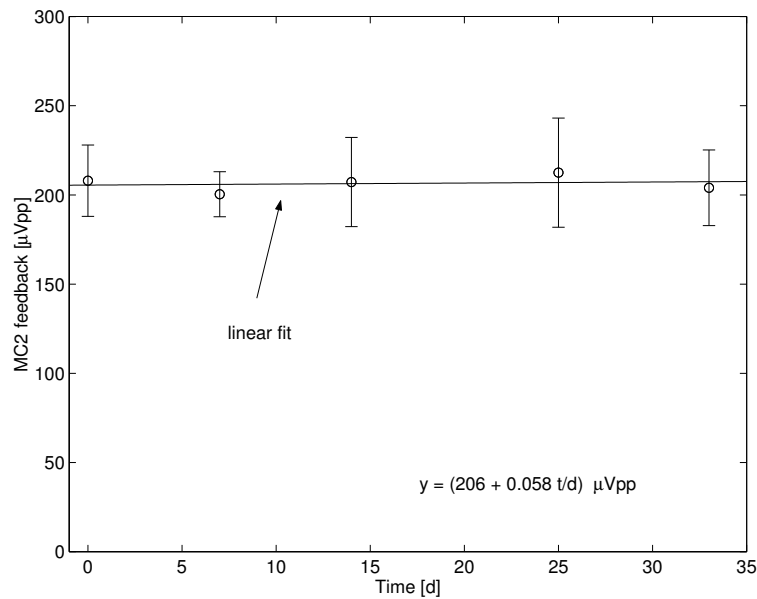


Figure 1.10: Calibration factor of the east electrostatic drive over one month. The errorbars on the 5 data points reflect the fluctuation of the optical gain included in the calibration over a timescale of seconds. The drift of the calibration factor judged by the linear fit yields a drift of less than 3×10^{-4} per day.

Concerning the variation of the calibration with time, after pumping down of the system the ESD calibration factor was about two times larger than two weeks later. A possible reason might be a static charge on the testmass facing the ESD, which dissipated with time. Negative static charges (electrons) increase the calibration factor of the asymmetric drive using a positive bias voltage. However the calibration factor during the two week test run in 2002 showed a fairly constant calibration factor. After the settling of the calibration factor, the calibration of the east ESD was measured over one month, shown in Figure 1.10. These calibrations were done with the second method described in section 1.4.4, applying $U_{\text{fb}} = 6\text{ V}_{\text{pp}}$ at $f = 281\text{ Hz}$ to the east ESD and measuring the feedback voltage to mirror MMC2b.

¹⁰The displacement Δl of mirror **MCe** during calibration computes as follows: We have a modecleaner calibration factor $C_{\text{MC2}} = 4.6\text{ kHz/V}$ at $f = 281\text{ Hz}$. This translates to the displacement Δl according to $\Delta l = 2l\Delta f/f$. With the measured $U_{\text{MC2}} = 207\text{ }\mu\text{V}_{\text{pp}}$, $l = 1200\text{ m}$ and $f = 282\text{ THz}$ we get a $\Delta l = 8.1\text{ pm}_{\text{pp}}$. Note that this calculation is only valid if the calibration signal is applied to only one ESD.

The errorbars on the 5 data points reflect the fluctuation of the optical gain included in the calibration over a timescale of seconds. The drift of the calibration factor is judged by the linear fit, which yields a drift of less than 3×10^{-4} per day ¹¹.

1.4 Michelson lock

The Michelson interferometer (for short *Michelson*) is the basic instrument for the detection of differential length changes and thus gravitational waves. It is operated in the so called ‘dark fringe’ condition, in which ideally all carrier light incident to the Michelson from the input side is reflected back towards the power-recycling mirror, which enables the use of power recycling. The performance of the control system keeping the Michelson at the dark fringe operating point is crucial to achieving the overall design sensitivity. Deviations from the dark fringe increase noise couplings, for example, the coupling of amplitude noise into the Michelson output signal. Sufficient loop gain is necessary in order to compensate the free longitudinal motions of all suspended mirrors due to seismic ground motion.

Figure 1.11 shows the control scheme of the Michelson lock. The beam incident on the power-recycling cavity is phase modulated with EOM5 at a frequency f_{MI} , which we also call the *Michelson frequency*. f_{MI} is adjusted such that the phase modulation sidebands are resonant within the power-recycling cavity. This modulation scheme and the generated sidebands are called Schnupp modulation [Sch88] (also known as frontal modulation) and Schnupp sidebands, respectively.

For the power-recycled Michelson lock, a phase modulation frequency of $f_{\text{MI}} = 14.904920 \text{ MHz} \pm 20 \text{ Hz}$ is used, which is the 119th multiple of the FSR of the PR cavity, being $125251.4 \pm 0.2 \text{ Hz}$ ¹². This choice of modulation frequency just below 15 MHz was made in order to be able to use a HP30625A function generator which has the smallest phase noise of all the generators that were investigated for this purpose.

The Michelson arms have an intentional arm length difference (the Schnupp asymmetry) which was measured to be 69 mm. As a consequence, the Schnupp sidebands do not completely cancel at the Michelson output and beat with carrier light leaving the dark port in case of deviations from the dark fringe (heterodyne detection). The resulting signal is detected with photodiode PDO, demodulated with a properly phase shifted local oscillator at f_{MI} and serves as the error signal for the Michelson control loop. The actuation onto the differential Michelson arm length is split into two paths, using different electronic filter stages and actuators for each path.

The feedback signal applied to the two electrostatic drives passes two sqrt-circuits and a separate high voltage amplifier for each of the two ESDs is required. The amplifiers are TREK 601 c devices with an output range of -50 to +1000 V and a fixed gain of 40 dB. Low frequency feedback (below

¹¹Note that the applied calibration method assumes a constant calibration factor of the coil-magnet actuator at mode-cleaner mirror MMC2b. Thus the estimated drift rate is an upper limit for the drift of the modecleaner calibration as well.

¹²The errors on these frequencies represent the fact that the PR cavity length drifts with time. Its absolute length will be controlled with a slow servo (‘DC lock’) in the final setup of GEO 600, as stated earlier.

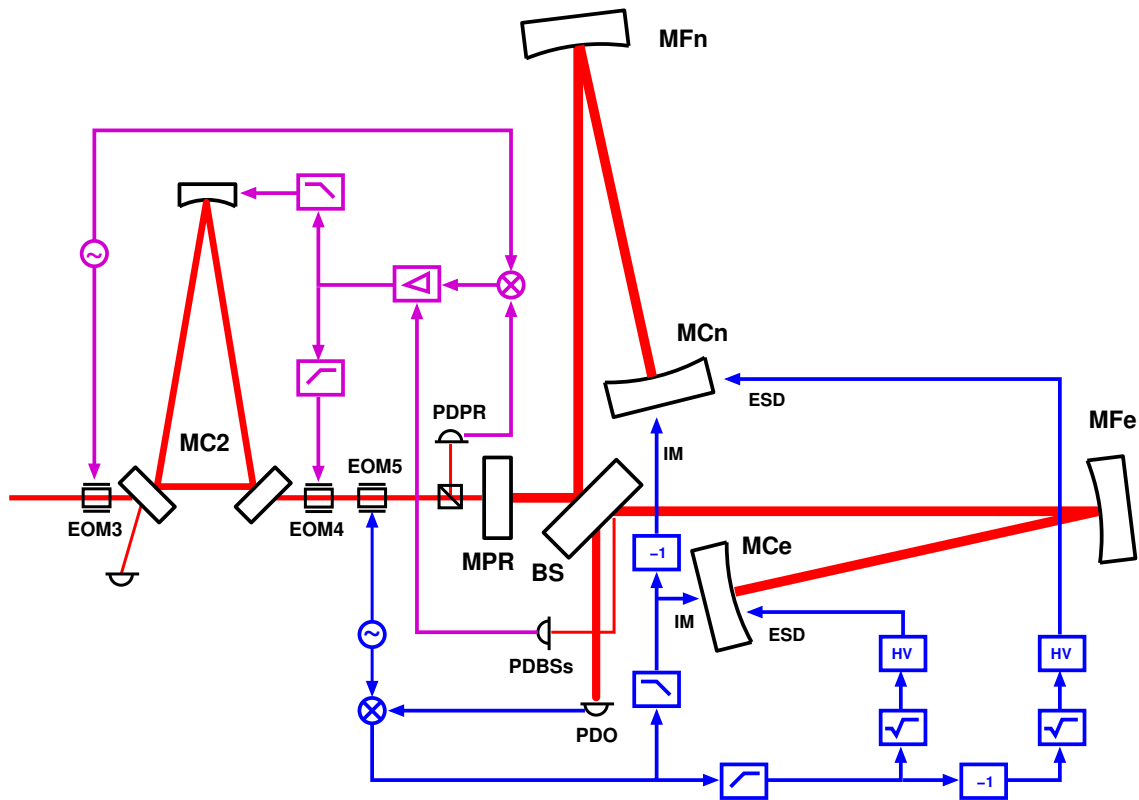


Figure 1.11: Michelson length control scheme. The power-recycling lock and the frequency control for MC2 (which is omitted for clarity) are identical to Figure 1.2. The incident beam on the power-recycling cavity is phase modulated by EOM5 with $f_{MI} = 14.904920\text{MHz} \pm 20\text{Hz}$ to give sidebands on the carrier light which are resonant within the power-recycling cavity. A small fraction of these Schnupp sidebands leave the beamsplitter towards detector PDO where they interfere with carrier light when the Michelson deviates from the dark fringe operating point (heterodyne detection). The resulting signal is demodulated with f_{MI} and fed back to the longitudinal position of end mirrors **MCE** and **MCn** differentially. The feedback path is split into two actuators: The intermediate mass (IM) and the electrostatic drive (ESD).

10 Hz) is applied to coil-magnet actuators mounted on the ‘intermediate mass’ pendulum stage above the testmass.

1.4.1 Determining the Schnupp frequency

In order to find the exact FSR of the power-recycling cavity and thus the proper Schnupp modulation frequency, the absolute optical path lengths from the power recycling mirror (**MPR**) to both end mirrors were measured by determining resonance frequencies of single arm cavities. For measuring the path length from **MPR** via **BS** and **MFe** to **MCE** for example, mirror **MCn** was misaligned. This configuration forms a Fabry-Perot cavity consisting of **MPR** and **MCE** with losses introduced by **BS**. An approximate value for the FSR of the power-recycling cavity can be calculated by the nominal mirror positions. The 119th multiple of this approximated FSR was applied as Schnupp modulation frequency and the coherently demodulated signal was observed at the Michelson (south) output. Sweeping the modulation frequency by several kHz, a minimum

in the signal can be observed if the initial frequency is close to an integer multiple of the FSR. By choosing the proper center frequency for the sweep, the pattern across the sweep can be made symmetrically, thus determining the proper Schnupp frequency.

The frequencies obtained were $14.904550 \text{ MHz} \pm 70 \text{ Hz}$ for the east arm, and $14.905400 \pm 50 \text{ Hz}$ for the north arm. The average of these frequencies is 14.904975 MHz , and with

$$l = \frac{cn}{2f} \quad (1.11)$$

(with n as the integer number of the FSR used) we get a length of the power-recycling cavity of $l = 1196.758 \text{ m}$. The resulting individual arm lengths are 1196.793 m for the east and 1196.724 m for the north arm. Thus the resulting arm length difference is 69 mm , as stated above. These measurements were done with the steel wire suspensions for **MCe**, **MCn** and **BS**. After the installation of the monolithic suspensions, the resonance frequency of the PR cavity was measured to be 14.904920 MHz , yielding a length of the PR cavity of $l = 1196.763 \text{ m}$. This shows a change of 5 mm , mainly caused by slightly different installation positions of the mirrors. Current indications are that the length drifts over a few months due to small temperature changes seem to be less than 1 mm .

1.4.2 Feedback design

1.4.2.1 Actuators

As we have seen, the locking of the Michelson interferometer to the dark fringe is achieved by acting differentially on the longitudinal positions of mirrors **MCe** and **MCn**. Figure 1.12 shows a (double) triple pendulum suspension with the arrangement of local control coils around the upper mass stages. Two individual suspension chains are used to suspend a mirror and a reaction-mass separately, in order to be able to apply control forces without introducing excess seismic noise. This kind of assembly is used for the endmirrors **MCe** and **MCn** located in the central building, while a single suspension of this type (without the reaction-mass chain) is used for the beamsplitter **BS** and the far mirrors **MFe** and **MFn**.

For the longitudinal actuation on **MCe** and **MCn** two actuators are used: A coil-magnet stage (not shown in Figure 1.12) at the intermediate mass, from which the mirror is suspended, and the electrostatic drive acting on the mirror level. A third stage of actuation (using coils and magnets) modifies the longitudinal positions of mirrors **MFe** and **MFn** at the upper mass level to compensate for differential arm length drifts with large amplitudes. This is important for long term locking and is only done for frequencies below 0.1 Hz (see section 1.6.4).

The main advantage of using the ESD rather than a coil-magnet system at the mirror level is, that no magnets have to be connected to the mirror. As magnets are subject to time dependent magnetic field gradients (at e.g. power line frequencies), such fields can directly produce unwanted forces onto the mirror. Moreover the attachment of small rigid bodies onto the mirrors might spoil the

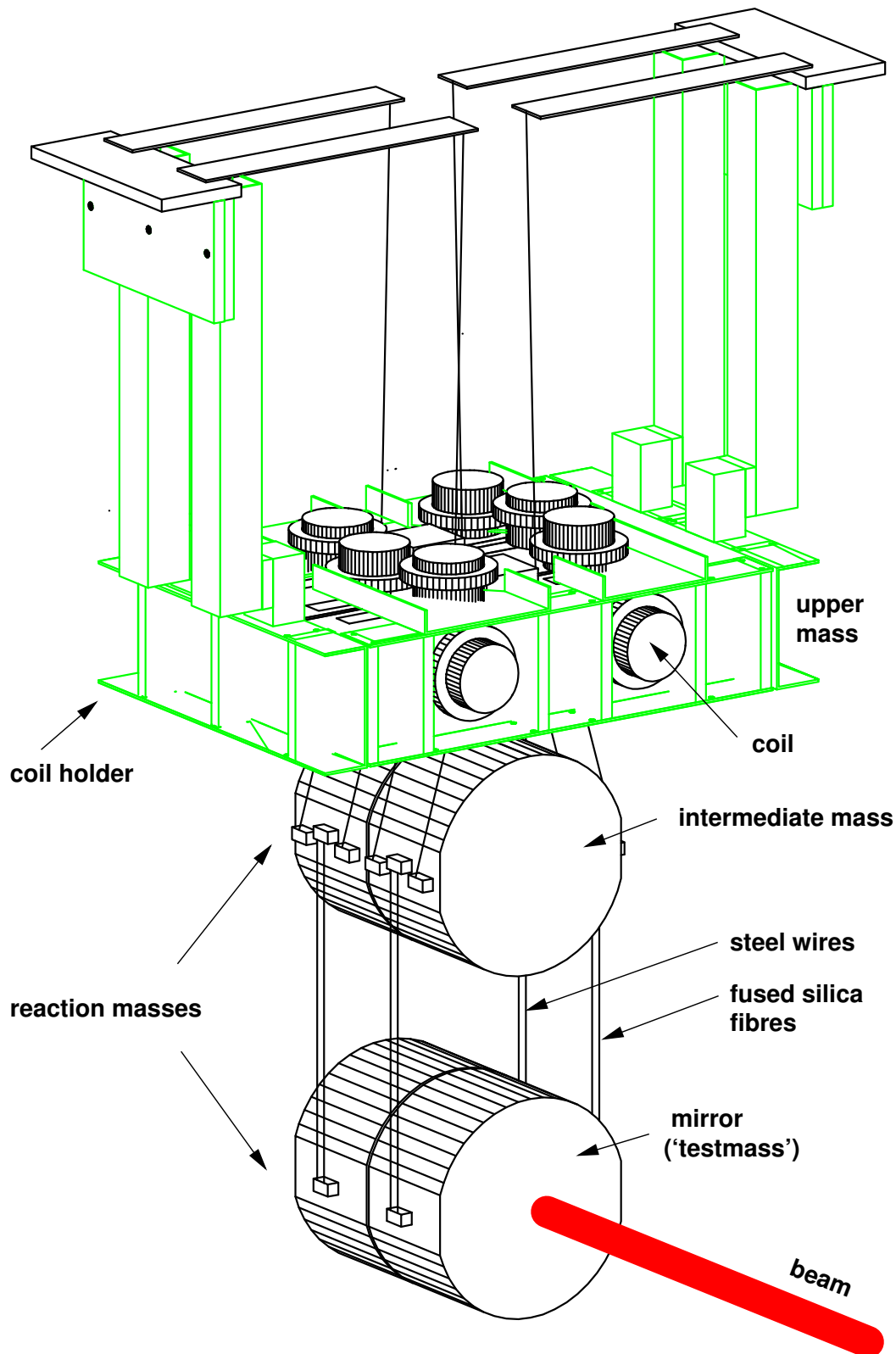


Figure 1.12: Triple pendulum suspension with local control coils around the upper mass shown. The arrangement implemented for **MCE** and **MCn** is shown, including a complete reaction mass suspension chain. The coil holder is carried by three 'stacks' (not shown) which are supporting structures, containing sensors and actuators for active seismic isolation.

very high quality factors of the mirror eigenmodes, thus possibly increasing the thermal noise level.

Using an electrostatic drive comes at the price of a smaller maximal force of this actuator (see section 1.4.3), which leads to the more complex design of split actuation, using a coil-magnet stage with larger force at the intermediate mass stage in conjunction with the ESD at the mirror level.

1.4.2.2 Loop filters

Figure 1.13 shows the gain and phase of the electronic filters, multiplied with the modelled transfer functions of the actuators. The resulting functions represent the open loop transfer functions of the Michelson lock.

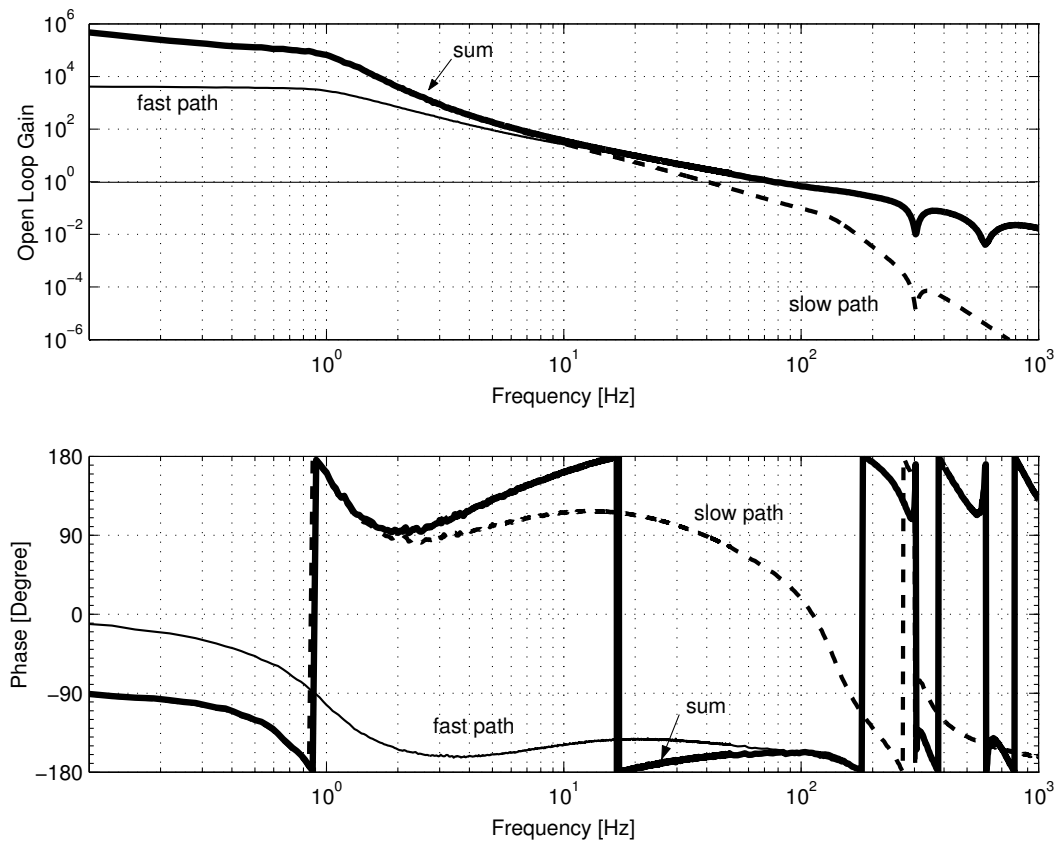


Figure 1.13: Open loop gain and phase of the Michelson lock. The transfer functions of the loop electronics for the slow and fast path were measured and multiplied with the modelled transfer functions of their corresponding actuators. The ‘sum’ plot shows the (complex) sum of both paths. The crossover frequency between the two actuators is around 10 Hz.

The gain curves show that the crossover frequency between the slow path (which serves as the intermediate mass coil-magnet actuator) and the fast path (ESD) is around 10 Hz. The overall unity gain frequency is slightly below 100 Hz. The control loop is designed to be only conditionally

stable, as a large gain is needed around 1 Hz which is achieved by steep integration of the signal below 10 Hz. Although the phase margin is only about 20° , the loop is stable over long time periods.

Initially the design of the feedback electronics was such that a unity gain frequency of 300 Hz could be achieved. However, it turned out that this loop was unstable due to oscillations at the violin mode frequencies (around 300 Hz) of the initial steel wire suspension of **MCe** and **MCn**. With the monolithic suspension of these mirrors, the violin modes are around 650 Hz, giving rise to the possibility of a higher control bandwidth.

The main problem with the steel wire suspension at **MCe** and **MCn** seems not to be the fact that the violin modes are close to the unity gain point, as experiences from prototypes show that this setup worked. The problem may have to do with the combination of electrostatic drive and steel wire suspension. A possible explanation for the loop instability at the violin mode frequencies could be that the ESDs apply forces not only to the mirror surface, but also directly to the steel wires. One indication for this fact is, that the force calibration of the ESD in case of applying e.g. 500 V against 0 V is larger than in the symmetric case of applying 250 V against -250 V. In the latter case the unipolar forces to the steel wire close by (which always has the electrical potential of 0 V) are zero.

To make the loop stable with a bandwidth of 100 Hz in conjunction with the steel wire suspension, it was necessary to implement notch filters in the feedback electronics, in particular for the fast path to the electrostatic drives. Figure 1.13 shows the effect of a notch filter at 300 Hz common to both paths and another filter at the second harmonic at 600 Hz for the fast path. With the change to the monolithic suspension, the notches were tuned to 650 Hz and 1300 Hz respectively, to match the new violin mode frequencies.

1.4.2.3 Locking performance

Figure 1.14 shows the longitudinal feedback applied to the intermediate mass level that is required to keep the Michelson interferometer locked. Above 10 Hz, the feedback is dominated by the ESD, while below 0.1 Hz, feedback is applied to the far mirrors, which is described in section 1.6.4. The rms value in the shown band from 0.5 Hz to 10 Hz is dominated by the micro-seismic peak around 0.15 Hz and amounts to about $1 \mu\text{m}_{\text{rms}}$. However, the micro-seismic peak does not have a constant amplitude. As it is partially caused by sea waves hitting the coastline of the north sea, it depends on weather conditions and energy stored in sea waves.

Dividing the feedback signal by the (slow path) open loop gain of the servo shown in Figure 1.13 reveals, that the rms deviation of the Michelson from the dark fringe is a few pm, depending on the actual gain and seismic noise¹³. The same information can be obtained of course by a direct measurement of the calibrated Michelson error signal spectrum.

¹³This seems satisfying for the final requirement, but likely some safety factor has to be added, which could be obtained with the larger bandwidth possible with the monolithic suspension.

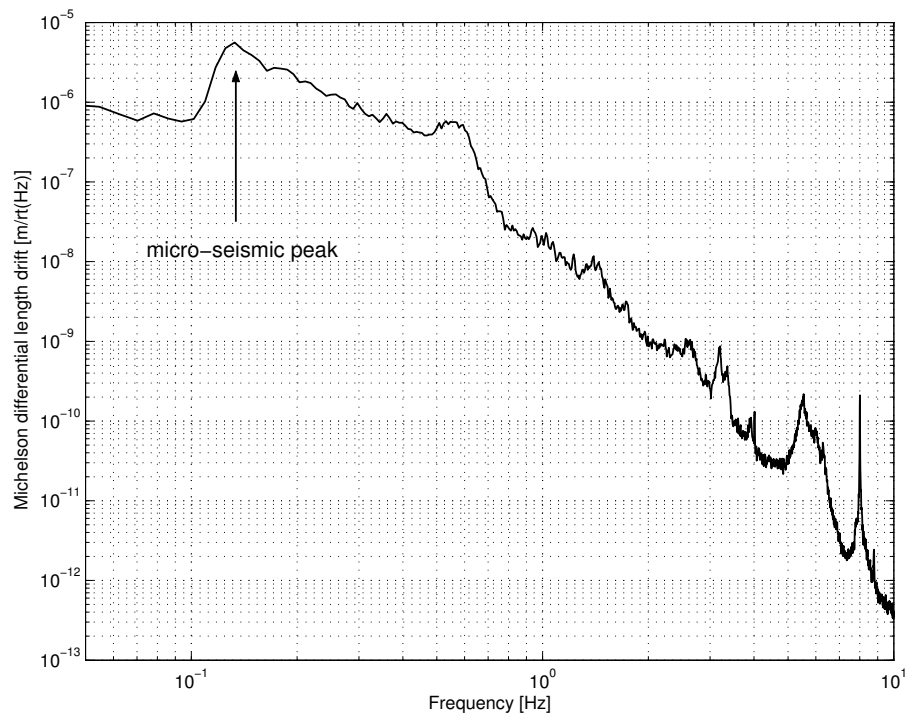


Figure 1.14: Longitudinal feedback to the intermediate mass, multiplied with the pendulums transfer function. This graph shows the longitudinal length correction that has to be applied in lock, in order to keep the Michelson interferometer at the operating point. In this particular measurement, the micro-seismic peak around 0.15 Hz dominates the rms motion.

1.4.3 Lock acquisition

The crucial point in lock acquisition is the question of whether or not the Michelson actuators at mirrors **MCE** and **MCn** can accelerate the mirrors fast enough to keep the differential arm length within the capture range of the error signal. Figure 1.15 shows the simulated Michelson error signal in case of a power-recycling mirror with $T_{PR} = 1.35\%$.

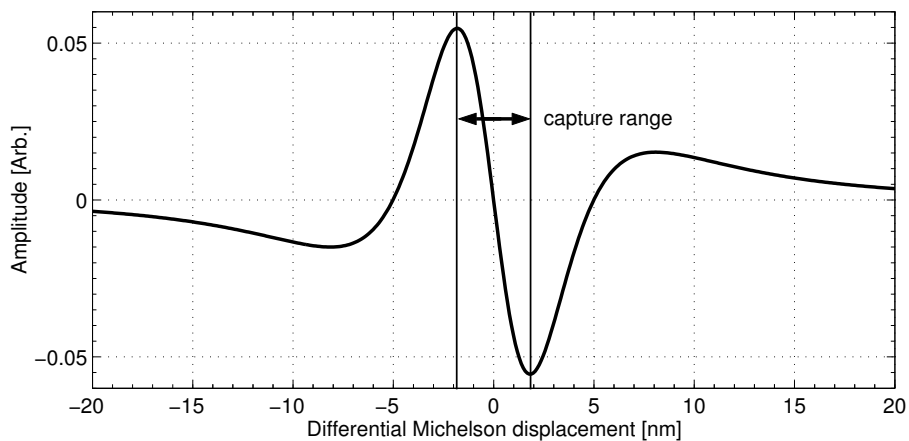


Figure 1.15: Simulated Michelson error signal. A (double sided) capture range can be defined as indicated.

A capture range d_c can be defined as indicated, which we call the double sided capture range, as it spreads symmetrically around the central zero crossing of the signal. We read a capture range of $d_c = 3.6\text{nm}$. The axis label ‘Differential Michelson displacement’ means that **MCE** and **MCn** are displaced into opposite directions by the denoted amount.

How large is the maximum mirror speed allowed to enable lock acquisition given the maximum force the ESDs can apply? The kinetic energy of a mirror computes to $W_{\text{kin}} = mv^2/2$, with m as mirror mass and v as the speed of the mirror. The ESD can apply an energy $W = Fs$ with F being the maximum ESD force and s the distance over which F is applied¹⁴. With $mv^2/2 = Fs$ we get

$$v = \sqrt{\frac{2Fs}{m}}. \quad (1.12)$$

If feedback is switched on at the central zero crossing of the error signal, the usable capture range will be $d_c/2$. With a maximum force of $F_p = 500\mu\text{N}$, $m = 5.6\text{kg}$ and $s = 1.8\text{nm}$ we get $v_{\text{max}} \approx 500\text{nm/s}$. Note that this result is valid for **MCE** and **MCn** individually. It assumes the same usable force and the same speed of both mirrors. Given an average fringe rate of the free Michelson of 2-3/s, it gets clear that lock acquisition is possible on most of the fringes with this setup, which is confirmed by the experiment. However acquisition would be much harder with a smaller capture range, like in the case for a higher power recycling factor.

Figure 1.16 shows time series of the Michelson error signal, the reflected light power from the power-recycling cavity and the light power inside the Michelson (measured by the beam from the beamsplitter’s AR coating side, detected with PDBSs - see Figure 1.11). The PR cavity is locked while the Michelson mirrors are oscillating freely without control of their longitudinal positions. Five *fringes* (transitions through the dark fringe operating point) occur within two seconds, representing a typical fringe rate of about 2-3/s. The error signal has the expected shape (see [Hei99a] and [Fre03b] for simulations of the error signal) with the dark fringe operating point at the central zero crossing of the fringe structure.

The slope of the PR reflected power signal is zero at the operating point, while there are two minima symmetrically around the operating point. These minima indicate the impedance matched state of the PR cavity, where the reflectivity of the MI interferometer equals the PR mirror’s reflectivity (losses included). Between these two minima the PR cavity is overcoupled. In the final GEO 600 setup the PR mirror’s transmittivity will be around 0.1 %, keeping the PR cavity closer to the impedance matched state than with the 1.4 % mirror currently used.

Looking at the error signal it can be seen that the sign of the feedback loop is only correct within a finite deviation of the Michelson tuning from the dark fringe. This fact represents the main difficulty in acquiring the locked state of the Michelson: The longitudinal force applied to **MCE** and **MCn** during lock acquisition has to be large enough to hold the Michelson error signal within the capture range.

¹⁴We are safe to assume $s \ll d$ (d is the distance between ESD and mirror), such that F can be taken as constant.

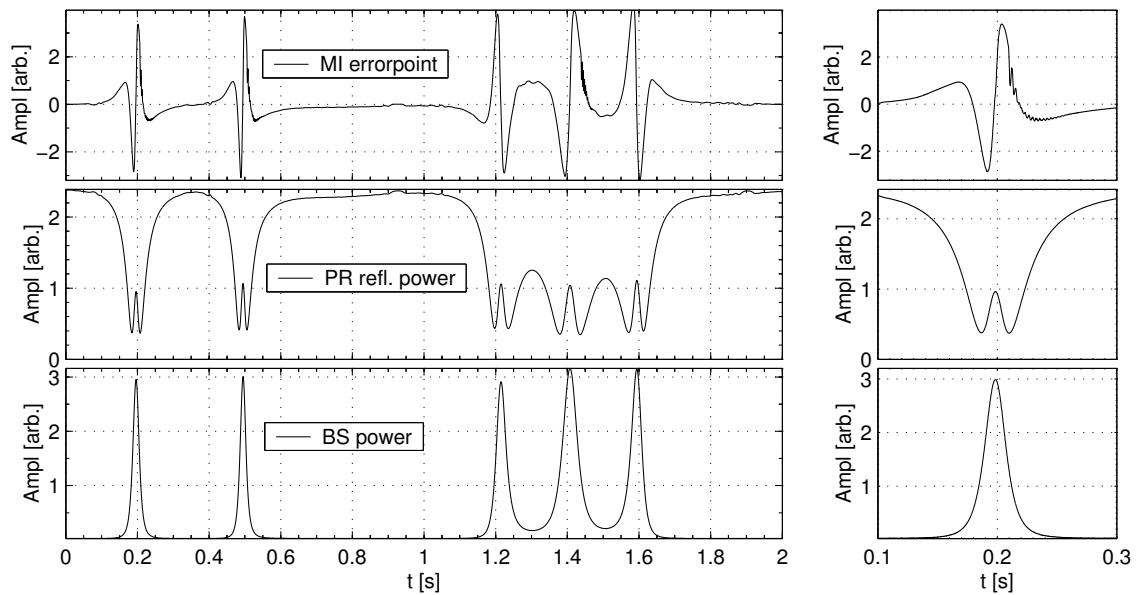


Figure 1.16: The free moving Michelson. From top to bottom: Michelson error signal, reflected light power from PR cavity and light power at the beamsplitter. The time series show the Michelson interferometer in free motion (not locked) while the PR cavity is locked. The right column shows a close-up of the first fringe on the left side.

As the displacement response of the intermediate mass actuator is proportional to f^{-4} (with f being the Fourier frequency) above the pendulum's main resonance, it is not a suitable device for the fast actuation required to stop the mirrors within the capture range. While possible in principle, this requires very large amplitudes, which in turn affect alignment and other suspension modes, making the whole acquisition process unstable. Therefore, the initial acquisition has to be done with the ESD, with the given limitation of its small force range. Switching on the ESD *and* IM feedback at the same time fails in almost all cases, because the initial feedback to the intermediate mass is too large. Therefore the intermediate mass feedback is added a few 100 ms after the ESD has been switched on, when the error and feedback signals have already settled a bit. In order to be able to do this, the ESD feedback has to be stable even without the intermediate mass feedback being active. This has to be taken into account in the loop design.

Historically this was one of the difficulties in achieving the first GEO 600 power-recycled Michelson lock. In the first locking experiments, the ESD feedback was heavily saturated by various noise sources. One of these sources was caused by the low light level inside the power-recycling cavity, due to high losses introduced by the initial beamsplitter, such that the signal to noise ratio was reduced. Another problem concerned pickup at the Schnupp modulation frequency, which was caused by strong radiation of the EOM driver due to sub-optimal ground paths of the modulator. This led to a strong radiation at the modulation frequency, being modulated by power line harmonics. After pickup and demodulation, the line harmonics were amplified with the large gain required for the ESD feedback, which lead to saturation at the line frequencies.

Figure 1.17 shows time series of relevant signals for a successful acquisition of the Michelson. The ESD feedback is switched on by a microcontroller at the time of a zero crossing of the Michelson

error signal, if the power level inside the power-recycling cavity has reached a minimum threshold level.

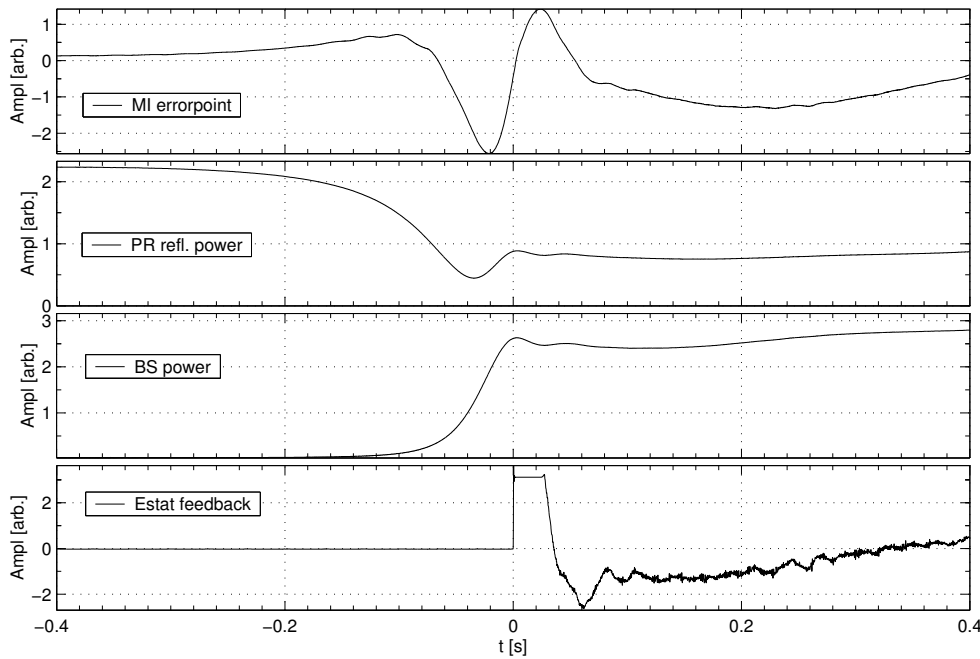


Figure 1.17: A successful lock acquisition of the Michelson interferometer. From top to bottom: Michelson errorpoint, power-recycling cavity reflected power, **BS** power (sampling the power in the east arm) and feedback to electrostatic drive. The ESD feedback is switched on at the time of a zero crossing of the Michelson error signal.

As GEO 600 evolves through different optical setups during the commissioning phase, the capture range and slope of the Michelson error signal changes significantly. The decreasing capture range in the series of optical changes makes the lock acquisition more difficult, while the increasing slope reflects the growing sensitivity of the instrument which has to be accommodated by adjusting the range of the output detector. Table 1.1 shows the calculated Michelson error signal's capture range and slope for different setups ¹⁵.

An additional increase of the slope (but not of the capture range) of factor 5 can be achieved by increasing the laser power from 1 W to 5 W at the input to the power-recycling cavity. This step will likely take place before the installation of the final MPR.

Lock acquisition with $T_{\text{MPR}} = 0.1\%$ will require a smaller fringe rate than 2-3/s or a significantly stronger ESD actuator (which would require high-voltage amplifiers with several kV output range). If neither can be obtained, one would have to wait for too long (of the order of minutes) for a sufficiently slow fringe. This is a problem as the alignment drift makes it hard to keep the required alignment accuracy within this time frame (see also section 3.2). If a lower fringe rate (for example by improving the local damping of the involved pendulums or the active seismic isolation system) cannot be achieved, a more drastic possibility could be to lower the finesse of the power-recycling

¹⁵The calculations are done with FINESSE.

Optical configuration with:	capture range [nm]	slope [Arb.]
BS with 7.5 % loss	9.5	0.0018
BS with 1 % loss	4.7	0.027
BS with 50 ppm loss (used for all below)	3.7	0.075
DR 1 %, 20 kHz detuned	3.5	0.01
DR detuned, final MPR (0.1 %)	1.2	0.02
DR broadband, test MPR (1.4 %)	0.5	0.5
DR broadband, final MPR (0.1 %)	0.15	2

Table 1.1: Capture range and slope of the Michelson error signal for different optical setups of GEO 600. BS: beamsplitter, DR: dual recycling.

cavity for the purpose of lock acquisition. Whether this is possible by artificially introducing losses inside the power-recycling cavity during acquisition remains to be seen.

1.4.4 Longitudinal calibration

Longitudinal calibration comprises the tasks of determining calibration factors for the Michelson error signal (which we also call the optical gain) and the intermediate mass (IM) and ESD actuators. The calibration process discussed here assumes a frequency independent sensitivity of the detector. For the power-recycled Michelson this is a good approximation, while it is no longer true for the signal recycled interferometer.

There are at least three independent methods, of which two have already been applied:

- Fringe counting by acting onto the intermediate mass actuator.
- Applying an asymmetric signal to one of the Michelson arms (using the IM or ESD actuator) which will show up as a length change of the power-recycling cavity and can then be traced back to the laser frequency calibration.
- Using a photon drive, whose action onto a testmass displacement is calculated from known parameters as the photon drive power, angle of incidence onto the mirror, etc.

For calibrating the intermediate mass feedback, a very simple method is the application of a low-frequency¹⁶ signal of known size. If the Michelson interferometer is not locked, the time sequence of constructive and destructive interference can be counted, with N being the number of complete interference cycles for an input signal of size S . The resulting calibration factor C_{IM} is

$$C_{\text{IM}} = \frac{N\lambda}{2S} \quad (1.13)$$

¹⁶Significantly lower than the lowest IM suspension longitudinal resonance frequency, which is at about 0.6 Hz.

with λ being the light wavelength. Multiplying this DC calibration factor with the pendulum's transfer function (which can be measured in lock) yields the actuator's calibrated transfer function. The calibration factor of the optical gain can then be obtained by applying a signal of known size to the intermediate mass, and observing its response into the Michelson errorpoint. The same can be done for the ESD: Applying a signal at an appropriate frequency to the ESD and measuring the response to the IM or Michelson errorpoint, where the calibration was obtained before.

The second method uses the fact that changing the length of only one arm of the Michelson interferometer introduces a common mode length change of half that size, which is identical to a length change of the power-recycling cavity. As the laser frequency is locked to the power-recycling cavity, the applied signal can be traced back to the laser, where the frequency calibration is done with another independent method. With this method the IM and ESD drive can be calibrated, whereas the optical gain can then be determined by applying a signal of calibrated size to either drive.

The last method is about to be installed, applying a modulated longitudinal force to one of the end mirrors (**MCE**) by photon pressure [CNSH01]. This gives a direct calibration of the optical gain, and in turn the IM and ESD drives can be calibrated by observing applied signal sizes in the Michelson output. By using a comb of different frequencies the frequency dependence of the optical gain can also be determined by this method in the case of dual recycling.

The first two methods for calibration have been used to date, and their results agree to within 15 %. (See [HGH⁺03] for a more detailed discussion of the calibration of the power-recycled Michelson in GEO 600.)

1.4.5 The evolution of lock

1.4.5.1 Mid fringe lock

The so-called 'mid fringe lock' was the configuration in which the GEO 600 Michelson interferometer was locked for the first time. In this configuration the power-recycling mirror, **MPR**, was misaligned such that it merely attenuates the light incident onto the Michelson interferometer, but does not form an optical cavity with the Michelson. No modulation technique is used to obtain an error signal, but the light power at the Michelson output is read out with an offset being subtracted, yielding a symmetric error signal around the 'mid fringe'.

The advantage of this method is a very large capture range of the order 100 nm, such that it was possible to study acquisition and achieve the first lock with the intermediate mass feedback only. This enabled calibration of the electrostatic drives which in turn enabled finalizing the crossover design between ESDs and IM actuators.

1.4.5.2 Test PRMI

After these first tests, the Michelson interferometer was locked in the power recycling mode, using ESD feedback for the lock acquisition of the Michelson and adding IM feedback shortly

after the acquisition. Under the label *Test PRMI* we summarize three subsequently implemented configurations:

- *Initial PRMI-A*: A test beamsplitter with a power reflectivity of the AR-coated side of about 7%; test optics for **MCe**, **MCn**, **MFe** and **MFn** with all mirrors being suspended in steel wire slings. Due to the power losses at the beamsplitter, the capture range was relatively large with a low power buildup inside the power-recycling cavity.
- *Initial PRMI-B*: The test optics of **MFe** and **MFn** were replaced by the monolithically suspended final mirrors. No major changes in the locking behaviour of the power recycled Michelson were observed.
- *Initial PRMI-C*: The beamsplitter was replaced with another test beamsplitter with an AR-coating reflectivity of about 1000 ppm. The power buildup of the power-recycling cavity increased accordingly and the capture range of the Michelson decreased slightly.

1.4.5.3 Final PRMI

In the *final PRMI* configuration, the test optics of **MCe**, **MCn** and **BS** were replaced with the monolithically suspended final optics. With this new setup, some features of the power-recycled Michelson lock changed significantly:

- The final optics have different radii of curvature. Thus they change the output mode pattern and losses, which in turn affects the signal to noise ratio. It turned out that the far mirrors **MFe** and **MFn** have a mismatch in radii of curvature that was partially compensated by a mismatch of the old near mirrors **MCe** and **MCn**. With the new near mirrors the Michelson contrast got worse and as a consequence, the Michelson interferometer also became more sensitive to misalignments. The frequency noise coupling gets larger with the reduced contrast. As absolute lengths changed, the Schnupp frequency had to be adjusted.
- The main resonances of the suspension are at different frequencies, because of a changed mass distribution (the final mirrors have a different mass than the test mirrors). This is important for the Michelson longitudinal lock and fast alignment system. An instability of the longitudinal Michelson lock appeared at 22 Hz and 31.75 Hz. Suppression of the excitation of these modes in lock with notch filters was necessary for the longitudinal as well as for the alignment feedback.
- The violin modes of the suspension changed in frequency and quality factor, which is important for the design of the Michelson longitudinal lock. Notch filters had to be adapted in frequency accordingly.

The mismatch in radii of curvature of **MFe** and **MFn** had the largest impact on the experimental progress. A stable lock of the power-recycled Michelson was not possible with the large power

mirror	measured ROC	design ROC
MCe	622 ±10 m	600 m
MCn	636 ±10 m	600 m
MFe	687 ±2 m	640 m
MFn	666 ±2 m	640 m

Table 1.2: In situ measured and design radii of curvature of the four final Michelson mirrors.

losses at the Michelson output of the order of 1 %. Table 1.2 shows the (in situ) measured and the nominal radii of curvature for the four final Michelson mirrors.

The installation of a heater, designed to change the radius of curvature of **MFe**, was required to cure the problem. With the technique of radiation heating of the mirror's rear face (the anti-reflective coated face) along the outer rim, the substrate on the rear face expands and 'bends' the mirror's high reflecting surface towards a smaller radius of curvature. A sufficiently low thermal conductivity coefficient of the fused silica substrate enables a constant heat gradient to be maintained within the mirror. Power losses at the Michelson output of less than 0.05 % of the light power circulating in the power-recycling cavity could be obtained and permanently adjusted.

Figure 1.18 shows a schematic of the heater setup as installed for mirror **MFe** in vacuum chamber TFe.

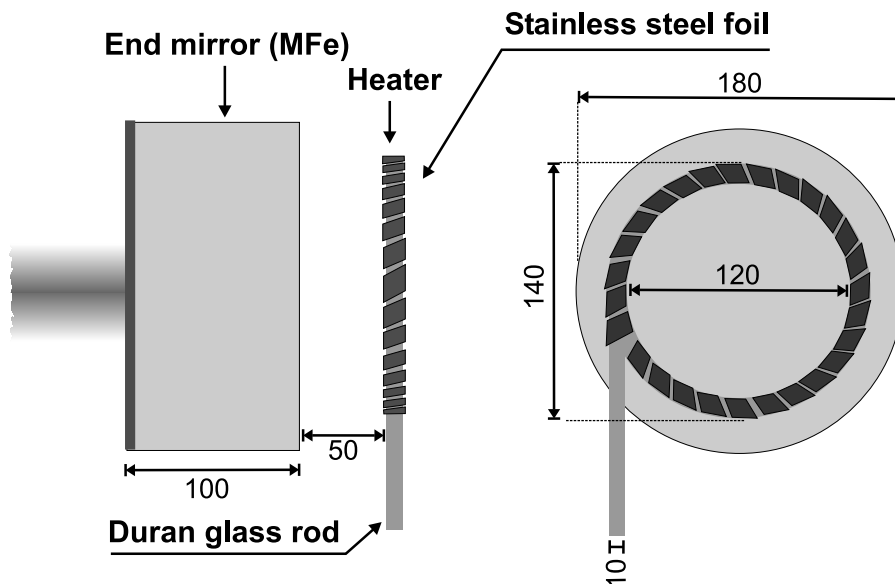


Figure 1.18: Heater setup for mirror **MFe** in vacuum chamber TFe. All sizes are given in mm.

1.5 Problems with scattered light

The optical arrangement on the output bench had to be optimized in order to avoid scattered light contributing to the Michelson readout signal. The preliminary detection bench layout used to date is shown in section 3.5.2.1. Two main sources of scattered light on the Michelson output detector PDO were identified:

- Light being scattered at optical components on the output bench and travelling back into the interferometer (back-scattering). This light contributes to the readout after another round trip within the Michelson.
- Light being scattered at optical components on the output bench and hitting the photodetector on a more or less direct way outside the vacuum system.

Light being scattered back into the interferometer is the more important contribution, as it is more difficult to minimize. As the output beam has a diameter of about 18 mm, it has to pass at least one focusing element to be detectable on a reasonably sized photodiode area¹⁷. While for the initial output bench setup a lens with 1 m focal length had been used to focus the beam onto the photodetectors, using a curved mirror to focus the beam yielded less back-scattering. Putting a Faraday isolator into the optical path of the output bench with the aim of attenuating back scattering from sources behind the Faraday was not successful. The Faraday itself (likely the polarizing beamsplitters at the Faradays input side) proved to be the dominating source of scattered light in this case.

The direct scattering from a scattering source on the detection bench onto the photodiode could be minimized by properly dumping any stray beams from intermediate surfaces. To allow convenient access to stray beams, components sometimes had to be slightly tilted with respect to the beam axis. Also it proved useful to have anti-reflection coated windows for the photodiodes in use.

The back-scattering of light into the interferometer can be reduced by attenuating the detected beam after it leaves the vacuum system. This attenuates the power of the light being scattered back into the interferometer by the square of the filter's power attenuation factor¹⁸, however this is not acceptable as a final solution, as the shot noise limited sensitivity is degraded by the square root of the filters attenuation factor with this method.

The effect of the scattered light shows up mainly as a non-stationarity of the output spectrum at frequencies below roughly 1 kHz. The non-stationarity appears to be modulated in time with a periodicity of the order of 1 s, such that it can be associated with pendulum motions inside the interferometer. Some experiments with longitudinally exciting individual mirrors were carried

¹⁷In the current configuration the focusing element is located on the detection bench, outside the vacuum system. In the final configuration (using an output modecleaner), a curved mirror within the vacuum system will be used to match the beam to the output modecleaner.

¹⁸The beam leaving the interferometer passes the attenuator twice on its way to the photodiode and back into the interferometer. This does not take into account the fact that the attenuator might be a source of direct backscattering itself.

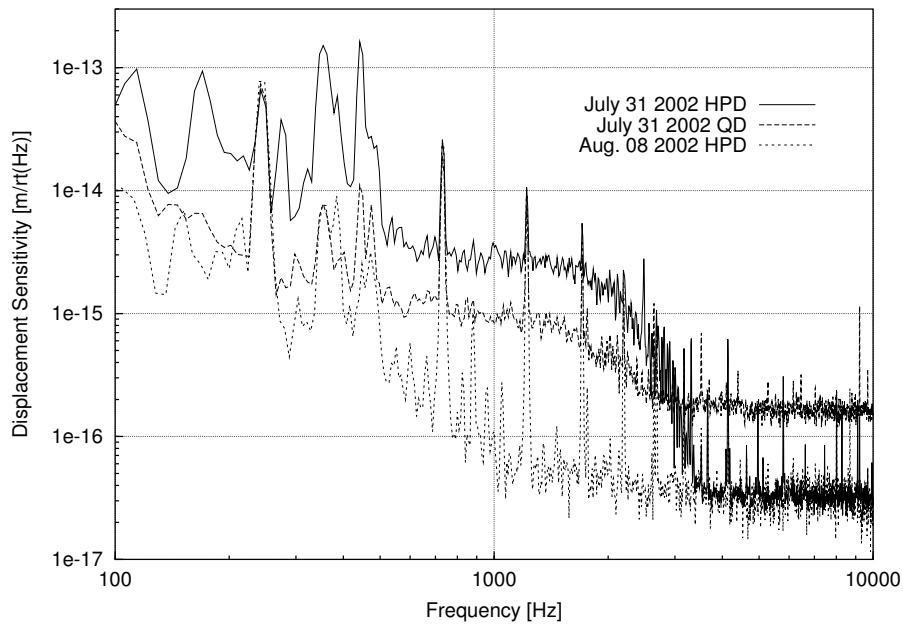


Figure 1.19: Sensitivity development due to scattered light investigations. QD = Quadrant detector, HPD = High power detector (see text below).

out, in order to identify a single culprit, which did not succeed at the time. There may be a source of scattered light within the power-recycling cavity at the backside of the reaction mass of **MPR**, which remains to be investigated.

Another modulation of noise was found around 8 Hz, which could be traced back to an oscillation at the north mirror **MCn** suspension.

For the ‘S1’ test run in August 2002 a compromise between stationarity of the Michelson output noise (the signal containing GW information) and the shot noise level of this signal was chosen. Figure 1.20 shows a typical sensitivity of the power-recycled Michelson to gravitational waves during this run. The maximum strain sensitivity of $8 \times 10^{-20}/\sqrt{\text{Hz}}$ is achieved above 2 kHz, where the noise is dominated by the photon shot noise of the total light power detected.

During the S1 run a high-power photodetector was used in addition to the standard quadrant photodetector, to increase the shot noise limited sensitivity of the Michelson error-signal readout.

The high power detector used consists of a single cooled diode, capable of detecting 200 mW of light (see [Sei02] for details on this type of high power detector). Another type of high power detector uses 16 diodes in combination which can detect a total light power of 2 W at the shot noise limit (see [JNSH02] for this detector). In order to distribute the light onto the 16 diodes, 15 beamsplitters have to be used, which (due to the many glass surfaces exposed to the light) easily can contribute to the scattered-light noise budget.

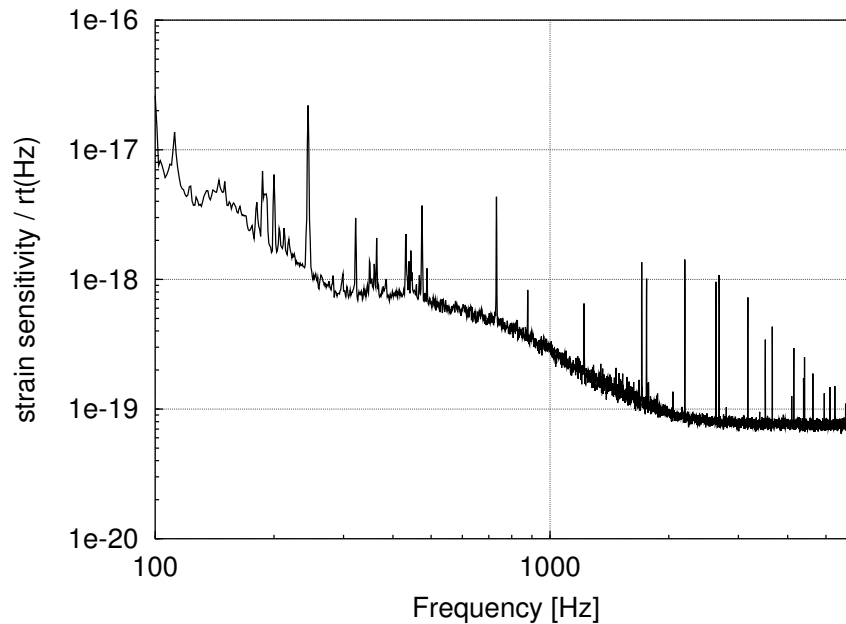


Figure 1.20: Typical sensitivity to gravitational waves during the S1 run. The maximum sensitivity of $8 \times 10^{-20}/\sqrt{\text{Hz}}$ is achieved above 2 kHz, where the noise is dominated by the photon shot noise of the total light power detected.

1.6 Lock automation

1.6.1 LabView

All major feedback loops are implemented with analog electronics within GEO 600¹⁹. However, parameters of the electronic circuits can be supervised and set with a computer controlled system based on LabView. The various electronic racks are equipped with their own digital bus system, which connects to a total of four PCs running a LabView program (LabView user programs are called Virtual Instruments - ‘VI’) communicating to a central process called ‘data socket server’.

The data socket server provides the interface between user computers and the computers connected to the digital bus system. The user computers are standard PCs, used for the control and automation of the modecleaners and main interferometer. See [CWR00] for further reference about the fundamentals of this computer control system.

Various virtual instruments that were developed and implemented as part of this work are used for monitoring and automation of the experiment. Concerning the power-recycling lock, a VI increases the loop gain and switches on the two integrator stages after a stable lock of the Michelson interferometer is recognized. Another VI implements the digital drift control of the Michelson differential arm length (see section 1.6.4) and three further VIs are used for the alignment and spot position control of the power-recycled Michelson as described in chapter 3.

¹⁹Exceptions are the digital longitudinal drift control for the Michelson differential arm length, the spot position controls, and the active seismic isolation system.

1.6.2 Microcontroller

The LabView control system has varying response times up to a few 100 ms for writing commands to the digital boards, as well as not strictly fixed sample rates. Therefore it was decided to implement a microcontroller stage, capable of response times of about 1 ms while several analog inputs can be sampled with 1 kHz. This system is fast and flexible enough for all aspects associated with locking the main interferometer.

The microcontroller chosen is the Infineon 16-bit controller C 167. It is implemented on a ‘hook up board’ named *mm 167* from Phytex, equipped with 128 kB flash ROM and 128 kB RAM. A RS-232 serial interface is used for transferring the compiled program to the flash memory, and can be used for communication with other devices. The current programming interface is produced by Keil and includes an IDE (Integrated Development Environment) under the Microsoft Windows operating system. The controller programs are written in C.

The mm 167 board is implemented on a standard-size GEO 600 analog electronics board, and uses a small (2 times 8 characters) LCD display for monitoring actual input signals and settings. A simple menu enables the change of parameters to optimize lock acquisition performance (see Figure B.8 for the electronics schematic). The change of parameters is not required for long term operation.

Table 1.3 shows a list of signals (using the standard naming convention if applicable) connected to the C 167.

Signal GEO name (if existent)	Controller name	type	description
G1:LSC_MID-EP-p	mi_ep	analog in	Michelson locking signal from PDO
G1:LSC_SRC-EP-p	sr_ep	analog in	Signal recyc. locking signal from PDBSs
G1:LSC_MIC.VIS	pr_reflpow	analog in	Reflected light power from MPR
G1:LSC_PWR E+N	pr_incav	analog in	Sum of east- and north arm power
G1:LSC_PWR dark	pr_dark	analog in	Light power at dark port
Master piezo feedback	pzt_fb	analog in	Master laser piezo feedback signal

Table 1.3: Input signals connected to the microcontroller unit. All analog input signals are sampled with 1 kHz and 10 bit resolution.

The signals are passed through four-pole anti-aliasing filters adjusted to the required bandwidth for the specific channel and then sampled with a rate of 1 kHz and 10 bit resolution. While the overall bandwidth is limited by the sampling rate, it is important for some of the channels to have almost no phase delay introduced by the anti-aliasing filters. Here a compromise between aliasing and phase delay has to be chosen. However as the signals are used for determining the detector status only, noise suppression is not of high priority, and only the radio frequency content needs to be filtered.

A listing of the microcontroller software can be found in appendix C.1.

1.6.3 Locking sequence

Figure 1.21 shows light power levels at different points along the optical path of GEO 600, during a fully automated locking sequence of the power-recycled Michelson. The signals from top to bottom are: Slave laser power, indicating that the slave laser is injection locked to the master laser; MC1 reflected power and MC2 reflected power, indicating that the laser frequency is equal to a modecleaner's resonance frequency; power-recycling cavity reflected power, indicating the laser frequency to be resonant within the power-recycling cavity; Michelson dark port power, measuring the light power at the Michelson output port; and the power in the east arm of the Michelson interferometer, being equivalent to the power buildup in the power-recycling cavity of the power-recycled Michelson.

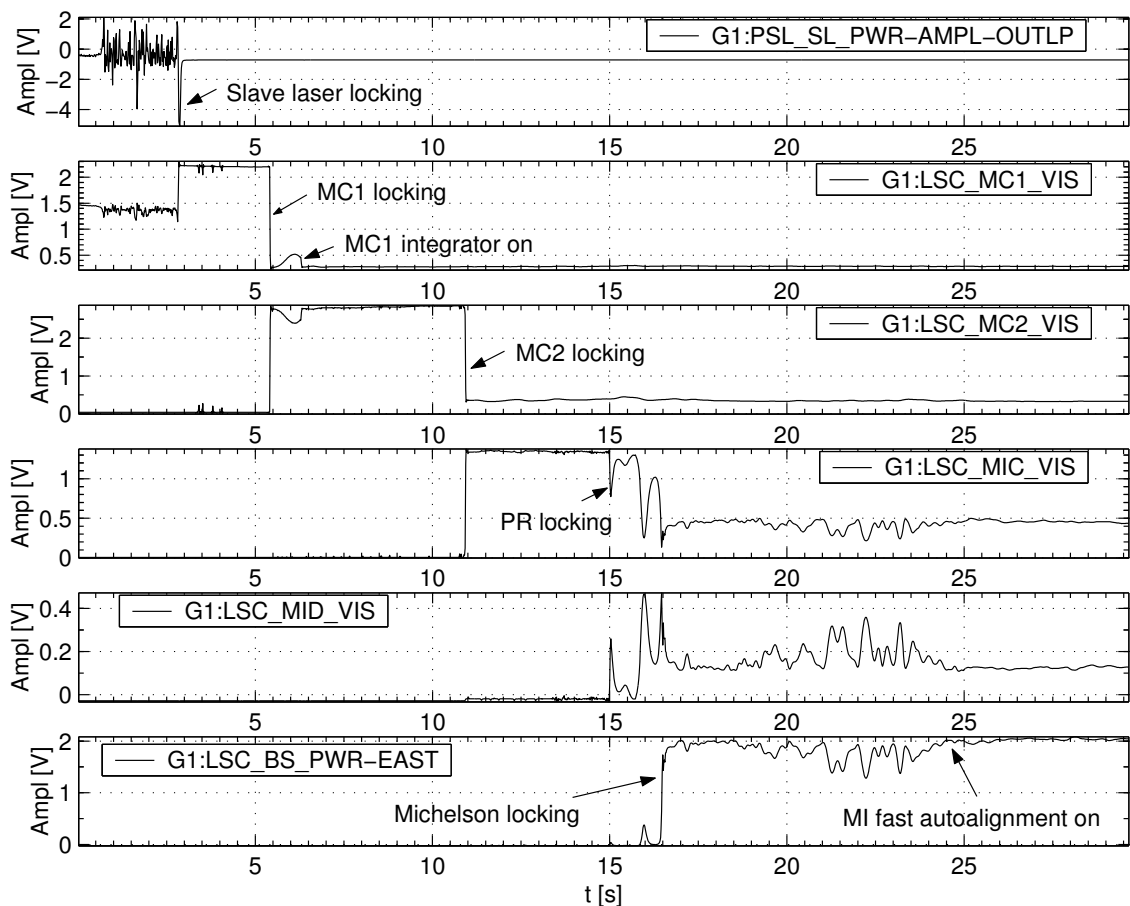


Figure 1.21: Light power levels during a fully automated locking sequence. From top to bottom: Slave laser power, MC1 reflected power, MC2 reflected power, power-recycling cavity reflected power, Michelson dark port power and power in the east arm of the Michelson.

1.6.4 Long time locking during the S1 run

In the so called ‘S1’ run from August 23 to September 9, 2002, GEO 600 was operated for 17 days as part of an international interferometer network. The ‘duty cycle’ of the power-recycled

Michelson, defined here as the time in lock divided by the overall time of the S1 run, was 98.9%. Table 1.4 shows the duty cycle of the two modecleaners, the power-recycling cavity and the (power recycled) Michelson interferometer individually for each day of the S1 run.

day	23.08	24.08 - 27.08	28.08	29.08	30.08	31.08	01.09
MC1	100%	100%	99.93%	99.96%	99.91%	100%	100%
MC2	100%	100%	99.91%	99.95%	99.88%	100%	100%
PRC	99.98%	100%	99.87%	99.94%	99.84%	100%	100%
MI	98.79%	100%	99.84%	99.90%	99.81%	99.97%	100%
day	02.09	03.09 - 05.09	06.09	07.09	08.09	09.09	
MC1	99.04%	100%	99.13%	100%	99.75%	99.94%	
MC2	98.86%	100%	98.82%	100%	99.62%	99.91%	
PRC	98.79%	100%	97.81%	100%	99.05%	99.76%	
MI	98.72%	100%	90.12%	100%	93.71%	99.72%	

Table 1.4: Duty cycle of the optical systems of GEO 600 during the S1 run in summer 2002. The longest continuous lock stretch of all systems lasted more than 120 hours.

The longest continuous stretch of lock achieved lasted more than 120 hours.

Causes of ‘loss of lock’ were investigated for the first two weeks of this period. Within this time only four losses of lock occurred outside the so-called ‘maintenance period’ which was a daily period of one hour, where operators were allowed to enter the central building of GEO 600 in order to observe or adjust parameters that were not accessible remotely. Table 1.5 shows the time and identified cause of lock loss of the power-recycled Michelson.

Nr.	GPS time	UTC time	cause
1	714575712	2002-08-28 13:14:59 (Wed)	Laser power noise spikes
2	714831277	2002-08-31 12:14:24 (Sat)	Misalignment of mirror MFe caused by control program bug
3	714984810	2002-09-02 06:53:17 (Mon)	Van passing east end building
4	715310724	2002-09-06 01:25:11 (Fri)	Italy earthquake mag. 6.1

Table 1.5: Complete list of losses of lock (outside maintenance periods) over two weeks of the S1 run.

As mentioned above, the longest continuous stretch of lock achieved was more than 5 days. To be able to lock such long periods, the differential length changes of the Michelson arms caused for example by tidal motions of the earth crust, have to be compensated. In principle this could be done with the intermediate mass actuators at **M_{Ce}** and **M_{Cn}**, however their useable low-frequency range is limited to 100 μ m. Besides the fact that this is not sufficient if the outside temperature changes considerably during a lock, there is another disadvantage using the IM actuators for the low frequency longitudinal correction: Longitudinal displacement of **M_{Ce}** and **M_{Cn}** couples into the alignment of these mirrors, even if this coupling is minimized. This is not a problem as long as

the lock is maintained, because the alignment system corrects for these misalignments. However when the lock is lost, **MCe** and **MCn** maintain their alignment (see the *offset shifting loop* in section 3.3.7.1, page 88), while the longitudinal offset is lost, resulting in a misalignment at the time the lock is lost. While this could in principle be cured by applying low-frequency longitudinal feedback to the upper masses of **MCe** and **MCn** digitally, it is desirable to keep the distance of **MCe** and **MCn** to their ESD reaction masses as constant as possible anyway²⁰. Consequently, low frequency feedback is applied to the far mirrors **MFe** and **MFn**.

Figure 1.22 shows a time series (upper graph) and amplitude spectral density (lower graph) of the Michelson differential feedback, applied to the far end mirrors **MFe** and **MFn**.

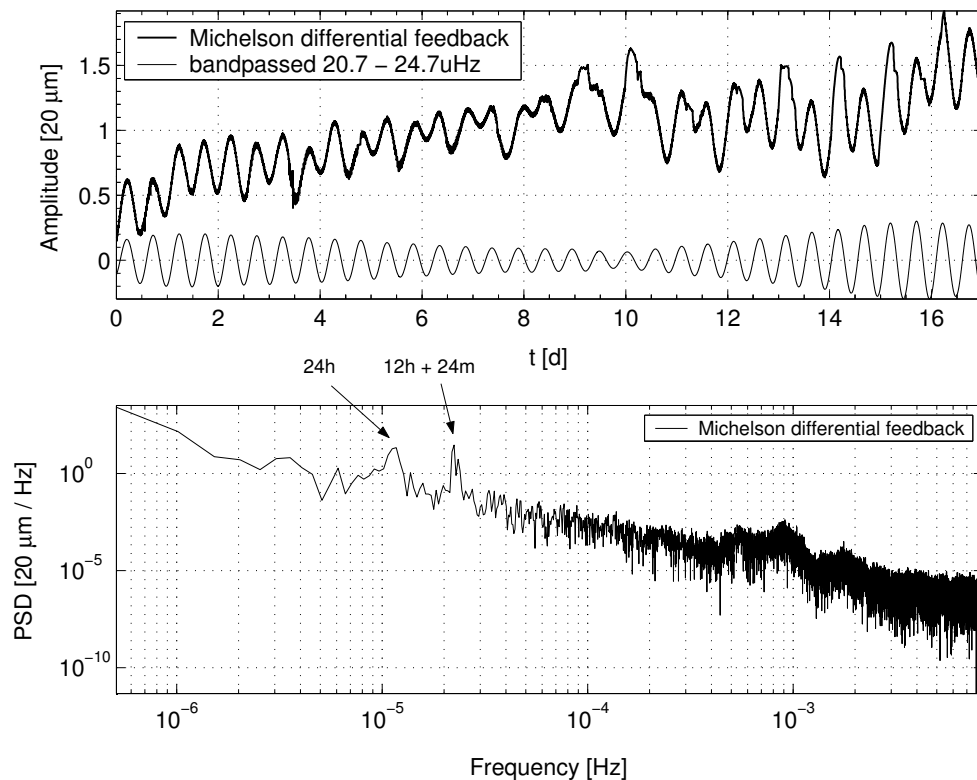


Figure 1.22: Time series (upper graph) and amplitude spectral density (lower graph) of the Michelson differential feedback, applied to the far end mirrors **MFe** and **MFn**.

The lower trace in the upper graph displays the applied feedback after processing by a digital band-pass filter with a transmission band from 20.7 to 24.7 μHz . The earth tides dominate the feedback and their modulation due to the relative position of moon and sun with a period of about 14 days can be seen. The amplitude spectrum of the time series shows peaks at periods of 24 hours and 12hours + 24minutes, related to the daily temperature changes and the earth tides respectively. The enhanced noise in the band from 0.4 to 1 mHz may be caused by the air conditioning system used during the S1 run, which was toggling between two states with a frequency of the order 1 mHz. It will be interesting to investigate this band with the new continuous regulating air conditioning system, in order to observe eigenmodes of the earth body, which are expected in this frequency range [MW95].

²⁰this is true as the ESD force depends on the distance between reaction mass and mirror as stated in section 1.3.

Chapter 2

The Dual Recycling Lock

2.1 Introduction

Proceeding from the power-recycled Michelson interferometer described in chapter 1 to the dual-recycling configuration is a major experimental step. Dual recycling is the combination of power recycling and signal recycling and involves the installation and control of an additional mirror (the signal-recycling mirror) at the output of the Michelson interferometer.

The principles of dual recycling and related experiments have been described by B. Meers [Mee88, Mee89], K. Strain [SM91], G. Heinzel [HSM⁺98, Hei99a], A. Freise [FHS⁺00, Fre03b] and others. A. Freise further investigates different final operating points of dual recycling for GEO 600 with FINESSE simulations (see [Fre03b], chapter 3.2). The current chapter of the work at hand briefly recalls the qualitative principles of dual recycling and then emphasizes on the implementation of dual-recycling control and the experimental test of a possible lock acquisition scheme for GEO 600.

We have seen in the previous chapter, that the carrier light power circulating in the Michelson interferometer can be resonantly enhanced by placing a mirror (the *power-recycling mirror*) into the Michelson input (or ‘west’) port. Similarly another mirror, the *signal-recycling mirror*, can be placed in the Michelson output (or ‘south’) port, to resonantly enhance the signal sidebands (and also the Schnupp modulation sidebands, as described below).

Figure 2.1 shows the principle distribution of light fields for dual recycling. The individual light fields are drawn spacially separated for clarity and the line thickness is an indication of the relative light power. The Michelson interferometer shown consists of the beamsplitter **BS** and mirrors **Me** and **Mn** at the ends of two orthogonal arms. Directions can be called ‘north’, ‘east’, ‘south’ and ‘west’ as indicated. In the dark fringe condition of the Michelson the carrier light can be resonantly enhanced within the power recycling cavity consisting of **MPR** and the Michelson interferometer. For this purpose the incident light has to be kept in resonance with the power-recycling cavity.

Signal sidebands (induced on the carrier light by a differential Michelson arm length modulation, caused for example by a gravitational wave) experience destructive interference towards the west

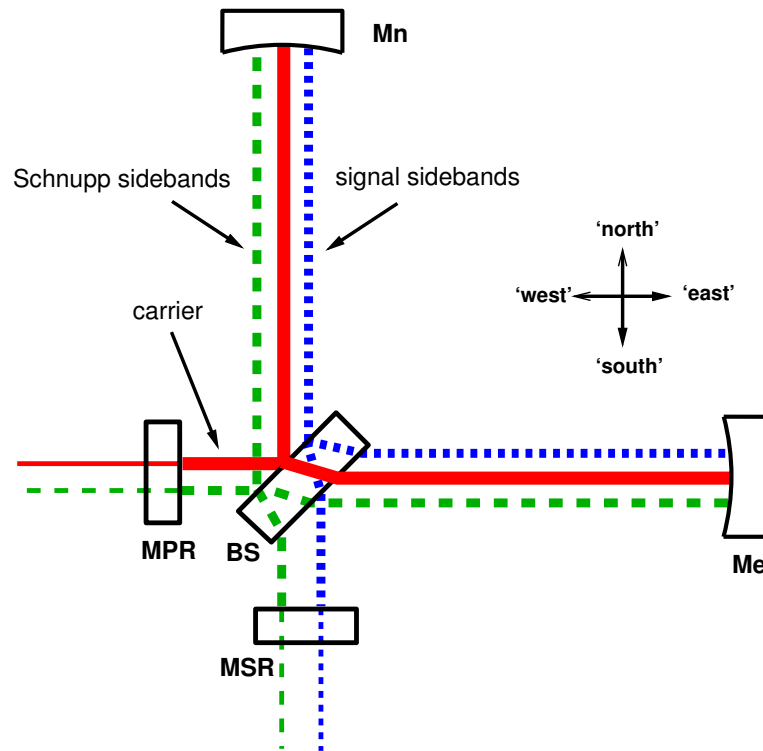


Figure 2.1: Principle distribution of light fields for dual recycling. The individual light fields are drawn spacially separated for clarity. The line thickness indicates the relative light power. In the dark fringe condition of the Michelson the carrier light is resonant within the power-recycling cavity consisting of **MPR** and the Michelson interferometer. Signal sidebands experience destructive interference towards the west input, but leave the beamsplitter to the south and are resonantly enhanced within the cavity formed by the signal-recycling mirror **MSR** and the Michelson interferometer. The Schnupp sidebands are resonant within the coupled cavity consisting of all mirrors.

input, but leave the beamsplitter to the south, because they are generated with opposite phase in each arm ¹. With a signal-recycling mirror **MSR** at the south port being in the appropriate longitudinal position, the signal sidebands are resonantly enhanced within the cavity formed by **MSR** and the Michelson interferometer in the dark fringe condition. This cavity is called the *signal-recycling cavity*.

While the beamsplitter looks essentially like a mirror with high reflectivity for the carrier light and the signal sidebands, it is *partially* transmitting the Schnupp sidebands (required for the heterodyne error signal generation). The Schnupp modulation sidebands are resonant within the coupled cavity consisting of all mirrors, where each sideband (of a pair of sidebands) has its own resonance condition. GEO 600 uses two independent Schnupp modulation frequencies f_{MI} and f_{SR} for the Michelson and signal-recycling control respectively. Depending on the actual interferometer tuning and the Schnupp frequencies chosen, the Schnupp sidebands experience different resonance conditions within the coupled four-mirror cavity. Using two independent modulations

¹Due to the arm length difference required for the Schnupp modulation technique, a tiny fraction of the signal sidebands will be reflected to the west port. However we can neglect this effect, which is important only for the Schnupp sidebands with their much higher frequency.

gives more flexibility in the choice of the frequencies, which is particularly useful for determining the operating point of the signal-recycling mirror.

Besides the power-recycling lock which controls the laser frequency to be resonant within the power-recycling cavity, and the Michelson lock, holding the Michelson on the dark fringe operating point, in dual recycling there is a third longitudinal degree of freedom to be controlled: The microscopic position of the signal-recycling mirror **MSR**, which is also called the *tuning* of the signal-recycling mirror. The tuning of **MSR** determines the frequency response (and thus the frequency of maximum sensitivity) of the detector: Different tunings of **MSR** change the resonance frequency of the signal-recycling cavity, such that a signal sideband of a distinct frequency is maximally enhanced (if the detector is tuned to a frequency unequal to 0 Hz, only one of the two signal sidebands is resonantly enhanced within the signal-recycling cavity). The bandwidth of the detector around this frequency of maximum sensitivity is determined by the reflectivity of the signal-recycling mirror (provided losses in the signal-recycling cavity are negligible).

Figure 2.2 shows simulated sensitivity plots for dual recycling ². Three different signal-recycling tunings with mirrors of different reflectivities are shown.

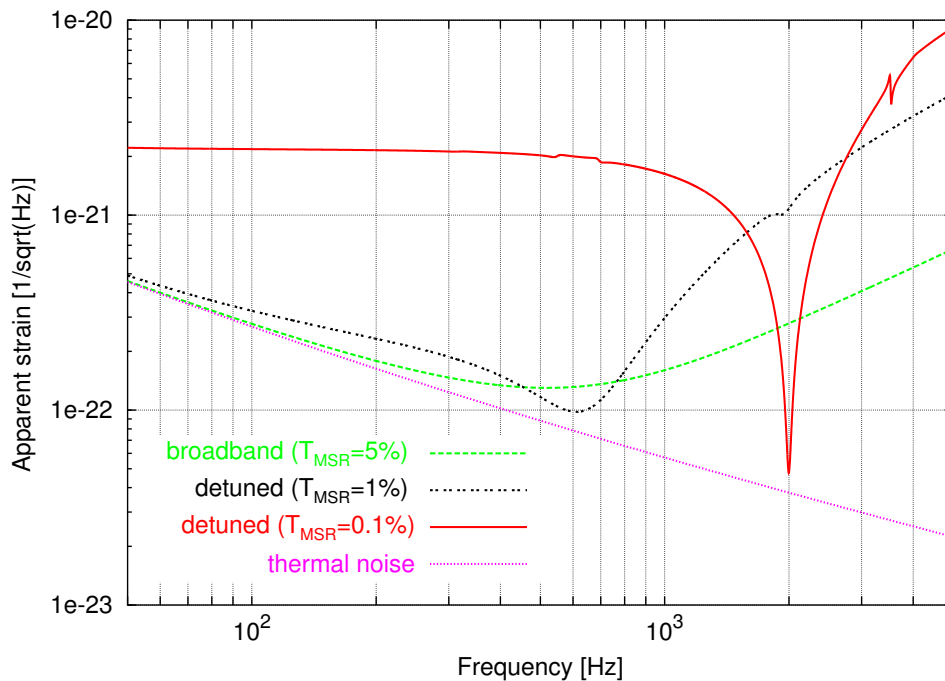


Figure 2.2: Simulated strain sensitivities for dual recycling in GEO 600. Only shot noise and the sum of thermal noise contributions are taken into account here.

If the signal-recycling tuning Φ_{MSR} is zero (which means that the carrier light is resonant within the signal recycling cavity), the dual-recycled Michelson is maximally sensitive to signal frequencies at DC. This is only sensible for signal recycling mirrors with reasonably high transmittance (for example $T_{\text{MSR}} = 5\%$), such that the signal-recycling bandwidth is sufficiently large to overlap with the gravitational wave measurement band. Therefore this tuning is also called *broadband*

²All optics simulations in this chapter are done with FINESSE [Fre02].

mode. However the reader should bear in mind that the signal-recycling bandwidth is not affected by the tuning. In the example of a broadband mode for GEO 600 in Figure 2.2, the sensitivity at low frequencies is limited by the expected thermal noise level [Cag02].

Two other terms are often used to describe signal-recycling operating points with $\Phi_{\text{MSR}} \neq 0$: These are called *detuned*, or *narrow band*, with the latter one used for emphasizing the use of a highly reflective signal-recycling mirror, which yields a small signal-recycling bandwidth. Two detuned modes for mirrors with different transmittance are shown in Figure 2.2.

2.2 Experimental setup

The control of the signal-recycling mirror depends on the other two control loops (power recycling and Michelson) and the acquisition process of the three loops in combination is rather complex. A suitable locking scheme for GEO 600 had to be developed, which is a scheme that enables initial locking of dual recycling in a detuned mode.

To maintain the tuning of the signal-recycling mirror with a feedback loop, a suitable error signal containing information about the microscopic longitudinal position of **MSR** has to be obtained. Assuming an ideal Michelson interferometer at the dark fringe (and omitting the very weak signal sidebands), there are only Schnupp sidebands (leaving the beamsplitter to the south port) impinging on the signal-recycling mirror. The phase of these Schnupp sidebands is shifted by longitudinal motions of **MSR**, but there is no carrier light at the south port (because the Michelson is at the dark fringe) with which the Schnupp sidebands could beat in order to detect them. Inside the power-recycling cavity, however, there is plenty of carrier light and a suitable error signal can be obtained by detecting a small fraction of it. The Schnupp sidebands resonant within the power-recycling cavity beat with the carrier light, to yield an error signal for the signal-recycling mirror's position. In GEO 600 the beam being reflected at the rear surface of the beamsplitter is used for this purpose. This surface has an anti-reflective coating which reflects about 50 ppm of the incident light power. In principle it would also be possible to sample the light transmitted at the end mirrors **MCE** and **MEN** for this purpose. However these beam spots are hard to access in GEO 600 due to limited space around the vacuum chambers TCE and TEN.

The Schnupp frequency for the signal-recycling control f_{SR} can be chosen such that **MSR** is at a tuning of $\Phi_{\text{MSR}} = 0^\circ$. We define this particular Schnupp frequency, which is close to an integer multiple of the free spectral range (FSR_{SRC}) of the signal-recycling cavity, as $f_{\text{SR},0}$. Both sidebands of the signal-recycling Schnupp modulation are resonant within the signal-recycling cavity in the case of $\Phi_{\text{MSR}} = 0^\circ$. An error signal for the control of **MSR** in the detuned case can be obtained by choosing f_{SR} as

$$f_{\text{SR}} \approx f_{\text{SR},0} \pm f_{\text{sig}} , \quad (2.1)$$

with f_{sig} being the frequency of maximum signal enhancement within the signal-recycling cavity [Hei99a, FHS⁺00]. Only one Schnupp sideband is resonant within the signal recycling cavity in the detuned case.

Simulations show that f_{sig} is not strictly proportional to f_{SR} [Mal03, Fre03b], such that the exact f_{sig} has to be determined experimentally (or by simulation) for a given f_{SR} . Nevertheless equation 2.1 is a good approximation and is used throughout this chapter. As for the control of signal recycling we are mainly interested in gaining a suitable error signal rather than determining the exact frequency of maximum sensitivity to Michelson arm length changes. The latter will become more important if a stable lock for small detunings is to be achieved, as the stability of the Michelson control loop may be affected by the Michelson transfer function (in dependence on the signal-recycling detuning).

The frequency f_{sig} translates into the tunings Φ_{MSR} according to

$$\Phi_{\text{MSR}} = 180^\circ \frac{f_{\text{sig}}}{\text{FSR}_{\text{SRC}}} \quad (2.2)$$

The tuning is equivalent to a longitudinal displacement of **MSR** according to

$$\Delta x_{\text{MSR}} = \lambda \frac{\Phi_{\text{MSR}}}{360^\circ} \quad (2.3)$$

Depending on the context, all three parameters are used to describe the tuning of **MSR**.

Figure 2.3 shows a schematic overview of the optical setup of the dual-recycling configuration together with the three longitudinal feedback loops required.

Compared to Figure 1.11 on page 20 the signal-recycling mirror **MSR** is added, together with a scheme for the longitudinal control of **MSR**. The signal recycling loop uses its own Schnupp modulation at a frequency of $f_{\text{SR}} = 9.18\text{MHz} \pm 60\text{kHz}$ (depending on the signal-recycling tuning), which is applied to EOM4 that is used for the light frequency correction of the power-recycling loop as well. The photodiode PDBSs samples the light reflected off the beamsplitter's AR coated side and is built in the standard design described in chapter 3.3.5 on page 83. The photocurrent is coherently demodulated with the modulation frequency, yielding an error signal for the longitudinal position of **MSR**. The beam leaving the vacuum system is focused with a lens of 1 m focal length, to obtain a suitable spot size of about 3 mm diameter on the detector PDBSs. Feedback is applied with a coil-magnet actuation system at the mirror level.

2.3 Locking strategy

2.3.1 Power-recycling control

First experiments with the signal-recycling mirror installed showed that (in contrast to previous experiments at the Garching 30 m prototype [HSM⁺98, Hei99a]) the power-recycling lock does not work under any arbitrary Michelson and signal-recycling tuning in GEO 600. This led to a closer investigation of the power-recycling error signal in the dual-recycling configuration.

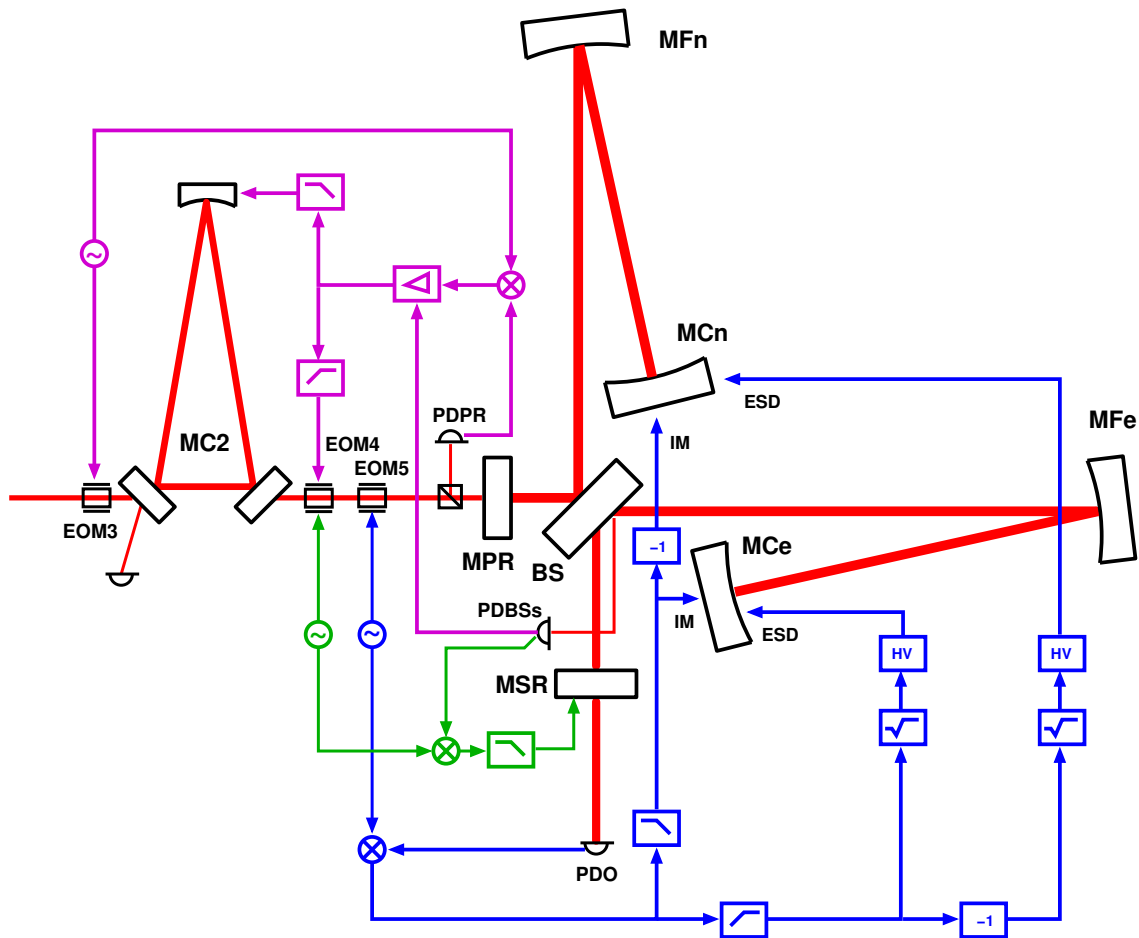


Figure 2.3: Dual-recycling lock control scheme. The frequency control for MC2 is omitted for clarity. The power-recycling and Michelson lock are identical to Figure 1.11. The signal recycling loop uses its own Schnupp modulation at a frequency around $f_{SR} = 9.18\text{MHz}$, applied to EOM4. The photocurrent of photodiode PDBSs (sampling the light of the beamsplitters AR coated side) is coherently demodulated with f_{SR} , yielding an error signal for the longitudinal position of **MSR**. Feedback is applied at the mirror level with a coil-magnet actuation system.

Figure 2.4 shows the power recycling error signal for 6 different tunings of **MSR**. Each image represents the PR error signal in the plane of power-recycling and Michelson tuning. The size of the PR error signal is coded in a non-linear greyscale in order to obtain a qualitative understanding of the signal distribution. Bright areas indicate a positive PR error signal, while darker colours show a negative signal.

The nominal operating points for the power-recycling lock are transitions from negative (black) to positive (white) values, if **MPR** moves from negative to positive tuning. The central vertical structure in the upper left graph (the signal-recycling mirror is tuned to $\phi_{MSR} = 90^\circ$ here) represents correct PR operating points. The power-recycling cavity can be locked for almost any Michelson tuning here. The Michelson is on the dark fringe, for MI tunings of $\phi_{MI} = 0^\circ$, corresponding to the center of the image.

The situation in this graph is similar to the power-recycled Michelson without signal recycling. We

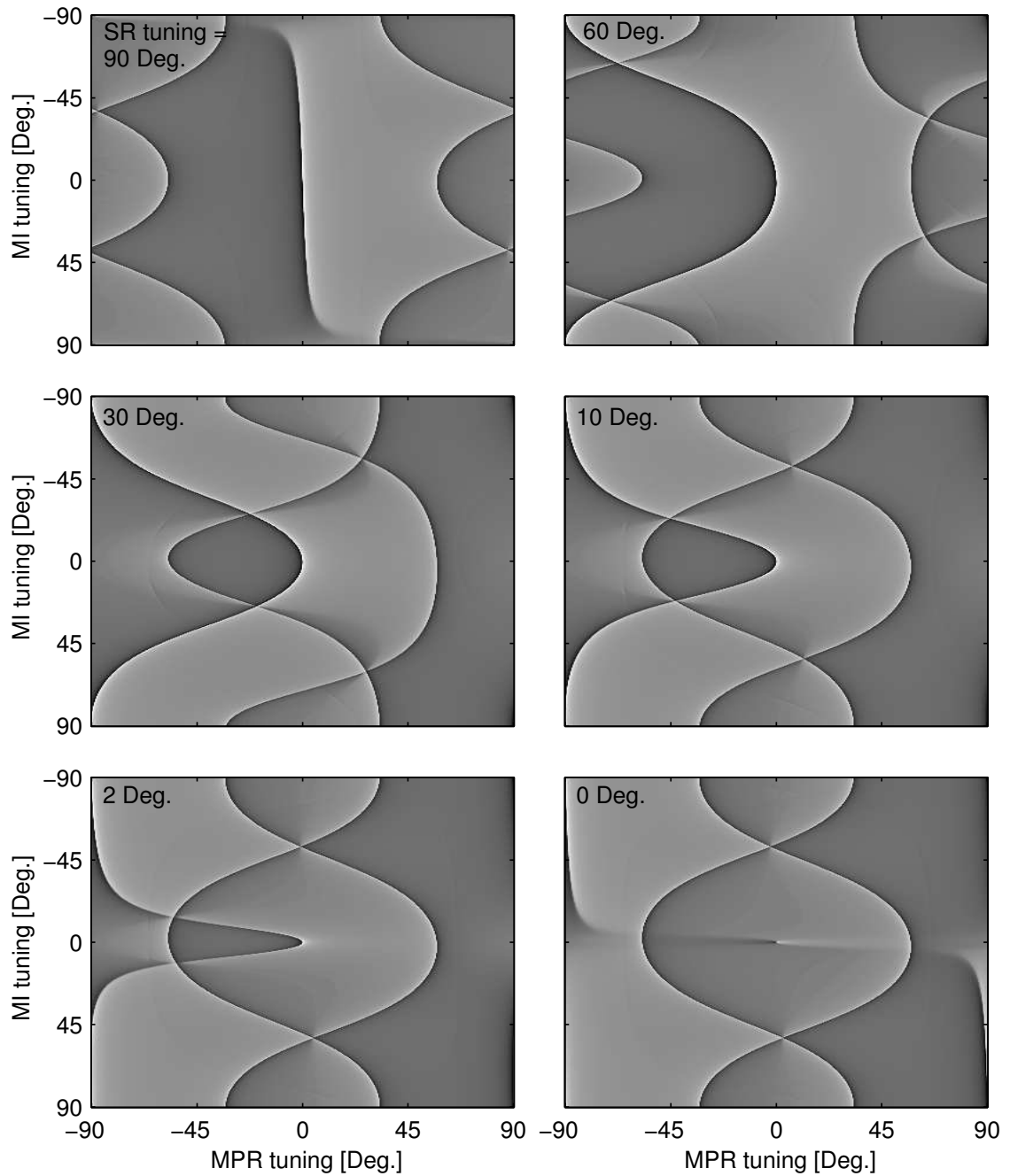


Figure 2.4: Power-recycling error signal for 6 different tunings of **MSR**. Each image represents the error signal in the plane of PR and Michelson tuning. A possible operating point for the PR lock is on a black to white transition for an increasing **MPR** tuning. The nominal operating point for the power-recycled Michelson lock is at the center of each image.

have seen, for example in Figure 1.16 on page 27, that the power-recycling cavity can be locked for almost any Michelson tuning. The ‘bent’ structures at the left and right side of the upper left graph in Figure 2.4 (which have a white-black transition for increasing ϕ_{MPR}) are caused by the Pound-Drever-Hall sidebands used for the power-recycling cavity lock. They are resonant within the main interferometer for certain combinations of signal-recycling and Michelson tuning.

The other 5 graphs show the PR signal for decreasing values of the **MSR** tuning, ϕ_{MSR} . The central structure of correct PR operating points gets ‘bent’ with smaller detunings of **MSR** and there are MI tunings where the central structure and the sideband structure cross each other. At these MI tunings, the PR cavity may lose lock, in particular for small detunings of **MSR**, which lead to a situation in which the PR signal is dominated by the ‘sideband signal’ with the wrong slope.

As a consequence of this result, the power-recycling cavity cannot lock under any arbitrary combination of the Michelson and signal-recycling tuning. This fact alone may not be very harmful, as long as the power-recycling cavity can be locked quickly after passing the ‘sideband barrier’ in the PR error signal plane. However this is not guaranteed, as the wrong information from the sideband structure will slightly accelerate the modecleaner mirror in order to control the laser frequency (compare Figure 2.3). Thus some recovery time may be required, until the PR cavity is locked to the proper zero crossing again.

The graphs in Figure 2.4 imply that it is almost impossible to lock dual recycling instantly to a useful final detuning of $\phi_{\text{MSR}} = 0 \dots 2^\circ$ by simultaneously switching on feedback to the MI and SR loop (at the moment the MI and SR tunings are at their nominal values). How would this scenario have to look? The Michelson can only approach a dark fringe without loosing PR lock, if the signal-recycling detuning is large enough (e.g. $\phi_{\text{MSR}} > 30^\circ$). Then the Michelson would have to stay close to the dark fringe, while **MSR** would have to move to a smaller detuning with $\phi_{\text{MSR}} < 2^\circ$. Such a sequence is very unlikely and may imply waiting in the order of hours for a single event. Given the fact that the pre-alignment of the main optics drifts in the order of minutes, this theoretical possibility seems completely impractical ³.

The situation improves if the Michelson and signal-recycling mirror are locked sequentially. We assume that the Michelson can be locked to the dark fringe for almost any detuning of **MSR** with $\phi_{\text{MSR}} > 25^\circ$. If the Michelson is locked, the operating point is fixed to the center of the images in Figure 2.4. In principle we could then wait for **MSR** to pass a desired small detuning and lock it there, without the danger of loosing the power recycling lock. However we will see in Figure 2.6 that the Michelson error signal gain strongly increases with **MSR** approaching small detunings. This makes it difficult to maintain the Michelson lock while **MSR** is freely moving. As the Michelson gain variations are smaller for large **MSR** detunings, it seems easier to initially lock **MSR** to a largely detuned operating point of e.g. $\phi_{\text{MSR}} = 30^\circ$. Furthermore, the capture range of the Michelson error signal (and also of the SR error signal) is larger for increasing signal-recycling

³For the locking of dual recycling at the Garching 30 m prototype, the feedback for the Michelson and signal-recycling loop is continuously applied during acquisition. The power recycling cavity can be locked permanently during the acquisition (there is no disturbing resonance of the PR locking sidebands) and the dual-recycling lock can be achieved when the Michelson and signal recycling mirror come close to their nominal operating points by chance. As the signal-recycling factor is smaller, the Michelson gain variation with changing detuning of the signal-recycling mirror is smaller as well.

detunings. Given the fact that the electrostatic drives are comparatively weak actuators, it is very useful for the Michelson lock acquisition if the capture range is not unnecessarily decreased. Thus a possible locking strategy is to lock the Michelson as often and long as possible and wait until **MSR** passes a largely detuned operating point. If **MSR** can be locked there, its detuning can be decreased in a controlled way while gain and phase changes can be normalized as required.

2.3.2 Michelson control

For all following discussions we assume the power recycling cavity to be locked. How does the Michelson error signal look then in the dual recycled case?

Figure 2.5 shows the Michelson error signal as it depends on the signal-recycling mirror tuning. The upper graph shows the error signal (again in a non-linear greyscale color code) for the full range of the two-dimensional parameter space of Michelson and signal recycling tunings. The lower left graph shows the indicated closeup and the lower right graph shows the Michelson error signal for a fixed signal recycling tuning of about $\phi_{\text{MSR}} = -28^\circ$. The Michelson can be locked to the dark fringe, if a signal with a white to black transition at $\phi_{\text{MI}} = 0^\circ$ for increasing ϕ_{MI} can be obtained. This is the case for a wide range of **MSR** tunings, except for the region with $\phi_{\text{MSR}} = +40 \dots +70^\circ$. In this region the Michelson error signal is dominated by signals caused by second order TEM modes, such that it cannot be used for longitudinal control.

For all simulations in Figure 2.5 the Michelson demodulation phase is fixed to the phase chosen for the shown Michelson error signal at $\phi_{\text{MSR}} = -28^\circ$. The signal looks similar to the one for the power-recycled Michelson lock, shown in Figure 1.16, except for a small asymmetry of the outer parts of the signal, caused by different resonance conditions for the two Schnupp sidebands. Figure 2.5 tells us that a suitable error signal for the Michelson lock can be obtained for most detunings of **MSR**. In particular it seems possible to change the **MSR** tuning *in lock* to smaller values, because the structure of the Michelson error signal is similar for most **MSR** detunings.

Besides the acquisition problem discussed above, the difficulty in controlling the Michelson and signal-recycling tuning is given by the fact that the available error signals depend on each other. One aspect of this dependence is the fact that the gain (i.e. the slope of the error signal at the nominal operating point) of both signals changes depending on the actual signal recycling tuning. Figure 2.6 displays the relative slope of the Michelson and signal-recycling error signals depending on the signal-recycling detuning. The Michelson gain variation is stronger than the gain variation of the SR error signal.

But not only the gain is a function of the signal-recycling tuning. This is also true for the optimal demodulation phase of the error signals (as mentioned above for the Michelson error signal): Figure 2.7 shows the optimal demodulation phase of the Michelson and signal-recycling error signals with respect to the signal-recycling detuning. While the phase for the Michelson varies largely only if the signal recycling mirror approaches the broadband tuning, the optimal demodulation phase for the SR loop varies strongly for large detunings. The SR phase is approximately proportional to the SR tuning in the range from 10 kHz to 60 kHz detuning.

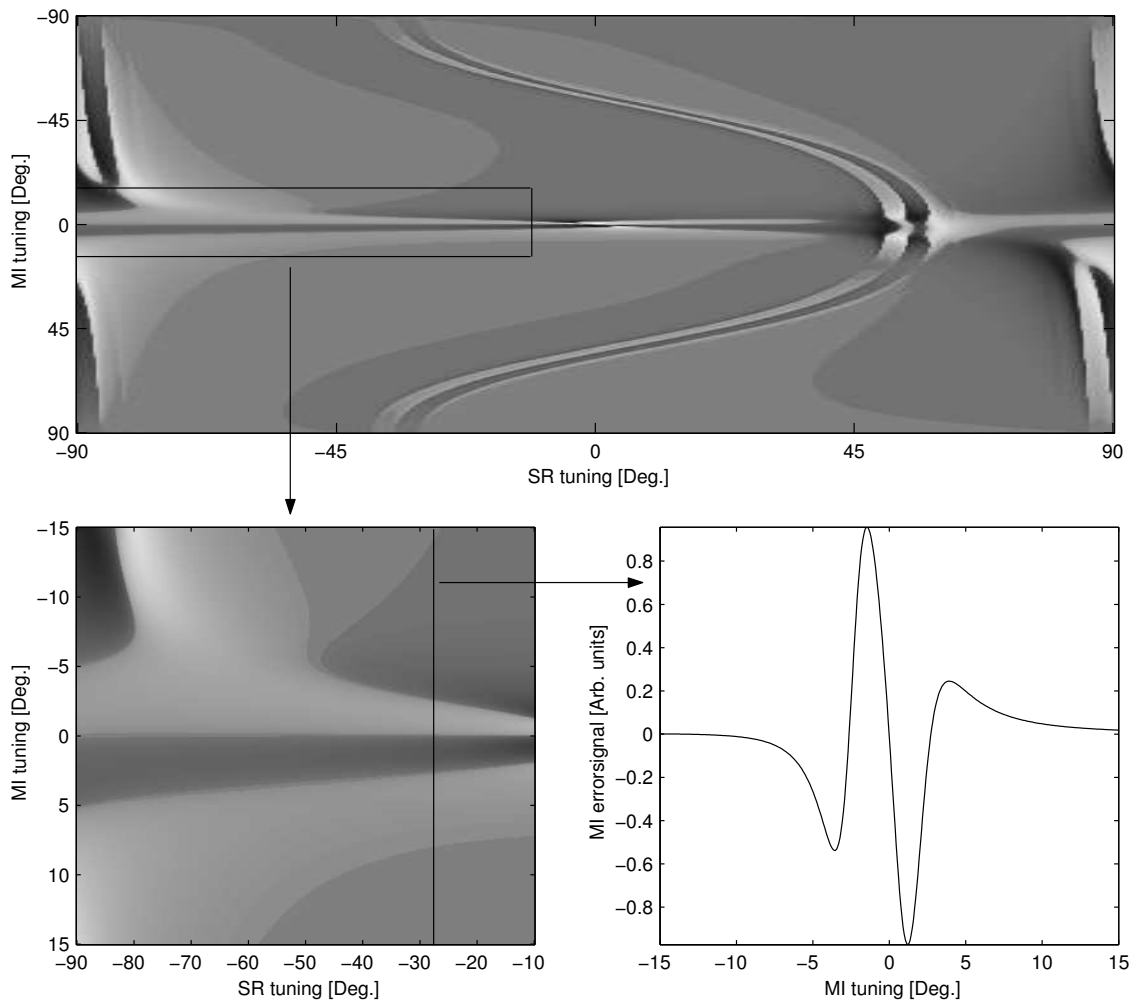


Figure 2.5: Michelson error signal with respect to the signal-recycling mirror tuning. The upper graph shows the Michelson signal in a greyscale color code for the full two-dimensional parameter space of Michelson and signal recycling tunings. The lower left graph shows the indicated closeup, and the lower right a crosssection for a fixed signal recycling tuning of about $\phi_{\text{MSR}} = -28^\circ$.

Figures 2.6 and 2.7 give an overview of how to adapt the Michelson and signal-recycling control loop if the detuning is to be changed in lock (as required for the locking procedure described above).

2.3.3 Signal-recycling control

The logical next question is, what does the signal-recycling error signal look like under the assumption that the power-recycling cavity and Michelson are locked. Figures 2.8 to 2.11 show the simulated signal-recycling error signal as a function of the (signal-recycling) mirror's microscopic position, varying different additional parameters, which turned out to be important to provide a proper error signal. All four figures are computed for a nominal signal-recycling detuning of about 28° , with the position of **MSR** being varied with $\pm 2\text{ nm}$ around this detuning on the abscissa.

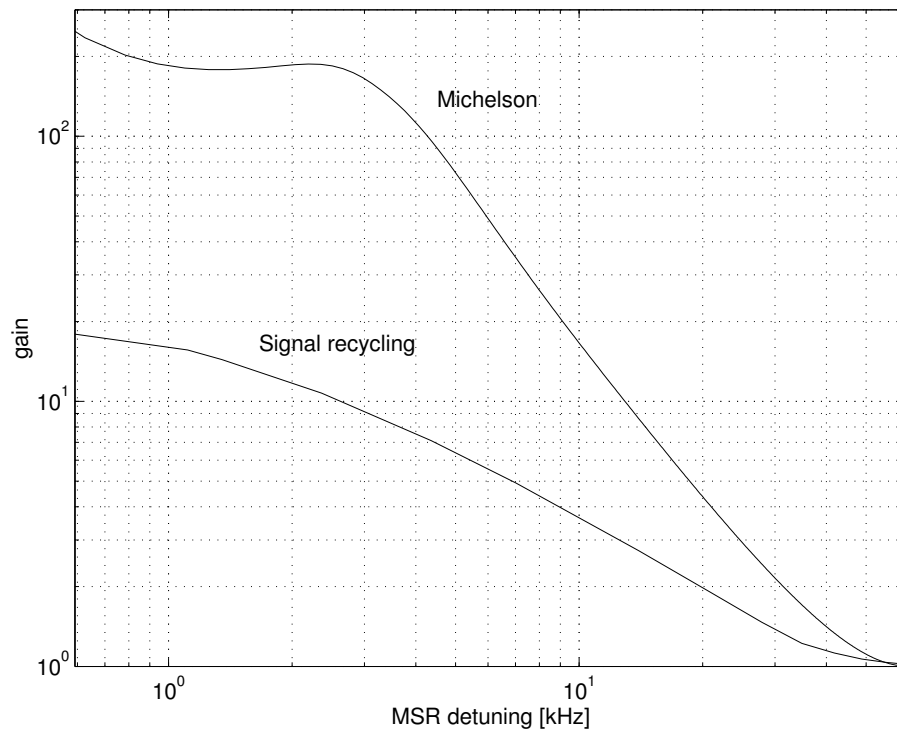


Figure 2.6: Slope of the Michelson and signal-recycling error signals with respect to the signal-recycling detuning.

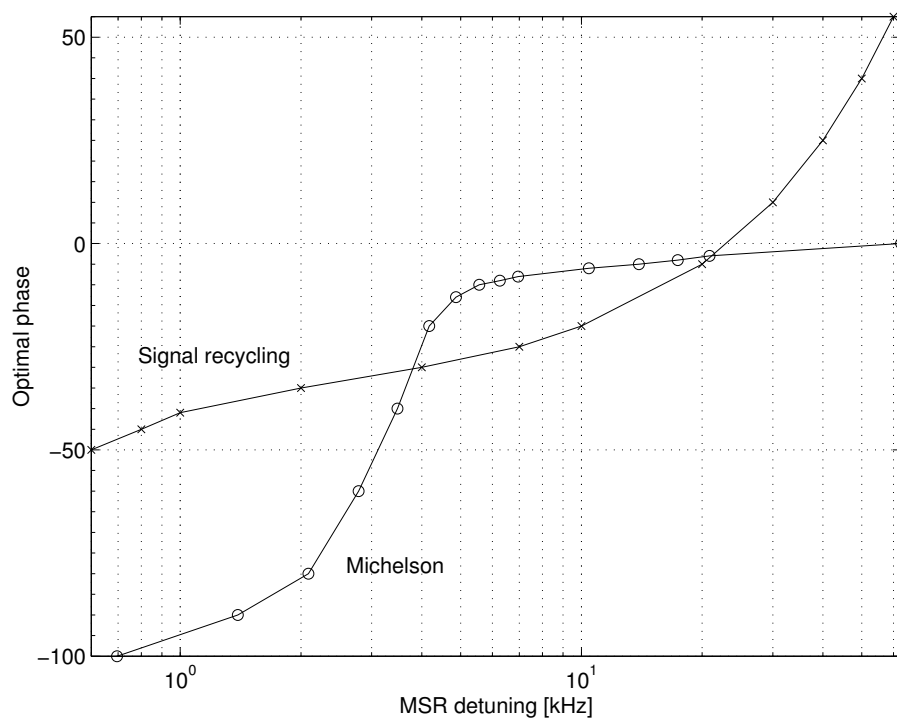


Figure 2.7: Optimal demodulation phase (in order to obtain a maximum signal slope) of the Michelson and signal-recycling error signals with respect to the signal-recycling detuning.

2.3.3.1 Signal-recycling demodulation phase

In Figure 2.8 the SR error signal is shown for four different SR demodulation phases, spaced by 30° . It can be seen that the range of a constant slope of the error signal around the nominal zero-crossing operating point decreases, if the phase is not chosen properly.

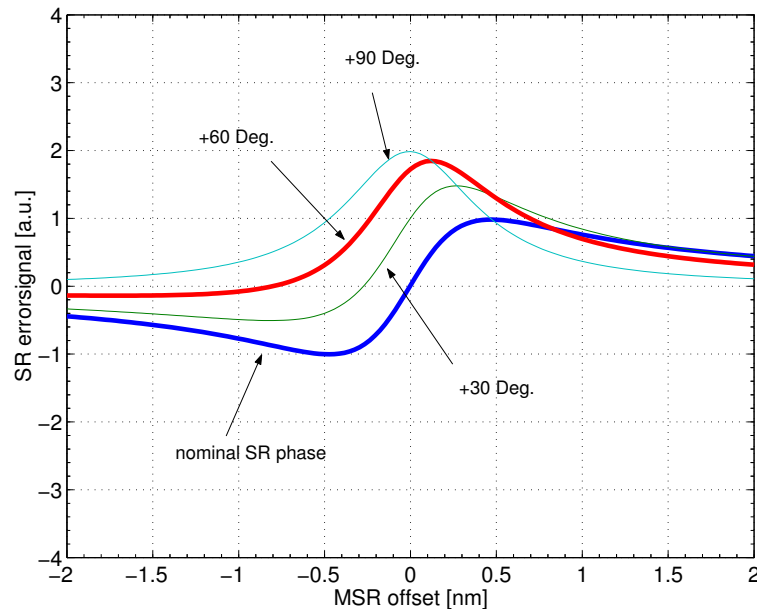


Figure 2.8: Simulated signal recycling error signal as a function of the (signal-recycling) mirror's microscopic position. The signal is shown for four different demodulation phases, spaced by 30° .

If the slope of the error signal decreases to one side of the capture range (compared to the case of a symmetric signal, like the one labelled 'nominal SR phase'), the lock can be lost more easily on this side, as there is less loop gain. Another principal effect of changing the demodulation phase is an offset from the zero crossing of the error signal from its position for the correct demodulation phase. The zero crossing of the error signal is shifted to a different tuning in this case, which means that the mirror is locked to a slightly different microscopic position, thus altering the frequency of maximum Michelson sensitivity to length changes ⁴.

2.3.3.2 Michelson deviation from dark fringe

Figure 2.9 shows the signal recycling error signal for different small deviations of the Michelson from the dark fringe. This can be an issue if the initial gain of the Michelson lock after acquisition is low, thus allowing for a relatively large deviation from the dark fringe.

The slope of the signal recycling error signal changes for small deviations of the Michelson from the perfect dark fringe. Note that the influence of the Michelson deviation on the signal recycling

⁴From Figure 2.8 we get a tuning change of approximately 10 pm per degree of demodulation phase change, corresponding to 2.3 Hz (per degree) shift in the frequency of maximum sensitivity.

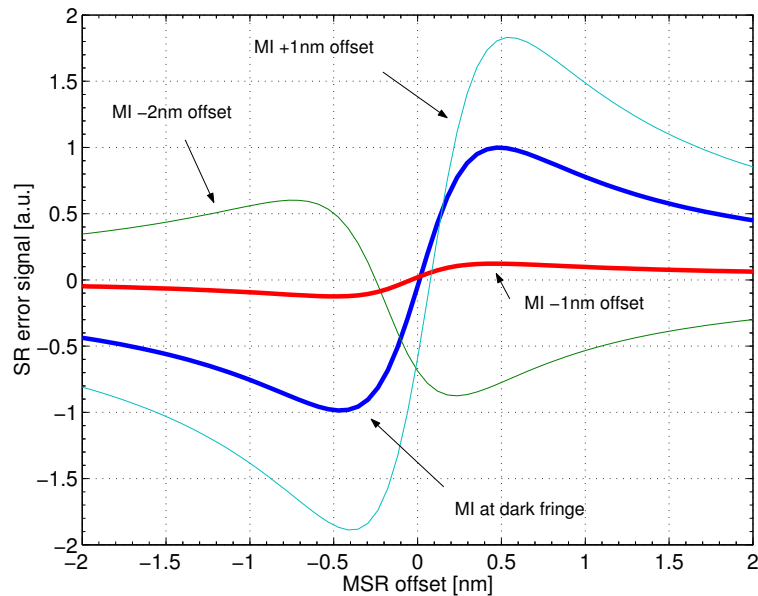


Figure 2.9: Signal recycling error signal as a function of the (signal-recycling) mirror’s microscopic position. The signal is shown for four different deviations of the Michelson from the ideal dark fringe. The influence of the Michelson deviation onto the signal recycling signal is not symmetrical about the dark fringe.

signal is not symmetrical on both sides of the dark fringe. A Michelson deviation of only -1 nm decreases the signal recycling signal slope by about factor 10 already, and slightly larger deviations even change the sign of the SR signal, such that **MSR** cannot be controlled at all.

However, keeping the Michelson within 0.3 nm to the dark fringe seems sufficient to maintain the dual-recycling lock. If we assume a free differential motion of the Michelson of the order $1\ \mu\text{m}$, dominated by frequencies around 1 Hz, a Michelson loop gain of the order 10^4 at 1 Hz is required. This loop gain is achieved if the intermediate mass feedback of the Michelson is used (together with the ESD feedback) and the unity-gain frequency of the Michelson lock is not too low (see Figure 1.13 on page 23 for the approximate Michelson loop gain of the current servo design).

2.3.3.3 PR resonance deviation from laser frequency

As important as the Michelson deviation from the dark fringe is the influence of the power recycling lock on the signal recycling error signal. Figure 2.10 shows the signal recycling error signal for different deviations of the power recycling cavity from resonance with the incident laser light. In this simulation the laser frequency is fixed and the power recycling mirror moved respectively.

In the experimental situation, the laser frequency is locked to the power-recycling cavity, as explained in chapter 1. However, the servo loop controlling the laser frequency has to suppress the frequency fluctuation that the free modecleaner would provide as the frequency reference. A detuning of the power-recycling mirror in the simulation corresponds to a frequency mismatch of the

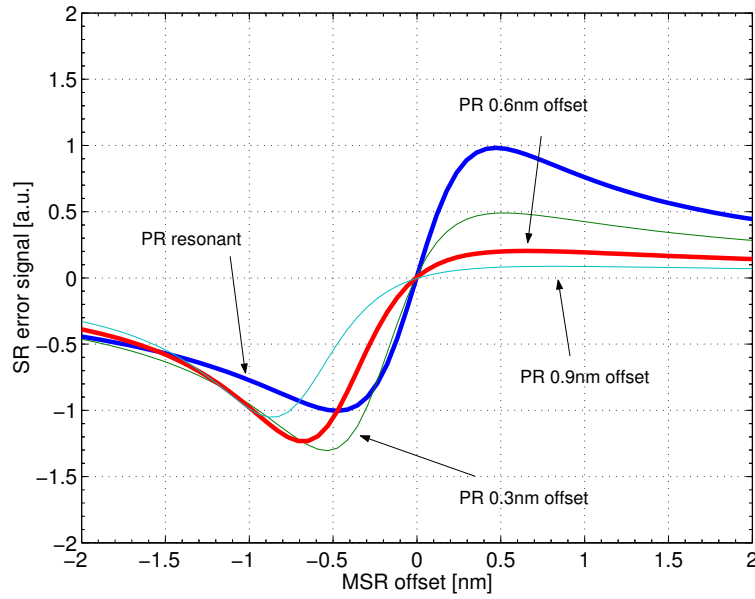


Figure 2.10: Signal-recycling error signal for different deviations of the power-recycling mirror from the position where the power-recycling cavity is resonant for the incident laser light.

laser light with respect to the power-recycling cavity. The mismatch Δf is calculated as $\Delta f = f \frac{\Delta l}{l}$. With $f = 282$ THz for the laser frequency and $l = 1200$ m as cavity length, we get

$$\Delta f = 235 \left[\frac{\Delta l}{1 \text{ nm}} \right] \text{ Hz} . \quad (2.4)$$

Aiming for at most $\Delta l = 0.1$ nm equivalent deviation of the power-recycling mirror, we want a rms frequency stability of about 20 Hz. Looking at Figure 1.5 on page 9, we find the free frequency noise of the second mode cleaner being a few MHz. With the acquisition loop gain of about 10^7 at 1 Hz (see Figure 1.3 on page 6), the suppression should be just sufficient. However, these results imply that shortly after the signal recycling lock acquisition the gain of the power recycling lock has to be increased by switching the additional integrators on. The effect of this coupling can be seen experimentally. If the integrators are not used, the dual recycled lock stretches are shorter.

2.3.3.4 Michelson differential alignment

Another critical parameter during SR acquisition is the alignment of the Michelson differential mode. Figure 2.11 shows the signal recycling error signal for different deviations of the Michelson from perfect alignment. A misalignment of not more than $2 \mu\text{rad}$ seems to be tolerable. It is possible to set the alignment manually within this accuracy, but it drifts freely in the order of minutes, such that the Michelson alignment has to be corrected, if the dual recycled lock is not achieved within this time⁵.

⁵The situation slightly improved regarding alignment drift with the installation of a new air conditioning system at the site, which is capable of holding the temperature in the central building within ± 0.5 K. Locking dual recycling gets very hard concerning pre-alignment if the air conditioning system is not operating.

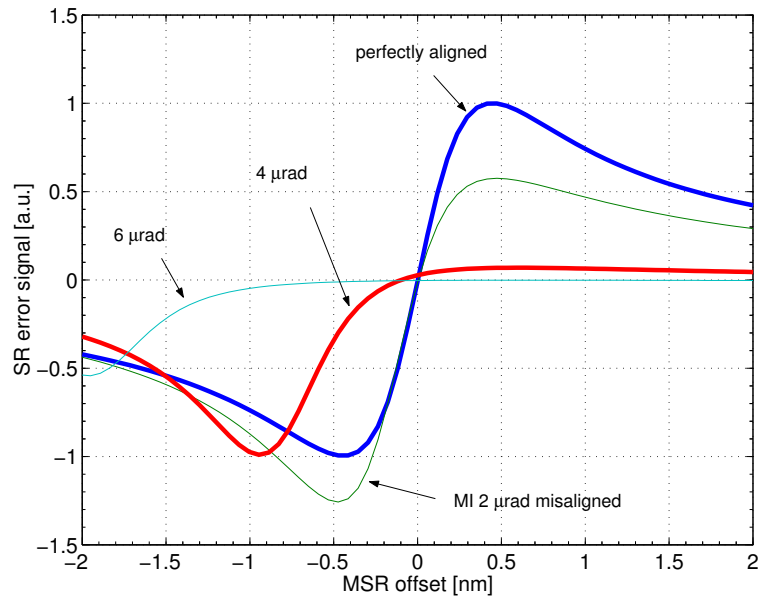


Figure 2.11: Signal-recycling error signal for different deviations of the Michelson from perfect alignment.

The alignment of the signal-recycling mirror is only a little bit less critical, and has to be corrected after several minutes as well. Locking dual recycling is harder at times of increased seismic noise, as the alignment fluctuations on a timescale of 1 s can easily be of the order $1 \mu\text{rad}$ then.

The alignment of the power recycling cavity and the spot positions on the end mirrors during acquisition of dual recycling can be done by the alignment system in its low bandwidth mode. This is true as the power recycling cavity is locked most of the time such that its alignment signals can be integrated over a few seconds. An automated pre-alignment system maintaining the Michelson and signal recycling alignment during acquisition would be helpful but also difficult to implement.

2.3.4 Summary

The main arguments concerning a locking strategy for the dual-recycling configuration can be summarized as follows:

- Due to the control sideband resonance, the power-recycling lock fails if the uncontrolled Michelson approaches a dark fringe while the signal-recycling detuning is small ($\Phi_{\text{MSR}} < 25^\circ$). Therefore it is almost impossible to find a situation in which the PR cavity is locked, the Michelson is close to a dark fringe and the signal-recycling mirror is close to a small detuning or the broadband case. This is different from the Garching 30 m prototype.
- The finesse of the power-recycling cavity and the signal-recycling cavity is larger than in the Garching 30 m prototype and thus the capture ranges for the Michelson and signal recycling error signals are smaller. In addition to this, the ESD is a comparatively weak actuator, setting a tight speed limit to the Michelson mirrors on acquisition. The capture ranges are even smaller for small SR detunings.

- The signal-recycling error signal strongly depends on the Michelson tuning, such that it seems most appropriate to lock the Michelson first. If the Michelson can stay locked for at least a fraction of the SR tunings, the chances of locking the signal-recycling mirror shortly after this are better than locking both loops at the same time.
- The acquisition rate could possibly be increased by normalizing the Michelson error signal by the actual optical gain determined by the signal-recycling tuning.

Following these arguments, a different approach for initially locking dual recycling in GEO 600 from the one for the Garching 30 m prototype seems most promising.

In this approach the Michelson is locked to the dark fringe first, which works (even without gain normalization) for a reasonable fraction of the SR detunings. When the signal-recycling mirror passes its detuned operating point (for example at 20 kHz detuning) while the Michelson is still locked, the signal-recycling loop tries to acquire lock. If this procedure was successful, the detuning can be decreased in a controlled way to proceed to smaller detunings which are required for increasing the sensitivity of the detector in the gravitational wave measurement band.

2.4 Feedback design

2.4.1 Actuators

Feedback to the signal recycling mirror is applied by a standard coil-magnet actuation setup. Three encapsulated coils, rigidly mounted onto a reaction mass and suspended as a triple pendulum, apply forces to three magnets, which are glued to the backside of the signal recycling mirror.

A current driver unit (of the type described in Appendix B.2) with three independent inputs for longitudinal, rotational and tilt motion of the mirror is used to apply control forces.

2.4.2 Loop filters

The feedback loop design has to provide sufficient loop gain at the pendulum's main resonance frequency around 1 Hz, and sufficient bandwidth to allow for lock acquisition. On the other hand, the bandwidth must not be too high, in order to prevent feeding in too much displacement noise which could couple into the gravitational wave signal. For this reason a design was chosen where the transfer function of the loop filter can be switched in lock between a high bandwidth mode for acquisition and a low bandwidth mode for normal operation. A two-pole lowpass at 1.5 kHz is added to avoid excitation of the mirror internal modes.

Table 2.1 shows the filter parameters for the two states.

Figure 2.12 shows the open loop gain and phase of the designed servos (including the actuator transfer function and the cavity pole) in its two states.

Loop type	pole [Hz]	Q	zero [Hz]	Q	pole [Hz]	zero [Hz]	zero [Hz]	pole [Hz]	zero [Hz]	pole [Hz]	pole [Hz]	Q
acquisition	-	-	-	-	1	10	15	1500	200	800	1500	2
run	0.1	1	5	2	1	5	5	50	-	-	1500	2

Table 2.1: Filter parameters for the signal-recycling mirror feedback loop. Two different designs are available: signal-recycling lock acquisition and low-noise run mode.

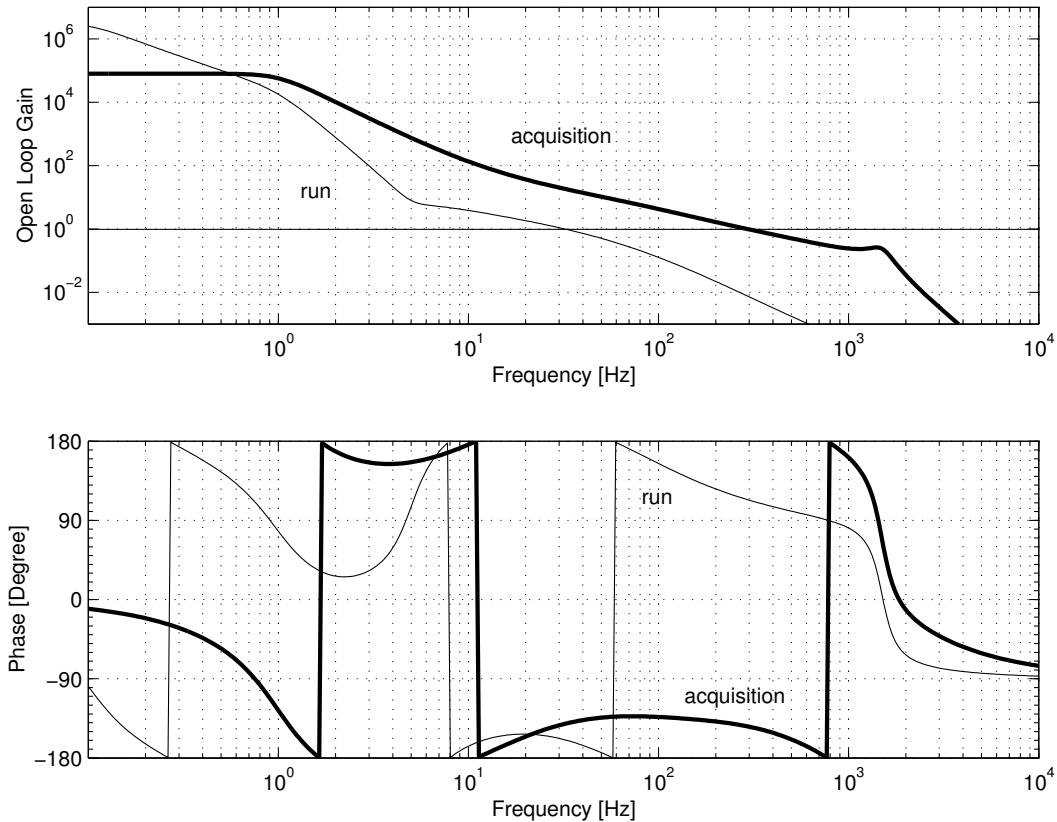


Figure 2.12: Open loop gain and phase of the signal recycling lock for two different states. The transfer function of the loop filters can be changed in lock, to enable a lock acquisition mode with higher bandwidth.

For the lock acquisition it is important to decelerate the mirror within the range of the correct error signal slope sign (the *capture* range) around the nominal operating point. Referring back to Figure 2.8, it can be seen that the (double sided) capture range is only about 1 nm around the operating point (with a transmittance $T_{\text{MSR}} = 1\%$). A high peak force is thus required to stop the mirror within this range.

When the lock acquisition succeeds, it is still important to hold **MSR** within the locking range, which sets a requirement to the loop gain around 1 Hz. The gain is important at this frequency, as the free mirror motion dominates its rms motion here. A gain of 5000 seems to be sufficient for not too large seismic noise levels.

For long-term drifts low-frequency feedback has to be applied to the upper mass of the **MSR** suspension chain. As in the case of the Michelson longitudinal drift control, this can be accomplished

by the digital LabView system.

2.5 Towards locking dual recycling

2.5.1 Finding the proper SR demodulation phase

As we have seen in the previous examples, the signal recycling error signal shape depends on different parameters. Hence determining the proper demodulation phase experimentally is difficult, if only the shape of the error signal is observed. A much more accurate method for determining the proper demodulation phase for a given signal recycling modulation frequency (and thus given detuning) is to apply a laser frequency test signal and minimize its coupling into the signal recycling error signal in the power-recycled Michelson configuration with the signal recycling mirror being misaligned. The coupling of such a light frequency test signal to the signal-recycling errorpoint can be minimized by the appropriate choice of the signal-recycling demodulation phase. Simulations show, that the demodulation phase of minimum coupling is very close to the correct phase yielding a symmetric error signal (like the one in Figure 2.8 for the nominal SR phase) in case of dual recycling. The advantage of this method is, that close to perfect alignment during the adjustment is assured by the alignment system of the power-recycled Michelson.

Figure 2.13 shows the simulation result of this method together with measured individual points.

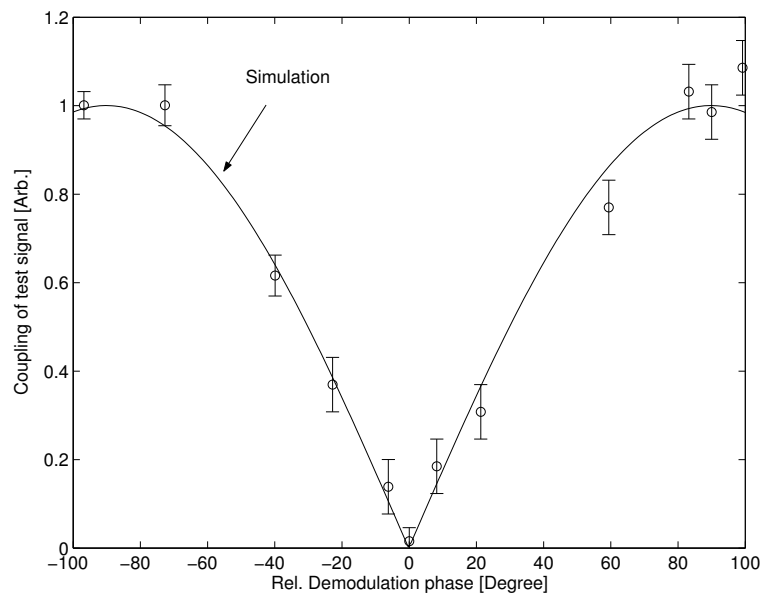


Figure 2.13: Coupling of a laser frequency test signal to the signal-recycling errorpoint in the power-recycled Michelson mode (With the signal-recycling mirror being largely misaligned, such that it acts as a beam attenuator only). The solid line is the simulation, while the distinct points display individual measurements.

2.5.2 Normalizing the Michelson gain

To allow for a more robust lock acquisition, some experiments were carried out to obtain a signal proportional to the actual gain that the Michelson feedback loop experiences, while the Michelson is locked and the signal-recycling mirror still changes its position arbitrarily. Such a signal could then be used to make the Michelson lock more independent of varying signal recycling tunings by an automatic gain control.

One possibility to measure the actual optical gain (the conversion factor with which a differential Michelson arm length change translates to a voltage after the mixer output) is the application of a test signal, modulating the differential Michelson arm length. By measuring the size of this signal in the Michelson output, the actual optical gain can be determined. However there are practical problems with the implementation of this method: To obtain a sufficient bandwidth of the optical gain information (e.g. 100 Hz), the frequency of the injected signal has to be significantly higher. This is a practical problem within GEO 600, as there is no fast actuator capable of providing sufficiently large amplitudes at this frequency. Large amplitudes are required as especially during the acquisition phase the background noise can be much higher than in the final state.

Another method is more promising, at the cost of requiring additional hardware: The optical gain can be measured by the power of the Michelson Schnupp sidebands at the first harmonic of the modulation frequency [Fre03a]. For this purpose the beam on the output bench is sampled with an additional photodetector ('2f' detector in Figure 2.5.2 on page 59). A dedicated circuit then detects the power in a small band around twice the modulation frequency, which we refer to as the '2f' signal.

While the desired signal size is still small, the advantage of this method is, that it uses the information at a radio frequency, which allows frequency selective detection on a smaller noise background⁶. Figure 2.14 shows a simulation of the '2f' signal together with the simulated Michelson optical gain. The upper graph is computed for perfect alignment, while in the lower graph, **MCE** is misaligned by $0.5 \mu\text{rad}$. Within the simulation the normalization signal is obtained by demodulating the Michelson output diode signal at $f_{\text{norm}} = 2 \times f_{\text{MI}}$ with the demodulation phase yielding the maximum signal. The simulated Michelson optical gain is computed by adding a test signal at 100 Hz to **MCE** and **MCn** differentially while demodulating the Michelson output photocurrent at f_{MI} and 100 Hz respectively. The two demodulation phases are fixed in this case, resembling the experimental situation of a fixed demodulation phase during acquisition.

The gain normalization with the '2f' signal will not work in the range where the higher order TEM modes are resonant and for small **MSR** detunings. However the '2f' signal matches the optical gain very well for **MSR** detunings from $-90 \dots -10$ degree. Locking dual recycling in the range of $+10 \dots +30$ degree detuning will be difficult, as the Michelson optical gain is very sensitive to alignment here (lower graph) and the '2f' signal is wrong even for small misalignments.

⁶The power in a band around a radio frequency can be detected by homodyne demodulation in both quadratures and processing the square root of the sum of powers in both quadratures. Another possibility is the heterodyne demodulation to a convenient intermediate frequency (IF), allowing for a flexible and simple choice of bandwidth. The power in the bandpassed IF band can then be measured with an rms to dc converter.

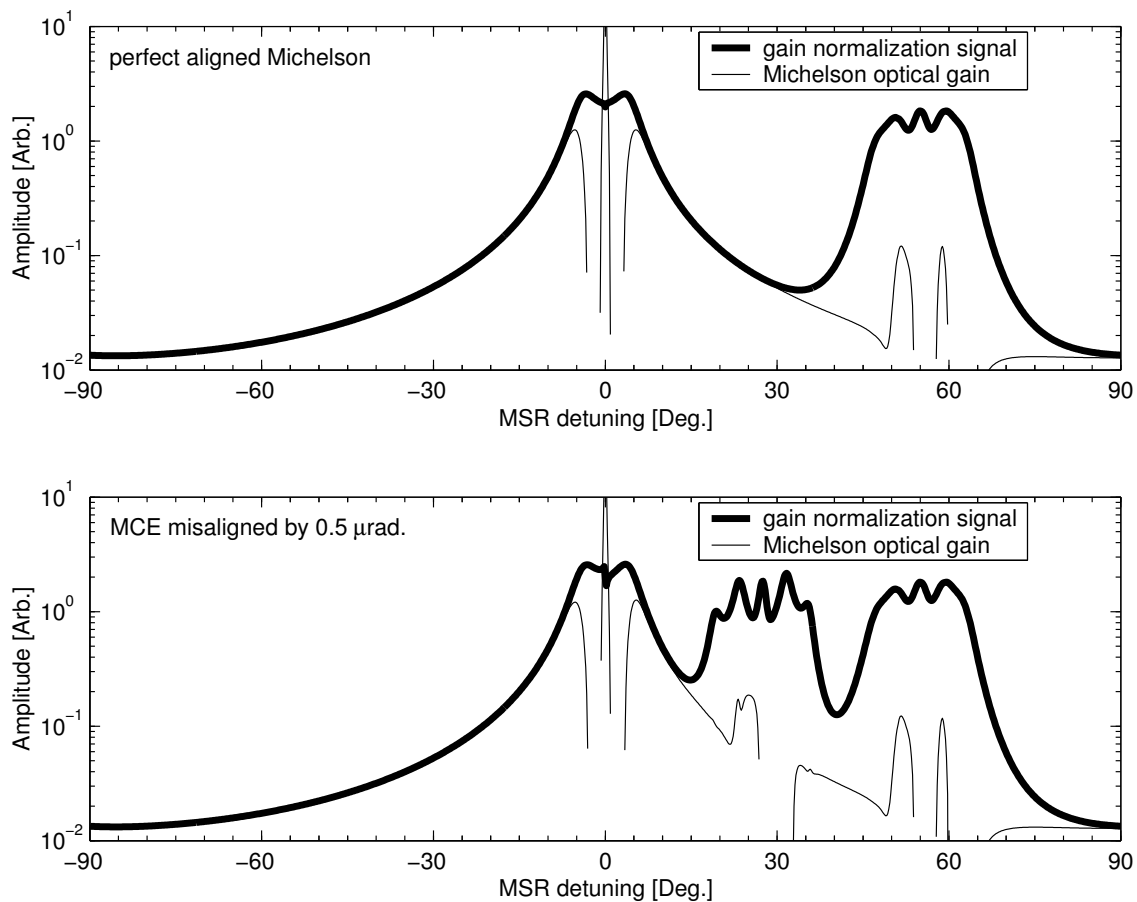


Figure 2.14: Simulation of the Michelson gain normalization signal and the Michelson optical gain. The upper graph is computed for perfect alignment, while in the lower graph, **MCE** is misaligned by $0.5 \mu\text{rad}$. The demodulation phase for the computation of the Michelson optical gain is fixed; therefore the optical gain gets negative (and thus is not displayed) if the demodulation phase is not optimized for some detunings. A fixed phase is adequate for the experimental situation of lock acquisition. The normalization signal matches the optical gain very well for **MSR** detunings from $-90 \dots -10$ degree.

For **MSR** detunings of $-90 \dots -10$ degree, the ‘ $2f$ ’ signal is also correct for Michelson misalignments. Once the Michelson is locked, the ‘ $2f$ ’ signal might indicate the approximate tuning of **MSR** in the range $-90 \dots -10$ degree. The signal can then be used to normalize the Michelson gain by analog division, or the signal can be used to move **MSR** towards its intended locking point ⁷.

⁷Shortly before printing this document, it was confirmed that the normalization of the Michelson error signal with the ‘ $2f$ ’ signal works, and extends the Michelson lock stretches to the dark fringe while the signal recycling mirror is not yet locked. More important, the ‘ $2f$ ’ signal can not only be used for gain normalization, it can also be used directly for the locking of the signal recycling mirror! For this purpose, a constant offset is subtracted from the ‘ $2f$ ’ signal, yielding a suitable control signal. It turned out that this locking scheme works much better for the initial lock acquisition of **MSR** than locking to the nominal sideband signal in the first place. After the lock (using the ‘ $2f$ ’ signal) has settled for a few seconds and gains have been optimized automatically, the control of **MSR** can be switched to the sideband signal, which turned out to work very well.

2.6 Experimental results

2.6.1 Acquisition

Initial locking experiments were performed by locking the signal recycling mirror to a detuning of 20 kHz. The SR demodulation phase was adjusted according to the procedure described above. Before having a look at the results of these experiments we can ask for the maximum allowable mirror speed to enable lock acquisition of signal recycling with the given **MSR** actuator and capture range of the error signal.

With a measured displacement calibration factor of the **MSR** coil-magnet actuator of 60 pm / V at 100 Hz, we obtain a force of $F_{\text{MSR}} = 137 \mu\text{N}/\text{V}$ (Equation 1.8 with $m_{\text{MSR}} = 2.9 \text{ kg}$ is used). Given a peak input range of 10 V for the current driver, we get a peak force $F_p = 1370 \mu\text{N}$. Equation 1.12 then yields the maximum speed for **MSR** to allow lock acquisition:

$$v_{\text{max}} \approx 600 \text{ nm/s.}$$

A single sided capture range of 0.5 nm is assumed for this calculation. The maximum speed obtained is similar to the maximum allowable speed of **MCE** and **MCn** to enable Michelson lock acquisition with the ESD at a signal-recycling detuning of 20 kHz⁸. However, we can expect a slightly smaller average speed of **MSR** than the average equivalent speed of the Michelson mirrors. This is true, as only the relative longitudinal motion of **MSR** with respect to the longitudinal motion of **MPR** (judged by their distances to the beamsplitter **BS**) is relevant for the locking of **MSR**.

Figure 2.15 shows longitudinal signals during a successful lock acquisition process of the largely detuned dual-recycling interferometer. The signals from top to bottom are: Power-recycling reflected power ‘PR refl.’, sum of power in both arms ‘E+N’, dark port power ‘Dark p.’, Michelson errorpoint ‘MI ep’, signal recycling errorpoint ‘SR ep’, IM feedback ‘IM fb’, ESD feedback ‘ESD fb’ and SR feedback ‘SR fb’.

From $t = 0.14 \text{ s}$ to $t = 0.23 \text{ s}$ the power-recycling cavity is not locked: The power levels of ‘E+N’ and ‘Dark p.’ are close to zero and almost all incident light power is reflected back to the mode-cleaners. At $t = 0.23 \text{ s}$ the power-recycling cavity is locked with the Michelson being arbitrarily tuned. The Michelson approaches a dark fringe as the dark port power decreases, while the sum of power of both arms increases. The ESD feedback is switched on on a zero crossing of the Michelson error signal at $t = 0.37 \text{ s}$. The power-recycled Michelson lock settles, and the intermediate mass feedback switches on after about 200 ms, at $t = 0.57 \text{ s}$. Approximately 50 ms later the signal-recycling errorpoint shows the typical error signal structure, indicating that **MSR** passes its detuned operating point. The signal recycling feedback is switched on on the zero crossing of this error signal at $t = 0.64 \text{ s}$ and the signal-recycling mirror is caught on its operating point, using the nominal sideband signal.

⁸The capture range of the Michelson error signal gets smaller with decreasing signal-recycling detuning, which can be seen in Figure 2.5. In the lower left graph the white and black areas get narrower for SR detunings approaching zero.

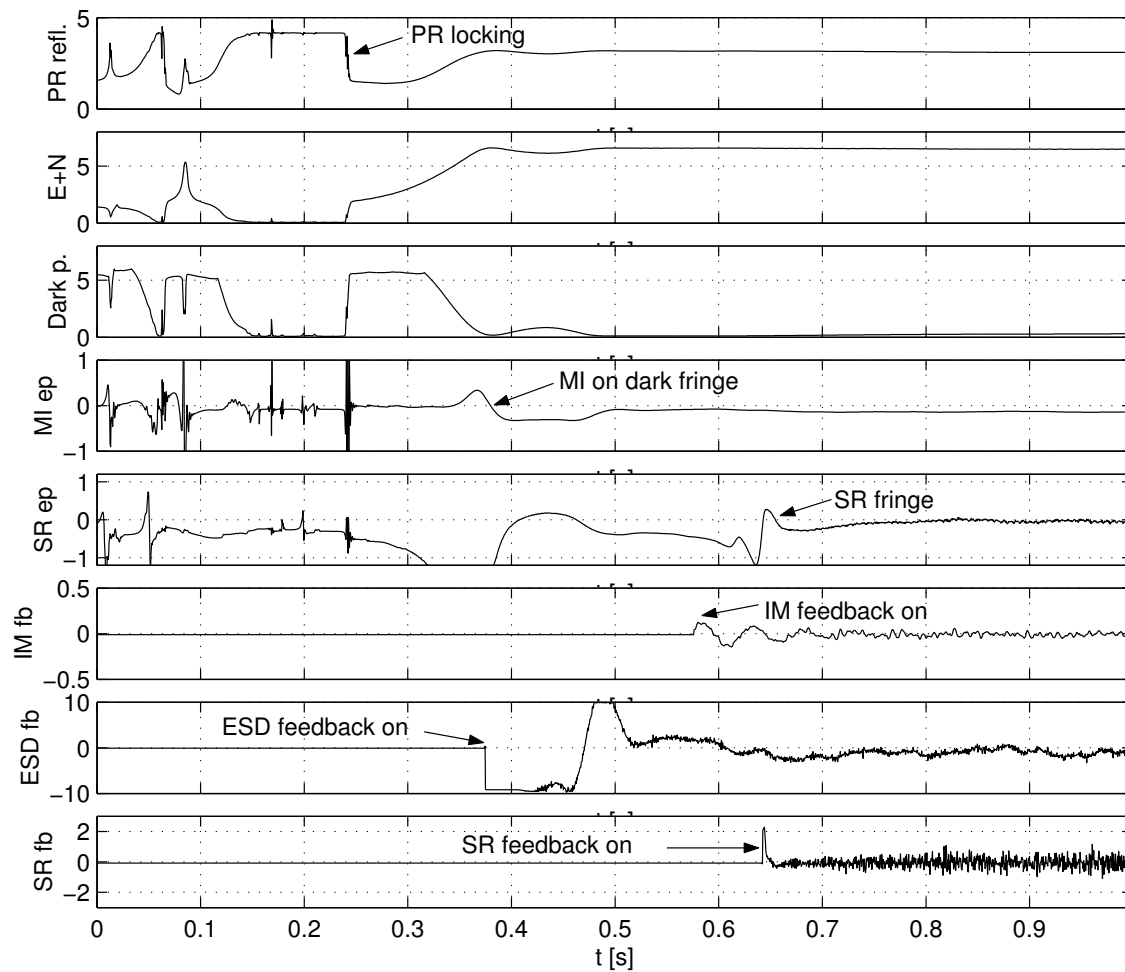


Figure 2.15: Acquisition of the largely detuned dual-recycling lock. The signals from top to bottom are: Power-recycling reflected power (PR refl.), sum of power in both arms (E+N), dark port power (Dark p.), Michelson errorpoint ‘MI ep’, signal recycling errorpoint ‘SR ep’, IM feedback ‘IM fb’, ESD feedback ‘ESD fb’, SR feedback ‘SR fb’. All signals are in Volt, as this is a practical unit for debugging the detector.

It can be seen that the signal-recycling error signal has an offset, which was not perfectly compensated at the time of this measurement. Due to the fact that the SR locking signal is obtained from the beam reflected at the beamsplitter’s AR-coated side with a reflectivity of only about 50 ppm, the signal is relatively weak with respect to offsets caused by RF pickup in the resonant circuit of the photodetector.

With this locking scheme, using the sideband signal for the initial acquisition of **MSR**, dual recycled lock stretches are rather rare and it often takes several 10 minutes until a lock can be achieved. A possible explanation for this could be that the free mirrors alignment fluctuation of the order $1\ \mu\text{rad}$ is just too large, as we have seen that the alignment requirements of the Michelson are close to this value.

The lock durations varied from $< 1\ \text{s}$ to 15 minutes. It seems that longer locks could not be achieved because of alignment drifts. The Michelson and power-recycling DWS autoalignment systems (see sections 3.4 and 3.5) work in the dual recycled case. It is unclear yet, if locks are

lost by a misalignment of the signal-recycling mirror. In some cases the dual recycled lock seems to be lost because of decreasing signal-recycling loop gain. Perhaps one of the parameters investigated in section 2.3.3 causes this behaviour. In particular, it could be that the Michelson or power-recycling loop gain is not sufficient.

2.6.2 Sensitivity

Maximizing the Michelson sensitivity to differential arm-length changes is of course the final goal of all locking attempts. For the largely detuned dual-recycling lock, the sensitivity in the nominal GW band from 50 Hz to 5 kHz is orders of magnitude below the final sensitivity. Nevertheless it is useful to measure the sensitivity in order to identify individual parameters contributing to the noise floor.

Figure 2.16 shows the equivalent **MCE** displacement sensitivity for largely detuned ($\phi_{\text{MSR}} = -28^\circ$) dual recycled lock stretches. The sensitivity improved with continued work on the lock. Offsets in the Michelson and signal-recycling error signals were minimized and more loop gain at low frequencies for the power-recycling cavity lock was provided. The calibration of the spectra was done by applying a longitudinal test signal at 244 Hz to the east electrostatic drive. This test signal is calibrated to yield an equivalent displacement of **MCE** by tracing it back to the laser frequency control.

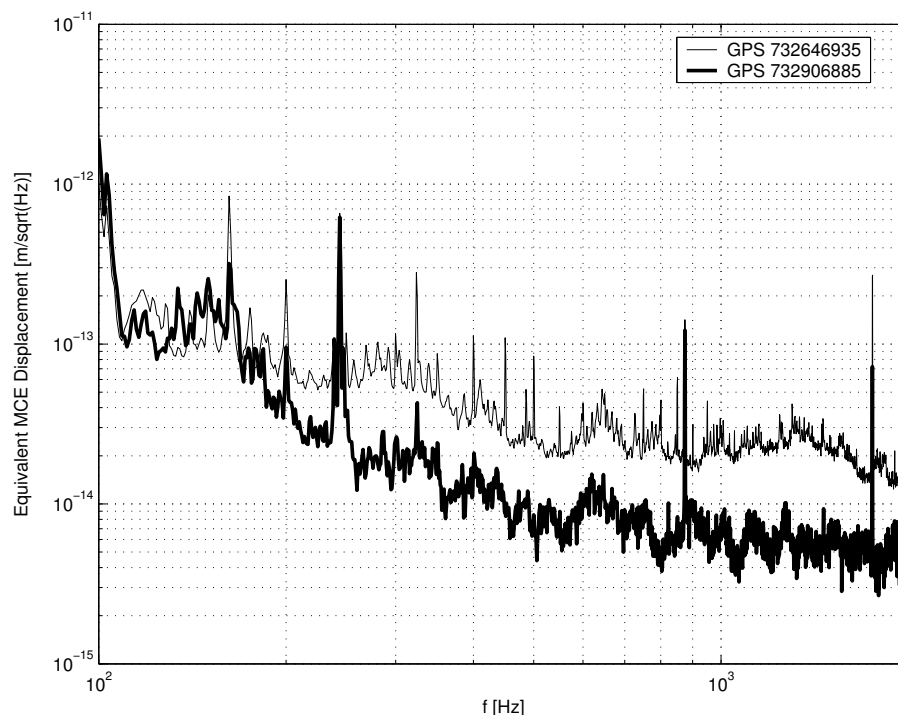


Figure 2.16: Equivalent **MCE** displacement sensitivity for largely detuned dual recycled lock stretches. The peak at 244 Hz is used for calibration.

Chapter 3

The GEO 600 Autoalignment

3.1 Introduction

Any interferometer can only work correctly if the interfering beams are properly aligned. Even in small-scale (e.g. table-top) experiments, acquisition of initial alignment and compensation of various drifts are challenging tasks for the experimentator. For the 600 m long arms of GEO 600 with its mirrors that are suspended as multiple pendulums which need to maintain their alignment for weeks, an automatic alignment system is indispensable.

The cavity and beam-steering mirrors within the vacuum system are suspended as pendulums for the purpose of seismic isolation. While this gives good attenuation of longitudinal and angular motions of the suspended components in the measurement band for gravitational waves (50 Hz - 5 kHz), the motions are enhanced at the pendulum resonance frequencies (typically around 1 Hz). Moreover, suspended components are subject to larger drifts over long time periods compared to rigidly mounted components.

To achieve an optimized performance and long term stable operation of the suspended optical cavities, an automatic angular alignment system is required for two degrees of freedom of each suspended mirror. This automatic alignment system has two goals:

- The propagation axes of interfering beams have to be superimposed. In particular the axes of optical cavities have to match the axes of their input beams to minimize coupling of incident beam geometry fluctuations into transmitted light power.
- All beam spots have to be centered on mirrors to minimize coupling of mirror alignment noise into longitudinal signals.

Control signals for these purposes are obtained by two methods within GEO 600: For superimposing two beam axes we use the *differential wavefront sensing* (DWS) technique, which senses the angles between interfering wavefronts. Beam axes have to be superimposed in the cases of

the two GEO 600 modecleaners, the power-recycling cavity, the Michelson interferometer and the signal-recycling cavity.

To control beam spot positions on mirrors, the small fraction of light that is transmitted through the mirror is detected by a spot position sensing device, for example a four-quadrant photodiode. Within GEO 600, the spot position on most of the mirrors has to be controlled, but we will see some cases where the spot position is fixed by parameters that cannot be controlled while the detector is operating.

3.1.1 Differential wavefront sensing

As differential wavefront sensing is the core method of the automatic alignment system, a short overview is given in this section. The method is described in more detail in e.g. [MMRW94, Hei99a].

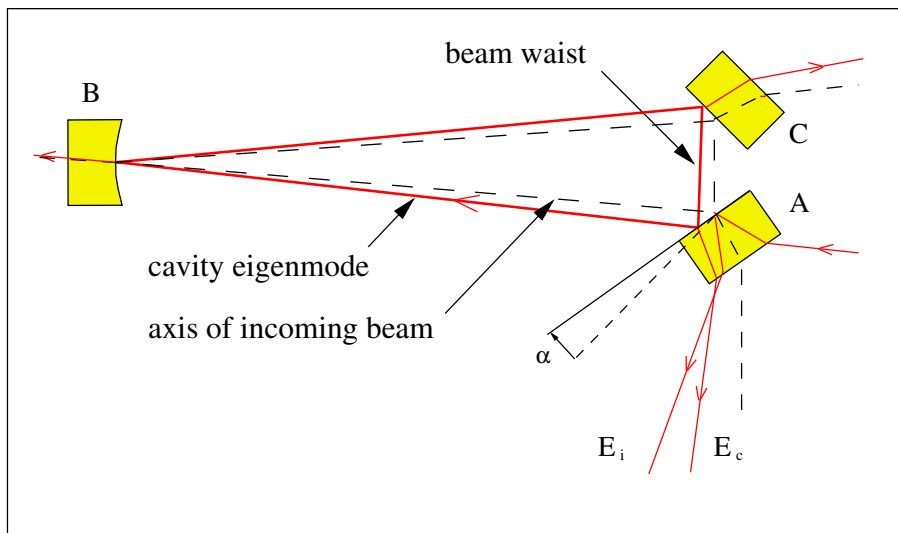


Figure 3.1: A schematic of a triangular ring cavity, consisting of two flat mirrors A, C and a curved mirror B. Mirror A is misaligned by an angle α .

Figure 3.1 shows a triangular ring cavity consisting of two flat mirrors A, C and a curved mirror B. Incident laser light impinging on mirror A is partly reflected in the direction of E_i and partly enters the cavity. The light circulating inside the cavity leaks out at mirror A as beam E_c . The figure shows a misalignment of mirror A, resulting in an angle between E_i and E_c . While here the misalignment is largely exaggerated, in a real situation the two beams cannot be separated, but their interference pattern can be detected with photodiodes. This combined beam is referred to as $E_i + E_c$.

The phase difference between the wavefronts of E_i and E_c is read out over the whole cross section of the interference pattern using Pound-Drever-Hall sensing. For this method, the incident light is being phase modulated at an appropriate radio frequency with an electro-optic modulator (EOM). The photocurrent of a diode illuminated with $E_i + E_c$ is then coherently demodulated. The resulting

signal is a measure for the match between the incident laser frequency and one of the cavity's resonant frequencies. Usually an appropriate feedback loop is used to keep the difference of these frequencies close to zero, what is referred to as 'locking' of a cavity.

If a cavity is locked (which is assumed for all following discussions), the DWS method can measure the *angle* between the wavefronts of $E_i + E_c$ by using a split photodiode and calculating the difference between the two demodulated photocurrents of the different photodiode sections. With a quadrant diode this can be done for the horizontal and vertical direction simultaneously.

The angle between the wavefronts is generally not identical with the angle between the axes of beams E_i and E_c ¹. But if the wavefront angles are measured at two different distances from the beam waist (which is located between mirrors A and C in the configuration of Figure 3.1), four different quantities can be obtained, giving full information about angular and parallel displacement of the cavities axis against the axis of the incoming beam.

More precisely; depending on the cavity geometry, individual mirror misalignments show up in a fixed combination of lateral and angular misalignment at the location of the beam waist. The kind of misalignment at the waist can conveniently be characterized by the angle Θ^W which can be defined as (see [Hei99a], Section 2.2)

$$\Theta^W = \arctan \frac{\gamma z_R}{\Delta x}; \quad (3.1)$$

with γ as the angle between the nominal beam axis and the axis of the misaligned beam, Δx the lateral beam displacement at the waist and z_R being the Raleigh range of the beam under consideration. $\Theta^W = 0$ describes pure parallel displacement, while $\Theta^W = 90^\circ$ describes pure angular misalignment of beams at their waist.

As the beam $E_i + E_c$ propagates away from the waist, an additional Guoy phase shift $\eta(z)$ between the TEM₀₀ and TEM_{10/01} modes of $E_i + E_c$ is introduced, depending on the propagated distance z :

$$\eta(z) = \arctan \frac{z}{z_R}; \quad (3.2)$$

with z_R being the Raleigh range of the cavity eigenmode².

The Guoy phase shift $\eta(z)$ adds to the angle Θ^W , resulting in the angle Θ^d defined as

$$\Theta^d = \Theta^W + \eta(z). \quad (3.3)$$

¹This is due to the fact that the wavefronts of the Gaussian beams considered here are curved (and not flat) in the general case

²We assume perfect modematching, such that the Raleigh range of the incident beam is identical with the Raleigh range of the cavity eigenmode.

Θ^d determines which linear combination of lateral and angular misalignment a DWS sensor at distance z from the beam waist is most sensitive to. By placing two sensors at different distances from the waist, different linear combinations of misalignments are sensed. The distribution of information on two DWS sensors depends on their relative distances from the waist. A DWS sensor at the beam waist is only sensitive to angular misalignment, while a sensor located at a distance $z \gg z_R$ from the waist (i.e. in the ‘far field’ of the detected beam) is only sensitive to lateral displacements.

If Θ^d at the two detector locations differs by 90° , the sensing coordinate system is orthogonal, yielding the maximum possible signal levels. Specific linear combinations of the four detected wavefront angles can be chosen to match the coordinate system of experimentally available independent actuators, enabling feedback controlled alignment. This feedback system is referred to as *DWS control*.

The complete automatic alignment system of GEO 600 uses two further control loop types: the *spot position control* (for centering beam spots on mirrors, as mentioned above), and the *centering control*, being used to center the detected beams $E_i + E_c$ on the DWS quadrant photodiodes. Subsystems like the centering control and the design of the DWS sensors - which are common to all GEO 600 DWS loops - are explained in the section about the modecleaner alignment.

Throughout this work the terms ‘rotation’ and ‘tilt’ are used (as still common in the GEO group) to describe mirror misorientations. A mirror rotation in this sense results in a *horizontal* misalignment of a reflected beam, while a tilted mirror changes the *vertical* direction of a reflected beam. Also common are the terms ‘yaw’ and ‘pitch’ for rotation and tilt, respectively.

3.2 Alignment requirements

Before looking at the experimental systems it is useful to gain an overview of the alignment requirements. Misalignments of interfering beam axes, and optical cavities in particular, can give rise to different performance degradations of an interferometric detector. Either a quantity is affected directly by misalignments, or the coupling of one quantity to another is established or enhanced. Some examples for the main interferometer (the power recycled Michelson with or without signal recycling) are given here, together with an estimation of corresponding alignment accuracy requirements.

The alignment requirements are different depending on a given purpose: We can ask for the alignment accuracy required for a stable operation (but not yet optimal noise performance) of the main interferometer, which is important for intermediate steps in the complete acquisition process. More important is the higher accuracy required to satisfy the design-sensitivity of GEO 600 in the final data taking mode.

The suspended mirrors have to be used as actuators for the alignment system, and their angular calibration is straightforward in most cases. Therefore simulations and requirements are computed for individual mirror misalignments in the following examples. All simulations are done with

FINESSE, using its Hermite-Gauss extension mode (see [Fre02]). The radii of curvature of all included mirrors are set to their design values, which are 600 m for **MCE**, **MCn**, and 640 m for **MFe** and **MFn**. All other involved mirrors are assumed to be flat. The simulation results are only slightly different for the real (measured) radii of curvature and all important conclusions remain the same.

3.2.1 Michelson light power

We start with an intuitive example: We expect the light power inside the power-recycling cavity to decrease with misalignments of individual mirrors.

Degradation of the power buildup inside the power-recycling cavity affects the light power available for the Michelson interferometer, which reduces control signal gains (just by the fact that less light is provided for detection) as well as the shot-noise-limited sensitivity of the instrument. Figure 3.2 shows the influence of individual mirror rotation misalignments onto the power buildup factor of the power-recycling cavity.

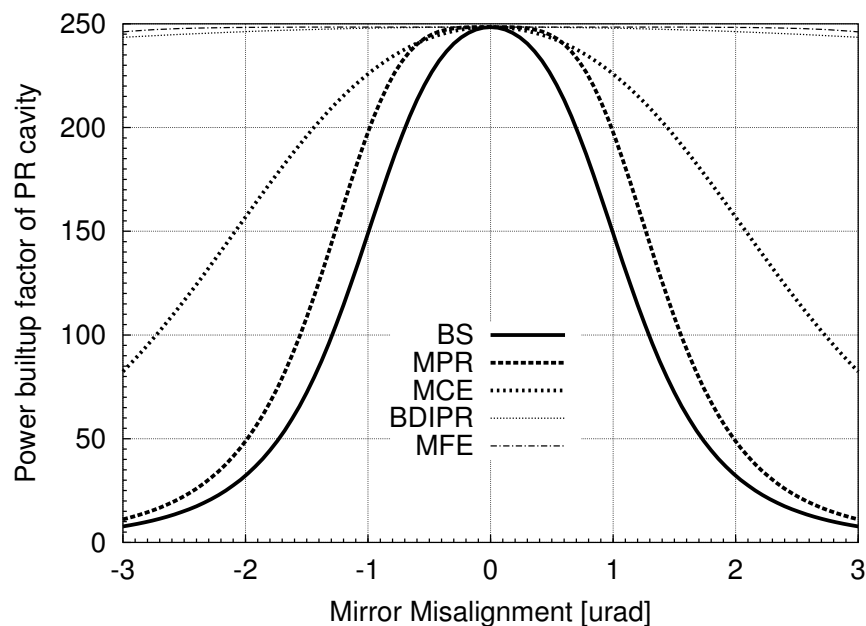


Figure 3.2: Influence of individual mirror rotation misalignments onto the power buildup in the power-recycling cavity.

The simulations were done with a power transmittance for **MPR** of $T = 1.35\%$ and no signal recycling³. The beamsplitter is the most critical component here. With a beamsplitter misalignment of $1.2\mu\text{rad}$ rms, half of the power is lost, which is confirmed by experimental observation. The couplings of misalignments in the other axis (tilt) to cavity power are of the same order. (Note

³Misalignment of a signal-recycling mirror has only a small influence on the power buildup.

that the maximum power buildup for perfect alignment is slightly limited by losses due to imperfect Michelson contrast here. These are caused by slightly mismatched radii of curvature of the Michelson mirrors.)

As the free beamsplitter alignment fluctuations are of the order $1\ \mu\text{rad}$ rms, dominated by frequencies around 1 Hz, the power fluctuates up to 50 %, which can be seen in the first 100 seconds of Figure 3.33 on page 117. The lower part of this figure shows the light power in the east arm of the Michelson interferometer which is proportional to the power in the power-recycling cavity. Locking stretches in the order of minutes are just possible with this alignment fluctuation, however a slightly increased seismic noise level makes locking stretches of more than a few seconds already rare. Allowing a maximal power drop of 50 % to maintain the lock in the acquisition phase, puts the minimal alignment requirement for the beamsplitter to $1.2\ \mu\text{rad}$ rms.

As beamsplitter misalignments have the largest influence onto the power buildup, this influence is compared for three different optical configurations of GEO 600:

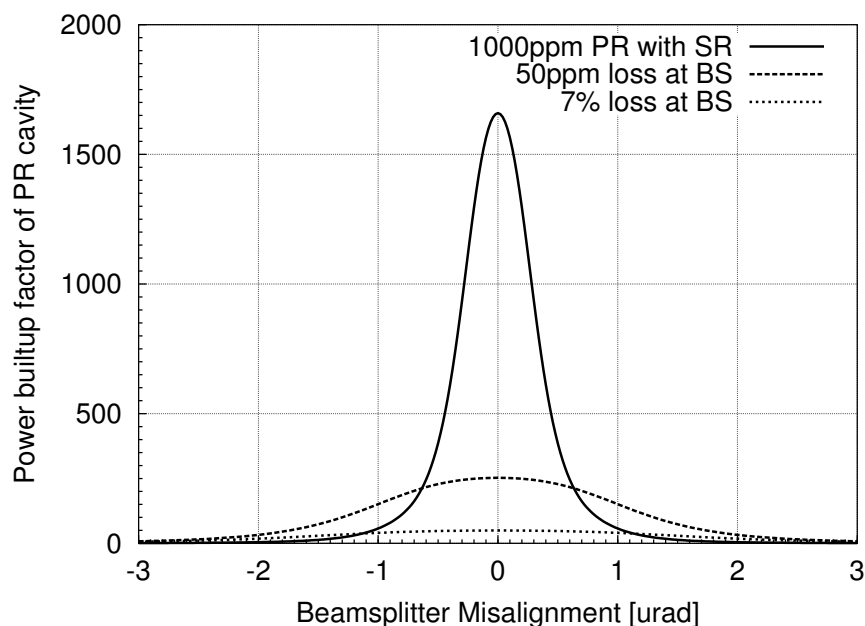


Figure 3.3: Influence of beamsplitter rotation misalignment onto power buildup in the power-recycling cavity.

The narrowest trace in Figure 3.3 (labelled ‘1000 ppm PR with SR’) shows the power buildup for a final configuration of GEO 600, using a power recycling mirror with $T_{\text{MPR}} = 1000\ \text{ppm}$ and signal recycling ($T_{\text{MSR}} = 1\%$ in broadband mode). This is the case with the largest coupling between misalignment and power buildup⁴. The middle trace (‘50 ppm loss at BS’) shows the buildup for the power recycling mirror with $T_{\text{MPR}} = 1.35\%$ (which was installed during all experiments in this work) and a reflectivity of the beamsplitter’s anti-reflective coating layer of 50 ppm (signal recycling was omitted here). The lowest trace (‘7 % loss at BS’) shows the buildup for large losses

⁴Note that the maximum power buildup does not reach the initially intended factor 2000. This is due to the power transmission at the endmirrors **MCe** and **MCn** of $T = 120\ \text{ppm}$ each, being larger than the specified 30 – 50 ppm.

in the east arm which were introduced by a faulty anti-reflective coating of a test beamsplitter installed during the first Michelson locking experiments with GEO 600 ('Initial PRMI-A').

If the power drop during the acquisition phase in the final optical configuration has to be less than 50 %, the beamsplitter misalignment must not exceed $0.35 \mu\text{rad}_{\text{rms}}$. This is only possible if the acquisition happens in a well aligned state with almost maximal power buildup, and then the alignment system is switched on within a few 100 ms after lock is acquired. The requirements might be relaxed slightly if the active seismic isolation system in the vacuum chamber holding the beamsplitter will have some noise suppression around 1 Hz.

3.2.2 Michelson error signal gain

The Michelson error signal is a measure for differential length changes of the Michelson interferometer. This signal contains gravitational wave information and is also used for the longitudinal lock of the Michelson to the dark fringe. A decrease in the Michelson error signal gain (its slope at the operating point, or, in other words, the calibration factor with which displacement is related to a signal voltage) will affect sensitivity and locking performance alike.

Figure 3.4 shows the influence of individual mirror misalignments on the gain of the Michelson error signal. As misalignment effects are symmetric around perfect alignment, we can concentrate on one misalignment sign. To estimate the Michelson error signal gain in the simulation, a test modulation at 50 Hz is applied differentially to the endmirrors longitudinal position. Then the size of this modulation signal in the Michelson error signal is computed. The detection phase is optimized for the perfectly aligned case and then fixed for the simulation ⁵.

The signal sizes in the left graph are computed for a power-recycling mirror with $T_{\text{MPR}} = 1.35 \%$ and in the right graph for $T_{\text{MPR}} = 1000 \text{ ppm}$. Both simulations use a signal-recycling mirror with $T_{\text{MSR}} = 1 \%$ in the broadband mode ⁶. With the exception of the signal-recycling mirror, **MSR**, the dependence on misalignments is similar to those for the power buildup factor. This tells us that the gain decrease of the Michelson error signal due to misalignment is mainly caused by light power loss.

In case of **MSR** the effects of misalignments are almost identical for the two graphs in Figure 3.4. This may have been expected, as the finesse of the signal-recycling cavity is not affected by changing the transmittance of the power recycling mirror **MPR**. Again the beamsplitter is the most critical component. With an rms misalignment of 150 nrad, 10 % of the Michelson error signal gain is lost, and with an rms misalignment of 350 nrad, 50 % of the signal gain is lost.

⁵This resembles the realistic situation that the detection phase is constant during operation. While the information in the two detection quadratures can be obtained for the gravitational wave information, only one quadrature will be used to obtain the Michelson error signal.

⁶Note that this simulation does not take into account slight length changes introduced by misalignments, which cause a Michelson deviation from the dark fringe and a mismatch of the power-recycling cavity with the incident laser frequency within the simulation. However it can be shown that for small misalignments ($< 1 \mu\text{rad}$ for $T_{\text{MPR}} = 1.35 \%$ and $< 0.15 \mu\text{rad}$ for $T_{\text{MPR}} = 1000 \text{ ppm}$) these effects are negligible for our purposes.

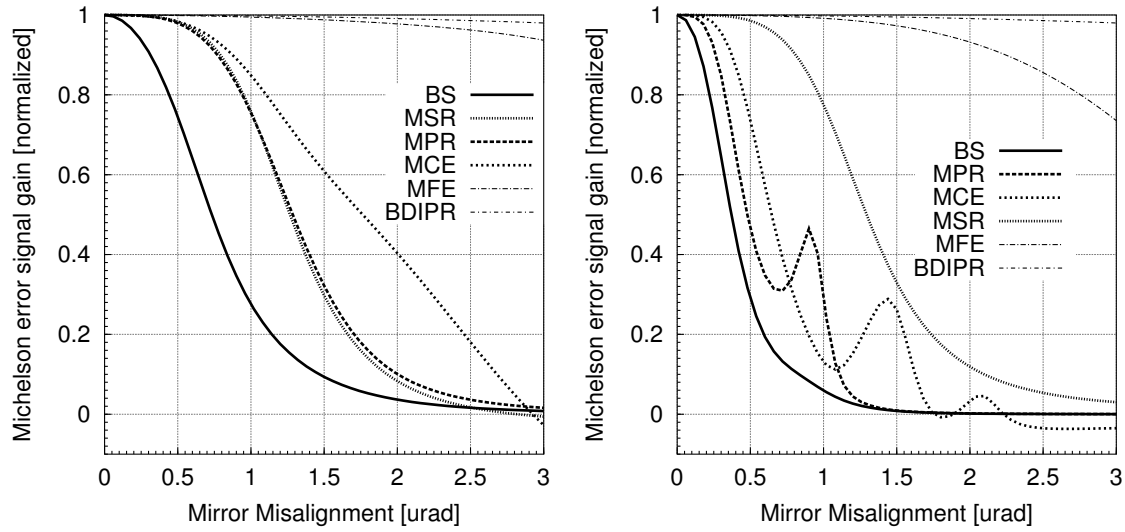


Figure 3.4: Influence of mirror rotation misalignments on the Michelson error signal gain. The left graph is computed for the low-finesse PR cavity (**MPR** with $T = 1.35\%$), the right graph shows the alignment dependence for the high-finesse cavity (**MPR** with $T = 1000$ ppm).

For the long term operation of the detector a gain fluctuation of the Michelson error signal of no more than 1% seems desirable. This is achieved with a beamsplitter rms misalignment smaller than 50 nrad.

It is interesting to compare this result to estimations for alignment requirements done by B. Meers and K. Strain in [MS91]. Their approach was to compare the losses at the Michelson output due to imperfect fringe contrast - caused by misalignments - to the unavoidable losses caused by imperfect mirrors. The signal-to-noise ratio of a power recycled Michelson concerning the sensitivity to length changes is degraded significantly, if the losses at the Michelson output port are of the order of the intrinsic losses.

Meers and Strain derive a formula, setting an alignment requirement for a maximum permissible degradation of the SNR, compared to the maximal possible SNR (SNR_{\max}) with perfect fringe contrast:

$$\Theta \ll \sqrt{\frac{2\lambda P}{\pi l}} \quad (3.4)$$

with Θ giving the maximum permissible angle between the interfering beams at the Michelson output; λ is the wavelength of the light used, P is the power loss per roundtrip in each arm, and l is the half roundtrip length.

With $\lambda = 1064$ nm, $P = 200$ ppm⁷ and $l = 1200$ m we obtain $\Theta \ll 300$ nrad. If the SNR is not to be degraded by more than 20% of SNR_{\max} , the safety factor has to be around 5, thus yielding

⁷The far mirrors (**MFe** and **MFn**) are assumed to have about 50 ppm power transmission, the end mirrors (**MCE** and **MCE**) have 120 ppm power transmission. As the far mirrors are hit twice per roundtrip, the total loss amounts to roughly 200 ppm.

an alignment requirement for the output beams of 60 nrad. This calculation holds for a power recycled Michelson without signal recycling. The power loss due to misalignment can be cured by narrowband signal recycling, thus relaxing the alignment requirement. Nevertheless the above number sets a useful conservative limit.

This result is of the same order as the limits set by the FINESSE model for the beamsplitter alignment requirements. Beamsplitter misalignment translates into an angle between the Michelson output beams with a coupling factor of unity for rotation and about $1/\sqrt{2}$ for tilt, making a rough comparison possible for this case ⁸.

3.2.3 Power noise coupling

Misalignments can increase the coupling of light power noise (which we call *power* noise here) of the light incident on the power-recycling cavity to the Michelson error signal. In general, power noise coupling is already more complex than the previous examples, as it is influenced nonlinearly by combinations of different imperfections.

Simulations were done with a power modulation test signal at 50 Hz and a modulation depth of 1000 ppm, imposed onto the laser power incident to the power-recycling cavity within the simulation ⁹. The magnitude of the Michelson signal at 50 Hz was then computed for different beamsplitter misalignments. This is a measure for the power noise coupling at 50 Hz, as there is no other signal apparent in the simulation and thus the power noise coupling dominates the output signal. The detection phase of the 50 Hz-signal is optimized for each computed data point, which means that the magnitude of the signal is detected, regardless of the phase with which it is introduced to the interferometer.

The coupling of power noise into the Michelson error signal (with perfect alignment) depends on the quality of the optical components and the longitudinal deviation of the Michelson from the dark fringe. The coupling is increased by any asymmetry between the two arms, for example, a mismatch in radii of curvature of the endmirrors, a deviation of the beamsplitter's radius of curvature from infinity, or a thermal lens effect within the beamsplitter substrate.

If the Michelson deviates from the dark fringe, power noise coupling into the Michelson error signal is introduced due to carrier light leaving the output port. Thus the amount of this coupling depends on the performance of the servo system locking the Michelson to the dark fringe in conjunction with the excitation of the mirrors given by the seismic noise level at the suspension point and its transfer function to mirror motion.

⁸The difference between rotation and tilt comes from the fact that the angle of the reflected beam with respect to beamsplitter tilt misalignments depends on the absolute angle of incidence, which is about 42° in case of the beamsplitter (see also [Fre03b]).

⁹Calculating the power noise coupling at the lower end of the gravitational wave measurement band is sufficient for a first estimation, as the power-recycling cavity in its final configuration filters power- and frequency noise with the response of a single lowpass with a corner frequency of 10 Hz. The power coupling in dependence on misalignments may need further investigations in case of narrowband dual recycling.

For these reasons, the estimation of how much misalignment causes how much power noise coupling, has to be done for a set of realistic imperfections of the optics and the dark fringe lock. Note that these imperfections have only a small influence on the results obtained in sections 3.2.1 and 3.2.2.

The beamsplitter alignment has the largest influence on the coupling, such that only the results for the beamsplitter are shown. Figure 3.5 shows power noise coupling to the Michelson output for different imperfections of the interferometer.

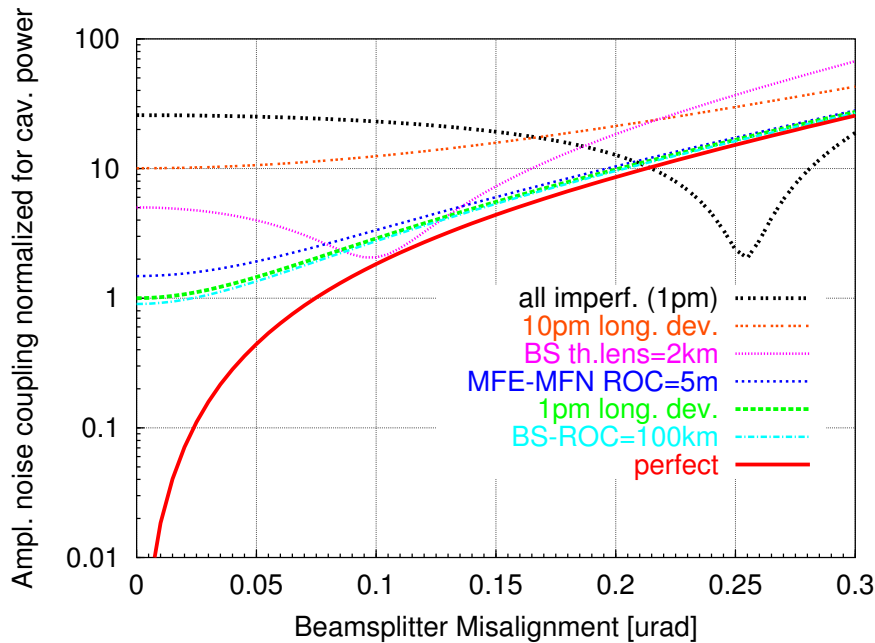


Figure 3.5: Influence of beamsplitter rotation misalignment on power noise coupling. Different imperfections of the interferometer cause different couplings (see text).

The traces are described from bottom to top (sorted by the coupling for a perfectly aligned beamsplitter with $\alpha_{BS} = 0$ rad): The lowest trace (labelled ‘perfect’) shows the power noise coupling for a perfect interferometer with large power-recycling factor ($T_{MPR} = 1000$ ppm) and broadband signal recycling ($T_{MSR} = 1\%$). All radii of curvature are at their nominal value. The coupling at $\alpha_{BS} = 0$ rad (which we call the residual coupling) is about 0.001 with respect to the normalized coupling of the third trace. Note that the ordinate uses logarithmic scaling.

The second trace (labelled ‘BS-ROC=100km’) is computed for a beamsplitter that is not perfectly flat. A residual coupling close to 1 is the consequence due to higher order TEM modes leaving the Michelson output port. Even if the optics were perfect, the interferometer cannot be held at the dark fringe perfectly. With a design gain of the Michelson lock of 10^6 at 1 Hz, the rms deviation from the dark fringe will still be of the order 1 pm (given a longitudinal displacement noise of order $1 \mu\text{m/s}$ at 1 Hz of the free Michelson). This unavoidable deviation causes residual power noise coupling as well, which is shown (and set to unity) in trace three (labelled ‘1pm long. dev.’).

Trace four (labelled ‘MFE-MFN ROC=5m’) displays the coupling if the difference in radius of

curvature (ROC) of the far mirrors **MFe** and **MFn** is 5 m^{-10} . If the final laser power of 5 W incident on the power-recycling cavity is used, the thermal lens formed in the beamsplitter substrate has to be taken into account. This is computed in trace 5 (labelled ‘BS th.lens=2 km’). Here we can see the effect that different sources of coupling can cancel each other: The coupling becomes smaller around $\alpha_{\text{BS}} = 0.1 \mu\text{rad}$. The sixth trace (labelled ‘10 pm long. dev.’) shows the coupling for a longitudinal deviation from the dark fringe of 10 pm. A large deviation from the dark fringe can be the case if the seismic noise level is enhanced, or the Michelson lock temporarily has less gain for any reason.

Finally the trace labelled ‘all imperf. (1 pm)’ computes the effect if all above imperfections (with the longitudinal deviation of 1 pm) are present in the interferometer. The residual coupling is larger than just the sum of the single imperfections. As in the case of trace 5, the coupling shows a local minimum (around $\alpha_{\text{BS}} = 0.25 \mu\text{rad}$ here) which might be an artefact of the simulation caused by the fact that microscopic longitudinal length changes caused by misalignments are not compensated for. However we are mainly interested in the simulation of the power noise coupling close to perfect alignment which is not affected by this effect.

The couplings caused by mode mismatch at the output port can be reduced if the output mode-cleaner is used. However a beamsplitter rms misalignment of not more than 60 nrad should be safe to suppress a coupling increase of more than a factor of 2 for the case with the unavoidable longitudinal deviation from the dark fringe.

3.2.4 Frequency noise coupling

The ‘normal’ way of incident laser frequency noise coupling to the Michelson output signal is by the Michelson arm length difference, setting a limit to the tolerable frequency noise. A ‘bad’ Michelson fringe contrast caused by mode mismatch or misalignment however, may increase the frequency noise coupling.

The frequency noise coupling is simulated by applying a frequency ‘noise’ signal (i.e. a frequency modulation) at 50 Hz to the incident laser light. Like in case of the power noise coupling the magnitude of this signal in the output is computed with the demodulation phase optimized for a maximum signal size in each data point. The dependence of the frequency noise coupling on the output mode mismatch and misalignment was computed.

Compared to the examples of the previous sections, the frequency noise coupling as a function of misalignments is negligible. Different imperfections of the optics, however, increase the frequency noise coupling coefficient with respect to a mismatched Schnupp frequency. The coupling is enhanced if the Schnupp sidebands are not properly resonant within the power-recycling cavity *and* with increasingly large output mode mismatches. (For further details see [Fre03b], Figure 2.24 in chapter 2.7.4.) Actually the frequency noise coupling is used in the real operation of GEO 600 to determine the proper Schnupp frequency experimentally by applying a frequency noise test peak and minimizing it in the output signal.

¹⁰The difference in ROC of **MFe** and **MFn** is actually 21 m if no thermal correction of the ROCs is used.

3.2.5 Summary

We have investigated in our simulations the required rms alignment of mirrors, which affect the alignment angle between interfering beams. With the simulations from above we find the strongest alignment requirement is set for the beamsplitter at about 50 nrad rms for the final run mode. The requirements are slightly relaxed for **MCE**, **MCn**, **MPR** and **MSR**, and requirements for **BDIPR** and the far mirrors **MFe** and **MFn** are even further relaxed. To have some safety margin, it seems desirable to achieve an accuracy of 10 nrad rms for the interfering beams of the main interferometer.

The rms value of the misalignment angle is usually dominated by mirror motions in a frequency band (e.g. 0.1 to 10 Hz) around the pendulums main resonances. For frequencies in the gravitational wave measurement band above 50 Hz, we have to look for other requirements, which are investigated in Section 3.6.5. We will see that these requirements are linked to the absolute spot positions on the mirrors, which have not been taken into account yet.

3.3 Modecleaner alignment

3.3.1 Overview

GEO 600 uses two modecleaners, each one consisting of three suspended mirrors which form a triangular optical cavity. Together with two suspended beam steering mirrors for each modecleaner, a total of 10 suspended mirrors and thus 20 angular degrees of freedom have to be controlled.

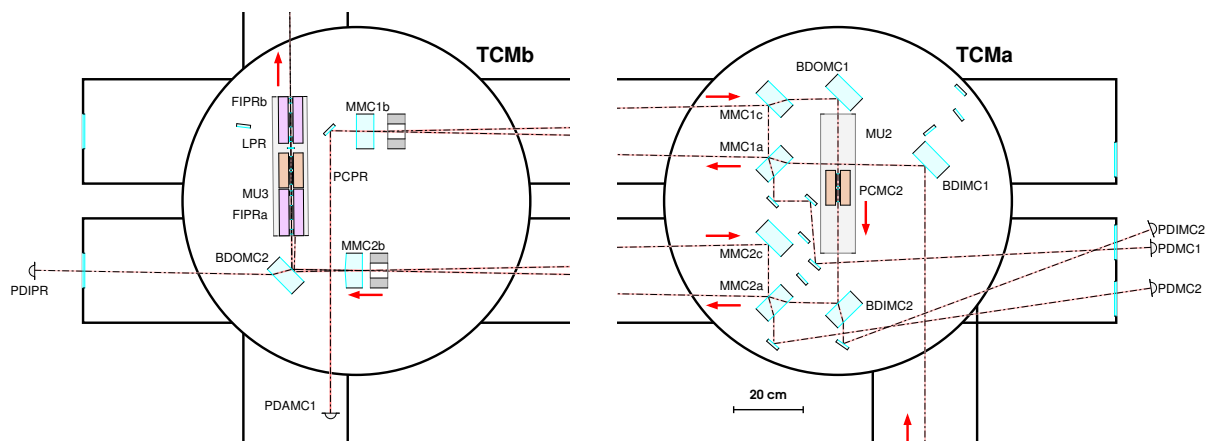


Figure 3.6: Optical setup of the two GEO 600 modecleaner cavities within the vacuum system. Arrows denote directions of light propagation. All photodetectors (including PDAMC1) are located outside the vacuum. The distance between the two vacuum chambers is 4 m, resulting in a round trip length of about 8 m for each modecleaner.

Figure 3.6 shows the optical setup of the two modecleaners within the vacuum system. Light from the laser bench enters the vacuum chamber TCMA from the lower right, is directed by beam steering mirror BDIMC1, and enters the first modecleaner (MC1), consisting of flat mirrors MMC1a, MMC1c and curved mirror MMC1b. The light leaving MC1 via MMC1c is steered by BDIMC1

and gets phase modulated by the suspended electro optic modulator PCMC2. BDIMC2 steers the beam towards the second modecleaner (MC2), consisting of flat mirrors MMC2a, MMC2c and curved mirror MMC2b. The light leaves MC2 via MMC2b and is finally directed towards the main interferometer by BDOMC2 in chamber TCMB.

All beams required for the alignment system are drawn, together with corresponding photodetectors. The photodetectors PDAMC1, PDIMC2 and PDIPR are single (4-element) spot position detecting photodiodes, while PDMC1 and PDMC2 symbolize more complex setups using two (4-element) photodiodes each (see Figure 3.8 for details).

The detection setups PDMC1 and PDMC2 provide the four DWS signals needed for each modecleaner. Error signals for the remaining 12 angular degrees of freedom of the 10 suspended mirrors of vacuum chambers TCMA and TCMB are taken from the beam spot positions on all 5 detectors (shown in Figure 3.6), and detector PDAPR in Figure A.1, which detects the position of the beam leaving BDOMC2.

3.3.2 Control signals

Before explaining the experimental setup in detail, we should have a look at the behaviour of a modecleaner cavity eigenmode for individual mirror misalignments. Figure 3.7 shows the perfectly aligned (upper graph) and a misaligned (lower graph) state of a GEO 600 modecleaner. The misalignment shown is caused by a rotation α_a of mirror MMC1a.

The beam spot positions are measured with respect to the indicated coordinate system. Angles are counted positive in the clockwise direction. Spot positions and beam angles were computed with respect to the perfect aligned case for small misalignments of the cavity mirrors. The results of these simulations are displayed in Table 3.1 for horizontal misalignments and Table 3.2 for vertical misalignments¹¹. For a better separation of horizontal and vertical misalignments we use mirror angles β and beam angles δ for the vertical case.

The only quantity we can measure with a DWS sensor is Θ^d (and thus Θ^W according to equation 3.3), carrying information about the kind and size of the cavity eigenmode misalignment against the axis of the incoming beam. We can see in Tables 3.1 and 3.2 that Θ^W is almost identical for a misalignment α_a (of mirror MMC1a) and a misalignment α_c (of mirror MMC1c). Therefore the DWS system practically cannot distinguish between misalignments caused by MMC1a or MMC1c, such that we define the linear combinations

$$\alpha_- = \alpha_a - \alpha_c, \quad (3.5)$$

$$\alpha_+ = \alpha_a + \alpha_c, \quad (3.6)$$

¹¹The calculations were done with a ray tracing program described in [Hei99a].

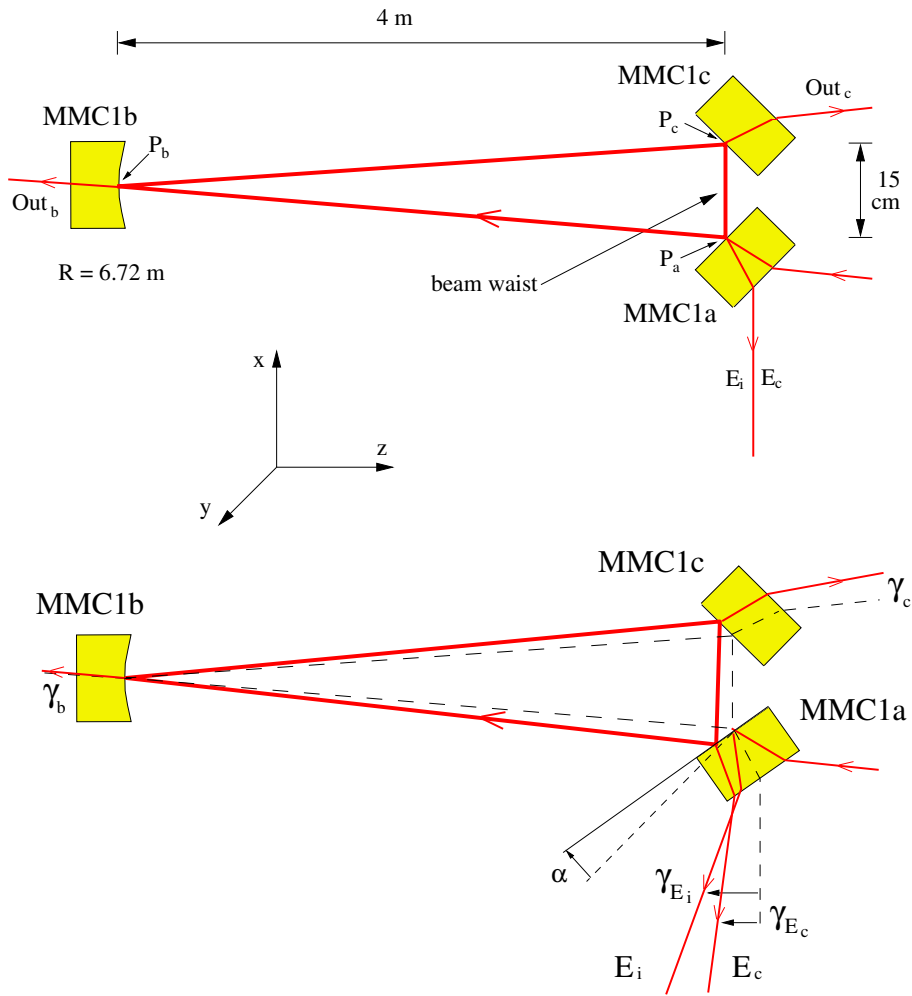


Figure 3.7: Aligned (upper graph) and misaligned (lower graph) GEO 600 modecleaner. The misalignment is caused by a rotation α_a of mirror MMC1a.

Cause	P _a		P _b	P _c	
	Δx	Δz		Δx	Δz
α _a	$-4.002 \text{ m} \cdot \alpha_a$	$-4.078 \text{ m} \cdot \alpha_a$	$-0.191 \text{ m} \cdot \alpha_a$	$3.851 \text{ m} \cdot \alpha_a$	$-3.924 \text{ m} \cdot \alpha_a$
α _b	$0.187 \text{ m} \cdot \alpha_b$	$0.191 \text{ m} \cdot \alpha_b$	$10.362 \text{ m} \cdot \alpha_b$	$0.187 \text{ m} \cdot \alpha_b$	$-0.191 \text{ m} \cdot \alpha_b$
α _c	$3.851 \text{ m} \cdot \alpha_c$	$3.924 \text{ m} \cdot \alpha_c$	$-0.191 \text{ m} \cdot \alpha_c$	$-4.002 \text{ m} \cdot \alpha_c$	$4.078 \text{ m} \cdot \alpha_c$
α ₋	$-3.926 \text{ m} \cdot \alpha_-$	$-4.001 \text{ m} \cdot \alpha_-$	$0.000 \text{ m} \cdot \alpha_-$	$7.853 \text{ m} \cdot \alpha_-$	$-8.001 \text{ m} \cdot \alpha_-$
α ₊	$-0.076 \text{ m} \cdot \alpha_+$	$-0.077 \text{ m} \cdot \alpha_+$	$-0.381 \text{ m} \cdot \alpha_+$	$-0.151 \text{ m} \cdot \alpha_+$	$0.154 \text{ m} \cdot \alpha_+$

Cause	waist Δz	E _c γ _{E_c}	Out _b γ _b	Out _c γ _c	E _i γ _{E_i}	Θ ^W
α _a	$-4.001 \text{ m} \cdot \alpha_a$	$1.028 \alpha_a$	$0.972 \alpha_a$	$-1.028 \alpha_a$	$2 \cdot \alpha_a$	38.6°
α _b	$0.000 \text{ m} \cdot \alpha_b$	$-2.542 \alpha_b$	$2.542 \alpha_b$	$2.542 \alpha_b$	$0 \cdot \alpha_b$	90°
α _c	$4.001 \text{ m} \cdot \alpha_c$	$1.028 \alpha_c$	$-1.028 \alpha_c$	$0.972 \alpha_c$	$0 \cdot \alpha_c$	40.2°
α ₋	$-4.0010 \text{ m} \cdot \alpha_-$	$0.000 \alpha_-$	$2.000 \alpha_-$	$-2.000 \alpha_-$	$1 \cdot \alpha_-$	39.4°
α ₊	$0.000 \text{ m} \cdot \alpha_+$	$1.028 \alpha_+$	$-0.057 \alpha_+$	$-0.057 \alpha_+$	$1 \cdot \alpha_+$	(90°)

Table 3.1: Beam displacements caused by small horizontal misalignments of individual cavity mirrors.

Cause	P_a Δy	P_b Δy	P_c Δy
β_a	$1.889 \text{ m} \cdot \beta_a$	$4.797 \text{ m} \cdot \beta_a$	$1.994 \text{ m} \cdot \beta_a$
β_b	$-6.720 \text{ m} \cdot \beta_b$	$-6.720 \text{ m} \cdot \beta_b$	$-6.720 \text{ m} \cdot \beta_b$
β_c	$1.994 \text{ m} \cdot \beta_c$	$4.797 \text{ m} \cdot \beta_c$	$1.889 \text{ m} \cdot \beta_c$
β_+	$1.942 \text{ m} \cdot \beta_+$	$4.797 \text{ m} \cdot \beta_+$	$1.942 \text{ m} \cdot \beta_+$
β_-	$-0.053 \text{ m} \cdot \beta_-$	$0.000 \text{ m} \cdot \beta_-$	$0.053 \text{ m} \cdot \beta_-$

Cause	waist Δz	E_c δ_{E_c}	Out _b δ_b	Out _c δ_c	E_i δ_{E_i}	Θ^W
β_a	$1.942 \text{ m} \cdot \beta_a$	$0.701 \beta_a$	$-0.727 \beta_a$	$-0.701 \beta_a$	$1.43 \cdot \beta_a$	-50.9°
β_b	$-6.720 \text{ m} \cdot \beta_b$	$0.000 \beta_b$	$0.000 \beta_b$	$0.000 \beta_b$	$0 \cdot \beta_b$	0°
β_c	$1.942 \text{ m} \cdot \beta_c$	$-0.701 \beta_c$	$-0.701 \beta_c$	$-0.727 \beta_c$	$0 \cdot \beta_c$	-49.8°
β_+	$1.942 \text{ m} \cdot \beta_+$	$0.000 \beta_+$	$-0.714 \beta_+$	$-0.714 \beta_+$	$0.714 \cdot \beta_+$	-50.3°
β_-	$0.000 \text{ m} \cdot \beta_-$	$0.701 \beta_-$	$-0.013 \beta_-$	$0.013 \beta_-$	$0.714 \cdot \beta_-$	(90°)

Table 3.2: Beam displacements caused by small vertical misalignments of individual cavity mirrors.

for rotation, and

$$\beta_+ = \beta_a + \beta_c, \quad (3.7)$$

$$\beta_- = \beta_a - \beta_c, \quad (3.8)$$

for tilt misalignments. The resulting signals for these linear combinations are shown in Tables 3.1 and 3.2 as well.

The four quantities obtained with two DWS sensors can be fed back to MMC1b (α_b and β_b) and MMC1a and MMC1b (α_- and β_+). Then we have two degrees of freedom of the three cavity mirrors left to be controlled. These are the two modes of mirrors MMC1a and MMC1c, which we defined as α_+ and β_- . Variations of α_+ and β_- show up in the direction of beam $E_i + E_c$, such that a suitable control signal for α_+ and β_- can be obtained by detecting the position of beam $E_i + E_c$.

3.3.3 Experimental setup

3.3.3.1 Setup schematic

Figure 3.8 shows the experimental setup for the automatic alignment system of the first modecleaner of GEO 600. The laser beam incident on MMC1a is phase-modulated with a radio fre-

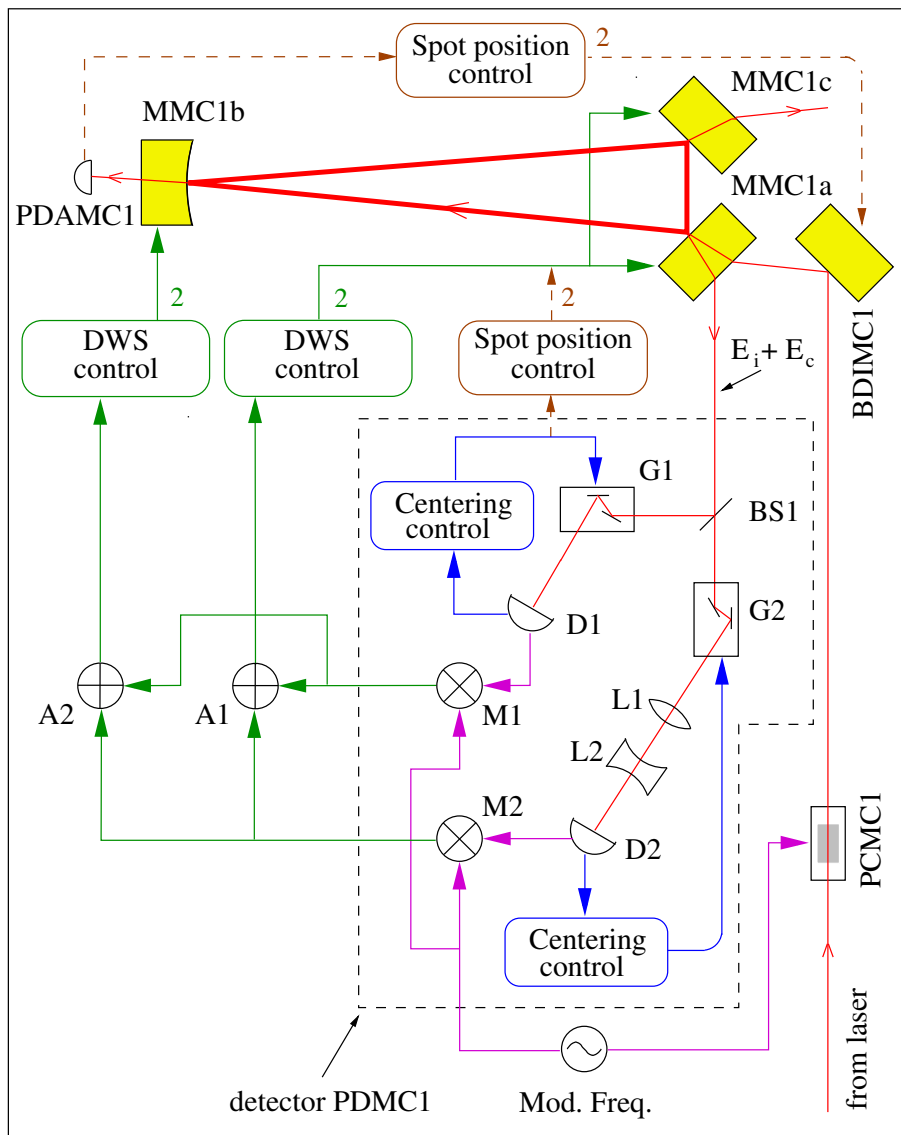


Figure 3.8: Schematic overview of the alignment control for one modecleaner. Details of the purpose of lenses L1 and L2, galvanometer scanners G1 and G2, photodiodes D1 and D2, mixers M1 and M2, and adders A1 and A2 are given in the text. The numbers at the control boxes denote the number of degrees of freedom controlled by each path.

quency of 25.2 MHz by the electro optic modulator PCMC1, to allow the use of the Pound-Drever-Hall locking and differential wavefront sensing. The free spectral range of MC1 is 37.48 MHz (37.16 MHz for MC2) such that the sidebands at 25.25 MHz from the carrier are off resonance.

Beam $E_i + E_c$ leaving mirror MMC1a (downwards in Figure 3.8) consists of the interfering fields of the directly reflected part of the input beam and the field leaking out of the cavity. This beam is split into two paths by the power beamsplitter BS1 which has a transmission of about 50%. The components G1 and G2 (described in section 3.3.4) are beam deflecting devices with the purpose of centering the beams on the photodetectors D1 and D2, respectively. The corresponding control loops are denoted as *centering control*. Lenses L1 and L2 in the light path to D2 are used to project

beam $E_i + E_c$ into the far field (see section 3.3.6).

Each of the detectors D1 and D2 (described in more detail in section 3.3.5) consists of a quadrant photodiode with associated electronics to yield information about the beam spot position, while the angle between the interfering wavefronts (the DWS signal) is available after coherent demodulation performed by mixers M1 and M2. Appropriate linear combinations of the DWS signals are then processed by analog electronic circuits A1 and A2, to generate feedback signals to individual mirrors. Amplified with an appropriate gain and frequency response, these signals are fed back to mirrors MMC1a, MMC1b and MMC1c.

The dashed lines show slow digital feedback loops being used for the spot position control. The spot position on mirror MMC1b is controlled by feeding back the PDAMC1 signals to BDIMC1, keeping the beam centered on mirror MMC1b.

We have seen that the direction of the beam $E_i + E_c$ has to be detected to yield a control signal for α_+ and β_- . As this beam is centered on D1 by G1 with high bandwidth (1 kHz), the information of the direction of beam $E_i + E_c$ is contained in the feedback to G1. This information is then fed back to MMC1a and MMC1c by another spot position control loop.

The alignment setup for the second GEO 600 modecleaner is identical (except for a phase modulation frequency of 13 MHz instead of 25.25 MHz, which is applied by PCMC2, see Figure 3.6).

3.3.3.2 Breadboard optical setup

Figure 3.9 shows the arrangement of optical components and photodetectors used for the alignment system and longitudinal lock of both modecleaners. The breadboard is located east of vacuum chamber TCMA.

The labels ‘from MC1’ and ‘from MC2’ denote the beams $E_i + E_c$ coming from MMC1a and MMC2a, respectively. Both beams can be attenuated by the combination of a $\lambda/2$ waveplate and a polarizing beamsplitter PBS. If the modecleaners are not locked, a maximum light power of about 10 W has to be dumped here, as almost all light incident to the modecleaner input mirror is reflected in this case. For this high power levels an attenuation by absorption filters is not feasible.

After attenuation, the beam from MC1 is split into its two paths, and centered on the corresponding detectors D1 and D2. The beam from MC2 is split first by a PBS to yield a beam being detected for the first design stage of the DC lock (see section 1.2.5). Then this beam is split into two paths again and centered on the detectors D1 and D2 belonging to MC2.

3.3.4 Beam centering scanners

Experience with the Garching 30 m prototype interferometer [Hei99a], GEO 600 and also TAMA 300 showed, that it is useful to center the beam $E_i + E_c$ (see Figure 3.8) on the detecting quadrant photodiode with auxiliary control loops. This concept enables an easier lock acquisition of the alignment system and compensates for drifts of the detected beam with respect to the photodetector.

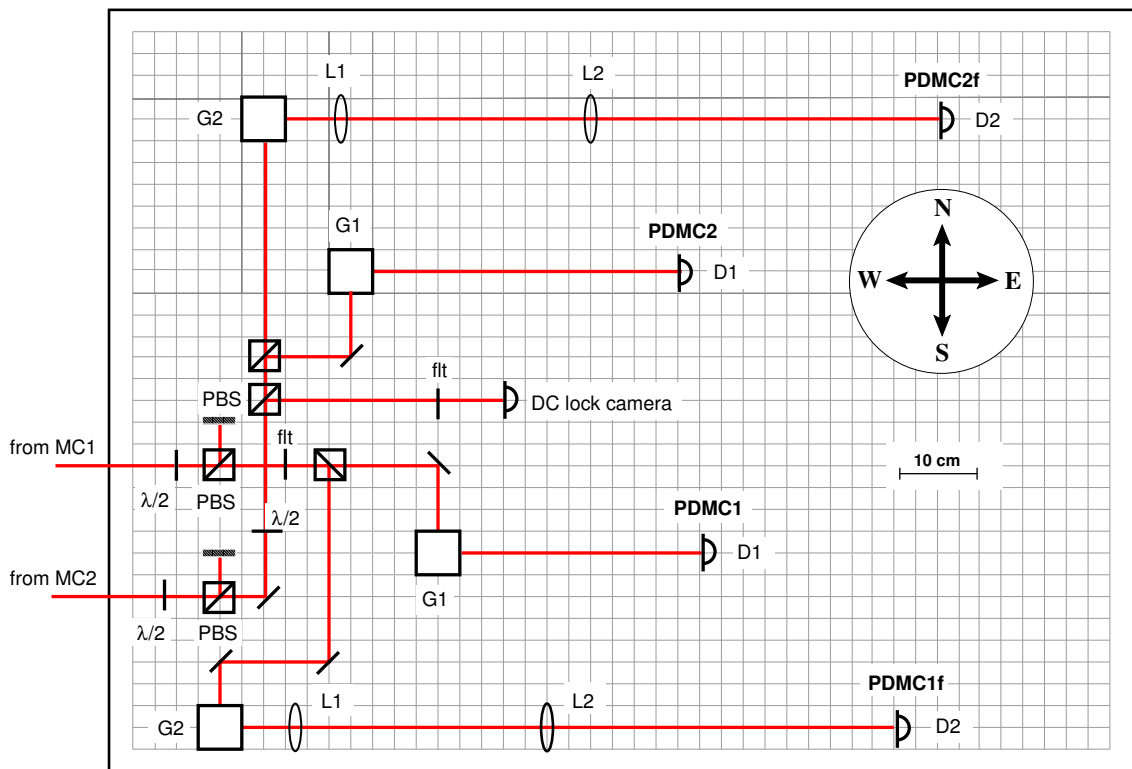


Figure 3.9: Optical layout of the breadboard east of TCMa. The beams $E_i + E_c$ from the modecleaners are attenuated with a $\lambda/2$ -wave plate and a polarizing beamsplitter (PBS) combination for each modecleaner. The beams are split into two paths and centered onto the quadrant photodetectors D1 and D2 by scanners G1 and G2 for each modecleaner. Lenses L1 and L2 adjust a desired Guoy phase shift in the path to D2. Neutral density filters (flt) are used to set proper light power levels. The light path from MC2 contains another $\lambda/2$ - PBS combination to extract a beam for another photodetector (DC lock camera).

If beam $E_i + E_c$ is not centered on the quadrant diodes, the DWS signal size decreases and can contain offsets caused by higher order modes (e.g. TEM_{20}). If for example beam $E_i + E_c$ deviates from the center of a diode by one beam radius, 86% ($1 - e^{-2}$) of the DWS signal is lost.

If the centering scanners of the first modecleaner are not used, an angular pointing error of beam $E_i + E_c$ of roughly $200 \mu\text{rad}$ leads to a decentering of one beam radius on detector D2 in Figure 3.8. Using the scanners, beam $E_i + E_c$ can be moved up to $\pm 2000 \mu\text{rad}$ while the beam is still well centered on D2, yielding the correct DWS signal. (The beam gets cut at the scanners mirror edges for larger pointings.) These numbers show that the dynamic range of the alignment detection system is increased by more than a factor of 10 due to the scanners. This allows successful acquisition of the automatic alignment system even in largely misaligned initial states, which is demonstrated by Figure 3.14.

It could be argued that beam $E_i + E_c$ can be centered on the quadrant diodes by feeding the spot position information from the diodes back to an appropriate cavity mirror alignment degree of freedom directly, or to the position of the quadrant diode itself. But the following facts have to be taken into account here:

- In case of a three-mirror cavity like the GEO 600 modecleaners, the approach of feeding the beam position information back to cavity mirrors would be possible for only one of the two scanners G1 and G2. If the beam would have to be centered on both of them with this method, another actuator (on the laser bench) would be required, determining the spot position on mirror MMC1a.
- Even if there are enough degrees of freedom available, or if the position of D1 and D2 is controlled e.g. by stepping motors (such as done in VIRGO), the critical point is the bandwidth of the centering loop. If its bandwidth is comparable to the associated DWS bandwidth, the control may be unstable due to mutual coupling of the DWS and centering control. If the bandwidth of the centering control is lower than the bandwidth of the DWS control, the DWS signals still can be contaminated by the rms deviation of the spot position on the quadrant. This is in particular true, if the rms deviation is dominated by pendulum resonances around 1 Hz, and the centering bandwidth is below. In this case the rms deviation may not be much reduced by the centering control.

3.3.4.1 Scanner design

G1 and G2 in Figure 3.8 consist of two commercial galvanometer scanners (General Scanning Inc., Type G102) each. Custom made mirror holders for $10 \times 15 \times 2$ mm mirrors were designed such that their moment of inertia (including the mirror) is centered around the scanner axis. If excited around the scanner axis, the first mechanical resonance of these holders (with mounted mirror) is at about 13 kHz. Thus the control bandwidth for the centering loop can be above the scanners free resonance, which is between 400 and 600 Hz ¹². With a perpendicular mounting of two scanners, one such pair can control the beam pointing in two degrees of freedom. The maximum angle for each direction is $\pm 2^\circ$.

The centering loops in Figure 3.8 control the spot position on the respective diodes with a bandwidth of around 1 kHz. The gain of this analog feedback loop is continuously normalized to the light power available on D1/D2 by analog division of the beam position error signals. The centering loops of D1 and D2 are automatically switched off as soon as the detected light power crosses an upper or lower threshold. (For example the scanners of the second modecleaner are switched off if the first modecleaner is not in lock and thus no light is incident on the second modecleaner.)

3.3.5 Photodetector design

The four quadrant photodetectors of PDMC1 and PDMC2 have essentially the same design (which is also used for the quadrant detectors for the power-recycling cavity and the Michelson interferometer). We use CENTRONICS QD50-3T quadrant photodiodes with a resonant electronic circuit

¹²This is the free rotation resonance around the scanners axes with mounted mirror. As the force of the scanner is not proportional to the elongation, the scanners resonance frequency depends on the amplitude.

for each of their quadrants, tuned to the modulation frequency of the detected beam ¹³. Figure 3.10 shows the equivalent schematic of the resonant circuit of a photodiode's quadrant with C as the junction capacity of the photodiode, R as the series loss resistor of the photodiode and L being a tunable inductance completing the serial resonant circuit.

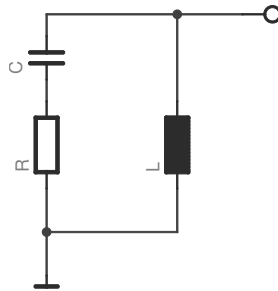


Figure 3.10: Equivalent schematic of the resonant circuit of a photodiode.

The resonant circuit rejects disturbances at frequencies different from the modulation frequency, e.g. signals caused by other modulation frequencies or the beating of modulation frequencies. Ideally, such information at different frequencies is rejected by the demodulation process, however, large signals at undesired frequencies can cause non-linearities, and they can also cause spurious signals after demodulation if the local oscillator contains the undesired frequency component as well. A schematic of the electronics around the resonant circuit is given in Figure B.1 on page 137.

The resonant circuit of each quadrant is followed by a double balanced mixer (Mini Circuits type TUF 3 H with 17 dbm local oscillator and max. 14 dbm signal input), which demodulates the signal coherently with the given radiofrequency that has been appropriately phase-shifted and amplified. Figure B.2 on page 137 shows the electronics used for the demodulation process. After demodulation and lowpass filtering the sum and differences of all four quadrant signals are processed, to give the information about the angles between the detected wavefronts in two degrees of freedom. In addition the sum of the demodulated signals from the four quadrants is obtained. This signal is used for the longitudinal lock of the corresponding cavity. Furthermore, signals for the spot position of the beam on the quadrant photodiode are produced (without demodulation) and are used as error signals for the beam centering scanners. Finally, the total detected power (sum of all photocurrents without demodulation) is made available for normalization and monitoring purposes.

¹³In our experiments, the QD50-3T diodes had significantly less cross talk between the quadrants compared to e.g. YAG444 quadrant photodiodes. The lower responsivity of about 0.22 A/W for the QD50-3T is not harmful for our purposes, as enough light power is available in all cases.

3.3.5.1 Which bias voltage to use?

Typically in these applications a reverse voltage U_{bias} is applied to the diode to reduce the junction capacity C and increase the slew rate and bandwidth, depending on the type of photodiode. If slew rate and bandwidth are not critical, the choice of U_{bias} can follow this path: Decreasing C (by increasing U_{bias}) increases the impedance of the resonant circuit Z_{max} on resonance according to $Z_{\text{max}} = L/RC$. (Again L is the tunable inductance of the resonant circuit and R is the series loss resistor of a photodiode quadrant.) As the resonance frequency $\omega_m = 1/\sqrt{LC}$ is determined by the modulation frequency, we get

$$Z_{\text{max}} = \frac{1}{\omega_m^2 RC^2}. \quad (3.9)$$

While the signal voltage across this impedance (being produced by the signal current) is *proportional* to Z_{max} , the thermal noise of the real part of Z_{max} is only proportional to $\sqrt{Z_{\text{max}}}$, thus the signal to (thermal-electronic) noise ratio increases proportionally with $\sqrt{Z_{\text{max}}}$, i.e. proportionally with $1/C$. Increasing Z_{max} by increasing U_{bias} is only useful until the photo electron shot noise of the detected light gets larger than the thermal noise of Z_{max} . Once the noise is dominated by shot noise, only increasing the detected light power will increase the signal to noise ratio. On the other hand, upper limits to the detectable light power are given by the direct power dissipation of the absorbed light power plus the electrically dissipated power which in turn depends on U_{bias} with $P_{\text{el.}} = U_{\text{bias}} * I_{\text{photo}}$. (A current limiting circuit prevents the photodiode from overheating due to false operating conditions that expose the diode to too much light power.)

In most cases a lower limit to U_{bias} will be set by the requirements of slew rate and bandwidth. In order to handle the required bandwidth even at large signal amplitudes, $U_{\text{bias}} = 30\text{ V}$ for the 25.25 MHz and 15 V for the 13 MHz detector were chosen. It is desirable to adjust the gain distribution within the detector such that the detector output is dominated by the thermal noise of the photodiode resonant circuit in case no light is incident, which means that the detector electronics does not contribute extra noise.

In our detectors, the noise-equivalent photocurrent I_{neq} is about $70\mu\text{A}$ per quadrant, which means that for photocurrents higher than I_{neq} , the output noise is dominated by the shot noise - which is the desirable situation. The maximum possible photocurrent is e.g. 2 mA per quadrant for $U_{\text{bias}} = 30\text{ V}$, allowing a power dissipation of 60 mW per quadrant.

3.3.6 Lens system and linear combination

The lens system consisting of L1 and L2 in Figure 3.8 is used to adjust the Guoy phase shift on D2 - relative to D1 - such that the sensing system is close to orthogonal. The computation of the lens system follows the procedure described in [HRS⁺99] and [Hei99a].

The calculated parameters of the lens system as shown in Figure 3.11 are $d1 = 2.5\text{ m}$, $d2 = 0.285\text{ m}$, $d3 = 0.5\text{ m}$, $L1 = +0.3\text{ m}$ and $L2 = -0.03\text{ m}$, yielding an additional Guoy phase shift of 90°

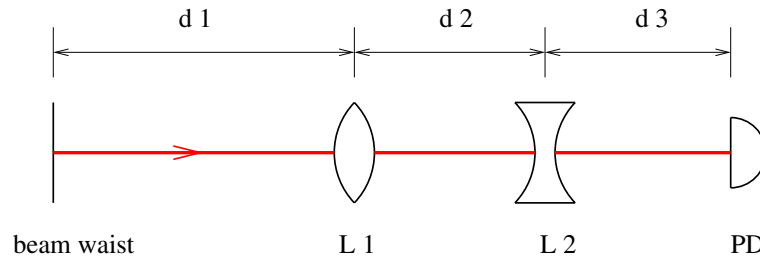


Figure 3.11: Lens system in beam path to D2 of Figure 3.8

between the TEM_{00} and $TEM_{10/01}$ modes on D2 (compared to D1) and a spot size of 2.8 mm on D2. Distance d_2 is the most critical parameter when setting up the lenses, as it most strongly influences the Guoy phase shift. However it is sufficient to adjust d_2 to an accuracy of ± 2 mm, to be close to the ideal orthogonal setup. (An accuracy of ± 2 mm is sufficient for the error signals to remain close enough to the ideal orthogonal situation.)

The next step of orthogonalization is the processing of the linear combinations of the DWS signals from D1 and D2, to match the set of chosen feedback points, which are mirror MMC1b and the combinations α_- and β_+ of mirrors MMC1a and MMC1c.

If we label the signals from the DWS cameras D1 and D2 as S_{near} and S_{far} respectively, we can calculate the linear combination of individual mirror misalignments sensed on each camera. With $\eta(z) = 37^\circ$ for D1 and $\eta(z) = 127^\circ$ for D2 we obtain

$$S_{\text{near}} = -2.016\alpha_b - 1.532\alpha_- + 0.023\alpha_+ \quad (3.10)$$

$$S_{\text{far}} = +1.519\alpha_b - 0.371\alpha_- - 0.017\alpha_+ , \quad (3.11)$$

for horizontal misalignments. As we have seen already in Table 3.1, the signals for variations of α_+ are small and thus practically cannot be detected in the DWS signals. (Therefore Θ^W is put into brackets in Table 3.1).

For vertical misalignments we obtain:

$$S_{\text{near}} = -1.232\beta_b - 0.214\beta_+ - 0.010\beta_- \quad (3.12)$$

$$S_{\text{far}} = -1.635\beta_b + 0.901\beta_+ + 0.008\beta_- . \quad (3.13)$$

Here the contribution from β_- is small and can practically be neglected.

Appropriate linear combinations from the signals S_{near} and S_{far} are processed with an analog electronic matrix which is adjusted by the following procedure: An alignment dithering signal at a fixed frequency is temporarily applied to mirror MMC1b and the corresponding signal levels from D1 and D2 are measured. Then an appropriate linear combination of D1 and D2 signals is adjusted such that the resulting signal is close to zero at the dithering frequency. This signal can then be used for the feedback to mirrors MMC1a and MMC1c (α_-). In the same way another linear combination of D1 and D2 is chosen to generate a feedback signal for MMC1b, which is zero if mirrors MMC1a and MMC1c are dithered ¹⁴. Note that due to the features of a triangular cavity, the linear combinations of D1 and D2 required for horizontal alignment are different from those for vertical alignment.

The orthogonalization achieved by the electronic linear combination is better than 1:10, meaning that dithering of MMC1b shows up with less than 10% in the signal for MMC1a and MMC1c and vice versa.

3.3.7 Control topology

In order to superimpose the eigenmode axis of the modecleaner on to the axis of the incoming beam, we feed the DWS signals back to four of the 6 angular degrees of freedom of the cavity mirrors. The opposite approach of actuating on the pointing and displacement of the incident beam to match the actual cavity axis would also be possible with appropriate actuators. The choice of which alternative to use depends on which of the two reference frames (the suspended first modecleaner or the laser) is ‘quieter’ with respect to a frame where the beam is to be used (the power-recycling cavity in case of GEO 600).

Measurements show that the beam jitter of the incident light on BDIMC1 in Figure 3.8 is of the same order of magnitude as the residual motion of the modecleaner axis for frequencies up to a few Hz, which dominate the rms motion. Thus the difference between the alternatives appears insignificant in case of the first GEO 600 modecleaner, and so for simplicity the cavity mirrors were chosen as actuators. For the second modecleaner there is no choice as the only possible alignment actuators are the suspended mirrors.

The hierarchy of feedback systems for the modecleaner automatic alignment as displayed in Figure 3.8 is as follows:

- The beam centering loops have the highest bandwidth (around 1kHz), thus ensuring correct DWS signals whenever the modecleaner longitudinal control loops are locked.
- Once the modecleaners are locked longitudinally, the feedback of the DWS signals via the DWS control loop to the cavity mirrors is switched on. These loops have a bandwidth of either 0.2 Hz or 6 Hz, depending on the type of feedback filter chosen (see section 3.3.8.2).

¹⁴The mathematical basis underlying this method is given in section 3.6.2.

- The digital spot position loops have the lowest bandwidth (below 0.1 Hz). The feedback loop centering the spot on mirror MMC1b in Figure 3.8 by controlling the alignment of BDIMC1 can only be switched on if the DWS control loop is working, such that the cavity axis follows the beam incident from BDIMC1.

Table 3.3 summarizes properties of the three feedback loop types.

feedback loop type	error signal	loop filter	actuator	bandwidth
DWS control	DWS signal (demod.)	analog	cavity mirrors	0.2 - 6 Hz
centering control	spot pos. on DWS sensor	analog	scanner	1 kHz
spot pos. control	spot pos. on QD/PSD	digital	steering/cavity mirror	<0.1 Hz

Table 3.3: Properties of the three feedback loop types of the automatic alignment system. These loop types are used in the power-recycling cavity and Michelson interferometer alignment systems as well.

3.3.7.1 LabView control

As in the case for the longitudinal locking, the computer control and automation of the alignment systems is based on LabView virtual instruments. Four tasks of this LabView control have to be distinguished:

- The analog electronic circuits of the DWS control loops are digitally supervised; the servo systems can be switched on and off and loop gains and offsets can be adjusted by software control. Mirrors can be pre-aligned by manually adjusting alignment offsets.
- Virtual instruments are used to guide the lock acquisition and automate the alignment control. In particular these VIs detect if a modecleaner is locked and switch the DWS feedback and spot position control on and off accordingly.
- A LabView based digital loop ensures well aligned cavities after a loss of lock. This *offset shifting loop* senses the analog *feedbacks* of the DWS loops and permanently adds digitally controlled offset voltages to these feedbacks, such that the DC-contents of the analog feedback signals are minimized. In other words: The alignment feedback information at very low frequencies is shifted from analog to digital feedback and can thus be reproduced after a loss of lock.
- The digital spot position control is implemented by virtual instruments as well, running with time steps of 50 ms.

Figure 3.12 shows how these LabView guided tasks work together (only the spot position control is not shown here).

The digital feedback is permanently applied, such that the cavity is close to perfect alignment even after a loss of lock, when the analog feedback information is lost ¹⁵. The digital loop filter can be

¹⁵This loop type is not included in table 3.3, as it is only required for reliable relocking after a loss of lock, but is not essential while cavities are locked.

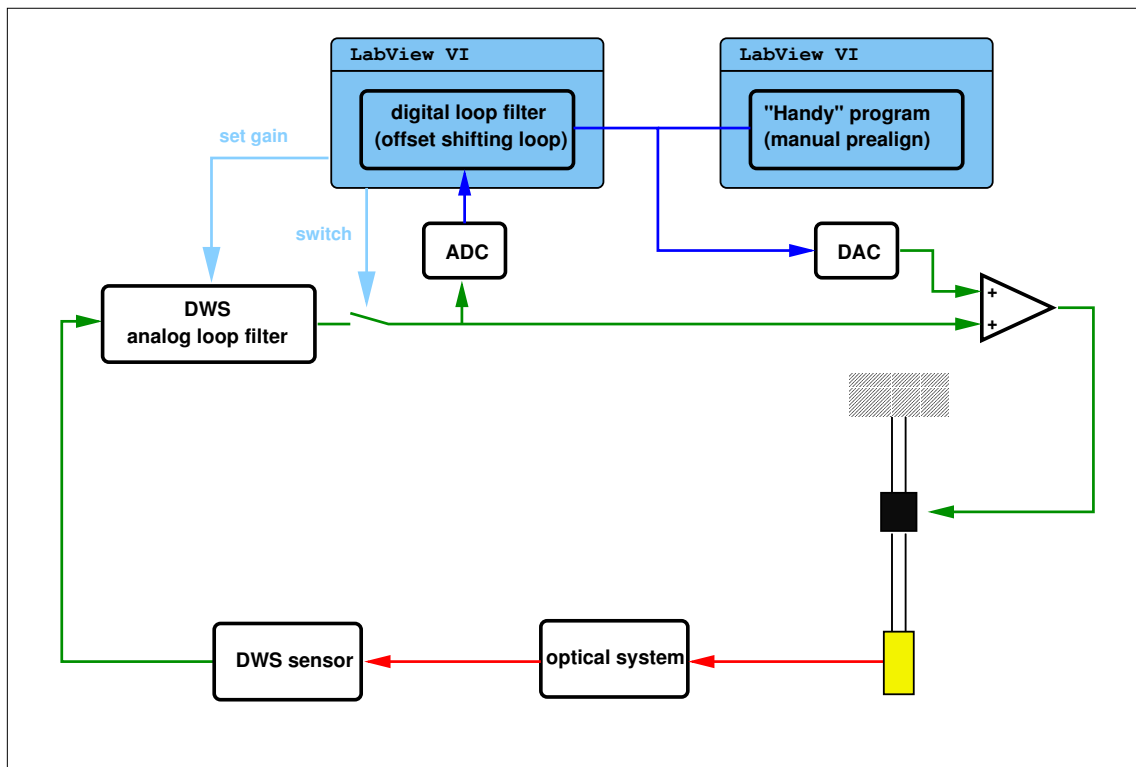


Figure 3.12: How the LabView system works together with the analog DWS feedback. For low frequencies, the analog DWS feedback is held close to zero by a shift of the applied feedback from analog to digital information. This *offset shifting loop* ensures well aligned cavities after a loss of lock, by which the analog feedback switch is opened. Note that the analog and digital feedback use the same actuator here, which is different for the alignment system of the main interferometer.

a linear filter (e.g. a simple integrator) or non-linear filter. In case of the modecleaners the filter is non-linear, continuously changing the digital offset as long as the analog DWS feedback is larger than a threshold. Note that the analog and digital feedback paths use the same actuator stage (at the intermediate mass level) on the modecleaner suspensions, as shown in Figure 3.12. We will see that this is different for the main interferometer alignment systems.

All of the above tasks - except the spot position control - are integrated within one VI for each modecleaner. Each of these VIs handles the four degrees of freedom obtained with the DWS method for one modecleaner. Dedicated sub-VIs are included for individual tasks like analog feedback detection and offset shifting. A third VI implements the spot position control for the 12 degrees of freedom of the 6 spots around the modecleaners to be controlled. The VIs are shown in appendix C.2, figures C.3, C.4 and C.5.

Table 3.4 summarizes the kind of alignment control applied to each suspended mirror of the modecleaner section, while Table 3.5 summarizes how the beam spot positions are determined on each suspended mirror of the modecleaner.

mirror	loop type	associated sensor
BDIMC1	spot pos. control	PDAMC1
MMC1a+MMC1c	DWS control	PDMC1 (DWS signal)
MMC1a-MMC1c	spot pos. control	PDMC1 (spot pos. on D1, from scanner feedback)
MMC1b	DWS control	PDMC1 (DWS signal)
BDOMC1	spot pos. control	PDIMC2
BDIMC2	spot pos. control	PDIPR
MMC2a+MMC2c	DWS control	PDMC2 (DWS signal)
MMC2a-MMC2c	spot pos. control	PDMC2 (spot pos. on D1, from scanner feedback)
MMC2b	DWS control	PDMC2 (DWS signal)
BDOMC2	spot pos. control	PDAPR (not shown in fig. 3.6)

Table 3.4: Alignment control signals for all suspended mirrors according to Figure 3.6.

mirror	spot position determined by	monitored by
BDIMC1	fixed beam pos. from laser bench	CCD for transm. beam spot
MMC1a	fixed by points on BDIMC1 and MMC1b	CCD mirror front image
MMC1b	spot pos. control acting on BDIMC1	PDAMC1
MMC1c	spot pos. control acting on MMC1a-MMC1c	PDMC1, CCD mirror front image
BDOMC1	determined by pos. on MMC1c	CCD for trans. beam spot
BDIMC2	spot pos. control acting on BDOMC1	PDIMC2
MMC2a	fixed by points on BDIMC2 and MMC2b	CCD mirror front image
MMC2b	spot pos. control acting on BDIMC2	PDIPR
MMC2c	spot pos. control acting on MMC2a-MMC2c	PDMC2, CCD mirror front image
BDOMC2	determined by pos. on MMC2b	PDIPR

Table 3.5: How the spot positions are determined and monitored for all suspended mirrors according to Figure 3.6.

3.3.8 Feedback design and performance

3.3.8.1 Actuators

The mirrors of the GEO 600 modecleaners are suspended as double pendulums with the possibility of applying orientation control at the intermediate mass stage ¹⁶. This mass carries four magnets, to which forces can be applied with coils that are rigidly connected to the pendulum suspension point. The same actuators are used for local control, which is used for damping the motion on the pendulum resonances.

¹⁶For mirrors MMC1b and MMC2b longitudinal feedback can be applied at the mirror level by coils suspended on a reaction chain pendulum. If it proves necessary, these coils might be used in future to apply orientation control to the according mirrors as well, increasing the possible alignment bandwidth for two degrees of freedom for each modecleaner.

The mirror is hanging in two steel wire slings and follows the motion of the intermediate mass with a frequency response of f^{-2} above the pendulum resonances which are around 0.9 Hz for rotation and 1.8 Hz for tilt motions of the mirror. Due to the response of the intermediate mass position to the coil current which has also a f^{-2} response, the overall transfer function from the coil current to the angular motion of the suspended mirror has a f^{-4} response above the pendulum resonances.

Table 3.6 shows the fitted parameters of the modecleaner mirror MMC1b alignment transfer function.

Mirror d.o.f.	pole [Hz]	Q	pole [Hz]	Q	zero [Hz]	Q	pole [Hz]	Q
rotation	0.439	0.51	0.932	2.8	1.52	0.088	4.97	1.4
tilt	1.54	4.5	2.57	0.43	7.52	1.0	5.45	1.6

Table 3.6: Fitted parameters of a measured alignment transfer function from intermediate mass current driver input to mirror alignment.

While the transfer function can roughly be approximated by fitting only two complex poles, the fit gets much more accurate with an additional complex pair of poles and zeros. Figure 3.13 shows the measured and fitted transfer function of MMC1b rotation (with the fitted parameters shown in Table 3.6).

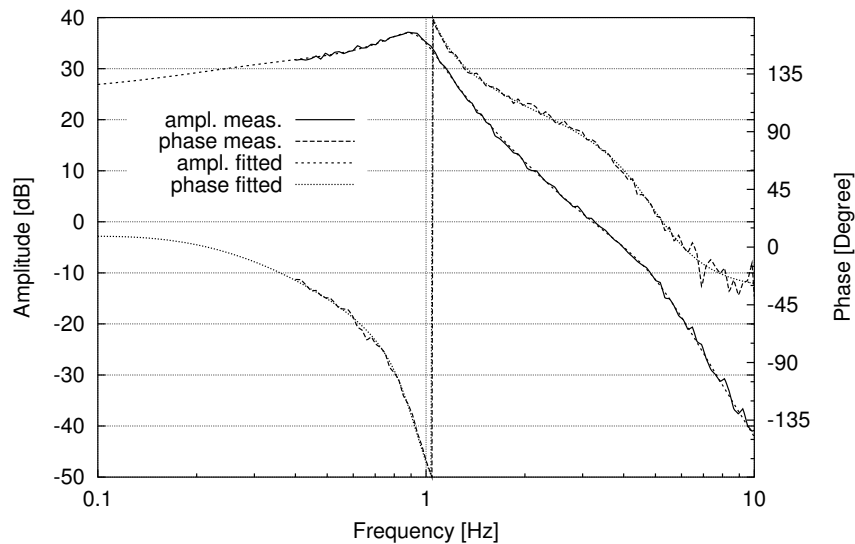


Figure 3.13: Measured and fitted alignment transfer function for MMC1b rotation input at intermediate mass level to mirror rotation.

3.3.8.2 Loop filters

In order to build a feedback loop with a bandwidth larger than the pendulum resonances (e.g. with a bandwidth of 6 Hz) with this type of actuator, the feedback filter has to provide in practice at

least 200 degrees of phase lead around the unity gain frequency. For this purpose we built analog electronic filters with two sequential biquadratic stages, yielding the desired 200 degrees of phase lead around 6 Hz.

Table 3.7 shows the filter parameters of the fast alignment feedback for MC1.

d.o.f. MMC1x	zero [Hz]	Q	pole [Hz]	Q	zero [Hz]	Q	pole [Hz]	Q	zero [Hz]	pole [Hz]	pole [Hz]	Q
a+c rot.	0.92	0.7	9	1	4.3	1.4	12	1	-	-	20	2
b rot.	4.3	1.43	16	1	0.6	-	10	-	1	20	30	2
a+c tilt	1.6	1	16	0.7	4.2	1.3	16	0.7	-	-	20	2
b tilt	1.6	2	14	0.7	5	1	20	1	-	-	40	2

Table 3.7: Filter parameters for fast alignment feedback with a bandwidth around 6 Hz. Additional integrators are active below about 0.7 Hz for each path.

Care must be taken with the gain distribution of these filters, as a large phase lead comes at the price of a large gain at frequencies higher than the loop bandwidth, which can easily lead to saturation if no additional lowpass filtering is applied or the filter input signal is very noisy.

A second version of the alignment filters follows a completely different design, as it is not aiming for a unity gain frequency above the pendulum resonances, but uses filters with a slope of $f^{-3/2}$ below the pendulums main resonance to have a high loop gain at DC with a unity gain frequency around 0.2 Hz. As experimental evidence shows that the 0.2 Hz loop is more stable in long term operation, it is currently used for both modecleaners of GEO 600.

3.3.8.3 Performance

The performance of the DWS control system with a bandwidth around 6 Hz for four degrees of freedom is shown in Figure 3.14.

The time series displays the light power reflected from the first modecleaner. Up to $t = 6$ s, the cavity is not locked and almost all light incident is reflected. Then the cavity is locked to an intentionally misaligned state with only 65 % of the possible light entering the cavity. At $t = 14$ s the DWS control is switched on for the two tilt degrees of freedom (MMC1B and MMC1A + MMC1C). At $t = 19$ s feedback to the two rotational degrees of freedom is enabled, reaching an optimally aligned cavity. The remaining reflected power level is due to a not optimized circular mode matching at the time of the measurement. It can be observed that in this state the power fluctuations are significantly smaller than in the misaligned case. Finally the graph shows the switching off in reverse order with the pendulums swinging back to their uncorrected positions.

Another result is the stable long term operation of the automatic alignment system which is in operation for the two GEO 600 modecleaners since spring 2001. No manual realignment of the modecleaner mirrors has been required since then (except for a maintenance period in May 2002 that included opening the vacuum system), whereas manual alignment corrections were necessary

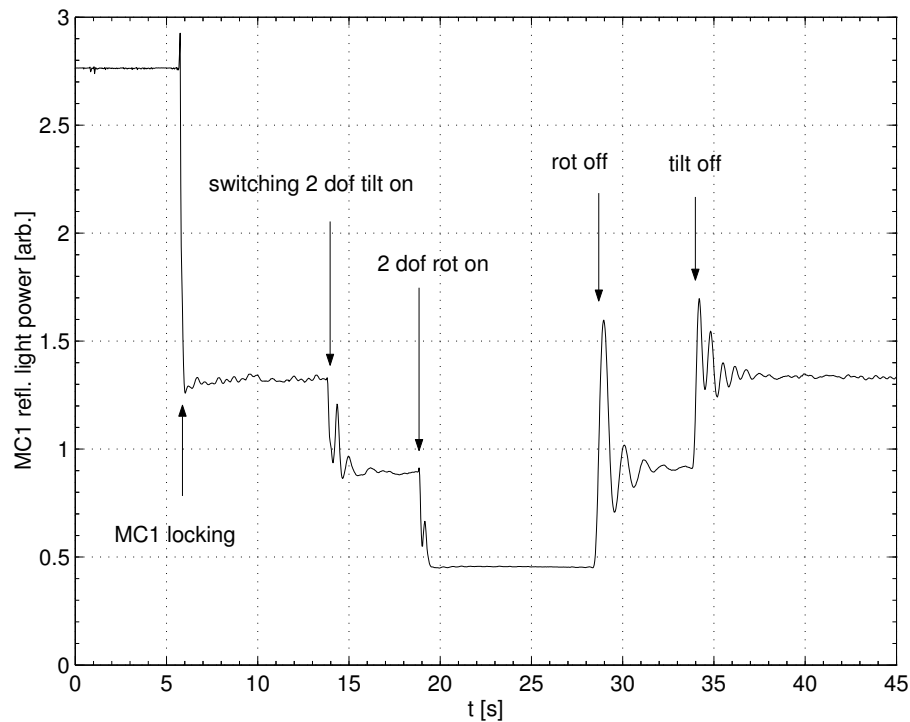


Figure 3.14: Time series of reflected light power from MC1. After the modecleaner is locked, tilt and rotation autoalignment are switched on sequentially at $t = 14$ s and $t = 19$ s. Switching off is done in reverse order around $t = 29$ s and $t = 34$ s.

at least every few days without the system. The automatic alignment system also enables long stretches of continuous locking, with more than 120 hours achieved on a test run period in August 2002 (see section 1.6.4).

3.4 Power-recycling cavity alignment

3.4.1 Introduction

In a simple picture the power-recycling cavity can be seen as a two mirror cavity, consisting of **MPR** and the Michelson operating at the dark fringe. This cavity has four alignment degrees of freedom determining the beam axis of the power-recycling cavity ¹⁷.

Again the most important alignment task is to superimpose the power-recycling cavity axis (simply called *cavity axis* in this section) with the axis of the beam incident on **MPR** from the west (called *input axis*). The input axis is defined by the alignment of mirrors **BDMC2** and **BDIPR**. Superimposing these axes is done by the differential wavefront sensing method, sensing the beam reflected from **MPR**.

¹⁷Although we have an east and north arm of the Michelson, the axis of the power-recycling cavity between **MPR** and **BS** is given by the ‘average’ position of the two beam axes in the long arms.

Figure 3.15 illustrates the alignment control setup for the power-recycling cavity and the Michelson interferometer (the Michelson alignment is described in section 3.5).

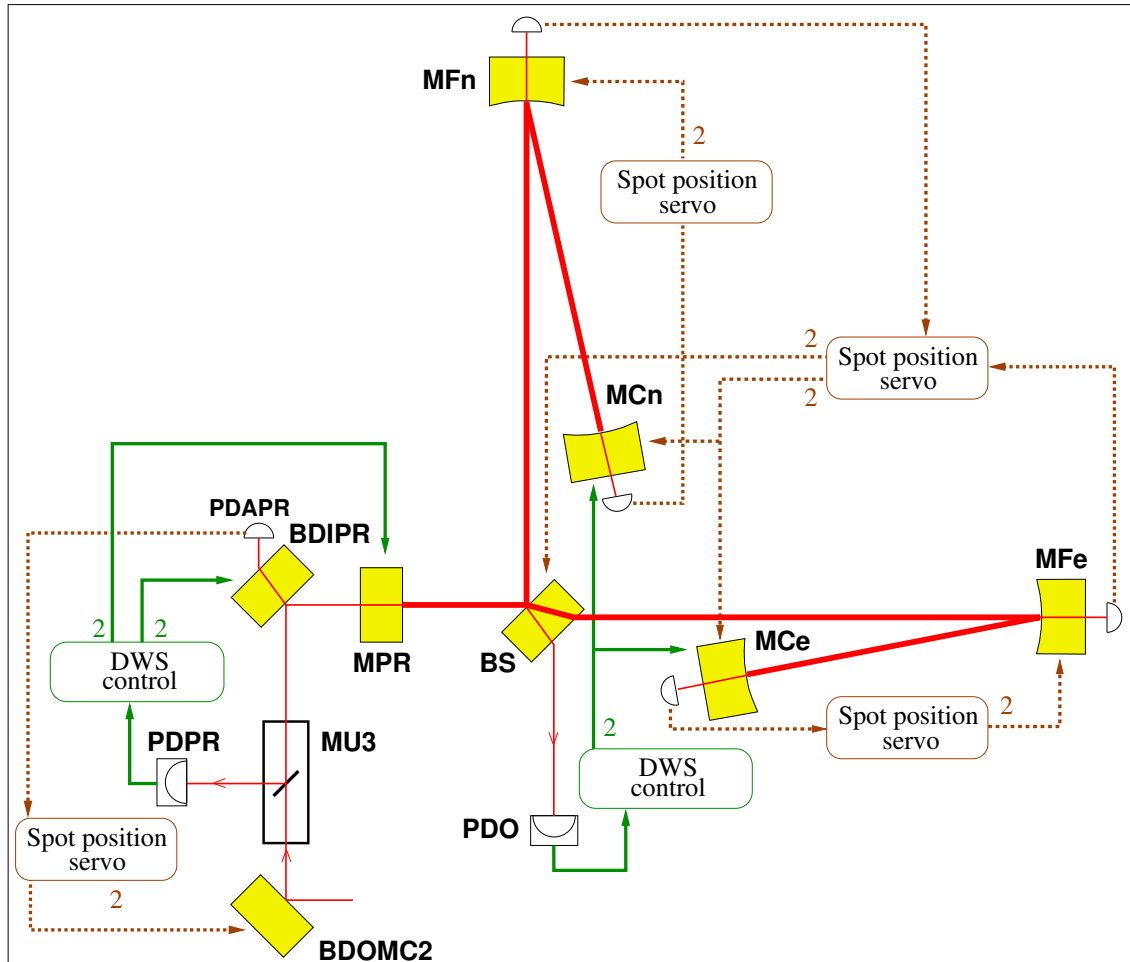


Figure 3.15: Schematic overview of the alignment control for the power-recycling cavity and Michelson interferometer. PDPR detects the light reflected from **MPR** and represents a complete DWS alignment setup for four degrees of freedom, while detector PDO at the Michelson output represents a DWS alignment setup for two degrees of freedom. The spot position control topology shown is a particular case of a more general solution derived in chapter 3.6.

The light incident on the power-recycling cavity via **BDOMC2** and **BDIPR** is partly reflected by **MPR** and interferes with the beam leaking out of the power-recycling cavity. The combined beam $E_i + E_c$ is extracted by a Faraday isolator on the suspended mounting unit MU3 [Klöö00, Fre03b] and detected by PDPR. Detector PDPR represents a complete DWS alignment setup for four degrees of freedom similar to the DWS setup for one modecleaner. The spot position control topology shown is a particular case of a more general solution derived in chapter 3.6.

3.4.2 Experimental setup

3.4.2.1 Beam rotating periscope

Before we have a look at the detection setup, Figure 3.16 shows how the beam is extracted by the Faraday rotator. Beam $E_i + E_c$ leaves the Faraday rotator with an angle against the horizontal plane of about 40° and is steered by a pickoff mirror in an approximately perpendicular direction to the Faradays axis.

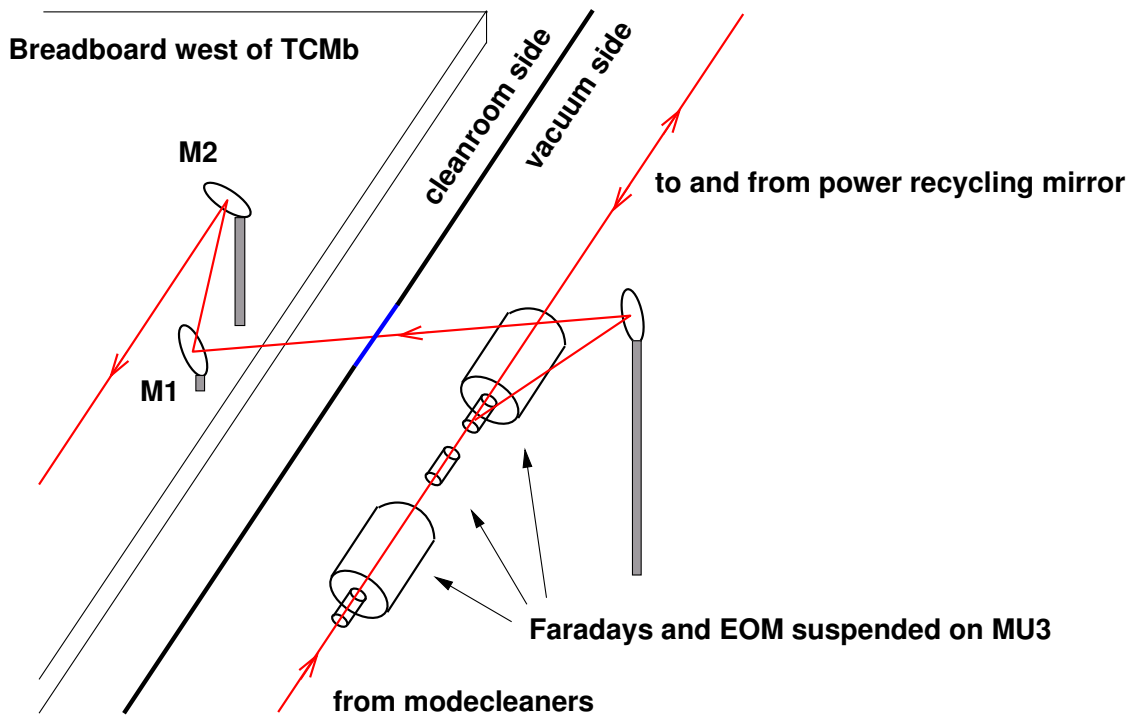


Figure 3.16: Arrangement of optical components around the beam extracting Faraday rotator. A beam rotation about its propagation axis is unavoidably introduced by the beam extraction in the vacuum system and corrected by the proper mirror arrangement of M1 and M2 on the breadboard.

By this arrangement the beam is rotated by approximately 35° around its propagation axis, thus also rotating its spacial information content. To compensate for this rotation, the beam is passed to the beam rotating periscope consisting of mirrors M1 and M2 outside the vacuum system, where the beam is rotated by approximately the same amount of 35° in the opposite direction¹⁸.

3.4.2.2 Breadboard optical setup

Figure 3.17 shows the optical setup on the breadboard west of TCMb.

¹⁸To separate horizontal and vertical alignment information it would in principle be possible to rotate the detecting quadrant photodiodes with respect to beam $E_i + E_c$ (instead of rotating the beam with the periscope). However this approach is impractical if beam centering devices (scanners) are used, as then the spot position information on the diodes would be rotated as well. This makes the centering control unstable, if the rotation angle is as large as 35° .

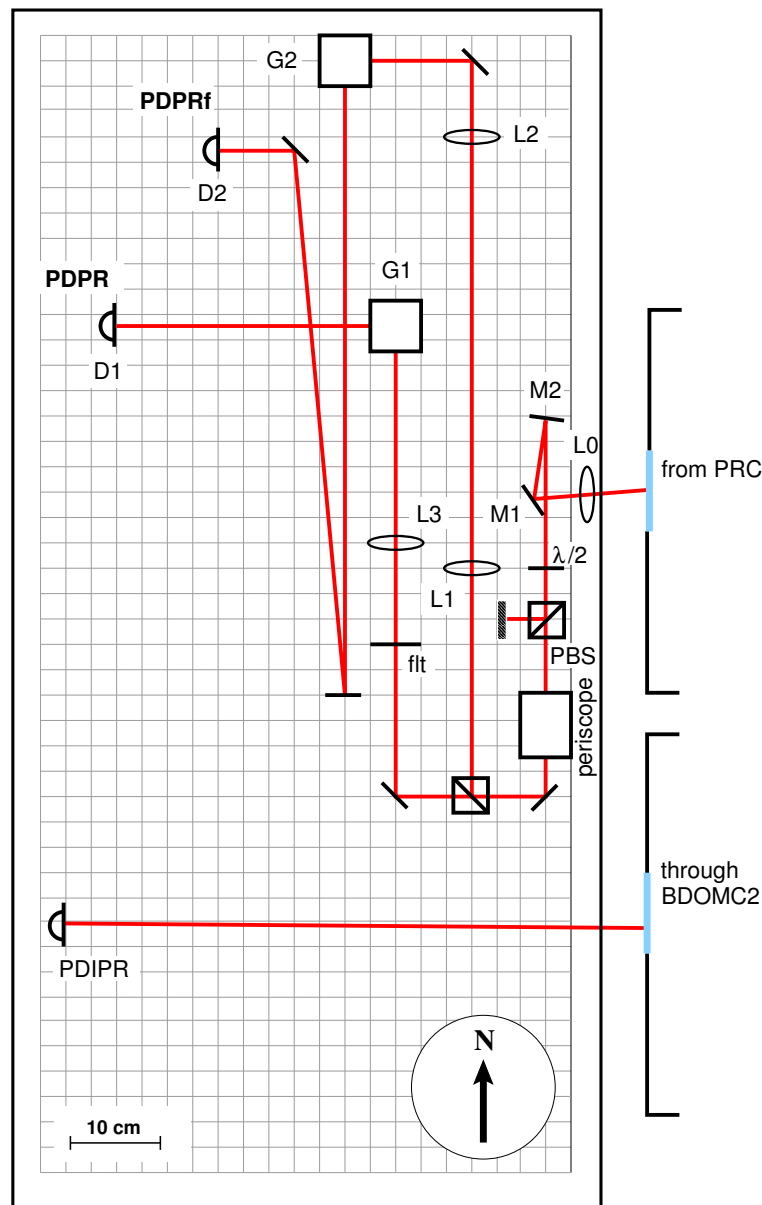


Figure 3.17: Optical layout of the breadboard west of TCMb. The beam reflected from the power-recycling cavity passes lens L0, is rotated by mirrors M1, M2 and attenuated by a $\lambda/2$ -wave plate and polarizing beamsplitter (PBS) combination. The beam passes a periscope to reach a convenient height and is then split into two paths. The path to the near quadrant camera, D1, contains a neutral density filter (fit). A beam diameter of approximately 3 mm on D1 is adjusted by lens L3. The path to the far field quadrant camera D2 contains the lenses L1 and L2 to adjust the desired Guoy phase shift with respect to D1. The beams are centered on D1 and D2 by scanner G1 and G2.

The first optical component in Figure 3.17 is lens L0 (for simplicity not shown in Figure 3.16), which is required, to reduce the beam diameter which is about 8 mm when the beam leaves the vacuum chamber TCMb. After being redirected and spatially rotated by fixed mirrors M1 and M2 (see Figure 3.16) the beam is attenuated by separating an adjustable amount of light power with the combination of a $\lambda/2$ wave plate and polarizing beamsplitter PBS. Up to 5 W of light power

can leave chamber TCMB here if the power-recycling cavity is not locked and thus almost all light incident on **MPR** is reflected.

After attenuation, the beam is split into the paths for the DWS sensors D1 and D2 in the near and far field. Lens L3 in the path to D1 can be seen as a simple Guoy-telescope with the main purpose of producing a proper beam spot size on D1. Lenses L1 and L2 are then chosen to yield an additional Guoy phase shift on D2 of about 90° with respect to D1. Scanners G1 and G2 are used to center the beams on both quadrant diodes.

3.4.3 Lens system and linear combination

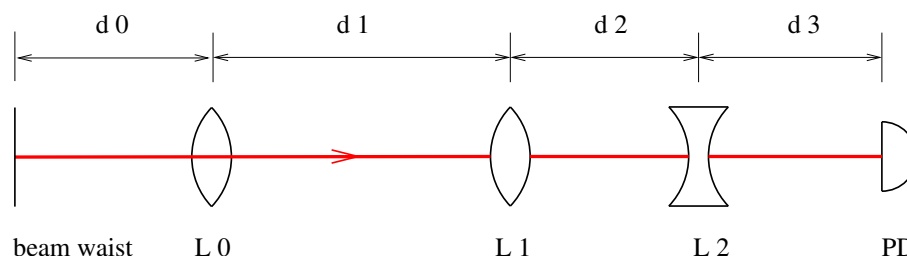


Figure 3.18: Lens system in beam path to D2 of Figure 3.17. The parameters are given in the text.

The calculated parameters of the lens system as shown in Figure 3.18 are $d_0 = 5.36$ m, $d_1 = 0.63$ m, $d_2 = 0.408$ m, $d_3 = 1.4$ m, $L_0 = +1$ m, $L_1 = +0.5$ m, $L_2 = -0.05$ m, and $L_3 = 0.3$ m, yielding an additional Guoy phase shift of 90° between the TEM_{00} and $TEM_{10/01}$ modes on D2 (compared to D1) and a spot diameter of 2.7 mm on D2. (The longitudinal position of L3 is not very critical, as the Guoy phase on D1 is not strongly affected by small changes in the position of L3.)

As in the case of the modecleaners, the most critical value of the telescope is distance d_2 . However, simulations show that the desired phase-shift as a function of d_2 occurs very close to a minimum spot size on the quadrant diode. Thus it is sufficient to initially set d_2 with an accuracy of a few mm and then fine tune d_2 for the minimum spot size on the far detector.

As for the modecleaner DWS control, linear combinations are processed from the two DWS sensors to match the set of chosen feedback points, which are **BDIPR** and **MPR** (see next section). The orthogonalization achieved for the two actuators is again better than 1:10; thus in the alignment signal for **MPR**, a misalignment of **BDIPR** shows up with less than 10% of the signal size compared to a misalignment of **MPR**, and vice versa.

3.4.4 Control topology

The first question in the control design is, which of the two axes (the cavity axis of the power-recycling cavity or the input axis of the light coming from the modecleaner) is taken as reference,

to which the other axis is aligned. This also determines which actuators can be used for the DWS control. In the current solution for GEO 600, a *linear combination* of the two axes is used as reference, to which the orthogonal linear combination of the two axes is aligned to. More precisely: The two actuators for the differential wavefront sensing loop of the power-recycling cavity are **BDIPR** (acting on the input axis) and **MPR** (acting on the cavity axis).

Why was this choice made? Several factors have to be considered here:

- The alignment noise at the pendulums main resonance (around 1 Hz) of the free mirrors. This affects the rms motion of an associated beam axis.
- The control bandwidth possible with each of the mirrors used as actuators.
- The effect that the misorientation of a mirror has on an associated beam axis, and whether or not this effect is distinguishable by the DWS system from the effect of any other mirror.

In general, the quieter axis should provide the reference to which the other axis is aligned. In the measurement band of GEO 600 (50 Hz to 5 kHz) the power-recycling cavity axis has the lowest alignment noise, as the suspensions of **MPR**, **MCE** and **MCn** provide better seismic isolation than those of **BDOMC2** and **BDIPR**. However, the alignment control bandwidth will likely not have to exceed 10-20 Hz. Hence we have to ask for alignment noise up to the DWS control bandwidth. The rms alignment noise of all suspended mirrors is dominated by the noise at the pendulum's main resonance frequencies (typically around 1 Hz). The uncontrolled alignment noise of **MPR** rotation is roughly $1 \mu\text{rad}/\sqrt{\text{Hz}}$ at 1 Hz (see Figure 3.22). The same order of magnitude for the alignment noise can be found for **MCE** and **MCn** ($0.4 \mu\text{rad}/\sqrt{\text{Hz}}$ at 1 Hz on a spot check for **MCE**), and also for **BDOMC2** and **BDIPR**. Thus this is a weak criterion for our purpose.

Mirrors **BDOMC2**, **BDIPR** and **MPR** can be aligned using coils in conjunction with magnets directly attached to the mirrors. However only **MPR** (of these) has an associated reaction-mass pendulum by which the coils are suspended as well. The coils acting on **BDOMC2** and **BDIPR** are attached directly to the base plate of the vacuum chamber ¹⁹.

As stated in chapter 1.4, **MCE** and **MCn** are equipped with electrostatic drives (ESD), making actuation above the pendulums main resonances more complex, as a split actuation system has to be designed. For this reason it is convenient not to use **MCE** and **MCn** as fast alignment actuators for the power-recycling cavity, as long as this is not required.

Investigating the specific action of **BDOMC2**, **BDIPR** and **MPR** on the relative orientation of the input and cavity axis experimentally, we find that **BDOMC2** and **BDIPR** have a similar effect to the input axes (with respect to the cavity axes) and thus cannot be distinguished by the DWS

¹⁹We can estimate the seismic noise that could be introduced by these coils: We take $10^{-7} f^{-2} \text{m}/\sqrt{\text{Hz}}$ (above 1 Hz) as ground motion applied to a coil that acts on a magnet mounted 5 cm off the mirror center. Even if we make the very crude assumption of a fixed (flat) coupling coefficient (from coil current to mirror displacement) for all frequencies, alignment disturbance, α , will be $\alpha = 2 \times 10^{-6} f^{-2} \text{rad}/\sqrt{\text{Hz}}$, yielding about $1 \text{ nrad}/\sqrt{\text{Hz}}$ at 50 Hz. As could be seen in Section 3.2 this is far from setting a limit onto the Michelson sensitivity, such that the fact that the coils of **BDOMC2** and **BDIPR** are attached to ground is no argument that they cannot be used for DWS feedback.

system with a good signal-to-noise ratio. For these reasons **BDIPR** and **MPR** were chosen as actuators. Mirror **BDOMC2** is then used to control the spot position on **BDIPR**, which is sensed by PDAPR (see Figure 3.6 on page 118).

3.4.4.1 Computation of control signals

Figure 3.19 shows a schematic diagram of the GEO 600 PR cavity seen from the side with the beamsplitter and Michelson north arm not shown.

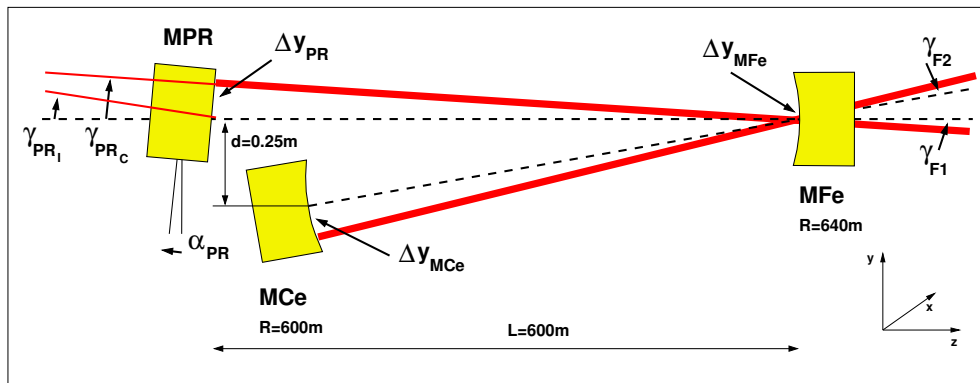


Figure 3.19: Schematic diagram of the GEO 600 PR cavity seen from the side.

Calculations for the deviation of the PR cavity eigenmode from its nominal position were computed for misalignments of the three cavity mirrors shown in Figure 3.19. The results that are almost identical for horizontal and vertical misalignments are shown in Table 3.8.

Cause	Δy_{PR}	γ_{PRc}	γ_{PRi}	Θ^W
α_{PR}	$-600\text{ m} \cdot \alpha_{PR}$	α_{PR}	$2 \cdot \alpha_{PR}$	20.7°
α_F	0	0	0	undefined
α_N	$600\text{ m} \cdot \alpha_N$	0	0	0°

Cause	Δy_{MFe}	γ_{F1}	γ_{F2}	Δy_{MCe}	γ_{MCe}
α_{PR}	0	α_{PR}	$-\alpha_{PR}$	$600\text{ m} \cdot \alpha_{PR}$	$-\alpha_{PR}$
α_F	0	0	$2\alpha_F$	$-1200\text{ m} \cdot \alpha_F$	$2\alpha_F$
α_N	$600\text{ m} \cdot \alpha_N$	0	$1.875\alpha_N$	$-525\text{ m} \cdot \alpha_N$	$1.875\alpha_N$

Table 3.8: Results of the ray-tracing program for the GEO 600 PR cavity.

The computations are included here for completeness. It can be seen that misalignments of **MCe** and **MPR** cannot be distinguished with a very good signal separation, as Θ^W differs only by about 20° for the two cases. This is another argument for the choice made above, using **BDIPR** and **MPR** as actuators for the PR cavity autoalignment.

3.4.4.2 LabView control

Figure 3.20 gives an overview of the LabView control scheme for the power-recycling cavity alignment system.

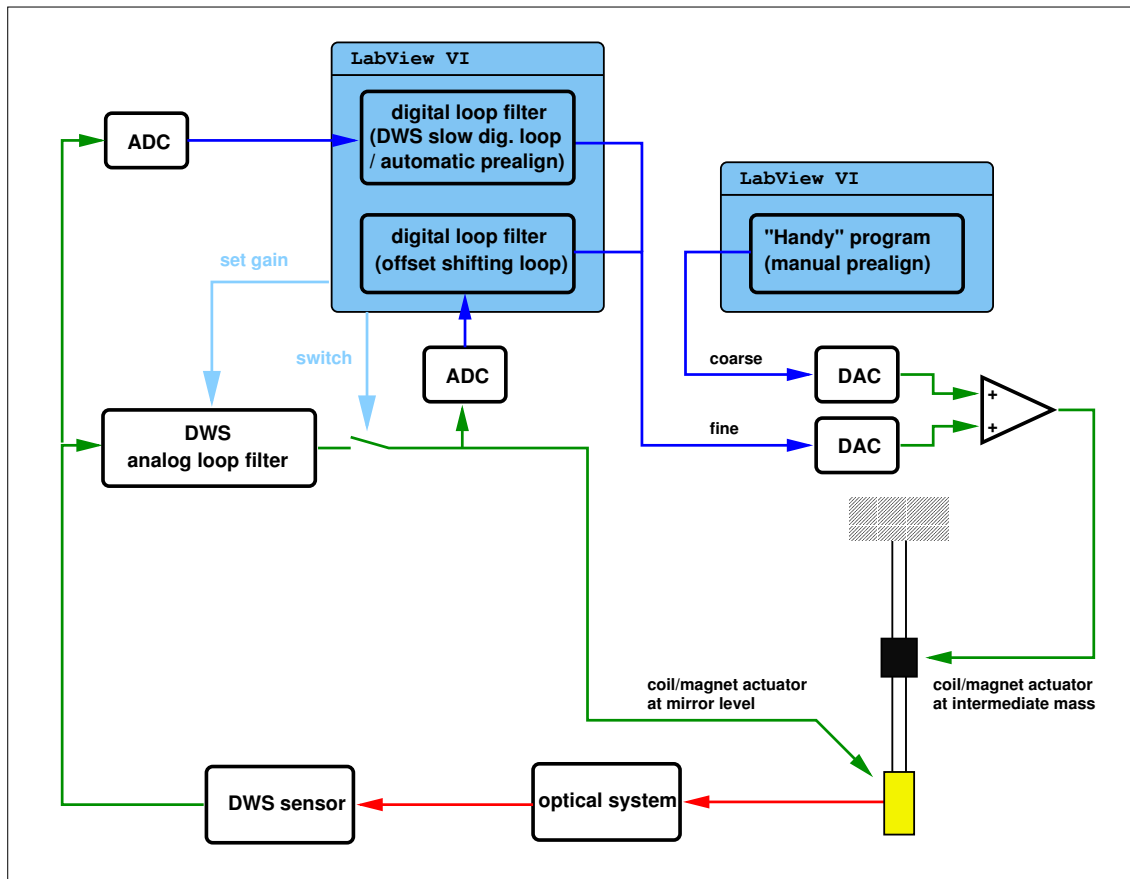


Figure 3.20: Integration of the LabView control with the DWS system for the power-recycling cavity alignment. The digital feedback has a finer resolution than that used for the manual coarse alignment. Different digital filters can be used for different purposes; digital feedback can be used together with analog feedback (offset shifting) or it can be used without analog feedback for test purposes or for a possible automated pre-alignment system.

As in the case of the modecleaners, a dedicated LabView VI implements the computer control for the DWS based power-recycling cavity alignment, including manual gain settings, feedback switching, automation of the alignment system and offset shifting. The spot position control (explained in section 3.6) is implemented by a further VI (see appendix C.2 for both VIs.)

The implementation of these tasks is slightly different than in case of the modecleaners:

- Additional fine resolution digital alignment channels are implemented for all main interferometer mirrors including **BDIPR**. These channels comprise digital to analog converters with a smaller gain factor than the standard converters used for coarse manual alignment via a ‘Handy’ VI. Thus the Handy VI is used for a coarse manual alignment only, while the

DAC with fine resolution allows for a better fine tuning of the alignment and is used by the automation. Nevertheless both DACs connect to the same physical actuator.

- The analog and digital DWS feedback use different actuators on the double pendulums of **BDIPR** and **MPR**. Both mirrors have coil-magnet actuators at the mirror level, used for analog feedback, while digital alignment feedback is applied to the intermediate mass.
- There are two modes in which the power recycling DWS feedback can be used: In the high bandwidth mode, the DWS analog feedback is enabled, and the fine resolution alignment offsets are used by the offset shifting loop in a nested feedback loop arrangement, thus continually minimizing the DC analog feedback. In the low bandwidth mode, no analog feedback is applied; only digital DWS feedback acts on the alignment channel with fine resolution. A future implementation of this mode could possibly be used as an automatic pre-alignment program, by sensibly interpreting the DWS signals even if the corresponding cavity is not locked longitudinally ²⁰.

3.4.5 Feedback design and performance

3.4.5.1 Actuators

As stated above, **BDIPR** and **MPR** can be aligned with three sets of coil-magnet actuators at the mirror level of each pendulum. A current driver unit with orthogonalization adjustments to minimize 6 unwanted couplings was designed (schematic in appendix B, page 139, Figure B.4). This unit has three inputs which are dedicated to rotation, tilt and longitudinal motion of the corresponding mirror. For each input, the action on the other two degrees of freedom can be minimized independently by adjusting a dedicated potentiometer.

The transfer functions of these actuators for rotation and tilt were measured by observing the position of the beam reflected from **MPR** with the power-recycling cavity not locked. The position of this beam is detected on PDPR (see Figure 3.15). Table 3.9 shows the fitted parameters to these transfer functions.

Mirror d.o.f.	pole [Hz]	Q
BDIPR rot.	0.824	2.5
MPR rot.	1.10	1.6
BDIPR tilt	3.54	6.0
MPR tilt	0.969	0.8

Table 3.9: Fitted parameters for **BDIPR** and **MPR** alignment transfer functions from coil-magnet actuators at mirror level to mirror alignment. The quality factors Q depend on the gain of the local control damping which was not changed for this measurement.

²⁰To do this, the DWS signals would have to be sampled fast enough and held each time the cavity is in resonance with the incident light.

Mirror d.o.f.	zero [Hz]	pole [Hz]	zero [Hz]	pole [Hz]	pole [Hz]	Q
BDIPR rot.	1.25	3.95	10	31.6	75	2
MPR rot.	2	6.32	16	50.6	75	2
BDIPR tilt	5	15.8	35	110	100	2
MPR tilt	2	6.32	16	50.6	75	2

Table 3.10: Filter parameters for all four degrees of freedom of the power-recycling cavity DWS loops.

3.4.5.2 Loop filters

Experience in the Garching 30 m prototype showed that, for this type of actuator, best alignment damping was achieved with a filter transfer function of gain $f^{1/2}$ for a frequency band above the pendulum main resonance (see [Hei99a], Appendix B.4). In the absence of other phase delays or resonances this gives an unconditionally stable servo with a phase margin of about 45° . The unity-gain frequency is designed to be 10 Hz.

As an example of such a feedback design, Figure 3.21 shows the measured and fitted open loop transfer function for **MPR** rotation.

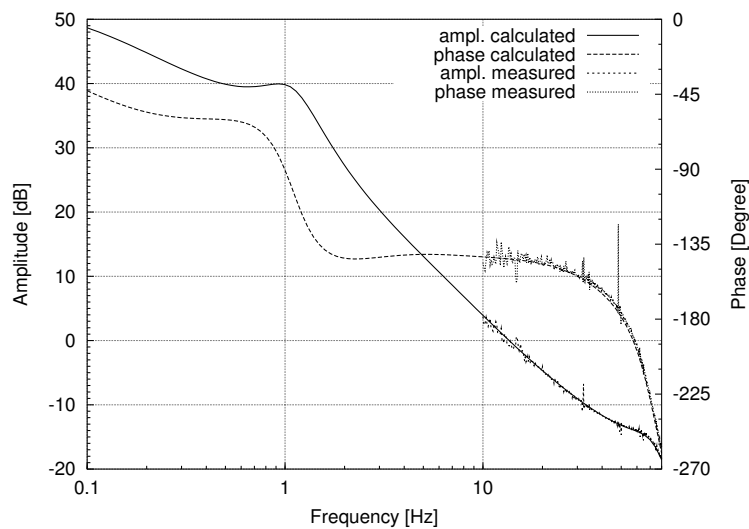


Figure 3.21: Open loop transfer function of alignment feedback for the power-recycling mirror rotation.

Table 3.10 shows the filter parameters for all four degrees of freedom of the power-recycling cavity DWS loops. The filters slightly deviate from an ideal $f^{1/2}$ characteristic in order to have a little more phase margin around 10 Hz.

3.4.5.3 Performance

The acquisition of these alignment loops is not critical. Typically the DWS feedback can be switched on automatically after a few seconds of a power recycled Michelson lock. If the power-recycling cavity misalignment in the moment of closing the DWS loop is large, it can happen that the cavity loses lock. Normally this will only be the case if the PR cavity had been unlocked for a long time and the pre-alignment was very coarse. In this case the PR DWS feedback can be used in the low bandwidth mode for about 1 min, to make the DC misalignment small enough to switch on the analog feedback.

Figure 3.22 shows the error signal for **MPR** rotation with the power-recycling cavity automatic alignment switched on (for all four DOF) and off²¹. The suppression of rotational alignment noise of **MPR** is about a factor 100 at 1 Hz. An additional transient integrator stage from 0.09 to 0.9 Hz was used here.

Also shown is the sensors dark noise of about 10^{-11} rad/ $\sqrt{\text{Hz}}$ being far below the residual alignment fluctuations.

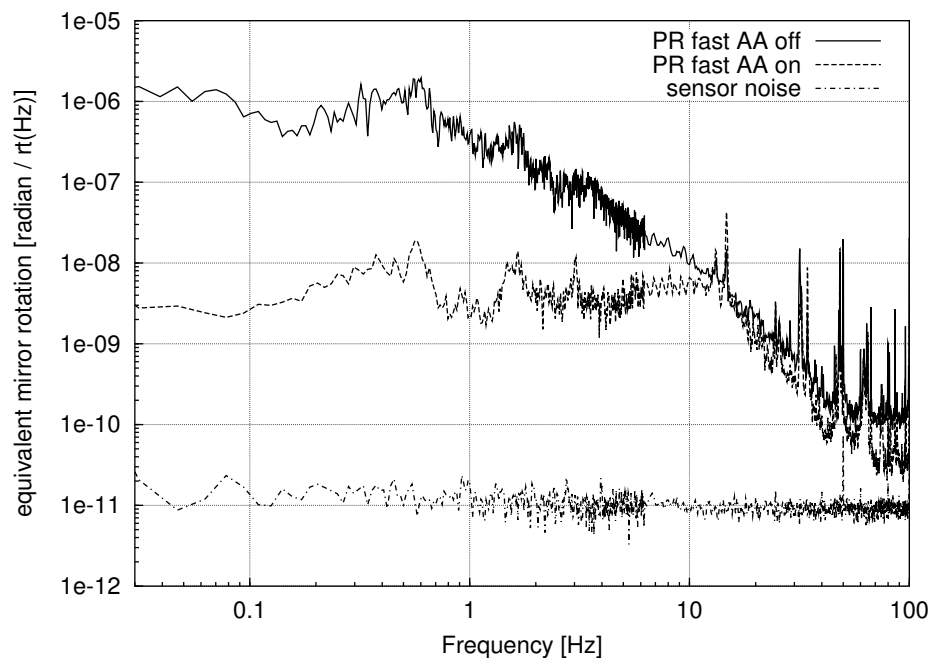


Figure 3.22: Amplitude spectral density of mirror **MPR** rotation with power-recycling fast autoalignment switched on and off. Also shown is the sensors dark noise. The rms misalignment in the band from 0.1 to 100 Hz without autoalignment is $0.93 \mu\text{rad}$, compared to $0.031 \mu\text{rad}$ with autoalignment switched on. An additional transient integrator stage from 0.09 to 0.9 Hz was used in this measurement.

The rms misalignment in the band from 0.1 to 100 Hz without autoalignment is $0.93 \mu\text{rad}$, compared to $0.031 \mu\text{rad}$ with autoalignment switched on. The alignment noise suppressions for the

²¹This measurement was done during the so-called ‘1200 m’ experiment, at a time when the beamsplitter **BS** was not installed yet. A folded Fabry-Perot cavity was formed by mirrors **MPR**, **MFe** and **MCe** (see [ams⁺02]). The performance of the power-recycling cavity autoalignment is very similar for the case of the power recycled Michelson.

other three degrees of freedom are of the same order, such that the specification estimated in section 3.2 is fulfilled.

3.5 Michelson alignment

3.5.1 Overview

The task of the Michelson autoalignment is to superimpose the beam axes of the east and north arm at the main output of the Michelson, south of the beamsplitter. There are only two degrees of freedom required for this task and the actuators are **MCE** and **MCn** in a differential alignment mode²².

Figure 3.23 shows the resulting beam misalignment, if both mirrors **MCE** and **MCn** are rotated counterclockwise by the same angle α , which we call a *differential* misalignment of the Michelson. While the common mode axis of the power-recycling cavity (which results from the average positions of the two Michelson arm axes) is unaffected, the two beams E_e and E_n leave the Michelson under an angle γ against each other. The DWS method is used again to obtain appropriate error signals, but now we do not measure the interference between a cavity input beam and a beam leaking out of a cavity. The interference pattern to be measured is the superposition of the two light fields of E_e and E_n from the east and north arm, respectively. We call the combined beam (leaving the Michelson to the south) $E_e + E_n$, and its wavefront angles can be measured with a DWS sensor.

3.5.2 Experimental setup

Figure 3.15 on page 94 shows the setup for the Michelson DWS alignment. The current chapter deals with the DWS control implemented for the Michelson interferometer, while its spot position control (as that of the power-recycling cavity) is explained in section 3.6.

As we have already seen in chapter 1, the beam incident on **MPR** from the west side is phase modulated with a Schnupp modulation frequency of $14.904920\text{MHz} \pm 20\text{Hz}$ such that the phase modulation sidebands are resonant within the power-recycling cavity. Any longitudinal deviation of the Michelson from the dark fringe will result in a phase difference between the interfering

²²The argument why only two degrees of freedom have to be controlled for the Michelson goes as follows: While in principle four degrees of freedom have to be controlled to superimpose two axes, in the case of the Michelson we have already fixed two degrees of freedom - the two beams leaving the beamsplitter towards the long arms originate from the same point on the beamsplitter surface. As the far mirrors **MFe** and **MFn** are hit twice by the beam passing along each tube, any alignment change of **MFe** and **MFn** can exactly be compensated by an alignment change of **MCE** and **MCn** respectively, such that the far mirrors are not important for our consideration. If we now for example let **MCE** define where the returning beam from the east arm hits the beamsplitter, then there are only the two alignment degrees of freedom of **MCn** left to match this point with the beam returning from the north arm. If this point on the beamsplitter is not identical with the point where they started on the beamsplitter, then this is just a misalignment of the power-recycling cavity, which will be compensated by **BDIPR** and **MPR** in our setup. To minimize this possible coupling of the Michelson alignment control to the power-recycling cavity alignment, Michelson alignment feedback is applied to **MCE** and **MCn** differentially.

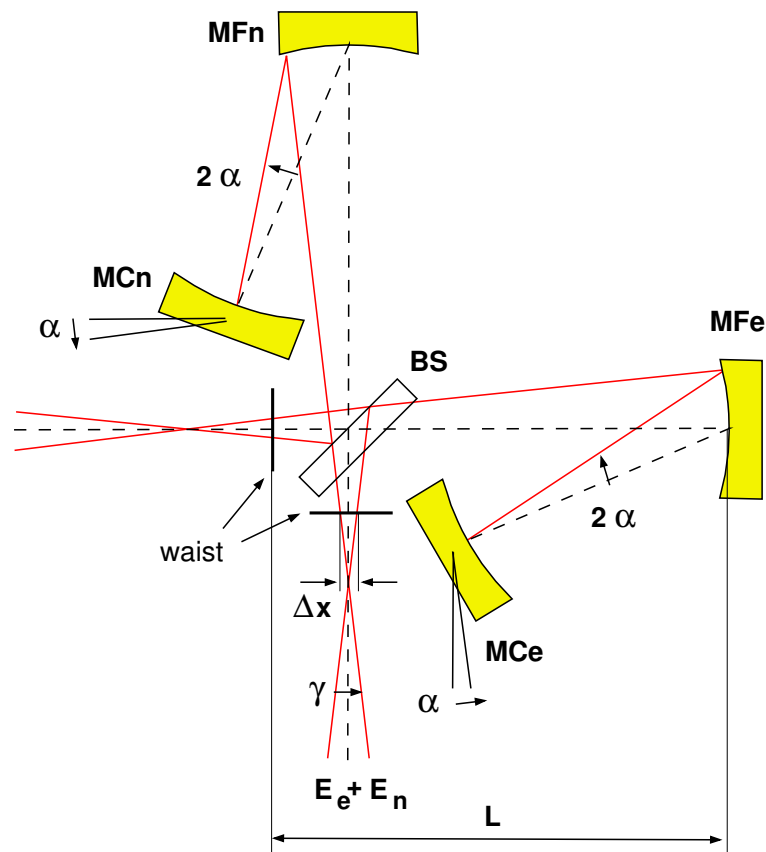


Figure 3.23: Michelson misalignment caused by a differential misalignment of the end mirrors **MCe** and **MCn**. The dashed lines show the beam positions for the perfect aligned case.

wavefronts integrated over the whole cross-section of the plane normal to the beam axis. This is the signal used for longitudinal locking of the Michelson to the dark fringe.

Detecting the spatial distribution of this interference pattern with PDO (Figure 3.15) gives us the required alignment information for the two interfering beams. Unlike for the modecleaners and the power-recycling cavity, DWS detector PDO consists only of one quadrant photodiode with a local beam centering scanner, because only two degrees of freedom need to be sensed here. The resonant circuit around the photodiode is tuned to the Michelson Schnupp frequency.

3.5.2.1 Detection bench layout

The preliminary layout of the optical components on the detection bench is shown in Figure 3.24. The detection bench layout will change in the final setup, when the output modecleaner with associated optics will be installed ²³. The beam leaving the vacuum system is focused by mirror MO1 with a radius of curvature of 6.72 m. A large radius of curvature was chosen to have an easy

²³In the final setup beam $E_e + E_n$ has to be obtained before the output modecleaner, to preserve the $TEM_{10/01}$ modes required for the DWS system. This will be done with the beam transmitted through BDO1 (see optical layout in Figure A.1, appendix A).

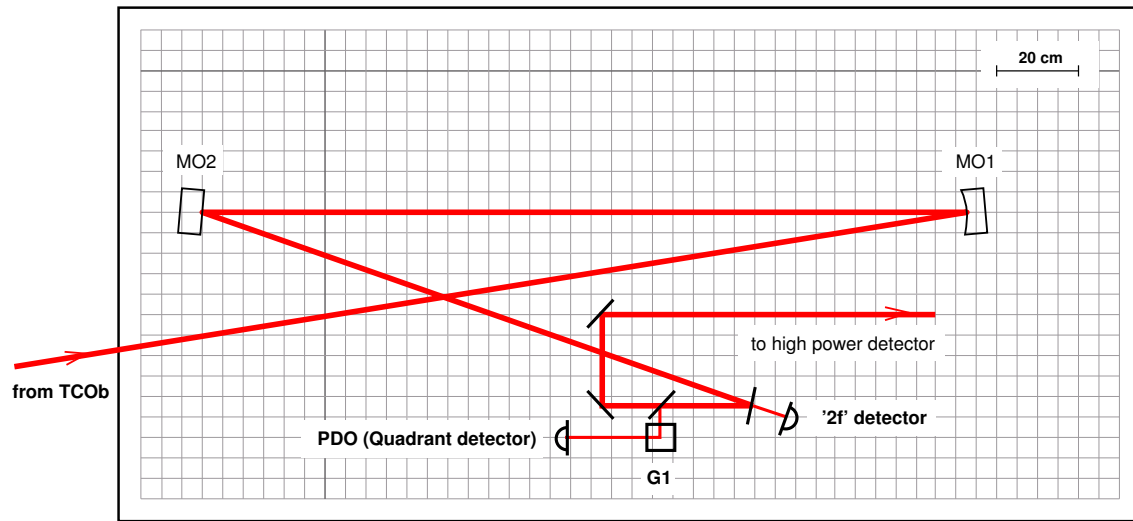


Figure 3.24: Preliminary optical layout of the detection bench, where the Michelson longitudinal error signal and the DWS signal are obtained. Mirror MO1 has a radius of curvature of 6.72m and focuses the beam which leaves the vacuum system with a diameter of about 18 mm. The ‘2f’ detector is explained in section 2.5.2.

possibility to pass the focused beam through a Faraday isolator if required ²⁴. The flat mirror MO2 directs the beam towards the detection optics.

The beam is split into two paths by a power beamsplitter. One path is used for the DWS sensor on which the beam is centered by scanner G1. The other path can be used to detect the beam with a high-power photodetector for the Michelson error signal (see section 1.5).

3.5.3 Lens system and control topology

As individual misalignments of **MCE** and **MCN** cannot be distinguished by the DWS method, feedback is applied to the differential alignment mode of both mirrors. The common mode alignment degrees of freedom of **MCE** and **MCN** affect the eigenmode axes of the power-recycling cavity and are used for spot position control (section 3.6).

Calculating the kind of misalignment at the beam waist Θ^W that is caused by differential misalignment of **MCE** and **MCN** can be done analytically. According to equation 3.1 we have to compute the angle γ and the displacement at the waist Δx of the misaligned beams against their nominal positions (see Figure 3.23). With some elementary geometry we obtain

$$\Delta x = 8\alpha d \left(1 - \frac{d}{R_F} \right) \quad (3.14)$$

²⁴Some experiments with a Faraday isolator in the output beam were done; see section 1.5.

and

$$\gamma = 4\alpha \left(2 \frac{d}{R_F} - 1 \right), \quad (3.15)$$

with α being the misalignment angle of both far mirrors **MCe** and **MCn**, d being the distance from the beam waist to the far mirrors and R_F being the radius of curvature of the far mirrors.

With $d = 600\text{m}$, $R_F = 670\text{m}$ and $z_R = 300\text{m}$ ²⁵ we obtain from equation 3.1:

$$\Theta^W = -62^\circ. \quad (3.16)$$

With the propagation of beam $E_e + E_n$ on the output bench we have to compute the angle Θ^D obtained at the DWS sensor. The ‘lens system’ currently used consists of mirror MO1 on the output bench as shown in Figure 3.24. With the actual distances we obtain $\Theta^D \approx 120^\circ$, yielding 86 % of the maximum possible signal being detected. As only one DWS sensor is used for the Michelson differential alignment, no linear combinations have to be computed.

3.5.3.1 LabView control

Like in the case of the power-recycling cavity alignment, a dedicated LabView VI integrates the computer control for the DWS based Michelson alignment (see appendix C.2 for this VI). Figure 3.25 gives an overview of the according control scheme.

The basic functionality of the LabView control is the same as for the power-recycling cavity. The important difference of the Michelson DWS system is the fact that the suspensions for the end mirrors **MCe** and **MCn** are triple pendulums with the digital alignment offsets being applied to the upper mass stage and the analog DWS feedback to the intermediate mass stage. (See Figure 1.12 on page 22 for the triple pendulum suspension with reaction mass chain.)

In addition to the feedback at the intermediate mass level, analog DWS feedback can also be used to act on the ESDs at the mirror level in order to increase the bandwidth and stability of the DWS feedback (see next section 3.5.4). A further task of the Michelson autoalignment VI is the digital control of the common alignment modes of **MCe** and **MCn**. As there are already four degrees of freedom aligned with the DWS system of the power-recycling cavity, spot position information is used for the common alignment modes of **MCe** and **MCn** (see section 3.6).

Table 3.11 summarizes the kind of alignment control applied to each suspended mirror of the main interferometer.

²⁵A Raleigh range of $z_R = 300\text{m}$ is obtained with radii of curvature of the near mirrors $R_N = 630\text{m}$, and $R_F = 670\text{m}$ for the far mirrors.

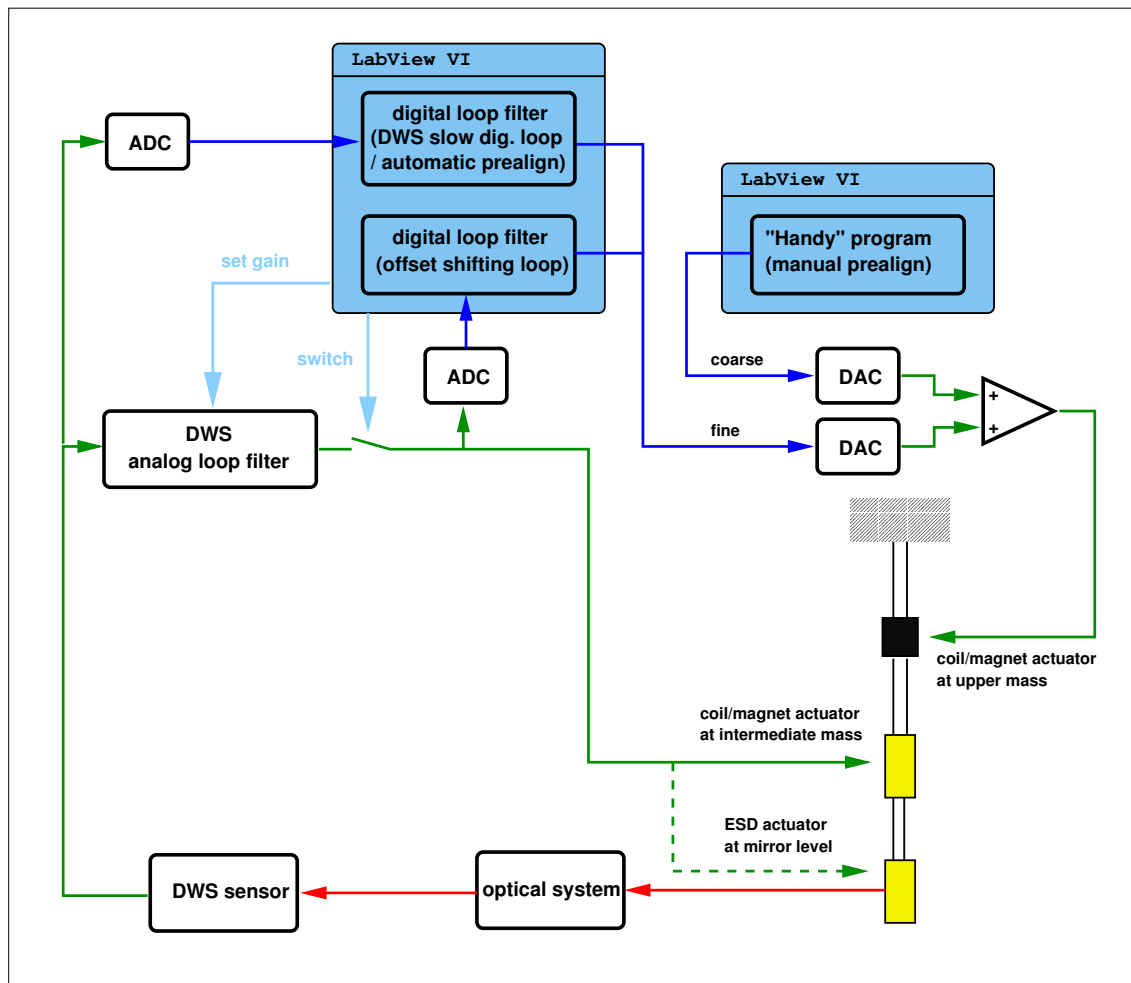


Figure 3.25: Integration of the LabView control with the DWS system for the Michelson alignment. As in case of the power recycling DWS system, the digital feedback has a finer resolution than used for the manual coarse alignment. Digital feedback can be used together with analog feedback (offset shifting) or without analog feedback (slow DWS feedback for test purposes or pre-alignment).

mirror	loop type	associated sensor
BDIPR	DWS control	PDPR (DWS signal)
MPR	DWS control	PDPR (DWS signal)
BS	spot pos. control	PDMFe + PDMFn
MCE - MCn	DWS control	PDO (DWS signal)
MCE + MCn	spot pos. control	PDMFe - PDMFn
MFe	spot pos. control	PDMCe
MFn	spot pos. control	PDMCn

Table 3.11: Alignment control signals for each of the suspended mirrors of the main interferometer.

3.5.4 Feedback design and performance

3.5.4.1 Actuators

Intermediate mass stage:

The intermediate mass (IM) stage has coil-magnet actuators, as already shown in chapter 1, Figure 1.12 (page 22). The same type of current driver unit as for the alignment control of **BDIPR** and **MPR** is used.

As an example, Figure 3.26 shows the transfer function from **MCE** IM tilt actuator to **MCE** mirror tilt motion for the steel wire suspension of the mirror. The transfer function was measured by misaligning **MPR** and **MCn** (with no **MSR** installed), and detecting the spot position of the beam reflected from **MCE** travelling via **MFe** and **BS** to the detection bench.

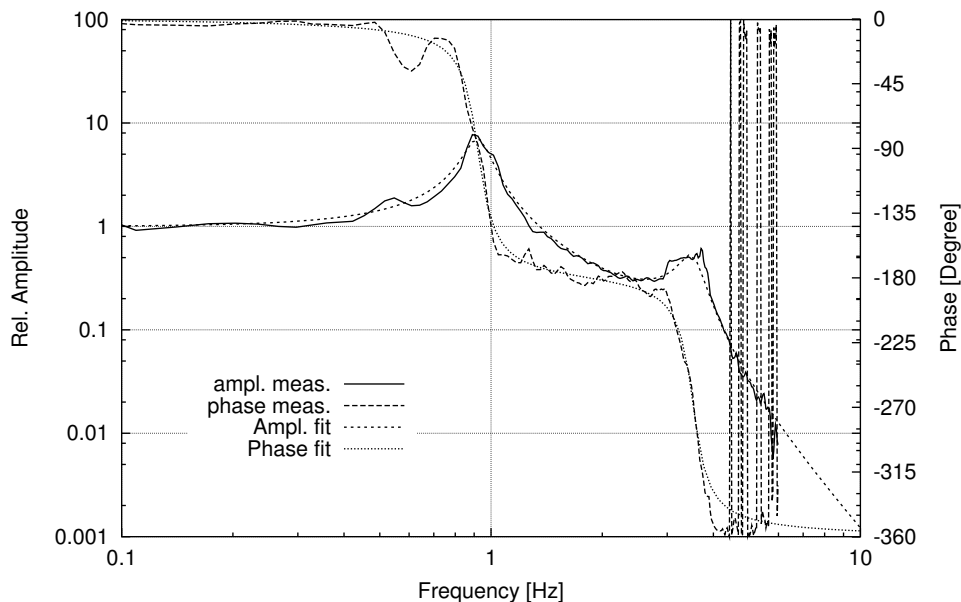


Figure 3.26: Transfer function of **MCE** intermediate mass current driver tilt input to mirror tilt. Also shown is the model fitted to the measurement.

Two pendulum resonances are clearly identified. A model with two complex poles was fitted to all four measured transfer functions (**MCE** / **MCn** rotation and tilt) with the resulting parameters shown in table 3.12 (upper table). After the mirrors were suspended monolithically, the four transfer functions were measured again; the new **MCE** tilt transfer function is shown in Figure 3.27.

While the overall shape of the transfer function is similar, additional resonance structures around 0.6 Hz and 2 Hz appeared, which were fitted with two additional complex pairs of poles and zeros. The fitted parameters for the monolithic suspension are shown in table 3.12 (lower table).

For the monolithic mirror suspension the influence of the local control gain setting onto the

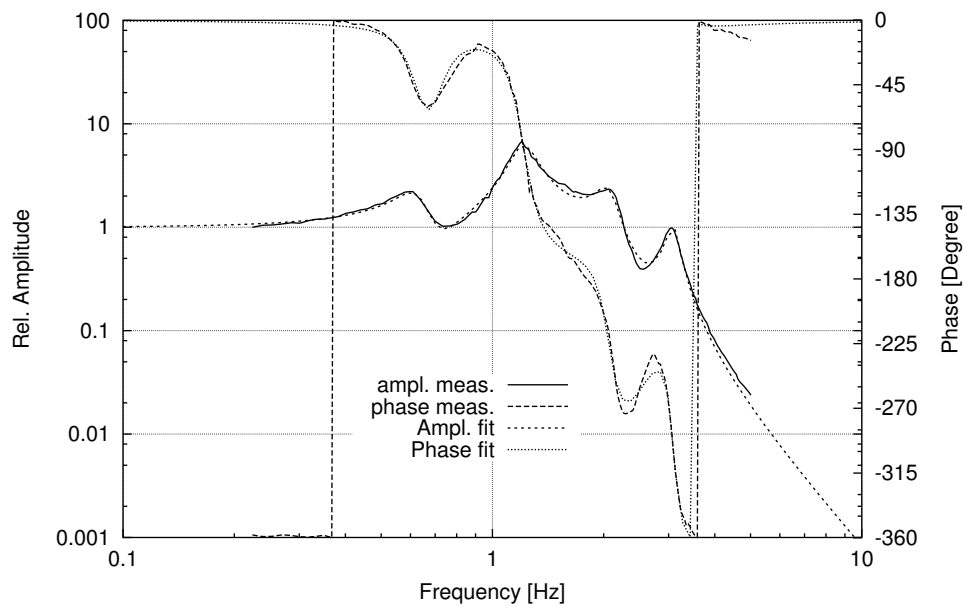


Figure 3.27: Transfer function of **MCE** intermediate mass current driver tilt input to mirror tilt for the monolithically suspended final **MCE**. Compared to Figure 3.26 additional resonance structures around 0.6 Hz and 2 Hz appeared

Mirror d.o.f.	p_1 [Hz]	Q	p_2 [Hz]	Q
MCE rot.	0.412	2.1	3.02	45
MCn rot.	0.53	0.78	3.00	10.5
MCE tilt	0.923	6.6	3.52	7
MCn tilt	0.965	5.7	3.60	12

Mirror d.o.f.	p_0 [Hz]	Q	z_0 [Hz]	Q	p_1 [Hz]	Q	p_{1a} [Hz]	Q	z_{1a} [Hz]	Q	p_2 [Hz]	Q
MCE rot.	—	—	—	—	0.461	0.59	1.48	3.4	1.47	0.99	3.23	27
MCn rot.	—	—	—	—	0.501	0.32	1.39	2.8	1.51	0.58	3.14	23
MCE tilt	0.631	4.9	0.707	4.6	1.22	6.1	2.07	7.3	2.53	2.8	3.09	13
MCn tilt	0.697	2.1	0.790	2.7	0.957	4.7	1.82	10	1.88	2.0	2.84	17

Table 3.12: Fitted parameters for **MCE** and **MCn** alignment transfer functions from intermediate mass current driver input to mirror alignment. The upper table refers to steel wire suspension of the mirror, the lower table to the monolithic suspension.

alignment transfer functions was investigated. Figure 3.28 shows three transfer functions of MCE rotation in the frequency range 1-4 Hz for different local control gain settings.

An intermediate gain setting was chosen resulting in quality factors, Q , for the resonance at 3.1 Hz of about $Q = 10$. With a very high gain setting (lowest Q) a long term instability of

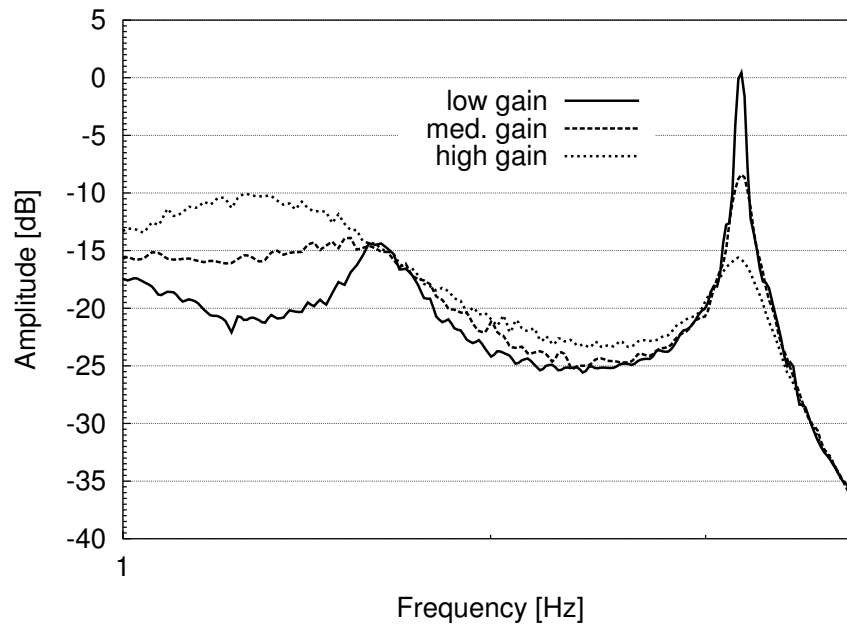


Figure 3.28: Transfer functions of MCE intermediate mass current driver rotation input to mirror rotation for different local control gain settings.

the local control loop may occur after some time ²⁶. On the other hand, a not too large Q is desirable, as the unity gain frequency of the DWS alignment servo is around 10 Hz, being close to the resonance and thus making acquisition more difficult in case of a large Q .

Electrostatic drive:

In order to enhance the bandwidth and stability of the DWS loop, the ESD feedback was extended for alignment use. While the high voltage (needed for biasing the ESD and longitudinal displacement control of the Michelson differential mode) is still applied to one comb of all four quadrants of each drive, the corresponding opposite combs of each quadrant can be driven with low voltage operational amplifiers individually, as shown in Figure 3.29.

An analog electronics adjusting matrix with two inputs for rotation and tilt allows adjustment of gain levels individually for each quadrant (A,B,C and D) and each alignment degree of freedom to minimize couplings (schematic in Appendix B, Figures B.5 and B.6). The alignment range of this actuator is limited, but sufficient to work at high frequencies (10 – 50 Hz) together with the IM feedback (below 10 Hz). The transfer function of this actuator to mirror alignment has a slope of f^{-2} above the pendulum's main resonance around 1 Hz.

²⁶It was observed experimentally that the local control loops started oscillating at some point in time, although they had been stable for days or weeks before. This oscillation might be caused by changing couplings between individual local control channels due to a slow DC drift of the absolute pendulum position.

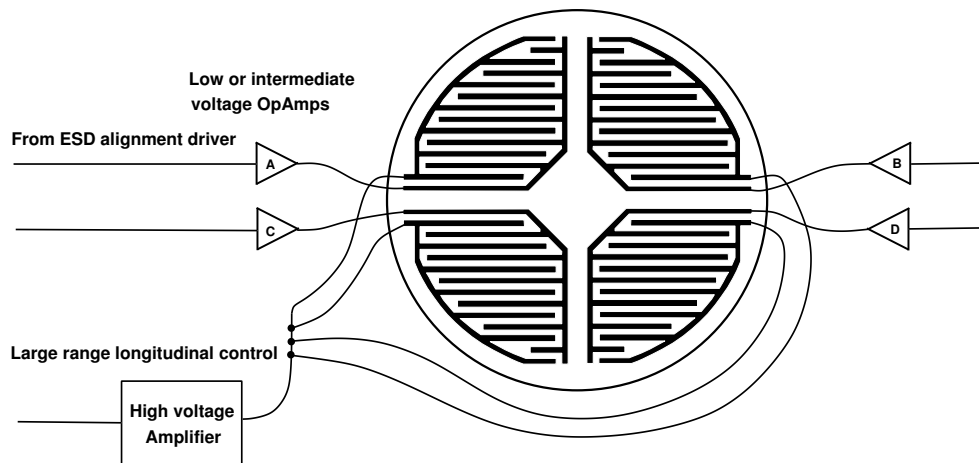


Figure 3.29: Schematic of electrostatic drive with high and low voltage amplifiers connected. The high voltage is used for all four quadrants A-D in common, while small forces can be applied to each quadrant individually.

3.5.4.2 Loop filters

In the initial implementation of the Michelson autoalignment, analog alignment feedback for the Michelson differential mode was applied to the **MCe** and **MCn** intermediate mass stages only, while in a later version, feedback at 10 – 50 Hz was added by the ESD drives at the mirror level. The latter attempt was made in order to be able to change the design of the IM feedback path slightly, such that close to unconditional stability of the feedback loop could be achieved. This seemed favourable for the initial experiments with locking of the dual recycled interferometer, as the Michelson autoalignment must not be very gain sensitive during acquisition of dual recycling, where the Michelson gain can vary strongly.

Like in the case of the fast DWS alignment for the GEO 600 modecleaners, the loop filters for the IM feedback have to provide about 200° of phase lead around the unity gain frequency of 10 Hz, to yield a stable feedback system without using ESD alignment. Achieving this goal is slightly easier in case of the Michelson alignment, as the second complex pole is at a higher frequency than the first pole (see table 3.12). Nevertheless the gain distribution within the filters can be critical.

Figure 3.30 shows the simulated open loop gain and phase of the initial implementation of the Michelson fast autoalignment for tilt. A unity gain frequency of about 10 Hz can be achieved with this design.

The loop is only stable and robust for a unity-gain frequency between 5 and 10 Hz. As the resonance frequencies according to table 3.12 do not differ much between **MCe** and **MCn**, only one filter was used, to drive one common mode alignment degree of freedom of both mirrors. The design of individual filters for each degree of freedom of each mirror could become necessary, if the resonance frequencies of the transfer functions would differ significantly.

Table 3.13 shows the filter parameters for the two degrees of freedom of the Michelson DWS feedback.

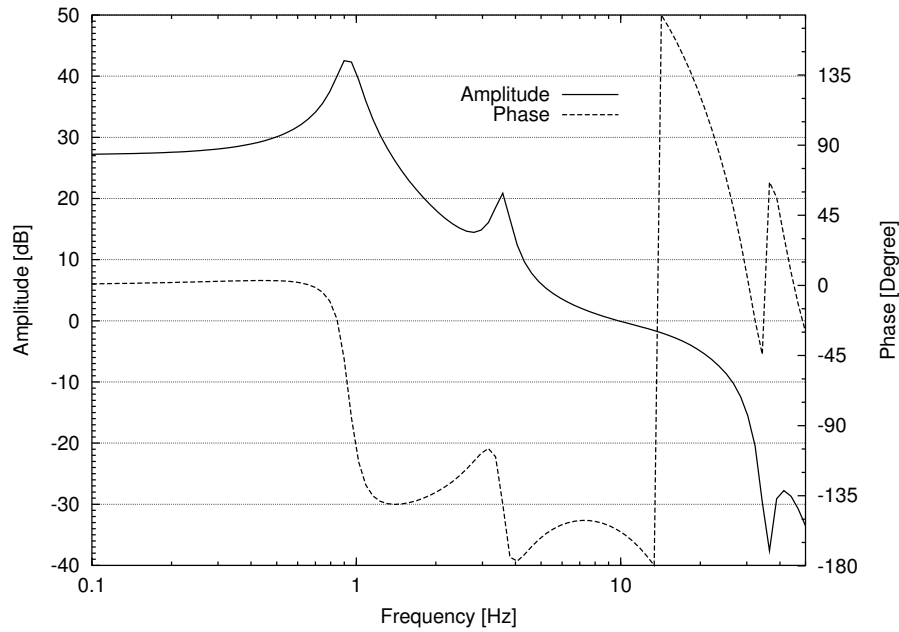


Figure 3.30: Simulated open loop gain and phase of the Michelson fast autoalignment for tilt.

Mirror d.o.f.	zero [Hz]	Q	pole [Hz]	Q	zero [Hz]	pole [Hz]	zero [Hz]	pole [Hz]	pole [Hz]	Q
MCe + MCn rot.	3.01	5.0	25	0.8	5	25	7	30	40	2
MCe + MCn tilt	3.56	2.0	25	0.8	5	25	5	30	40	2

Mirror d.o.f.	zero [Hz]	Q	pole [Hz]	Q	zero [Hz]	pole [Hz]	zero [Hz]	pole [Hz]	pole [Hz]	Q
MCe + MCn rot.	3.01	5.0	25	0.8	2	10	3	12	40	2
MCe + MCn tilt	2.7	2.0	20	0.8	1	8	3	15	40	2

Table 3.13: Filter parameters for the Michelson DWS feedback with the intermediate mass actuators of **MCe** and **MCn**. The upper table shows the parameters used for the steel wire suspension, and the lower table those for the monolithic suspension of **MCE** and **MCN** respectively. Additional notch filters are used to suppress longitudinal mode resonances of the suspension wires and fibres.

The upper table shows the parameters used for the steel wire suspension, which were modified to the ones displayed in the lower table for the monolithic suspension of **MCE** and **MCN**. The changes in the filter function for the monolithic stage are made for unconditional stability and a slightly lower unity gain frequency of the intermediate mass feedback. By using the IM feedback together with the ESD alignment feedback, the bandwidth and stability of the Michelson DWS loops can be enhanced. However, this requires a sufficiently low noise level of the Michelson DWS signals in order to prevent saturation of the ESD alignment feedback.

Figure 3.31 shows the open loop gain and phase of the DWS loop if ESD alignment feedback is

added.

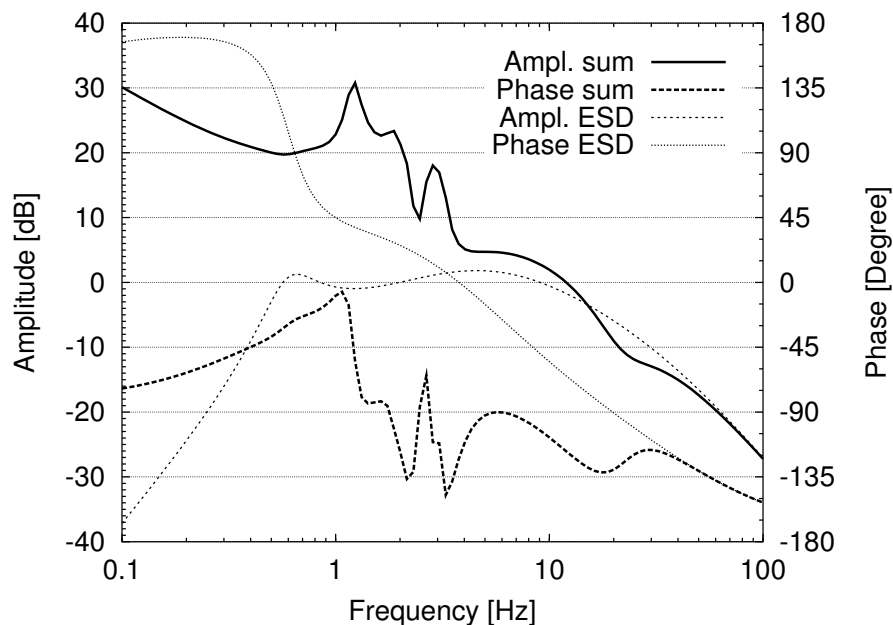


Figure 3.31: Open loop gain and phase of the Michelson fast autoalignment for tilt using additional ESD alignment feedback. The contribution of the ESD feedback is shown separately. The crossover frequency between ESD and IM feedback is around 10 Hz. The overall bandwidth can in principle be increased up to 100 Hz.

The crossover frequency between ESD and IM feedback is around 10 Hz. The overall bandwidth can in principle be increased up to 100 Hz, if the dynamic range of the ESD is sufficient. The maximum possible bandwidth depends on residual alignment noise at low frequencies and the overall noise of the DWS readout, which might saturate the limited ESD range. The range (and thus feedback bandwidth) can be extended, if higher voltages for the ESD alignment are used.

3.5.4.3 Performance

After the Michelson is locked longitudinally, the Michelson DWS fast feedback can be switched on. However the acquisition of the DWS fast feedback is somehow critical. If the deviation from perfect Michelson alignment at the moment of closing the alignment loop is too large, locking of the alignment loop is not achieved as the Michelson alignment gets disturbed too much during initial alignment oscillations, such that the longitudinal lock is lost.

To enable a safe acquisition of the DWS loop, the LabView control VI was programmed to close the loops only if the corresponding error signals are close to zero. This procedure typically needed 1-3 s to close the loops, and sometimes failed, due to the relative slow response time of the LabView system (of the order 100 ms). While working sufficiently well with the initial optics, lock acquisition became harder after changes to the ‘final’ optics. Due to the mismatch in radius of curvature of the far mirrors **MFe** and **MFn** which was not compensated any more by the test optics

of **MCE** and **MCn**, the Michelson contrast was degraded, making the power recycled Michelson more alignment sensitive.

To lock this configuration it is required to switch the Michelson DWS feedback on at the same time as the longitudinal feedback at the intermediate mass stage is switched on by the microcontroller. This is done using the controller signal directly for switching, such that the response time of the LabView system is avoided. Additionally, the gain of the Michelson DWS loops is ramped by hardware from zero to its nominal value over approximately 1 s, to enable a soft acquisition of the system.

Once locked for the first time, it turned out that the alignment fast feedback became unstable after a few minutes with an oscillation building up at 35.6 Hz. This frequency likely corresponds to a vertical mode of the steel wire suspension that **MCE** and **MCn** were suspended with at the time. Due to the large phase lead required for a stable feedback loop, the electronic gain is at its maximum around 35 Hz, thus easily exciting closeby resonances which don't have sufficient phase margin. The oscillation could only be suppressed by adding notch filters at this frequency to both degrees of freedom (The effect of the notch filters is visible in the open loop design shown in Figure 3.30). After changing to the monolithic suspension, notch filters were required for 31.7 Hz and 22 Hz.

Further critical parameters for the stability of the Michelson DWS fast alignment are the beam spot positions on the four end mirrors. In particular the spot positions on mirrors **MCE** and **MCn** are important to control, as these mirrors are used for the DWS feedback. If a spot is not centered on a mirror here, the coupling of angular mirror motions (e.g. caused by the DWS feedback) to longitudinal displacement is altered. If the bandwidth of the Michelson longitudinal feedback loop is low, there can be a coupled oscillation of the DWS and longitudinal feedback loop. Only after these spot positions were fixed by control loops could continuous locking times exceed many hours.

Figure 3.32 shows the amplitude spectral density of **MCE** and **MCn** rotation errorpoint and feedback ²⁷ signals for the power recycled Michelson configuration. As the interferometer is not sufficiently stable without fast Michelson alignment feedback, the free alignment motion can only be measured indirectly by the applied feedback of the alignment system in use.

The feedback noise measured is multiplied with the measured (and then fitted) alignment transfer function of the IM current driver (see Table 3.12). The measurement shown is obtained with the new feedback loop design for the monolithic suspension ('Final PRMI'). The rms alignment noise of the error signal is about $80\mu\text{rad}$. This is only a factor 10 smaller than the rms signal of the feedback applied. Note that the loop was designed for almost unconditional stability at the prize of low-frequency loop gain. The loop gain can definitely be increased by additional integrators, but possibly the fast ESD alignment correction has to be used in this case as well in order to maintain the robustness of the loop.

²⁷the feedback signal available at the front panel of the Michelson alignment module is prewhitened with respect to the 'true' feedback signal (shown) which is the input to the current driver units. The whitening filter has a single pole at 0.3 Hz and a DC gain factor of 32.

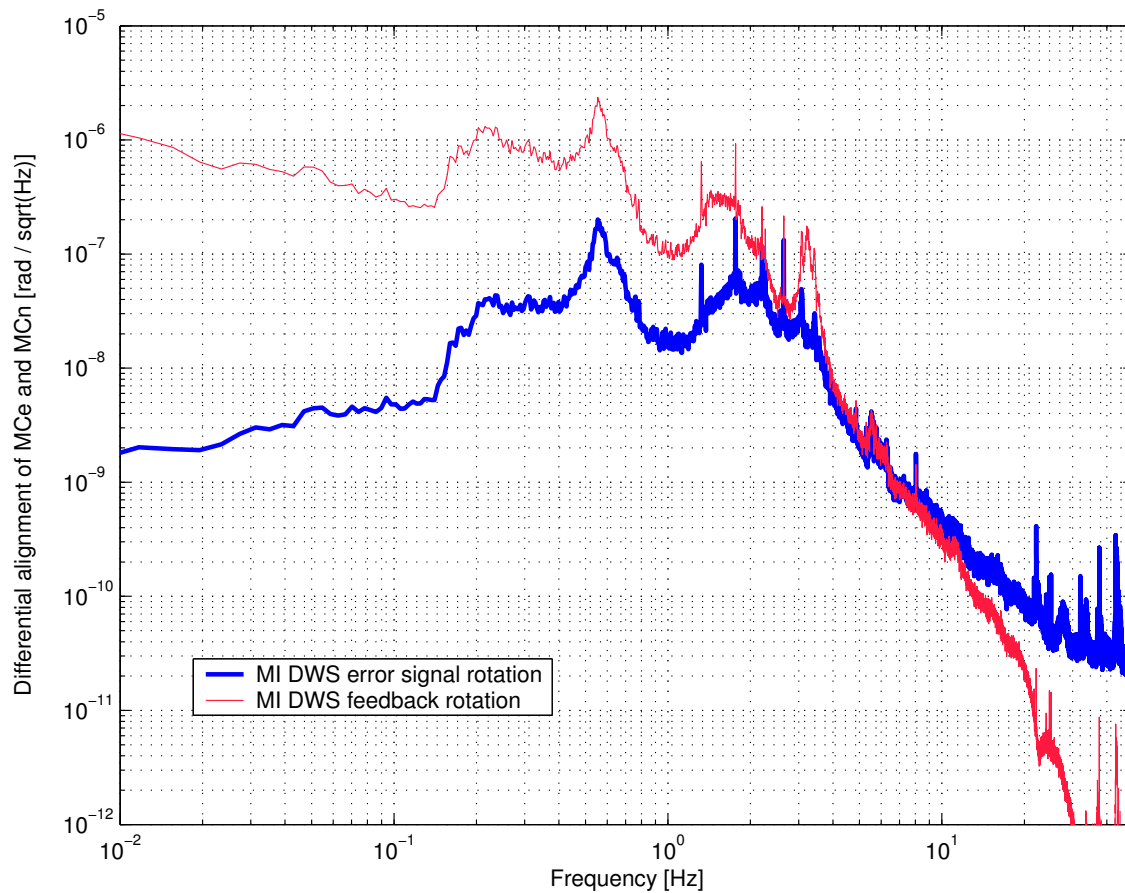


Figure 3.32: Amplitude spectral density of DWS signals for **MCE** and **MCN** rotation with the monolithic suspension. The alignment system is switched on on both traces.

Figure 3.33 shows a time series of the light power at the dark port (upper trace) and the power in the east arm of the Michelson (lower trace). At $t = 100$ s the fast alignment feedback of the Michelson is switched on. After changing optics to the final version, the power recycled Michelson could not be locked without fast DWS feedback, such that a power fluctuation like in Figure 3.33 could not be observed, as it would have been too large to maintain the lock.

Figure 3.34 shows the amplitude spectral density of the light power at the dark port. The two traces are computed from the time series in Figure 3.33 (upper trace) for the states with and without fast alignment feedback. The measurements in Figures 3.33 and 3.34 were done in the ‘Initial PRMI-B’ configuration with **MCE** and **MCN** suspended with steel wires.

The Michelson DWS alignment is the most critical alignment task concerning the stability of longitudinal locking. While locking of the Michelson with the high-loss beamsplitter was long-term stable with only a slow Michelson DWS feedback (bandwidth < 0.2 Hz), a fast Michelson DWS feedback (bandwidth ≈ 10 Hz) became essential for stable locking of the Michelson with the higher finesse achieved using the final low-loss beamsplitter.

As already mentioned, the situation worsened with a bad Michelson contrast, requiring a fast acquisition of the DWS feedback immediately after the longitudinal lock acquisition.

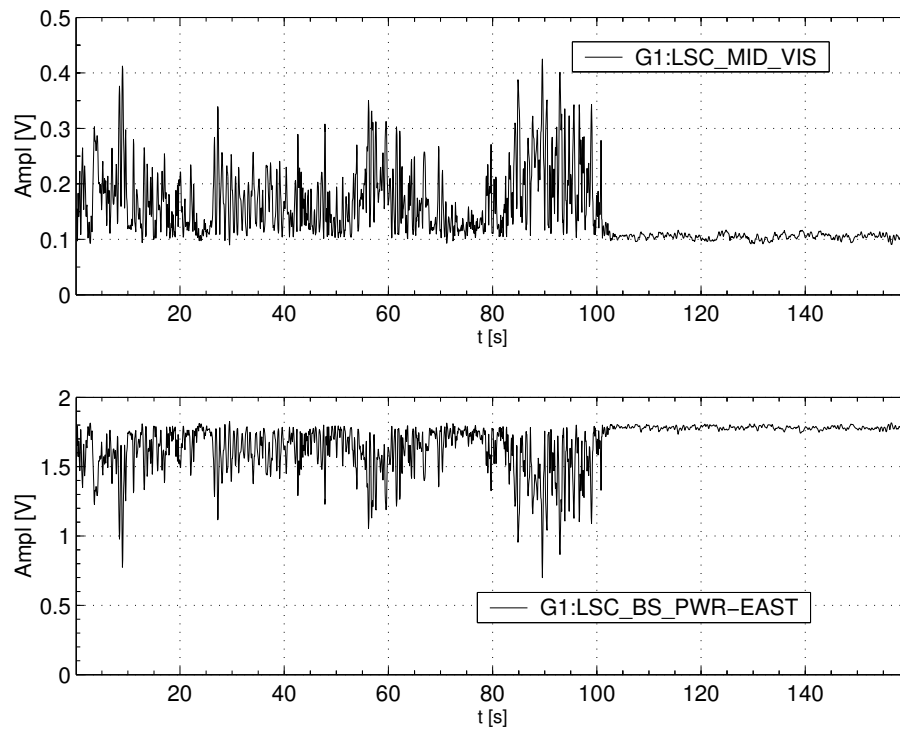


Figure 3.33: Time series of Michelson interferometer power levels with Michelson DWS control switched on around $t = 100$ s. The upper trace shows the light power at the Michelson output port (measured by PDO), the lower trace displays the power in the east arm of the Michelson (measured by PDBSs). Without autoalignment, the interferometer is almost unstable in this configuration.

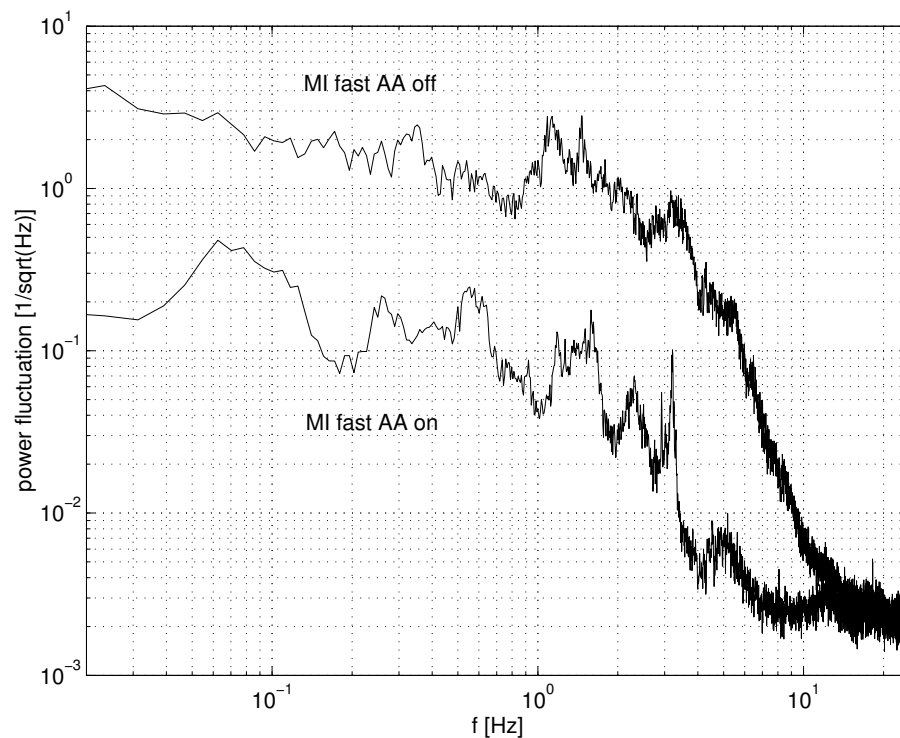


Figure 3.34: Relative amplitude spectral density of light power at dark port with Michelson DWS control switched on and off.

The results shown are obtained with merely the intermediate mass DWS feedback being active. With additional ESD alignment feedback active, a slight increase in bandwidth and stability was demonstrated with the system working on an interferometer with steel wire suspension for **MCe** and **MCn**. The measured alignment calibration factors of the ESD matched the expected values.

3.6 Michelson spot position control

The DWS alignment system for the power-recycling cavity and the Michelson interferometer covers 6 degrees of freedom to superimpose all beam axes of the main interferometer. While the spot position on **BDIPR** is controlled by **BDMC2**, the beam spot positions on the endmirrors **MCe**, **MCn**, **MFe** and **MFn** remain to be controlled (see Figure 3.15 on page 94). These are 8 alignment degrees of freedom, to be controlled by the yet unused alignment degrees of freedom of the beamsplitter **BS**, mirrors **MFe** and **MFn** and the common alignment mode of **MCe** and **MCn**.

3.6.1 How individual mirror misalignments affect the eigenmode

To get some more understanding about the spot position control, we can investigate the TEM_{00} eigenmode position shift of the Michelson interferometer east arm for individual mirror misalignments, shown in Figure 3.35. The dashed lines show the nominal axes of the eigenmode with all beam spots centered on the mirrors. One mirror is misaligned in each graph by an angle α , resulting in a spot position shift on the mirrors of the denoted size. The position shift for the north arm is equivalent for the corresponding mirrors ²⁸.

While case b will not affect the superposition of the cavity's axes with the incoming beam, this will be the case for a and c. Here we have to bear in mind that the superposition of the axes is cared for by the power recycling DWS system with a higher bandwidth than the spot position control. If **MPR** is misaligned (case a), the DWS system will compensate for this by turning **MPR**, meaning that **MPR** cannot cause spot position changes ²⁹.

If **MCe** is misaligned (case c), the DWS system will compensate for this by turning **BDIPR** and **MPR**. As the spot position (of the beam incident on **MPR** from the west) on **MPR** is determined by **BDMC2**, **MPR** will be turned such that the beam is centered on **MPR** again. (This is a result of the fact that the cavity's axis is aligned to the incoming beam's axis. Thus as a result of the superposition of the axes, the spot position from the cavity side will match the spot position of the incoming beam on **MPR**.)

Figure 3.36 illustrates this situation: If **MCe** is misaligned and the power-recycling cavity DWS system compensates the matching of the axes, then mainly the spot position on the far mirror **MFe** is affected.

²⁸If a beamsplitter is added, its misalignment has the same effect to the eigenmode shift of the north arm as misaligning **MPR**. This is true because **BS** and **MPR** are both flat and are located close to each other with respect to the total arm length.

²⁹Of course this is an idealization valid only within the control bandwidth. More precisely, the spot position changes caused by **MPR** are suppressed by the power recycling DWS loop gain.

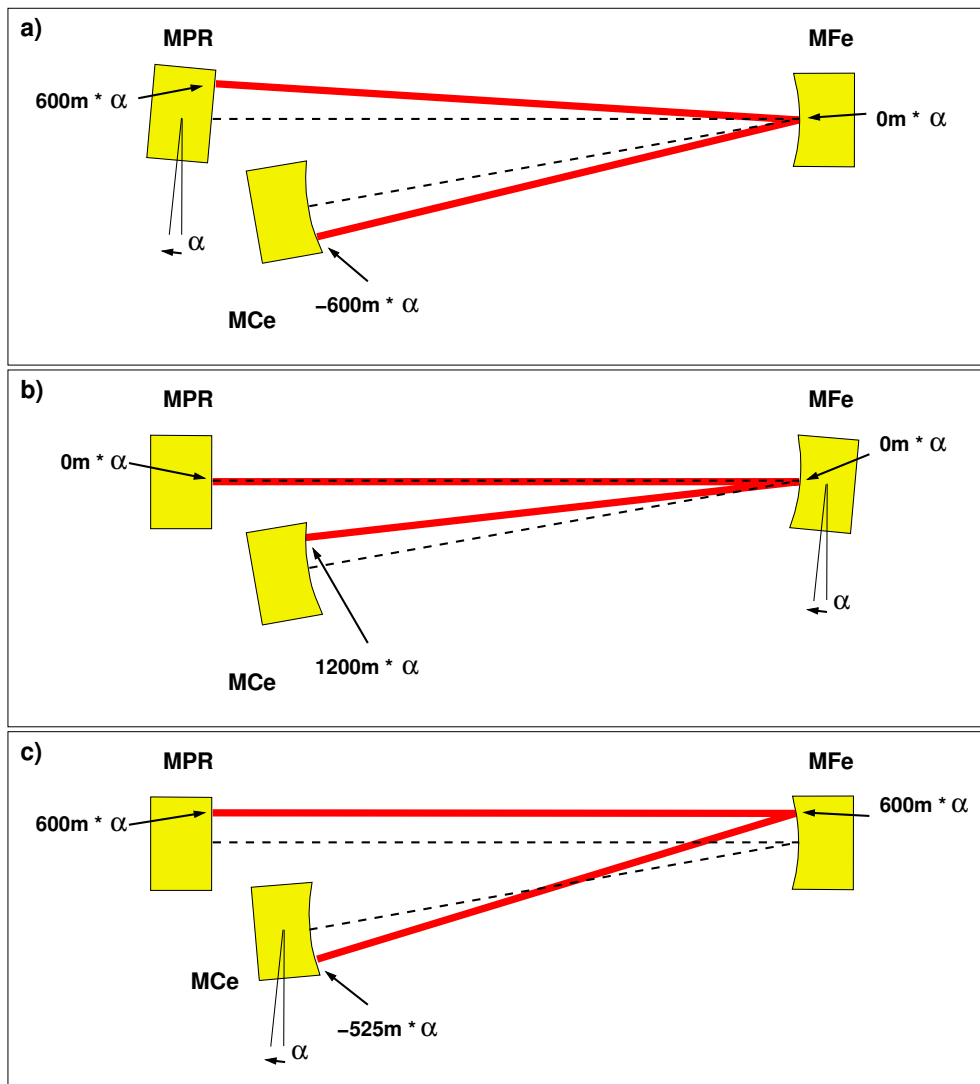


Figure 3.35: Eigenmode position shift of the Michelson interferometer east arm for individual mirror misalignments. The three arrows in each case indicate by how much a spot moves with one of the mirrors misaligned by an angle α . The dashed line shows the nominal position of the eigenmode with spots being centered on the mirrors. The reflecting surface of **MPR** is flat, while **MFe** and **MCe** have radii of curvature of $R_{MFe} = 640\text{m}$ and $R_{MCe} = 600\text{m}$. For the calculation of the eigenmode shift a ray tracing program [Hei99a] was used, with mirror distances set to 600 m (**MPR** to **MFe** and **MFe** to **MCe**). The same results are obtained with a FINESSE simulation.

If both the north and west arms are present, a misalignment of **MCe** will influence the superposition of the axes of the two beams at the Michelson output as well as the power-recycling cavity axis. As feedback of the Michelson DWS loop is applied differentially to **MCe** and **MCn**, the alignment disturbance caused by **MCe** cannot be removed by the Michelson DWS feedback. Instead the Michelson output beams are superimposed and the axis of the power-recycling cavity is affected, but is then corrected by the power-recycling cavity DWS system. In the end, a spot position shift of the kind shown in Figure 3.36 will result. Before we take a look at the control topology for this problem, it is interesting to see how in general a problem of this kind can be solved.

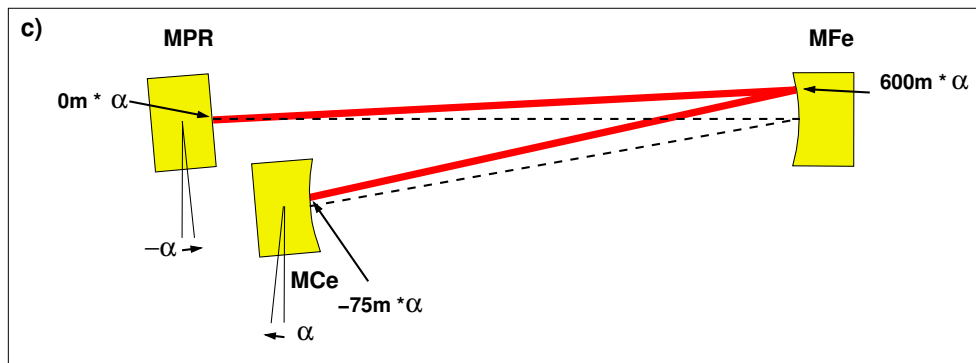


Figure 3.36: A misalignment of MCE can partially be compensated by aligning MPR. This is the case if the DWS feedback for the power-recycling cavity is used.

3.6.2 Control signals for n-dimensional problems

Let's assume a linear control system with n actuators, n sensors and an arbitrary but fixed effect - a coupling constant - of each actuator to each sensor³⁰. How can control signals be generated for each of the n actuators with minimized couplings between the n feedback loops?

The information we have about the system are the coupling constants, which can be calculated from the knowledge of the system, or possibly can be measured experimentally. Let c_{jk} be the coupling constant of actuator A_j to sensor S_k . We then obtain the n times n coupling factors

$$\begin{matrix}
 c_{11}, c_{12}, \dots, c_{1n} \\
 c_{21}, c_{22}, \dots, c_{2n} \\
 \dots\dots\dots \\
 c_{n1}, c_{n2}, \dots, c_{nn}
 \end{matrix}
 \tag{3.17}$$

Each coupling factor c_{jk} can be viewed as the response of sensor S_k to a unity elongation of actuator A_j , while the actual sensor signal of S_k in a working physical system is affected by all actuators and any disturbance of the system.

In the general case, a control signal E_j for an actuator A_j is generated from a linear combination of all sensor signals:

$$E_j = a_{j1}S_1 + a_{j2}S_2 + \dots + a_{jn}S_n
 \tag{3.18}$$

with factors a_{jk} which have to be determined. The basic idea for decoupling all feedback loops of the system, is to choose factors a_{jk} , such that for all $j \in \{1, \dots, n\}$, $E_j = 0$, if any actuator E_k with $k \neq j$ is perturbed.

³⁰It is not required to think in the frequency domain here; for our purpose it's sufficient to assume that the transfer function from one actuator to each sensor is identical except for the coupling factors. If this is not the case, the model just has to be evaluated for each frequency of interest independently.

With this we get a system of equations determining the a_{jk} for actuator j :

$$\begin{aligned}
 a_{j1}c_{11} &+ a_{j2}c_{12} &+ \cdots &+ a_{jn}c_{1n} &= 0 \\
 a_{j1}c_{21} &+ a_{j2}c_{22} &+ \cdots &+ a_{jn}c_{2n} &= 0 \\
 &\dots &&& \\
 a_{j1}c_{(j-1)1} &+ a_{j2}c_{(j-1)2} &+ \cdots &+ a_{jn}c_{(j-1)n} &= 0 \\
 a_{j1}c_{j1} &+ a_{j2}c_{j2} &+ \cdots &+ a_{jn}c_{jn} &\neq 0 \\
 a_{j1}c_{(j+1)1} &+ a_{j2}c_{(j+1)2} &+ \cdots &+ a_{jn}c_{(j+1)n} &= 0 \\
 &\dots &&& \\
 a_{j1}c_{n1} &+ a_{j2}c_{n2} &+ \cdots &+ a_{jn}c_{nn} &= 0
 \end{aligned} \tag{3.19}$$

If the system can be solved unambiguously, it follows that *only* when actuator A_j is perturbed, the resulting signal distribution among the sensors (caused by A_j) yields a control signal $E_j \neq 0$, where E_j is calculated according to equation 3.18.

This means that if a system disturbance is caused by an actuator of the system itself, the described method of calculating a control signal will identify the actuator causing the disturbance. Doing so, correcting actuation can be restricted to the place where the disturbance is caused, which minimizes couplings between the feedback loops. The alignment control of an interferometer is such a system. Misalignments are caused by individual mirrors, and the actuators correcting the alignment are the mirrors as well. If a misalignment caused by mirror A is partially corrected by mirror B, a new misalignment will appear in the system, which in turn has to be corrected by any other mirror than B. While this kind of coupling between the feedback loops can make the system unstable if it is too large, even in case of a small coupling the dynamic response is not optimal.

A multitude of solutions of 3.19 will exist if there are *different* actuators causing the *same* signal distribution on the sensors. If no other actuators or sensors can be found in such a case, there will remain uncontrolled degrees of freedom of the system.

3.6.3 Formal approach to obtain control signals

With the above formalism and some a priori knowledge about the power recycled Michelson, we can derive how control signals for the spot positions can be obtained. We rename mirrors and sensors in this chapter according to Figure 3.37, in order to get simplified symbols and write the coupling factors as:

$$\begin{aligned}
 c_{A1}, c_{B1}, c_{C1}, c_{D1} \\
 c_{A2}, c_{B2}, c_{C2}, c_{D2} \\
 c_{A3}, c_{B3}, c_{C3}, c_{D3} \\
 c_{A4}, c_{B4}, c_{C4}, c_{D4}
 \end{aligned} \tag{3.20}$$

We can eliminate some of them with the knowledge obtained in section 3.6.1: Misalignment of mirror C will only couple to sensor S1, and misalignment of D only to sensor S2, thus $c_{C2}, c_{C3}, c_{C4},$

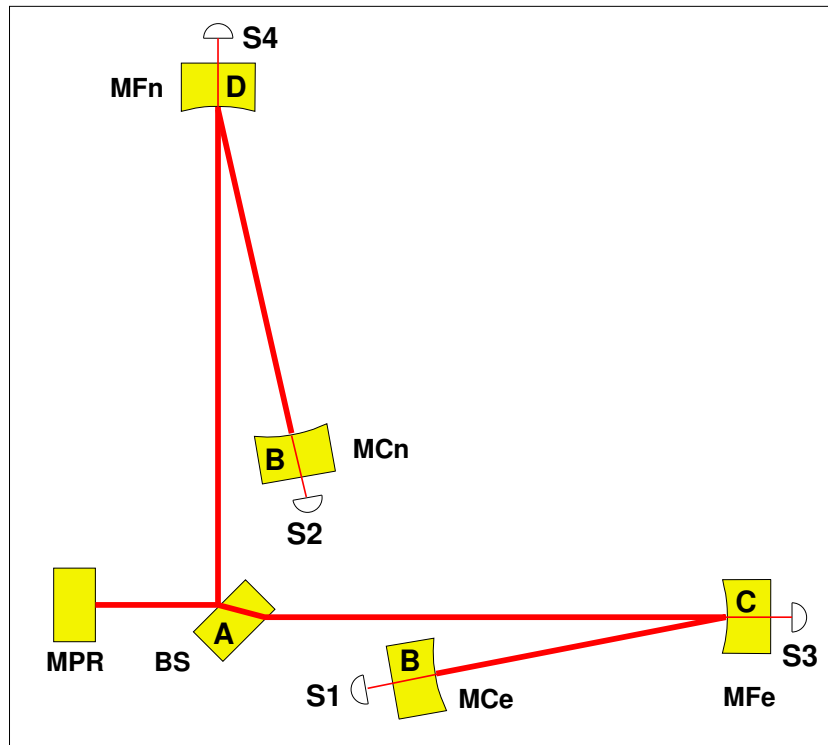


Figure 3.37: Actuators (A,...,D) and sensors (S1,...,S4) for the spot position control of the main interferometer. As the two differential alignment degrees of freedom of **MCe** and **MCn** are used for the Michelson DWS feedback, only their two common modes remain for spot position control, and therefore both are labelled identical. **MPR** is not used for spot position control.

c_{D1} , c_{D3} and c_{D4} are zero. For symmetry reasons (both arms have identical endmirrors) $c_{B3} = c_{B4}$ and $c_{B1} = c_{B2}$. Thus we obtain factors c_{jk}

$$\begin{aligned}
 &c_{A1}, c_{B1}, c_{C1}, 0 \\
 &c_{A2}, c_{B1}, 0, c_{D2} \\
 &c_{A3}, c_{B3}, 0, 0 \\
 &c_{A4}, c_{B3}, 0, 0
 \end{aligned} \tag{3.21}$$

If we arrange the factors a_{jk} (which we want to determine) in a matrix, we can write down the four systems of equations with a total of 16 equations to be solved for the four control signals. The diagonal entries on the right hand side matrix represent a gain factor for each of the four feedback signals. For simplicity it is set to 1 in this calculation.

$$\begin{pmatrix} a_{A1} & a_{A2} & a_{A3} & a_{A4} \\ a_{B1} & a_{B2} & a_{B3} & a_{B4} \\ a_{C1} & a_{C2} & a_{C3} & a_{C4} \\ a_{D1} & a_{D2} & a_{D3} & a_{D4} \end{pmatrix} \begin{pmatrix} c_{A1} & c_{B1} & c_{C1} & 0 \\ c_{A2} & c_{B1} & 0 & c_{D2} \\ c_{A3} & c_{B3} & 0 & 0 \\ c_{A4} & c_{B3} & 0 & 0 \end{pmatrix} = \begin{pmatrix} 1 & 0 & 0 & 0 \\ 0 & 1 & 0 & 0 \\ 0 & 0 & 1 & 0 \\ 0 & 0 & 0 & 1 \end{pmatrix} \tag{3.22}$$

Solving these equations (which is equivalent to computing the inverse matrix of the c_{jk}) we get

$$\begin{pmatrix} a_{A1} & a_{A2} & a_{A3} & a_{A4} \\ a_{B1} & a_{B2} & a_{B3} & a_{B4} \\ a_{C1} & a_{C2} & a_{C3} & a_{C4} \\ a_{D1} & a_{D2} & a_{D3} & a_{D4} \end{pmatrix} = \begin{pmatrix} 0 & 0 & \frac{1}{c_{A3}-c_{A4}} & \frac{1}{c_{A4}-c_{A3}} \\ 0 & 0 & \frac{c_{A4}}{c_{B3}(c_{A4}-c_{A3})} & \frac{c_{A3}}{c_{B3}(c_{A3}-c_{A4})} \\ \frac{1}{c_{C1}} & 0 & \frac{c_{A4}c_{B1}-c_{A1}c_{B3}}{c_{B3}c_{C1}(c_{A3}-c_{A4})} & \frac{c_{A3}c_{B1}-c_{A1}c_{B3}}{c_{B3}c_{C1}(c_{A4}-c_{A3})} \\ 0 & \frac{1}{c_{D2}} & \frac{c_{A4}c_{B1}-c_{A2}c_{B3}}{c_{B3}c_{D2}(c_{A3}-c_{A4})} & \frac{c_{A3}c_{B1}-c_{A2}c_{B3}}{c_{B3}c_{D2}(c_{A4}-c_{A3})} \end{pmatrix} \quad (3.23)$$

With these factors a_{jk} we can now obtain proper control signals according to equation 3.18.

Referring to Figure 3.37, we get the result that the beamsplitter **BS** is controlled by a linear combination of the far end spot position sensors S3 and S4, and the same is true for the common mode of **MCE** and **MCn**. No signals from sensors S1 and S2 are used, as this would generate control signals if the far mirrors were misaligned.

The control signals for the far mirrors **MFe** and **MFn** are a linear combination of all spot position sensors *except* the one behind the opposite far mirror. The linear combination is calculated such that the control signal remains zero if **BS** or **MCE** + **MCn** is misaligned; it remains zero as well if the respective other far mirror is misaligned, as its corresponding spot position is not used in the linear combination.

Implicitly the above formalism was used to adjust the linear combinations of the modecleaner and power-recycling cavity DWS signals (see, for example, section 3.3.6 on page 85). In these cases control signals for particular actuators were chosen such that these control signals are close to zero if another actuator is perturbed.

3.6.4 Spot position sensors

The spot position sensors for **MCE** and **MCn** are mounted directly next to the vacuum windows of vacuum chambers TCE and TCN, respectively. The beams transmitted through **MCE** and **MCn** are steered with rigidly mounted pick-off mirrors to vacuum windows with 100 mm diameter. As the beam diameter is about 18 mm in the central cluster, it is focused with a lens of focal length $f = 75$ mm and 75 mm diameter. The lenses and the spot position sensors are mounted on small optical benches attached to the vacuum windows. The position of each lens is chosen such that the respective photodiode is placed behind the focus - at a place where the beam diameter is about 4 mm (the distance between each lens and the photodiode is approximately 100 mm). The photodiodes are Advanced Photonics SD 380 quadrant diodes with a diameter of 10 mm.

The situation at the far mirrors **MFe** and **MFn** is slightly different. In principle we have two beam spots here, the beam coming from the beamsplitter and the beam returning from the endmirrors **MCE** or **MCn**. If all DWS alignment systems are working, the two beam spots are superimposed on the far mirrors and, due to the angle of the beam axes, they form a horizontal interference pattern. One possibility to determine the spot position is to measure the ‘center of mass’ of the interference pattern by detecting the photocurrent distribution of a position sensing diode (PSD).

However it is also possible to distinguish between the two beams impinging on each far mirror, by separating them with appropriate optics. The spot position control works equally well regardless if only one beam is detected or the interference pattern of both beams combined is evaluated.

Figure 3.38 shows the arrangement of optical components used for the spot position control on the far end mirrors **MFe** and **MFn**.

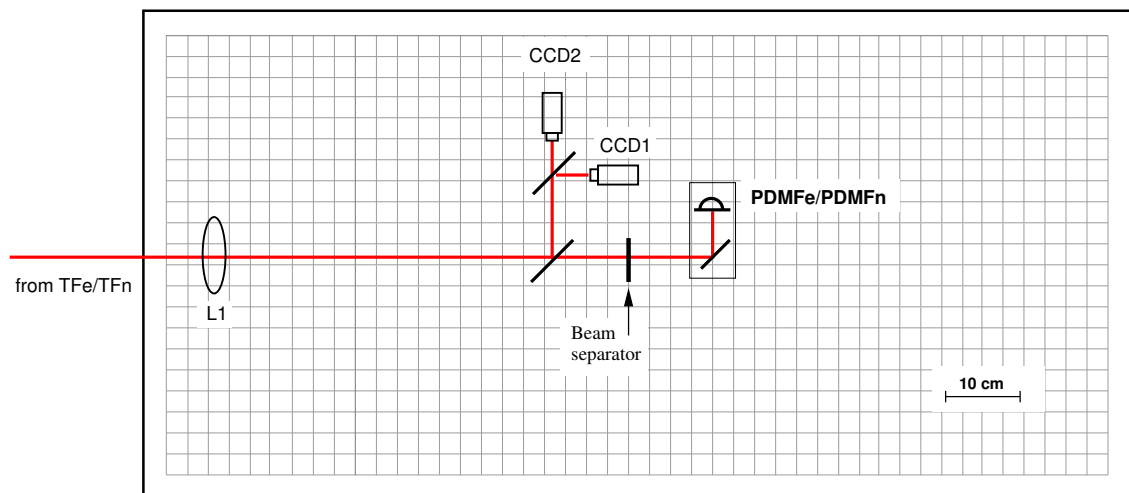


Figure 3.38: Optical layout of the breadboards in the two far end stations. Both beams leaving a far end vacuum chamber are focused with lens L1 and split into two paths for spot position detection and CCD imaging.

The beam passing the far mirror is focused by lens L1 with a focal length of $f = 560\text{mm}$. Two beamsplitters are used to provide images onto two CCD cameras which can image the near or far field of the beam. The beam transmitted at the first beamsplitter is detected by a spot position sensor. The separation of the two beams by the ‘beam separator’ in Figure 3.38 can be done with a razor blade mounted at the focus of L1. This was used for debugging purposes, but is not required for normal operation.

Table 3.14 summarizes how the beam spot positions are determined for each suspended mirror of the main interferometer.

mirror	spot position determined by	monitored by
BDIPR	spot pos. control acting on BDMC2	PDAPR
MPR	fixed by spot pos. on BDIPR	PDAPR
BS	fixed by spot pos. on MPR and MFe	PDAPR + PDMFe
MCE	spot pos. control acting on MFe	PDMCE, CCD
MCn	spot pos. control acting on MFn	PDMCn, CCD
MFe	spot pos. control acting on BS, MCE + MCn	PDMFe, CCD
MFn	spot pos. control acting on BS, MCE + MCn	PDMFn, CCD

Table 3.14: How the spot positions are determined and monitored for all suspended mirrors of the main interferometer.

3.6.5 Spot position fluctuations

The spot position fluctuations on mirrors are important, as deviations of the spot position from the center of a mirror increase the coupling of that mirror's alignment noise into optical path length changes, as illustrated by Figure 3.39³¹.

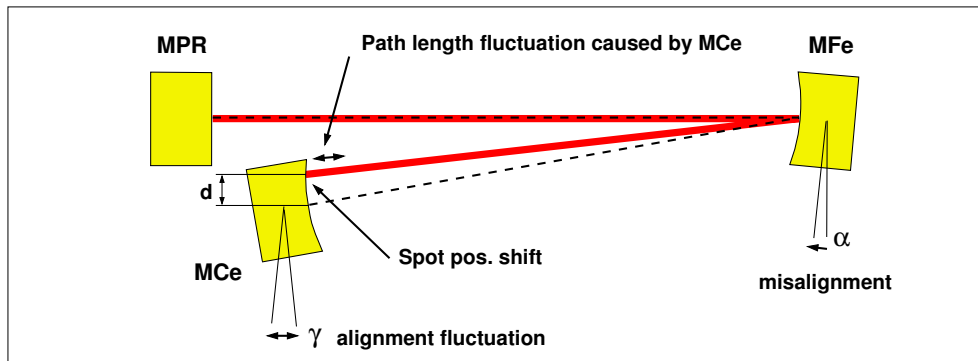


Figure 3.39: Spot position deviations from the center of rotation of a mirror cause couplings of residual alignment fluctuations into optical path length changes.

In this example a misalignment, α , of mirror **MFe** causes a spot position shift, d , on **MCe**. This results in a coupling of **MCe** alignment fluctuations, γ , into pathlength changes, δ , with $\delta = d\gamma$.³²

Two main sources of a mirror's angular noise can be distinguished:

- Seismic alignment noise resulting from ground motion in conjunction with the suspension transfer function, including local control damping. For a particular mirror, the resulting residual alignment noise may be further suppressed by the alignment system.
- Electronic noise introduced to the suspension chain. The local control as well as the alignment system may impose additional alignment noise, mainly for frequencies above their control bandwidths.

Concerning the spot position deviation on a mirror, we have to look for its rms value over all frequencies. The spot positions on the end mirrors (**MCe**, **MCn**, **MFe** and **MFn**) are controlled with a bandwidth below the responsible mirror-pendulum's main resonance frequencies (see table 3.14 for reference). Thus the spot positions rms value is dominated by the pendulums angular motion around its main resonance. With a currently observed pendulum motion of the order $1\mu\text{rad}_{\text{rms}}$ and an optical lever of 600 m, the spot position fluctuations are of the order 1mm_{rms} .

The spot position fluctuation on the beamsplitter is significantly lower, as it is mainly determined by mirror **BDMC2**. Although the alignment of **BDMC2** has a low bandwidth as well³³ the

³¹ Another reason to avoid spot position fluctuations is that inhomogeneities on the mirror surface may cause a varying level of scattered light.

³² Because of the beam path folding, a spot position deviation on **MFe** couples to a pathlength change with $\delta = 2d\gamma$.

³³ The spot position alignment bandwidth for **BDMC2** could be extended without too much effort, as actuators at the mirror level of **BDMC2** are already installed.

resulting spot position fluctuation on the beamsplitter is smaller, because of the shorter distance from **BDOMC2** to the beamsplitter **BS**. The rms position fluctuation on **BS** will thus be smaller than $10\mu\text{m}$.

The permanent DC deviation of the spot position on the beamsplitter will likely be larger than $10\mu\text{m}$. This leads to the question: On which nominal point has the spot on a mirror to be located, such that the couplings of alignment noise into path length changes are really zero. Depending on the suspension, this point is not necessarily identical to the geometric center of the mirror and has to be determined experimentally. This has to be done for a frequency in the measurement band where the coupling is important.

The alignment fluctuations causing path length changes due to spot position deviations are only important in the gravitational wave measurement band. In particular the alignment noise at the lower end (50 Hz) of this band is of interest for specifying limits, as residual alignment noise from the attenuated seismic noise as well as additional electronic noise will be largest at this end. Note that the introduction of electronic noise possibly enhancing alignment fluctuations due to DWS feedback only applies to mirrors **MCE** and **MCn**.

We can estimate the requirement for the rms deviation of the spots on the end mirrors as well as for the residual alignment noise of the respective mirror above 50 Hz. Including a safety factor of, for example, 5, the product $\delta = d\gamma$ must not exceed about $\delta = 2 \times 10^{-20} \text{ m}/\sqrt{\text{Hz}}$ (with d given in meters and γ in $\text{rad}/\sqrt{\text{Hz}}$). With a typical alignment fluctuation of the mirrors (that determine spot positions) of about $\alpha = 1\mu\text{rad}_{\text{rms}}$, we get roughly $d = 1 \text{ mm}$ spot position deviation on a far mirror. With this we obtain an alignment noise limit of $\gamma = 2 \times 10^{-17} \text{ rad}/\sqrt{\text{Hz}}$ above 50 Hz.

3.6.5.1 Spot position measurements

Figure 3.40 shows the measured vertical spot position fluctuations on mirrors **MCE** and **MCn**. The upper graphs show the spectral density of the spot position fluctuations, while the lower graphs show the resulting integrated rms position fluctuations. The integration is done from high to low frequencies in order to see the contribution of noise sources to the rms fluctuation as a function of frequency. The rms spot position deviation is about 0.6 mm on **MCE** and 0.4 mm on **MCn** for this measurement with a rather ‘normal’ seismic noise level. The spot position fluctuations can be significantly larger at times of enhanced seismic noise, which can be caused by strong wind or earthquakes.

Both rms motions are dominated by the pendulum resonance frequencies around 1 Hz. Below about 0.2 Hz, the spot positions are stabilized, as explained above. The spot position spectrum of **MCn** shows a narrow peak with a width of $\text{FWHM} = 15 \text{ mHz}$ at 8.055 Hz. This line was also observed with the seismometers built into the suspension in the north tank TF_n, however its origin is yet unclear.

Figure 3.41 shows the coherence of the spot positions on **MCE** and **MCn**. The coherence gives an estimation as to what extent two signals are caused by a common signal. A coherence of

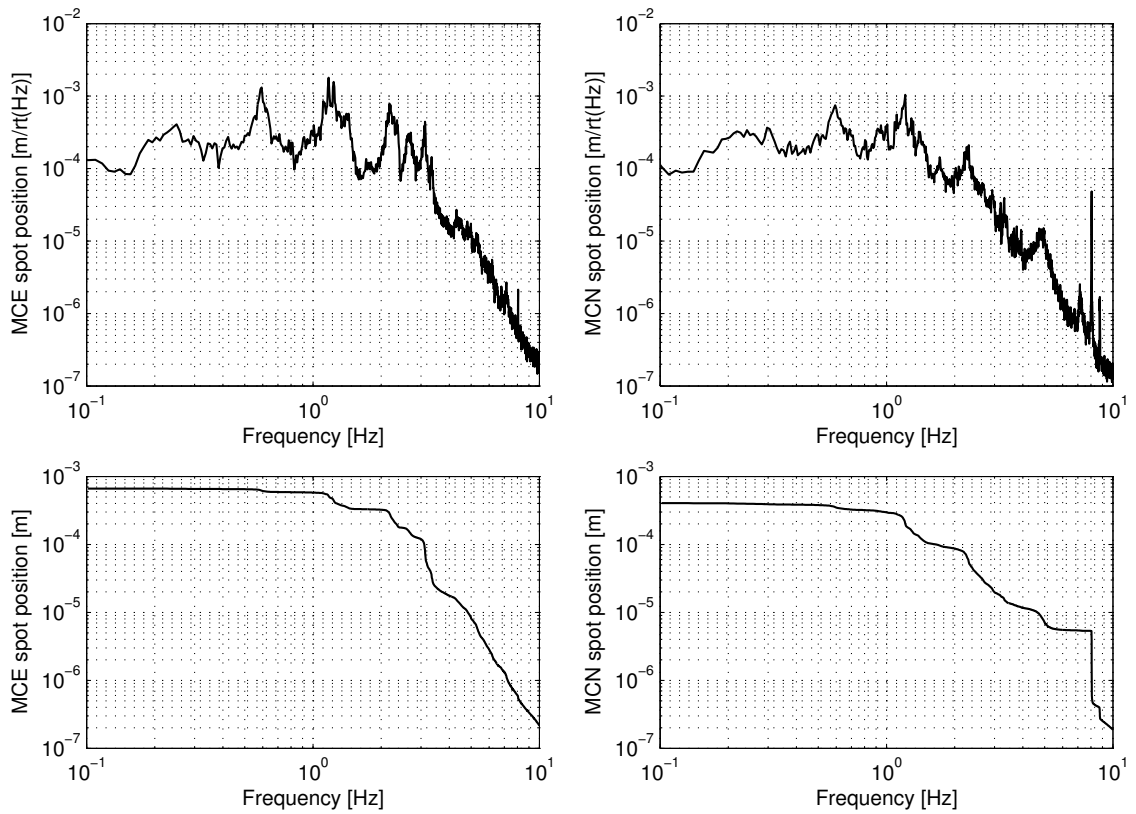


Figure 3.40: Vertical spot position fluctuations on end mirrors **MCE** and **MCN**. The upper graphs display the spectral density of the spot position fluctuations, the lower graphs show the corresponding integrated rms position fluctuations. The integration is done from high to low frequencies in order to see the contribution of noise to the rms fluctuation as a function of frequency. The rms spot position deviation is about 0.6 mm on **MCE** and 0.4 mm on **MCN** for this measurement.

unity denotes a completely common source of two signals, while a coherence of zero indicates statistically independent signals.

A coherence of these spot positions can be caused by alignment fluctuations originating in the central cluster, mainly by beamsplitter alignment fluctuations³⁴. Correlations can be seen around 1.8, 4.5, and 7 Hz which may be suspension resonances of the beamsplitter suspension, being slightly different for the far mirror suspension. At frequencies where the alignment noise as shown in Figure 3.40 is larger than the baseline noise, no correlations are observed.

3.6.5.2 DWS feedback measurement

The measurement of the DWS alignment feedback applied to **MCE** and **MCN** gives an estimation of the introduced alignment noise at 50 Hz and above. The feedback signal applied to the coil

³⁴There may be coherences due to common seismic excitation as well. However if so, these are rather expected at low frequencies (below 1 Hz).

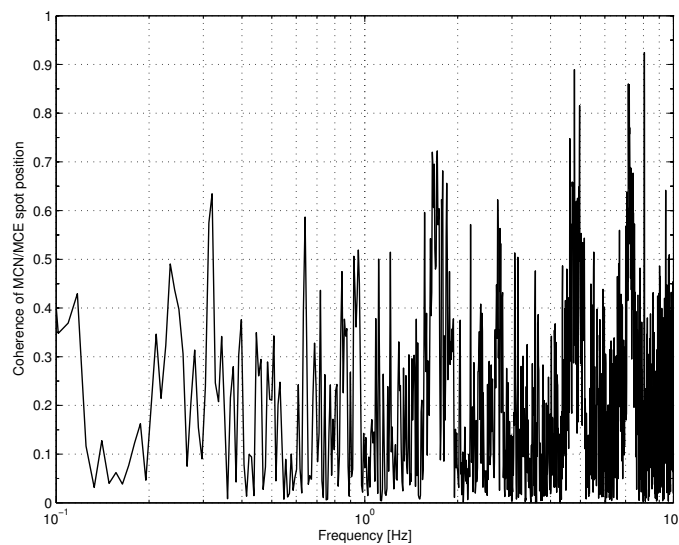


Figure 3.41: Coherence of the spot positions on **MCE** and **MCn**. Correlations can be seen around 1.8, 4.5 and 7 Hz.

drivers is multiplied with the respective calibrated alignment transfer function as shown in table 3.12 on page 110.

Figure 3.42 shows the resulting alignment noise introduced, multiplied with a spot position deviation on **MCE** and **MCn** of 1 mm. Thus the displayed quantity is the differential Michelson length noise introduced by alignment feedback noise.

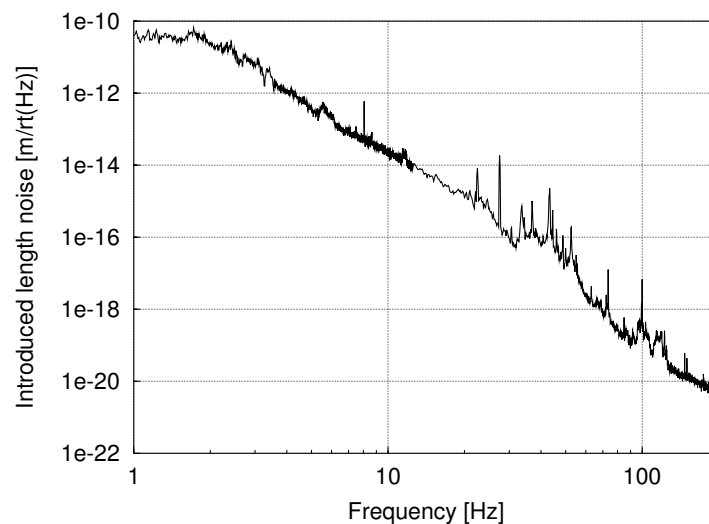


Figure 3.42: Differential Michelson length noise introduced by the DWS alignment feedback on **MCE** and **MCn** intermediate mass actuators. The DWS feedback was measured and then multiplied by the measured pendulum's transfer function. The resulting alignment noise is scaled for a spot position deviation of 1 mm.

The alignment noise requirement of $\delta = 2 \times 10^{-20} \text{ m}/\sqrt{\text{Hz}}$ is safely reached above approximately 150 Hz. Between 50 Hz and 150 Hz, the noise may decrease with a larger optical gain factor of

dual recycling, which can reduce the feedback noise. Another possibility to reduce the noise is the use of the fast ESD alignment feedback, which would allow for less gain in the intermediate mass path for frequencies above 50 Hz, and thus would introduce less noise.

3.6.6 Faster alignment control for MCE and MCn common mode

The LABVIEW based control system cannot exceed about 0.2 Hz control bandwidth, as write commands need up to 100 ms time, and other virtual instruments on the same computer are not executed during this latency time.

However there are two fast alignment actuators that are currently used with the slow LABVIEW control only. For the possibility that a faster alignment control for MCE and MCn common mode will be required in future, electronics for real-time communication between the endstations was developed. A realtime data exchange between the endstations and the central building with a bandwidth of 1 kHz for three channels sampled with 12 bit can be established. Thus it is possible to send spot position information from the far ends fast enough to be used for alignment feedback to MCE and MCn common mode with a bandwidth above the pendulums main resonance frequencies if required ³⁵.

The system is based again on INFINEON C167 microcontrollers. Communication is performed by optical fibres using RS232 protocol. The system can also be used to send spot position information in realtime from the central station to the endstations. However it remains to be seen whether this is useful, as the control bandwidth of the far mirror's alignment is severely limited by the lack of fast actuators. Probably not much larger bandwidth than 1 Hz can be achieved here due to the large phase delay when acting onto the upper mass of the suspension chain.

3.6.7 Long term drifts

During the data taking run in August/September 2002 ('S1' run), the interferometer was continuously operated for 16 days. Figure 3.43 shows the beamsplitter rotation alignment feedback (top) and the central cluster temperature (bottom) during this period.

The alignment fluctuations of the uncontrolled mirror (measured by the applied feedback) are about $50 \mu\text{rad}_{\text{pp}}$. Without spot position control this would lead to a spot position deviation of $60 \text{ mm}_{\text{pp}}$ on the far end mirrors MCE and MCn. It can be seen that the alignment signal is strongly dominated by the temperature in the central cluster, which is dominated by a period of 24 h.

³⁵The beamsplitter, BS, uses the same spot position information, but has no actuation stage below the upper mass.

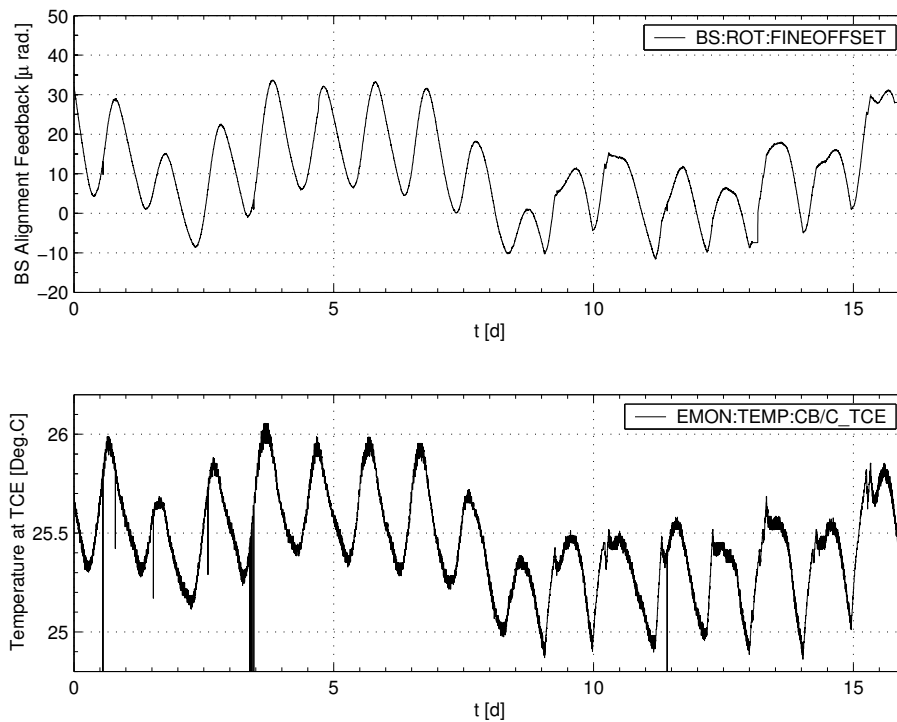


Figure 3.43: Beamsplitter alignment feedback (top) and central cluster temperature (bottom) over 16 days of the ‘S1’ run.

3.7 Alignment calibrations

3.7.1 Analog feedback

The analog alignment inputs to the coil driving units at the intermediate mass stage were calibrated at a signal frequency of 0.1 Hz by observing the spot position deviation on a far end mirror with a CCD camera. The camera image was calibrated with an aperture of known size close to the imaged spot position. The calibration factor for other frequencies can be calculated then by use of the measured transfer function of the alignment input (see table 3.12 on page 110).

3.7.2 Digital feedback

The digital offsets which are applied to the coil driving units of the upper mass by 12-bit digital to analog converters located on the ‘digiboards’, are calibrated by applying known misalignments to the mirrors.

The most straightforward calibration method is to measure a beam deflection for a small alignment offset applied. A slight variation of this idea is to determine the two offset settings required to steer the reflected beam to each end of an object of known size. This method was used for calibrating the alignment actuators of mirrors **BDIPR**, **BS**, **MCe** and **MCn**. With CCD video cameras mounted behind the end mirrors **MFe** and **MFn**, the spot image on the respective mirror can be observed,

where the vacuum output window forms a visible aperture of 100 mm (if the full window aperture was not visible, an artificial aperture of 4 cm was used for calibration). The beam being reflected from mirror **MPR** back to **MU3** is detected by quadrant cameras on the breadboard at **TCMb**. In this setup, **MPR** can be calibrated by applying a known alignment offset to **BDIPR**, and thereby determining the required alignment offset to **MPR** to compensate for the beam deflection caused by **BDIPR**. For this purpose the spot position on **PDPR** is observed, which does not need to be calibrated, but can easily be so after the calibration of **MPR** is known.

The alignment feedback of the far mirrors **MFe** and **MFn** can be calibrated by observing the interference pattern on these mirrors while applying alignment offsets to them. The interference pattern is clearly visible as long as the beam reflected from a far mirror hits the reflection-coated surface of the corresponding folding mirror in the central cluster, as the beam is retro-reflected on the folding mirrors. The coating's diameter on **MCE** and **MCn** testmirrors was 80 mm. The final mirrors **MCE** and **MCn** are coated over their full diameter of 180 mm. It is also possible to judge the spot position on **MCE** and **MCn** by the angle and spacing of the interference pattern on the respective far mirror. This procedure is used to pre-align the beam spots manually by inspecting the corresponding CCD images.

Table 3.15 shows the calibration factors obtained for the three layers of descriptors.

Mirror	rotation	tilt	rotation	tilt	rotation	tilt
	fine	fine	medium	medium	standard	standard
BDIPR	0.10	0.07	-	-	10	2.1
MPR	0.16	0.25	-	-	2.6	6.3
BS	0.24	0.06	-	-	6.7	4.4
MCE	0.078	0.016	n.u.	n.u.	17	2.2
MCn	0.068	0.021	n.u.	n.u.	21	3.3
MFe	n.u.	n.u.	0.51	0.15	4.4	2.3
MFn	n.u.	n.u.	0.74	0.16	2.6	2.5

Table 3.15: Alignment feedback calibration factors for the main optics digital control in μ radian/increment. The numbers are given for the resulting beam angles, the mirror angles are half of these values. The terms 'fine', 'medium', and 'standard' refer to individual digital to analog converters with different fixed gains. 'n.u.' denotes currently not used alignment descriptors.

Appendix A

Optical layout of GEO 600

The optical layout of GEO 600 can conveniently be drawn with the OPTOCAD program written by Roland Schilling [Sch02]. OPTOCAD is a ray-tracing program for Gaussian beams which uses dedicated input files to describe optical setups. The input file describing GEO 600 can be found on the GEO documentation server.

Figure A.1 shows the complete optical layout of GEO 600 in the final configuration. The laser bench and the two modecleaners are located on the south side of the central building.

Figure A.2 displays a close-up of the central interferometer area (and the north end mirror) but without the modecleaners. The final configuration uses an output modecleaner and associated optics as shown. All experiments described in this work were done with no mirror in tank TCOa and a single flat mirror installed in vacuum chamber TCOb. The detection bench setup used to date is shown in Figure 3.24 (on page 106).

Currently it seems likely that a so-called ‘compensation plate’ will not be used in the final configuration. A compensation plate was included in earlier versions of the optical layout with the principal idea to compensate for beam distortions caused by the beamsplitter substrate that the east arm beam has to pass. These distortions are dominated by the ‘thermal lens’ of the beamsplitter, caused by inhomogeneous heating of the bulk material in the beam path. A compensation plate consisting of a cylindrical silica mass of the same size as the beamsplitter (with two anti-reflective coated surfaces) would be installed in the central tank TCC (in parallel to the beamsplitter, but north of it). The beamsplitter’s thermal lens effect could then approximately be compensated for, by imposing a thermal lens effect on the north beam as well.

The disadvantage of a compensation plate (besides the necessary installation work to be done) is a possibly increased noise level due to thermo-refractive noise [Cag02]. Due to the successful compensation of the radius of curvature of MFe with a heater (Figure 1.18) it is now planned that the beamsplitter thermal lens effect can be compensated for by an adaptive optics technique as well.

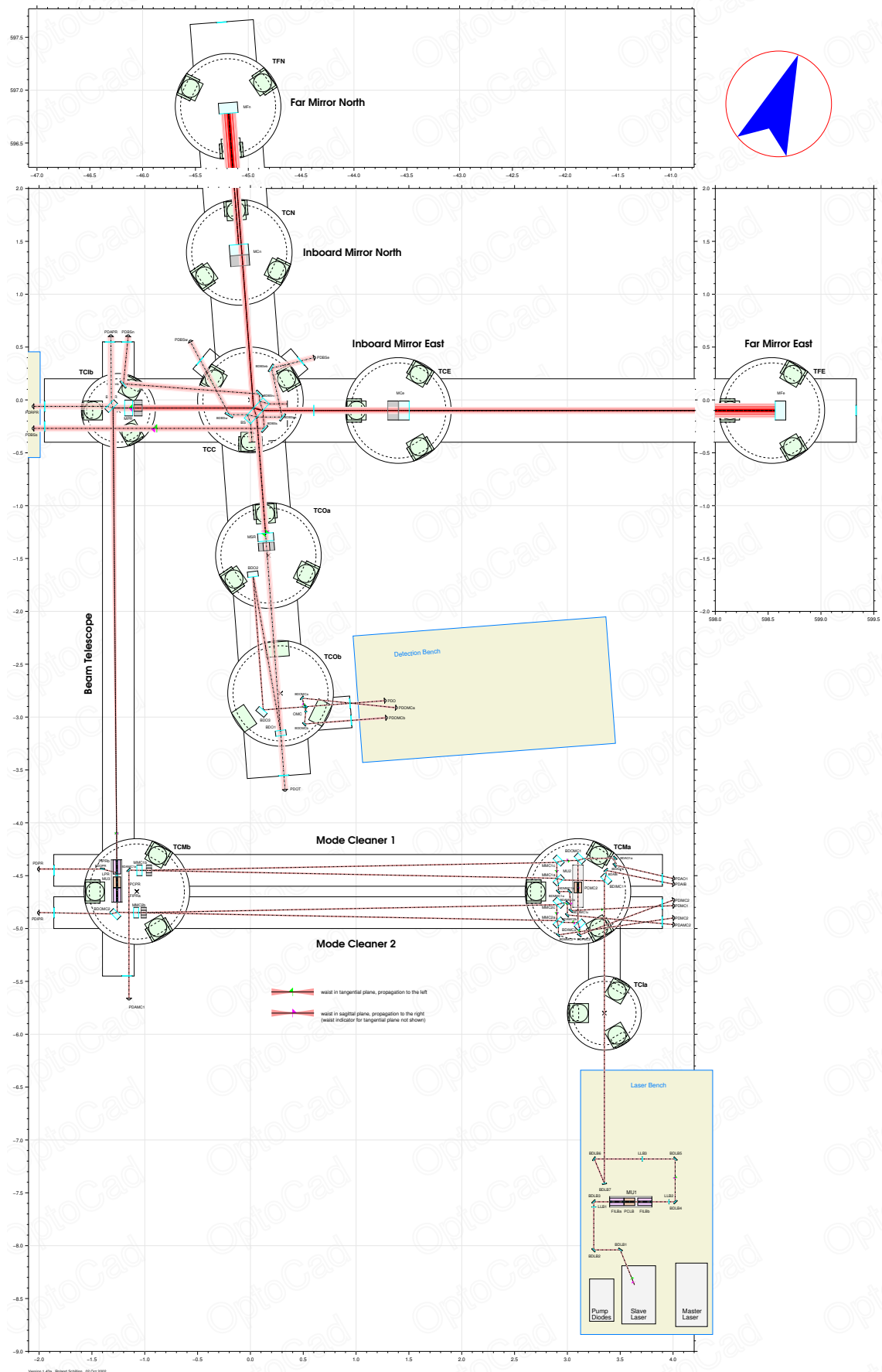


Figure A.1: Complete optical layout of GEO 600 in the final configuration, including the laser bench and modecleaners.

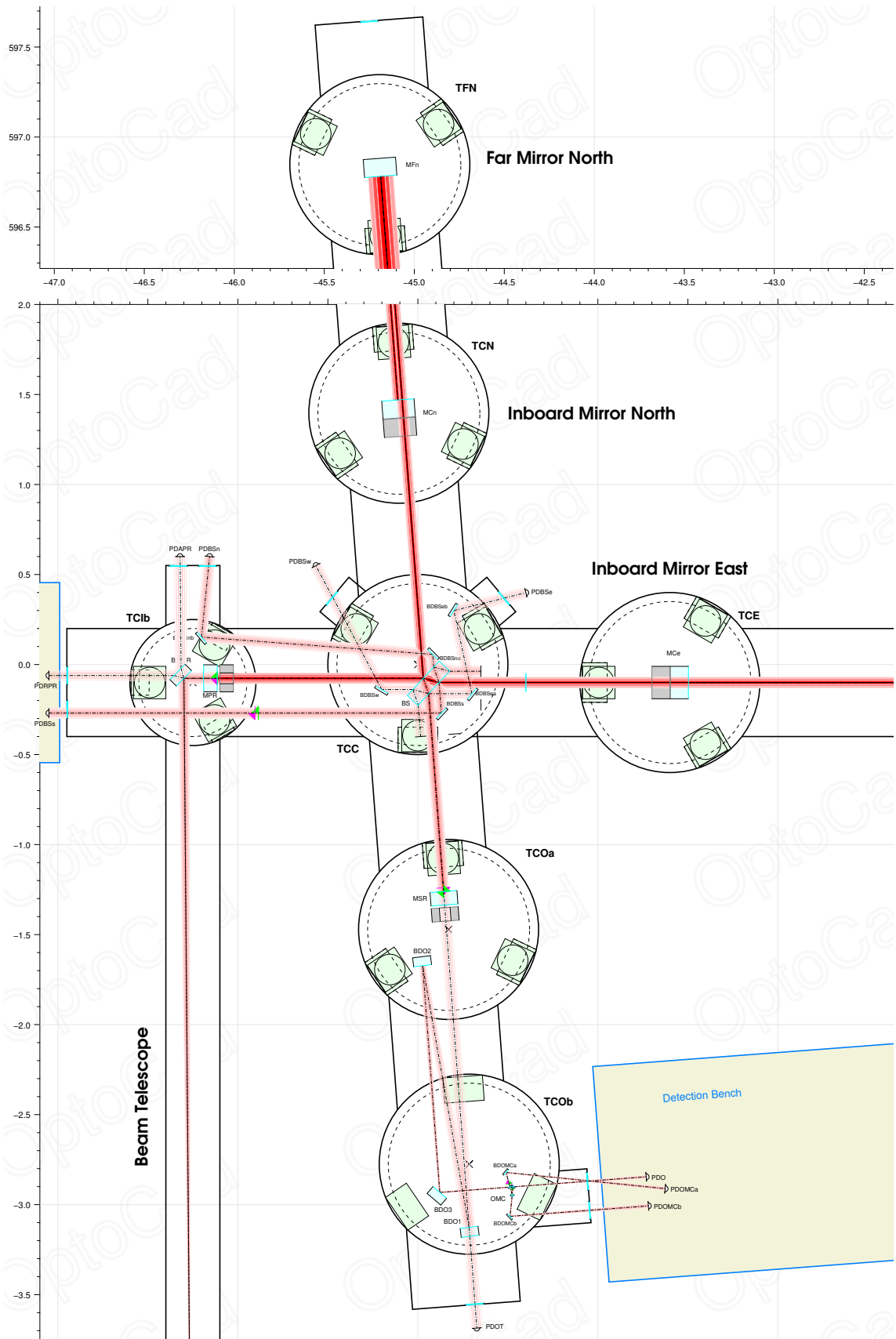


Figure A.2: Optical layout of the central interferometer area (and north end mirror) in the final configuration. The north end vacuum chamber is shown as well.

Appendix B

Electronics

For the design of electronic circuits, in particular filter stages, the simulation and fitting program LISO, written by Gerhard Heinzl, was used [Hei99b]. In particular the fitting capabilities in conjunction with the optimization of dynamic range, noise performance and stability at the same time, make LISO an extremely valuable tool for the design of low-noise electronics.

B.1 Resonant quadrant cameras

The term ‘quadrant camera’ denotes a standard design used for the quadrant photodiodes of GEO 600 with associated electronics. Figure B.1 shows the quadrant photodiode electronics with a current limiting circuit (around T1 and T2), the resonant circuit consisting of L_A and two amplifiers for the DC and RF output, respectively. For bias voltages larger than 40 V, we use transistors of the type MPSA 92 for T1 and T2. Diodes D7 and D8 are required to prevent forward currents through individual quadrants of the photodiode, by keeping the bias voltage always positive.

Figure B.2 shows the electronics used for the demodulation of the RF signal from one quadrant. Four of these circuits (except for the pre-amplifier of the local oscillator signal, N1A, which is used in common for four channels) are located in one housing together with the circuit shown in Figure B.1. Additional electronics in the same housing is used to process the difference and sum signals of the four quadrants for the DC and demodulated RF output, respectively.

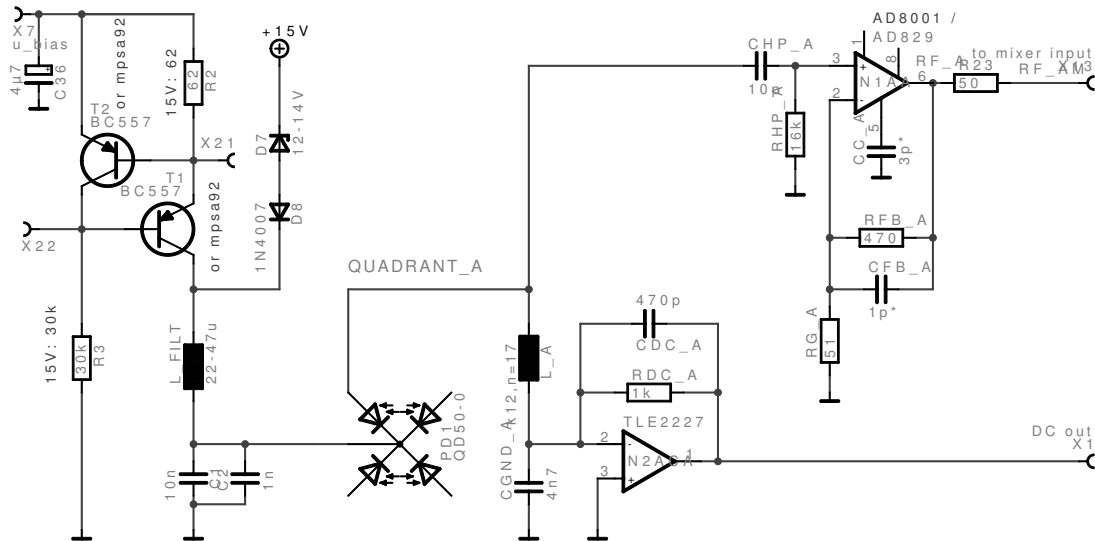


Figure B.1: Electronics around resonant quadrant photodiode. Current limiting circuit, resonant photodiode's quadrants and amplifiers for DC and AC signals.

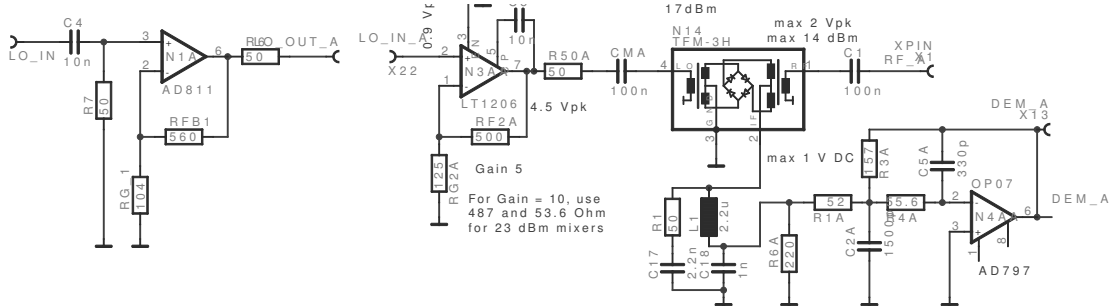


Figure B.2: Demodulation electronics for one quadrant of a resonant photodiode.

B.2 Orthogonal current driver

The ‘orthogonal’ current drivers are used to provide as pure rotation, tilt, and longitudinal motion to a mirror as possible. A driver unit distributes three input signals for rotation, tilt, and longitudinal motion to three coils. The arrangement of coils is different on the 5 suspensions that use this type of coil driver, as shown in Figure B.3.

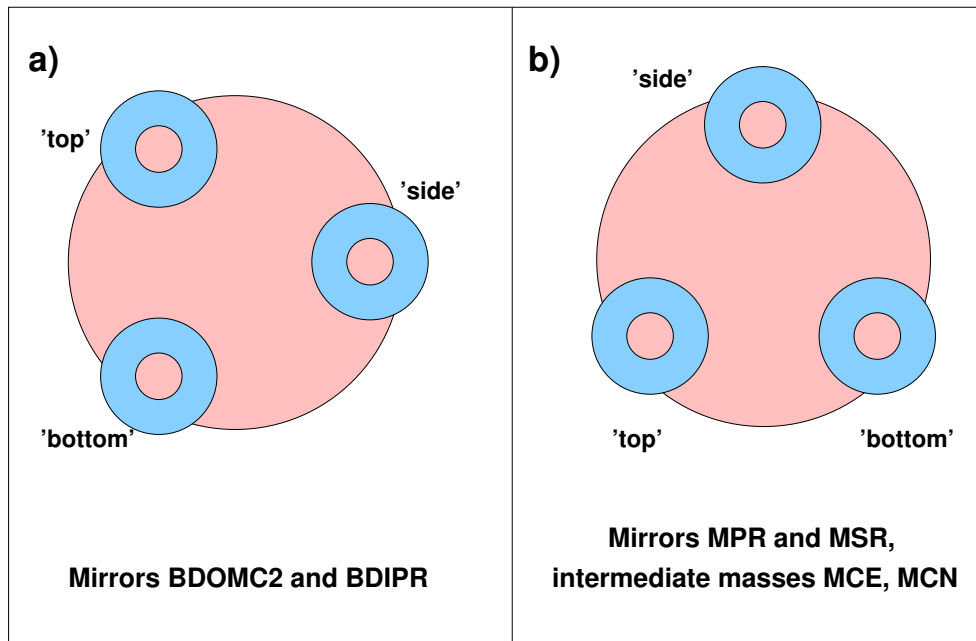
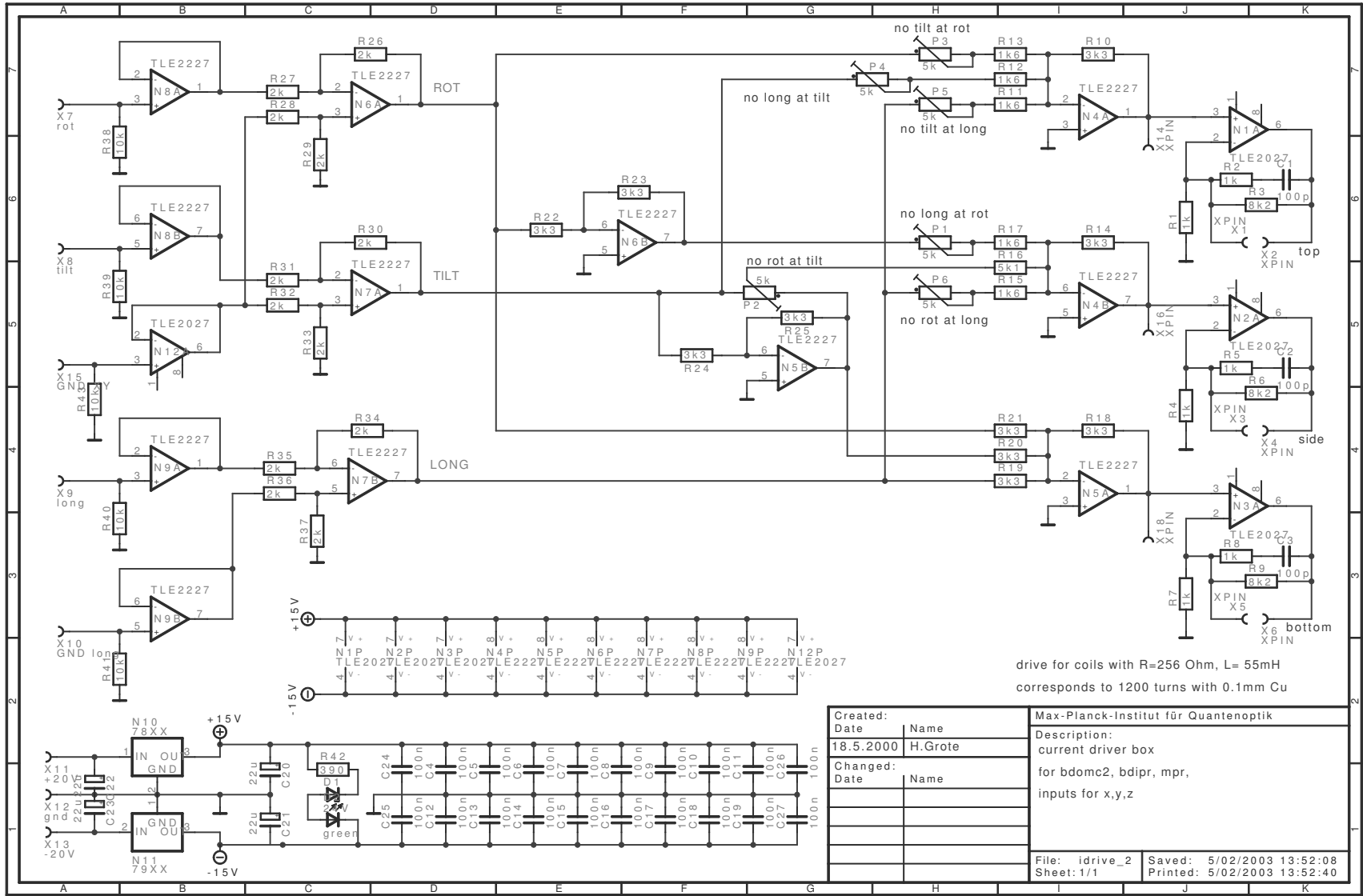


Figure B.3: Arrangement of coils connected to the orthogonal current driver on 6 suspensions. The labels ‘top’, ‘side’, and ‘bottom’ refer to the three output channels of the current driver and they can be unambiguously defined in case a). In case b) then, the coil positions are rotated by 90°.

The arrangement a) is chosen for BDOMC2 and **BDIPR** in order to have a sufficiently large clear aperture in the center of the mirrors to let a fraction of the main beam pass for spot position detection purposes. (The mirror plane has an angle of 45° with the laser beam axis for these suspensions.) Mirrors **MPR**, **MCE**, and **MCn** use arrangement b).

Figure B.4 (on page 139) shows the current driver circuit. The 6 potentiometers are labelled to denote the specific influence they have to the orthogonalisation matrix. The labelling refers to the coil arrangement of case a) in Figure B.3. For the arrangement of case b), the inputs ‘rotation’ and ‘tilt’ have to be swapped. The circuitry shown is located in the cleanroom of GEO 600, close to each vacuum chamber of a mirror to drive.

Figure B.4: 'Orthogonal' current driver unit.



B.3 ESD alignment driver

The ESD alignment drivers are used to balance the forces on the four quadrants of a drive such that as pure rotation and tilt motions as possible can be obtained. (The circuit can easily be extended to provide a low-range longitudinal input to the ESD. Such an input might be required to lower the possible noise contribution from the ESD to mirror displacement, as explained in section 1.3.)

The electronics shown in the schematics of Figures B.5 and B.6 is located in a module of 'rack C' in the control room. The module contains the circuitry twice, for the ESD of **M_{Ce}** and **M_{Cn}**, respectively.

Figure B.5 contains electronic filters that are used for the ESD alignment feedback.

Figure B.6 shows the circuitry for the adjustment of the coupling matrix. The outputs of the four operational amplifiers for each drive are connected to the quadrants of an ESD as shown in Figure 3.29 on page 112.

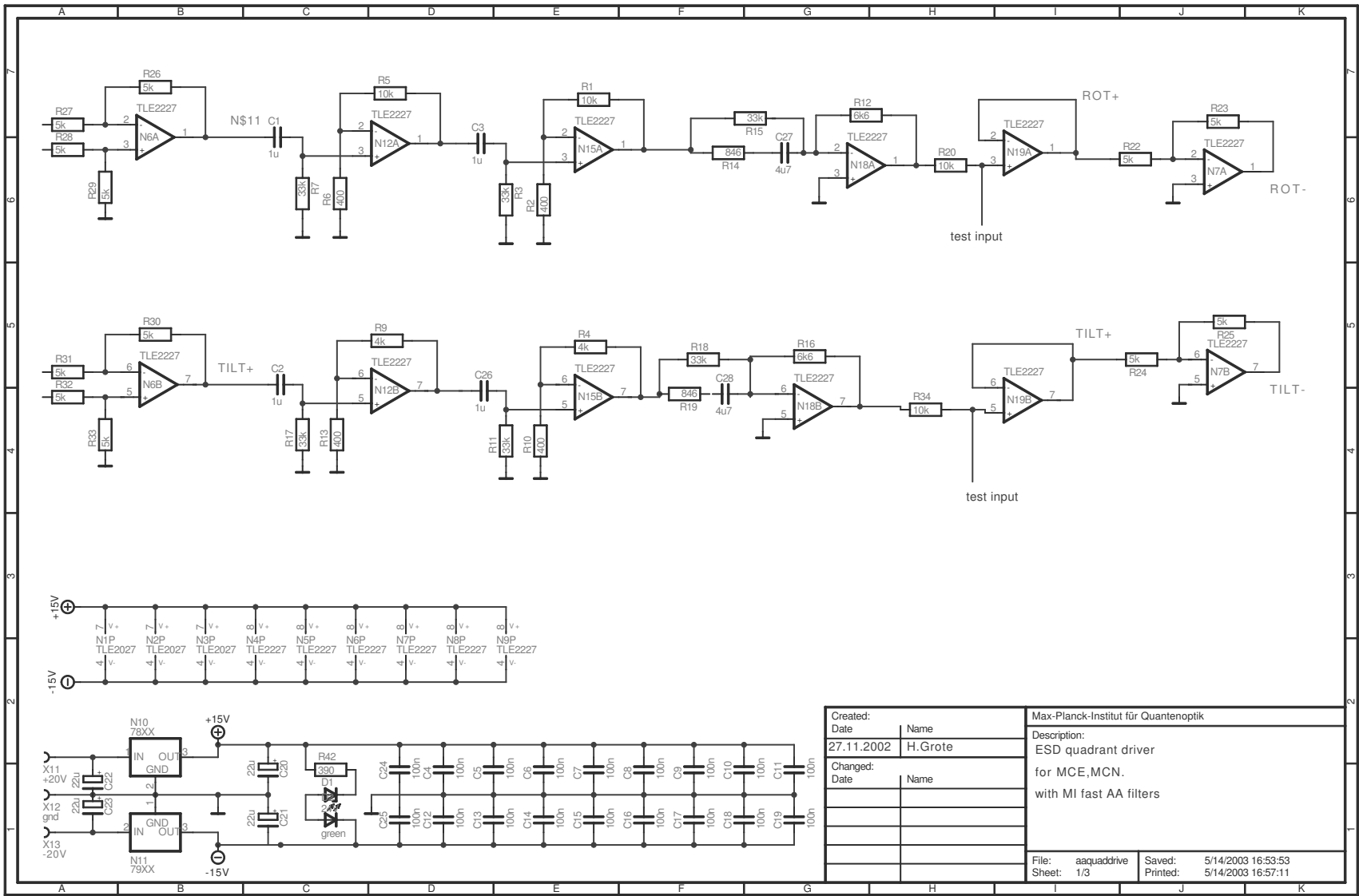
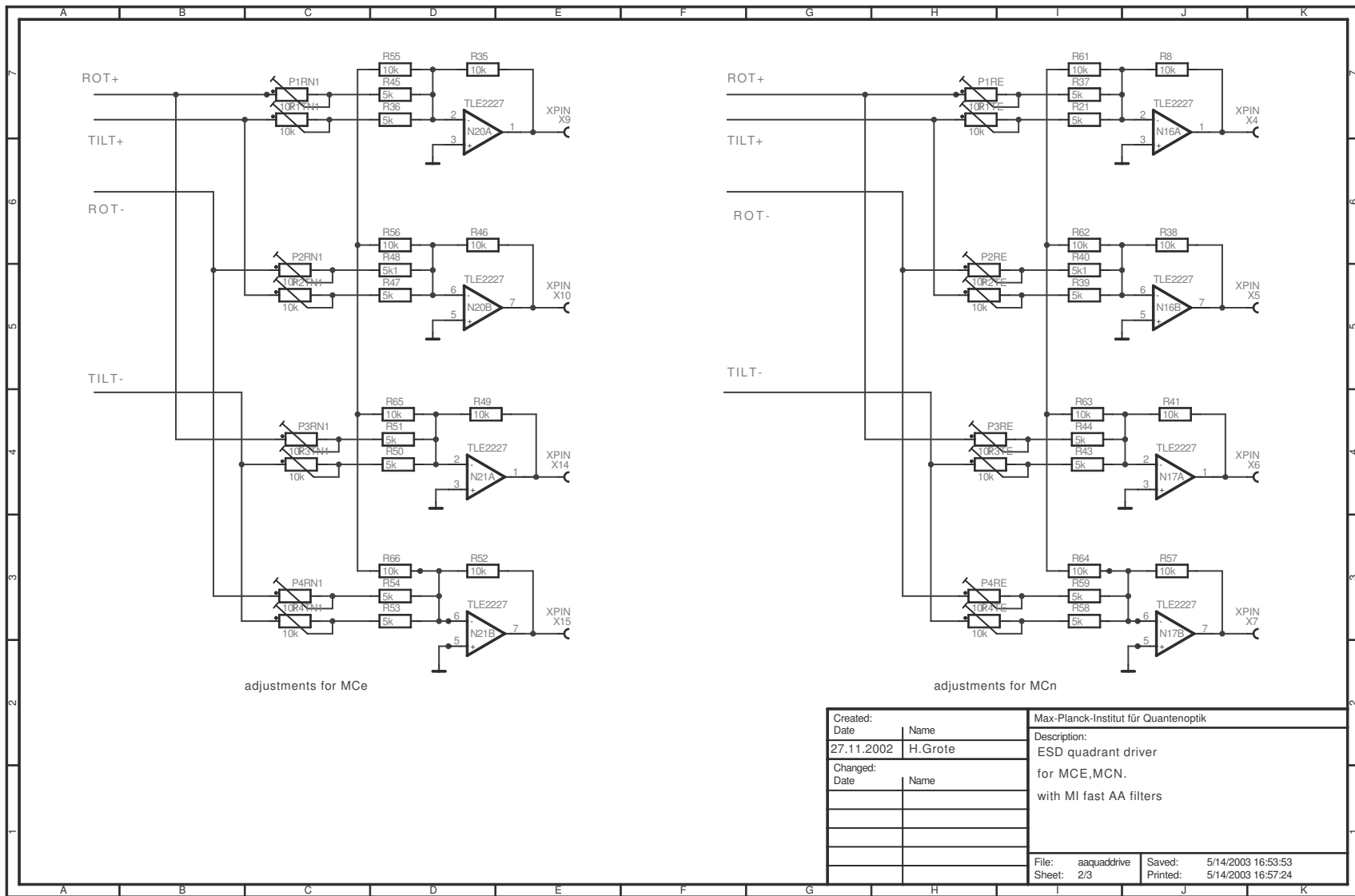


Figure B.5: Filter electronics for ESD alignment feedback.

Figure B.6: Orthogonalization electronics for ESD alignment feedback.



B.4 Microcontroller and spot positions

The INFINEON C167 microcontroller is embedded on a printed circuit board from PHYTEC. The on-chip, 10-bit, AD converters are extended by 8 12-bit channels with a MAX197 AD converter with a byte-wide parallel output. Digital to analog conversion is done with MAX537 converters.

The circuit in Figure B.8 (on page 144) shows the microcontroller with the additional AD and DA converters. Further the board is equipped with standard four-pole lowpass filters for anti-aliasing purposes with Tschebycheff-characteristic (not shown).

Also contained in these modules are two identical circuits to process the appropriate sums and differences from four quadrants of a spot position detector. One of these is shown in Figure B.7. From the four quadrants A,B,C, and D, the horizontal beam position $DX1$ is calculated as $DX1 = G_x \times (A - B - C + D)$, and the vertical position as $DY1 = G_y \times (A + B - C - D)$, respectively. The gains $G_{x/y}$ are set by resistors R77 and R78, according to

$$G = 1 + \frac{50k\Omega}{R} \tag{B.1}$$

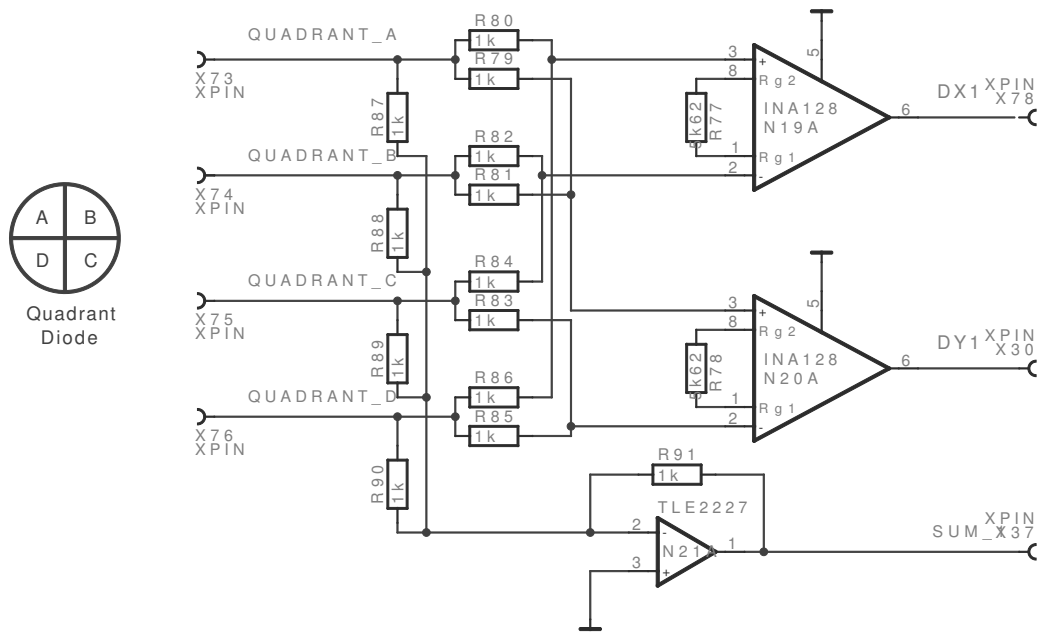


Figure B.7: Processing sums and differences from quadrant diode signals.

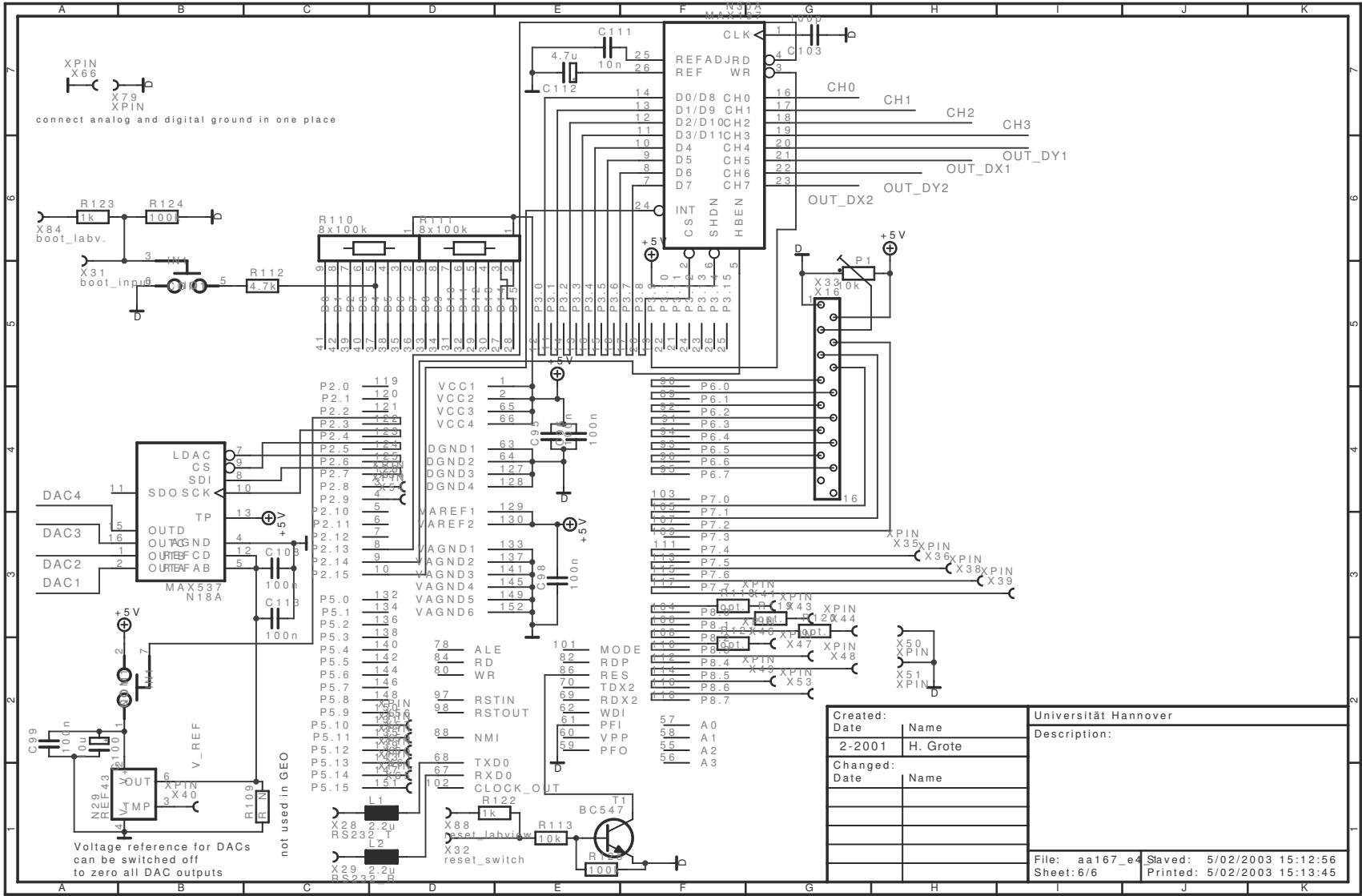


Figure B.8: Infineon C167 microcontroller with periphery.

Created:	Name	Universität Hannover
Date	H. Grote	Description:
2-2001		
Changed:	Name	
Date		
		File: aa167_e4
		Sheet: 6/6
		Printed: 5/02/2003 15:13:45

Appendix C

Software

C.1 Microcontroller code

C.1.1 Flow diagrams

Figure C.1 shows a simplified flow diagram of the main loop controlling the acquisition DC lock and the power recycling lock.

Figure C.2 shows a simplified flow diagram of the subroutine controlling the dual recycled lock. The routine is called from the main loop shown in figure C.1 and is quit to the main loop if the Michelson feedback (which precedes the signal recycling lock) cannot be switched on *or* a lock stretch ended.

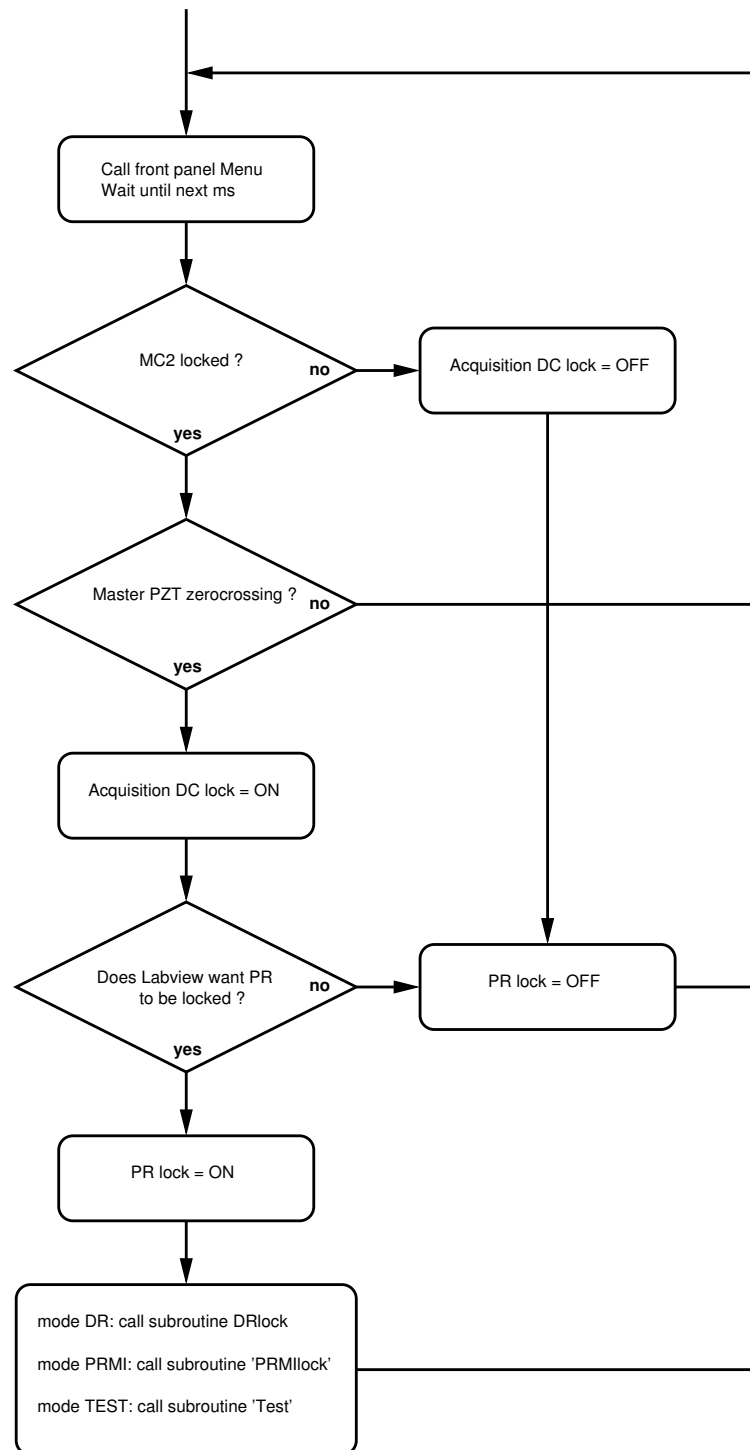


Figure C.1: Simplified flow diagram of the main loop controlling the acquisition DC lock and power recycling lock.

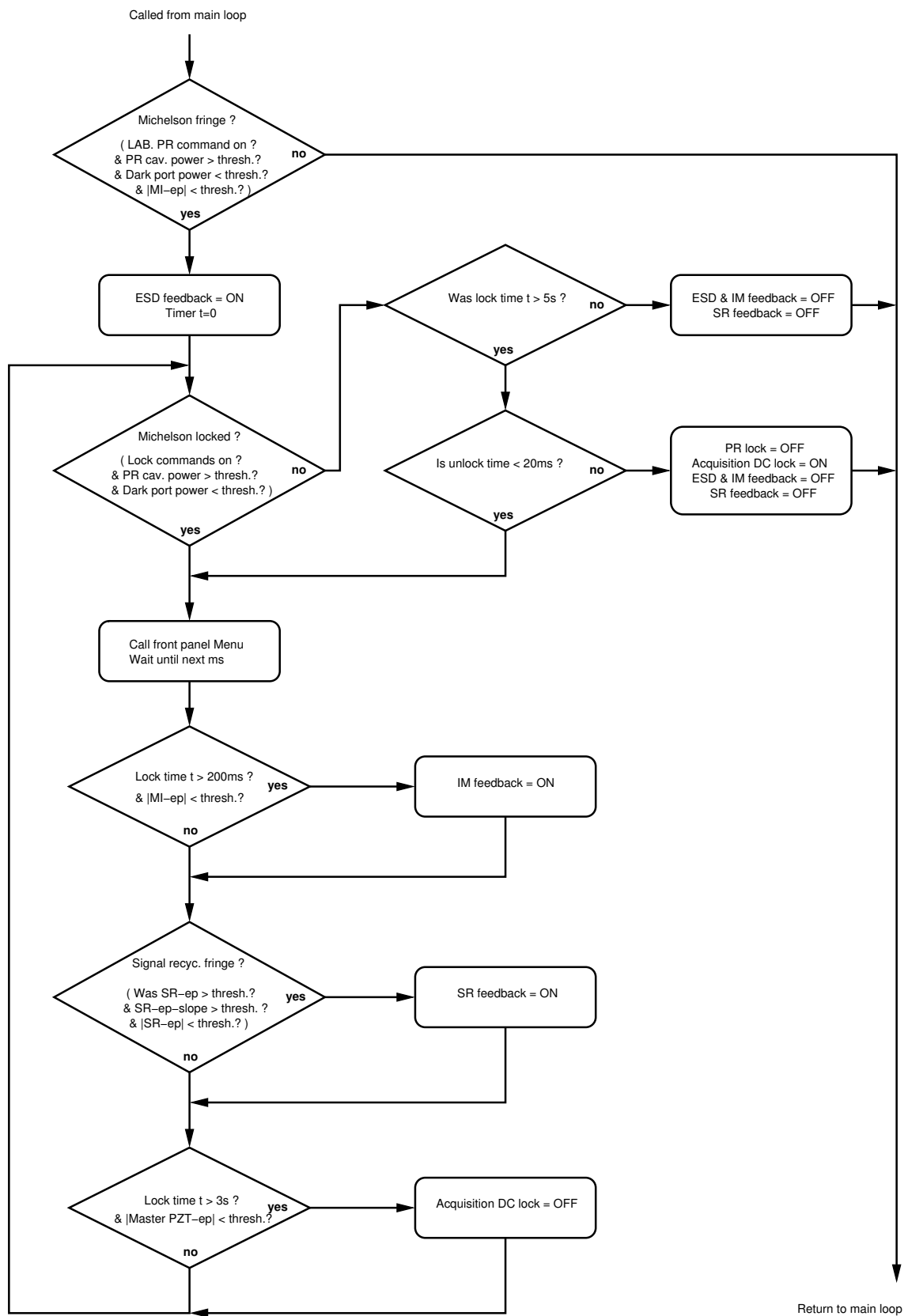


Figure C.2: Simplified flow diagram of the subroutine controlling the dual recycled lock. The routine is called from the main loop shown in figure C.1.

C.1.2 C code

The microcontroller is programmed in C, using a compiler with IDE from Keil. Parts of the code required for the interferometer locking procedures are given in this section. Additional code is used for the menu structure, display driving, initialisations, and other purposes.

C.1.2.1 Main loop

The C-routine 'main()' contains an infinite while loop, being executed after initialisations of the hard and software. Depending on the chosen mode (stored in the variable 'mode'), different routines are called to perform cavity locking tasks or test routines.

```
// ----- global variables: -----
int idata t1000, menu_c, ms_timer;          // ms - timer
bit idata t1000_flag;
bit idata menu_flag, newdata_flag, damp_flag, tried_damp_flag;
int tsec, mode = 0, mdclock;              // sec. - timer
int idata av1[16], av2[16], av3[8], avsr[8], pr_sum, mi_sum2, mi_sum1, sr_sum;
int idata refl;
BYTE idata av1count, av2count, av3count, avsrcount;

int idata pr_reflpow, mi_ep, sr_ep, pzt_fb, pr_incav, pr_dark;
int idata thresh[5];
BYTE idata adchancount;
BYTE lastkeys;
int menucount;
int test = 0;

void
main ()
{
    int reflc = 0, i;
    long reflsum = 0;
    static bit idata mc2lock_flag = 0;
    int mc2count = 0;

    Inits ();                             // general initialisations after booting
    ModeInit ();                           // initiate settings for chosen operating mode
    DA_ON = 1;                             // DA converter MAX 537 / Referenz voltage

    SetSRphase (SRPHASE20KHZ);

    inidis ();                             // display init.

    for (i = 0; i < 16; i++)               // initialize running averages
    {
        av1[i & 0x0f] = 0;
        av2[i & 0x0f] = 0;
        av3[i & 0x07] = 0;
        avsr[i & 0x07] = 0;
    }
    av1count = pr_sum = 0;
    av2count = mi_sum2 = 0;
    av3count = mi_sum1 = 0;
}
```

```

avsrcount = sr_sum = 0;

refl = 0;
mode = 0;
damp_flag = 0;

thresh[0] = 5;           // MI or SR errorpoint slope threshold
thresh[1] = 280;        // intracavity power threshold
thresh[2] = 2;          // MI ep threshold level
thresh[3] = 40;         // MI dark port threshold
thresh[4] = 80;         // PR refl. threshold

mdclock = 1;           // mdclock enabled

menucount = 7;
display (menucount);

while (1)
{
    // endless loop

    Menu ();
    while (!newdata_flag); // wait for next sampled data.
    newdata_flag = 0;

    if (!mc2lock_flag)
    {
        if (pr_reflpow > (refl >> 4))
        {
            if (++mc2count > 100)
            {
                mc2lock_flag = 1; // switch DC lock on
                ms_timer = 0;
                mc2count = 0;
            }
        }
        else
            mc2count = 0;
    }
    else
    {
        if (pr_reflpow <= (refl >> 5) + 3)
        {
            if (++mc2count > 100)
            {
                mc2lock_flag = 0;
                mc2count = 0;
            }
        }
        else
            mc2count = 0;
    }

    if (mdclock && mc2lock_flag)
    {
        if (pzt_fb < 4 && pzt_fb > -4)
        {
            // only switch on zerocrossing of feedback signal
            PZT_SW = 1; // switch DC lock on
            LED_YEL = 1;
        }
    }
    else
    {
        PZT_SW = 0; // switch DC lock off
    }
}

```

```

        LED_YEL = 0;
    }

    if (!PR_SW && PZT_SW && ms_timer > 4000)
    {
        // PR to be locked ?
        PRL_SW = 1;           // switch PR lock on
    }
    if (PR_SW || !PZT_SW)
    {
        PRL_SW = 0;           // switch PR lock off
    }

    switch (mode)             // Here subroutine depending on mode is called
    {
    case 0:
        ms_timer = 30000;
        break;
    case 1:
        damp_flag = 0;
        PRMIlock ();
        break;
    case 2:
        damp_flag = 1;
        PRMIlock ();
        break;
    case 3:
        Testmode ();
        break;
    case 4:
        DRlock ();
        break;
    }

    if (pr_reflpow > (refl - 20))
    {
        // Compute average of reflected power
        if (++reflc < 1000)
            reflsum += pr_reflpow;
        else
        {
            refl = reflsum / 1000;
            // refl is reflected power if PR cavity
            reflsum = reflc = 0;           // is not locked
        }
    }
}
// end while 1
}

```

C.1.2.2 Power-recycled Michelson lock

The power-recycled Michelson is locked by the routine ‘PRMIlock()’. Conditions for the Michelson passing across the dark fringe are tested at the beginning of the routine. If a dark fringe cannot be recognized, the routine is quit back to main(). Otherwise, feedback to the ESDs is switched on and if the lock succeeded, the intermediate mass feedback is added after some settling time. Feedback is applied as long as locking conditions are true. The routine is finally left after a loss of lock has been recognized and the feedback has been switched off.

```

void
PRMIlock (void)
{
    int lockendcount;
    MILG_SW = 1;                // interm. mass feedback off

    if (damp_flag)
        FringeDamp ();

    if (ms_timer < 10 || !PZT_SW || !PRL_SW || pr_reflpow < (refl >> 4)
        || pr_incav < thresh[1] || mi_ep > thresh[2] || mi_ep < -thresh[2]
        || (mi_sum2 >> 1) - mi_sum1 > thresh[0] || (mi_sum2 >> 1) - mi_sum1 < -thresh[0])
        // running into MI fringe ?

    return;

    LED_RED = 1;                // fast FB on
    tsec = t1000 = 0;
    ms_timer = 0;
    lockendcount = 0;
    while (!lockendcount || (ms_timer > 5000 && lockendcount < 20))
    {
        while (!newdata_flag);    // wait for next sampled data.
        newdata_flag = 0;

        while (!PR_SW && pr_reflpow > (refl >> 5)
            && mode != 0 && pr_incav > (thresh[1] >> 2))
        {
            // MI locked as long as some light in cavity
            lockendcount = 0;
            Menu ();
            //-----
            // call Testmode(); here if required
            //-----
            while (!newdata_flag);    // wait for next sampled data.
            newdata_flag = 0;

            if (ms_timer > 3000 && pzt_fb < 30 && pzt_fb > -30)
            {
                PZT_SW = 0;
                // switch DC lock off after 3 sec. in lock. if feedback is not too large
                LED_YEL = 0;
            }

            if (ms_timer > 250 && mi_ep < thresh[2] && mi_ep > -thresh[2])
            {
                MILG_SW = 0;
                // add interm. mass feedback after 500 ms if mi_ep is close to zero
            }
        }
        lockendcount++;          // condition count for end of lock
    }

    // MI-lock off

    LED_RED = 0;                // fast FB off
    MILG_SW = 1;

    if (ms_timer > 5000)
    {

```

```

    PRL_SW = 0;                // switch PR lock off quickly after lock of > 5 sec.
    PZT_SW = 1;                // switch DC lock on, not regarding zerocrossing,
    // to try to save MC2 lock.
    LED_YEL = 1;
    ms_timer = -6000;          // wait until integrator is switched off by labview
    // PR lock must not be switched on again before
    // Integrator is off
}
else
    ms_timer = 30000;
}

```

C.1.2.3 Dual Recycling lock

The structure of the routine ‘DRlock()’, responsible for the locking of dual recycling, is similar to the one for the power-recycled Michelson lock. After the ESD was switched on, and the Michelson is locked to the dark fringe, the controller tries to recognize if the signal recycling mirror passes through its operating point. If so, the feedback to the signal recycling mirror is switched on. The Michelson feedback will be switched on, as long as the Michelson is close to the dark fringe (judged by light power levels).

Rather than waiting for the signal recycling mirror to pass its operating point, another strategy can be chosen by the user and performed by this routine: The detuning frequency can be swept to find the actual tuning of the signal-recycling mirror. To get proper signal recycling error signals, the phase has to be swept as well, which is done according to a list of variables stored at the top of the code shown in section C.1.2.5 (‘mi_map[6]’). The numbers stored here represent the simulated optimal demodulation phase changes in dependence of the detuning, as shown in Figure 2.7 on page 51.

```

void
DRlock (void)
{
    int lockendcount;
    int ramp_count;
    int sramp, srampinc, migain;
    int ph_out;
    int sr_acq;
    static bit idata miramp_flag;

    MILG_SW = 1;                // interm. mass feedback off

    // A reminder of the 5 thresholds used:
    // thresh[0] : (SR) slope threshold
    // thresh[1] : intracavity power threshold
    // thresh[2] : MI ep zerocrossing tolerance threshold
    // thresh[3] : Dark port power threshold
    // thresh[4] : PR refl. power threshold (not so very important here)

```



```

if (ms_timer < 10 || !PZT_SW || !PRL_SW || pr_reflpo < thresh[4]
    || pr_incav < thresh[1] || pr_dark > thresh[3]
    || mi_ep > thresh[2] || mi_ep < -thresh[2])           // running into MI fringe ?
                                                         // MI EP slope not regarded here

    return; // no MI fringe was recognized: back to main

LED_RED = 1;           // ESD feedback on
tsec = t1000 = 0;     // reset timer
ms_timer = 0;         // reset ms-timer
lockendcount = 0;     // reset counter for end of lock conditions
miramp_flag = 1;      // no gain ramp!
migain = 2047;
sramp = 0;
srampinc = -10;
ramp_count = 0;
sr_acq = 0;

while (!lockendcount || (ms_timer > 5000 && lockendcount < 20))
{
    while (!newdata_flag);           // wait for next sampled data.
    newdata_flag = 0;

    while (!PR_SW && pr_reflpo > (refl >> 4)
        && mode != 0 && pr_incav > (thresh[1] >> 1)
        && pr_dark < (thresh[3] << 2))
    {
        // MI locked as long as some light in cavity

        lockendcount = 0;
        if (SR_SW == 0)
            Menu ();           // only call menu if SR is already locked
        while (!newdata_flag);   // wait for next sampled data.
        newdata_flag = 0;

        if (ms_timer > 3000 && pzt_fb < 15 && pzt_fb > -15 && SR_SW==0)
        {
            PZT_SW = 0;         // switch DC lock off after 3 sec. in lock. if feedback
            LED_YEL = 0;       // is not too large.
        }

        if (ms_timer > 50 /* && MILG_SW == 0 */)
        {
            //Is MI at least [time] on ?

            //--- ramps for DR -----
            if (++ramp_count >= 10)
            {
                ramp_count = 0;           //Reset counter: Ramp changes only every 10ms

                if (SR_SW == 1)
                {
                    //SR lock still OFF?
                    sramp += srampinc;
                    if (sramp < -820)
                    {
                        sramp = -820;     //is -1 volt
                        srampinc = 10;    // go up now
                    }
                    if (sramp > 0)
                    {
                        sramp = 0;        //is 0 volt
                        srampinc = -10;   //go down now
                    }
                }
                // DA537(2,sramp);       //set new value for SR freq. ramp;
            }
        }
    }
}

```

```

// ph_out = SRPHASE20KHZ - (sramp * 6)/82;
//60 Deg offset for -40kHz offset
// SetSRphase(ph_out); //set new value for SR demod. phase.
// SetMIgain(-sramp);

}
else
{
    if (sramp < 0)
    {
        sramp += 4;
// DA537(2,sramp); //set new value for SR freq. ramp;
// ph_out = SRPHASE20KHZ - (sramp * 6)/82;
//60 Deg offset for -40kHz offset
// SetSRphase(ph_out); //set new value for SR demod. phase.
// SetMIgain(-sramp);
    }
}
}
//--- ramps for DR end.
// new algorithm to find time to switch on SR feedback:
if (sr_ep > 18) // 36 is 1V
    sr_acq = 1;
if (sr_ep < -18)
    sr_acq = -1;

if (SR_SW == 1)
{
    // SR lock still off
    if ( ((sr_acq == 1 && sr_ep <= 4
        && ((sr_sum >> 1) - sr_ep) > thresh[0])
        || (sr_acq == -1 && sr_ep >= -4
        && ((sr_sum >> 1) - sr_ep) < -thresh[0]))
        // && mi_ep < (thresh[2]<<3) && mi_ep > -(thresh[2]<<3)
        // && (mi_sum2>>1) - mi_sum1 <= 50
        && (mi_sum2>>1) - mi_sum1 >= -50
        // running into SR fringe with minimum slope ?
    )
    {
        SR_ON; // SR feedback on;
        ms_timer = 0;
        sr_acq = 0;
    }
}
else
{
    // SR lock is on already
    if (ms_timer > 100 && (sr_ep > 36 || sr_ep < -36))
    {
        SR_OFF;
        sr_acq = 0;
    }
}
}

//if(ms_timer > 200 && ((mi_sum2>>1) - mi_sum1) < 20 ){
//looks for small MI slope only
if (ms_timer > 200 && mi_ep < (thresh[2] << 3)
&& mi_ep > -(thresh[2] << 3))
{
    //looks for MI zerocrossing
    MILG_SW = 0; // add interm. mass feedback after 200 ms
}
}

```

```

        ms_timer = 0; // if mi_ep is close to zero
    }
}
lockendcount++; // condition count for end of lock
}

// MI-lock off

MILG_SW = 1;
LED_RED = 0;
SR_OFF;
DA537 (2, 0); //back to center freq.
SetSRphase (SRPHASE20KHZ);
DA537 (1, 2047); // MI acqu. gain 1
if (ms_timer > 5000)
{
    PRL_SW = 0; // switch PR lock off quickly after lock of > 5 sec.
    PZT_SW = 1; // switch DC lock on, not regarding zerocrossing,
    // to try to save MC2 lock.
    LED_YEL = 1;
    ms_timer = -6000; // wait until integrator is switched off by labview
    // PR lock must not be switched on again before
    // Integrator is off
}
else
    ms_timer = 30000;
}

```

C.1.2.4 Fringe damping

Fringe damping can be used only in the power-recycled Michelson mode yet. The fringe damping routine tries to determine if the Michelson is approaching a dark fringe. If this information can be obtained *before* the zero-crossing of the Michelson error signal is reached, feedback can be applied by the electrostatic drives, in order to slow down the mirrors on approaching the dark fringe. Doing so, the chances for a successful lock acquisition can be increased. The de-accelerating feedback is produced by the microcontroller via a DA channel connected to the ESDs. When the Michelson passes across the dark fringe then, the DA signal is disconnected from the ESDs, while in turn the analog feedback is enabled on the zero-crossing as usual. The algorithm also tries to determine the speed of the mirrors in order to adapt the digital feedback applied. While the fringe damping works for the power-recycled Michelson mode, it cannot be used for dual recycling yet, as the light power levels are much harder to interpret in this case.

```

int
FringeDamp (void)
{
    int sign, slope;
    long daval;

    if (pr_reflpow >= (refl - 20))
        tried_damp_flag = 0;
    if (PZT_SW && PRL_SW && !tried_damp_flag &&
        pr_reflpow > (refl >> 1) && pr_reflpow < (refl - 40) &&

```

```

    (slope = (pr_sum >> 3) - pr_reflpow) > 2)
{
    // rising power in MI cavity ?

    sign = 0;
    if (mi_sum2 < -10)           // rising or falling MI errorpoint ?
        sign = 1;
    if (mi_sum2 > 10)
        sign = -1;

    if (sign)
    {
        ms_timer = 0;
        daval = sign * slope * 100;           // 10V
        if (daval > 2047)
            daval = 2047;

        DA537 (3, daval);
        tried_damp_flag = 1;
        slope <<= 2;
        while (ms_timer < 20 && pr_reflpow > (refl >> 5))
        {
            // damping time 2 - 20 ms is proportional to fringe speed
            while (!newdata_flag); // wait for next sampled data.
            newdata_flag = 0;
            daval *= 900; // exponential decay as decelerating function
            // 900 makes approx.25 ms decaying pulse

            daval >>= 10;
            DA537 (3, daval);
        }
        DA537 (3, 0);
    }
    // end pr_reflpow
}
else
{
}
return 0;
}

```

C.1.2.5 Input / output routines

Input / output routines are used for different purposes. AD and DA conversions can be started with the routines ‘StartAD (BYTE chan)’ and ‘DA537 (WORD chan, int val)’, respectively. The routine ‘SetSRphase (int phase)’ takes an integer number as input and sets a DA-channel to a voltage interpolated from a look-up-table (stored in ‘ph_map[28]’). This voltage output can be connected to the phase shifter for the signal recycling lock which will then set the adjusted phase shift for the signal recycling Schnupp frequency. The accuracy of this method was tested to be within $\pm 2^\circ$ over the full range of 0 to 260° . This routine is used along with the method of sweeping the SR modulation frequency in order to find the actual position of the signal recycling mirror (as described above).

```
// global variables
```

```

int ph_map[28] =
  { -2048, -1740, -1500, -1300, -1138, -1000, -885, -788, -702, -631, -567,
    -504, -445, -388, -330, -266, -201, -131, -52, 36, 135, 245, 378, 529, 706,
    931, 1215,
    1215
};
/* phase map for SR 20kHz to 60kHz DETUNING */
/* SR phase: 20kHz: 175Deg. -> 60kHz 235Deg. linear.*/
/* phase shifter is not linear with voltage, see labbok page 657 */

int mi_map[6] = { 2047, 1024, 682, 585, 487, 487 };

/*-----*/
/* AD-Wandlung an MAX197 initialisieren */

void
StartAD (BYTE chan)
{
  static unsigned int idata com;
  DP3 |= 0x00ff;          // output
  com = (P3 & 0xff00) | 0x0048; // intern. clock, int. acquis., +-5V
  P3 = com | (chan & 0x07);
  AD_CS = 0;
  AD_WR = 0;
  AD_WR = 1;
  AD_CS = 1;
  DP3 &= 0xff00;          // input
}

/* DA-Wandlung an MAX537 */

void
DA537 (WORD chan, int val)
{
  static WORD idata i, data;          // val is -2048 ... 2047
  data = (chan & 0x03) << 14;
  data |= 0x1000 | ((val + 2048) & 0x0fff);

  DA_SCK = 0;
  DA_CS = 0;
  for (i = 0; i < 16; i++)
  {
    DA_SCK = 0;
    if (data & 0x8000)
      DA_SDI = 1;
    else
      DA_SDI = 0;
    DA_SCK = 1;
    data <<= 1;
  }
  DA_CS = 1;
}

void
SetSRphase (int phase)
{
  int ph_ind, ph_rest, ph_o;
  if (phase < 0 || phase > 260)
    return;
  ph_ind = phase / 10;
  ph_rest = phase - 10 * ph_ind;
  ph_o =
    ph_map[ph_ind] + (ph_map[ph_ind + 1] - ph_map[ph_ind]) * ph_rest / 10;
}

```

```

    DA537 (0, ph_o);
}

void
SetMIgain (int ra)
{
    int mi_ind, mi_rest, mi_o;
    if (ra < 0 || ra > 820)
        return;
    mi_ind = ra / 205;
    mi_rest = ra - 205 * mi_ind;
    mi_o =
        mi_map[mi_ind] + (long) (mi_map[mi_ind + 1] -
                                mi_map[mi_ind]) * mi_rest / 205;

    DA537 (1, mi_o);
}

```

C.1.2.6 Interrupts

Interrupts are used to provide timers and the sampling of the analog channels connected to the controller. The timer routine 'T2int (void)' is executed once per millisecond and at its end, the first AD conversion (of the on-chip 10-bit converters) is started. If the conversion has finished, the routine 'ADfinished (void)' is called automatically (i.e. as an interrupt). The data is processed and made available for the programs determining the interferometer state. Next conversions are started subsequently according to the case structure within the routine, until all channels have been sampled. An interrupt calling the routine 'AD197int (void)' is generated if a conversion of the external AD converter has finished (not used in the current code).

```

void
T2int (void)
interrupt 0x22
{
    // timer interrupt with 1 kHz

    T2 = T2RELOAD;
    t1000_flag = 1;
    if (++t1000 >= 1000)
    {
        t1000 = 0;
        ++tsec;
    }
    if (++menu_c >= 100)
    {
        //call menu only every 100 ms
        menu_flag = 1;
        menu_c = 0;
    }
    if (++ms_timer > 32760)
        //prevent rollover of ms timer
        ms_timer = 32760;
    adchancount = 0;
    ADCON = 0x008a;
    // start internal AD conversion on channel 10
}

```

```

void
ADfinished (void)
interrupt 0x28
{
    switch (adchancount)
    {
        case 0:
            pr_reflpow = (int) (ADDAT & 0x03ff) - ADOFFSET - 9;
            pr_sum += pr_reflpow - av1[av1count & 0x07];    // running average of last 8 values
            av1[av1count++ & 0x07] = pr_reflpow;

            adchancount = 1;
            ADCON = 0x008b;                                //start conversion channel 11
            break;
        case 1:
            mi_ep = (int) (ADDAT & 0x03ff) - ADOFFSET;
            mi_sum2 += mi_ep - av2[av2count & 0x03];        // running av. of last 4 values
            av2[av2count++ & 0x03] = mi_ep;

            mi_sum1 += mi_ep - av3[av2count & 0x01];        // running av. of last 2 values
            av3[av3count++ & 0x01] = mi_ep;
            adchancount = 2;
            ADCON = 0x008c;                                //start conversion channel 12
            break;
        case 2:
            pzt_fb = (int) (ADDAT & 0x03ff) - ADOFFSET - 11;
            adchancount = 3;
            ADCON = 0x008d;                                //start conversion channel 13
            break;

        case 3:
            pr_incav = (int) (ADDAT & 0x03ff) - ADOFFSET - 10;
            adchancount = 4;
            ADCON = 0x008e;                                //start conversion channel 14

            break;
        case 4:
            sr_ep = (int) (ADDAT & 0x03ff) - ADOFFSET - 9;
            sr_sum += sr_ep - avsr[avsrcount & 0x01];        // running average of last 2 values
            avsr[avsrcount++ & 0x01] = sr_ep;

            adchancount = 5;
            ADCON = 0x008f;                                //start conversion channel 15
            break;

        case 5:
            pr_dark = (int) (ADDAT & 0x03ff) - ADOFFSET + 1;

            newdata_flag = 1;

            break;
    }
}

// called when conversion ready:

void
AD197int (void)
interrupt 0x1f
{

```

```
static int idata temp;
AD_HBEN = 1;
AD_CS = 0;
AD_RD = 0;
temp = P3 << 8;
AD_HBEN = 0;
temp |= P3 & 0x00ff;
AD_RD = 1;
AD_CS = 1;

}
```

C.2 LabView code

Some examples of the LabView code developed for the autoalignment system are given in this section.

C.2.1 Modecleaner alignment

Figure C.3 shows the panel for the DWS alignment control of the first modecleaner. Two other VIs of this kind are used for the autoalignment of modecleaner MC2 and for the power-recycling cavity as well. The four DWS error and feedback signals can be observed in the time domain. Gains for the DWS feedback loops can be set and the operating mode (manual or automatic switching the feedback) can be chosen.

Figure C.4 shows the according diagram containing the program flow.

Figure C.5 shows the VI for the spot position control of both modecleaners. The digital control loops stabilizing the spots to the center of the displayed grids (or to an offset value if desired) can be switched on and off individually.

C.2.2 Michelson alignment

A dedicated VI is used for the DWS control of the Michelson interferometer. The general functionality is similar to those used for the modecleaners. The VI is also responsible for the ‘offset shifting’ of the DWS feedback as described in section 3.3.7.1 for the modecleaners. Figure C.6 shows the diagram of a sub-VI of the latter, responsible for the offset shifting and common mode digital alignment of **MCe** and **MCn**.

Finally, Figure C.7 shows VI displaying and controlling for the four beam spot positions on the Michelson end mirrors. Offsets to the nominal beam positions can be set without the necessity of moving the spot position detector. This might be required in order to minimize coupling of DWS feedback noise to longitudinal mirror displacement (section 3.6.5).

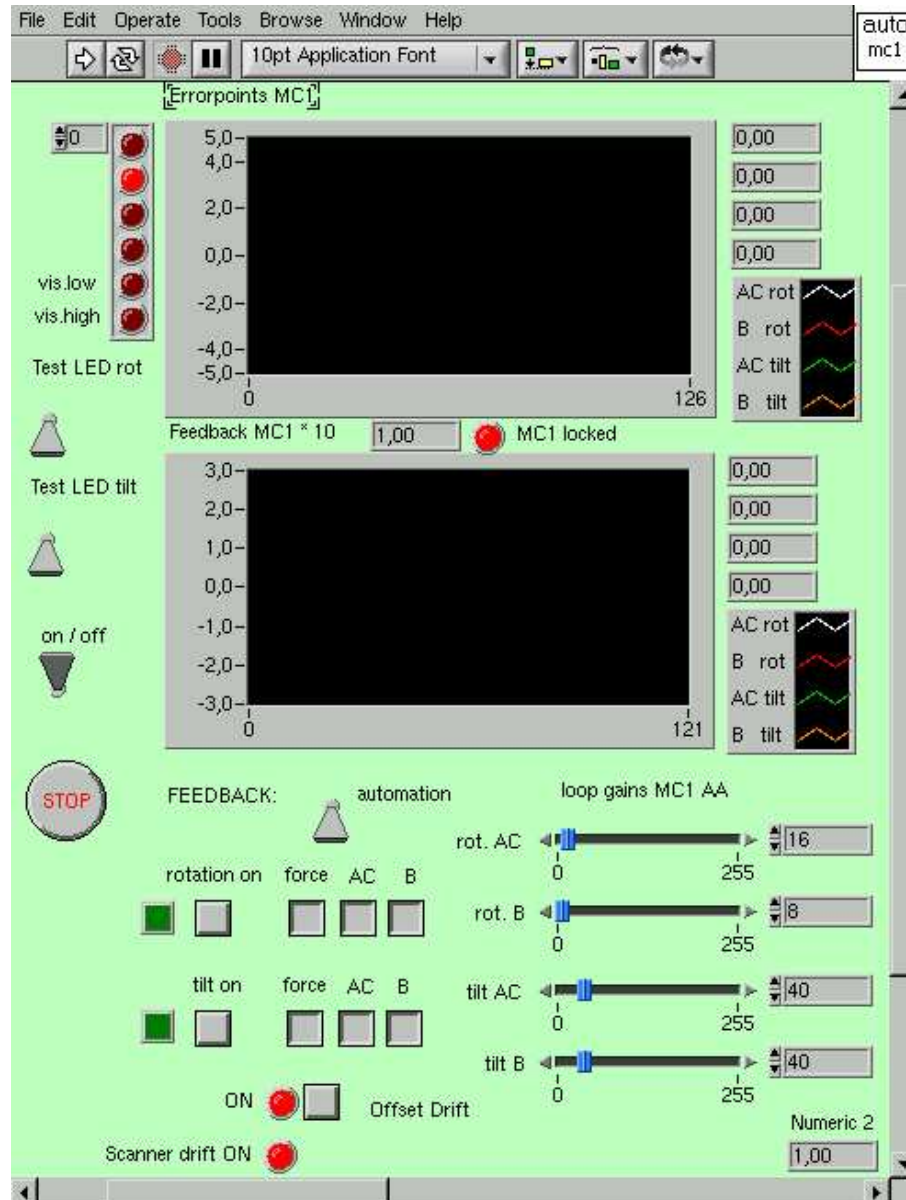


Figure C.3: Modecleaner 1 alignment supervising VI panel.

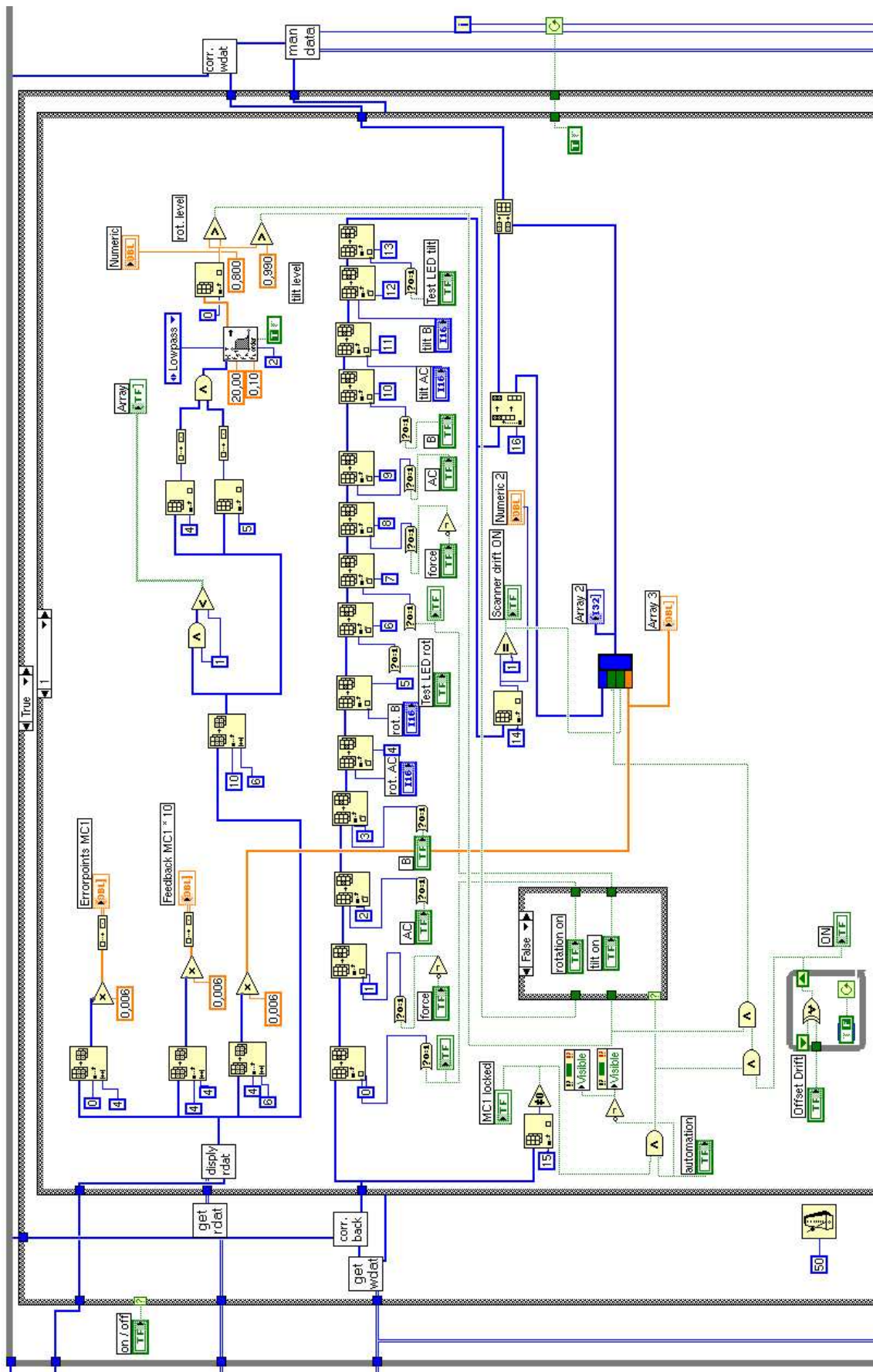


Figure C.4: Modecleaner 1 alignment supervising VI diagram.

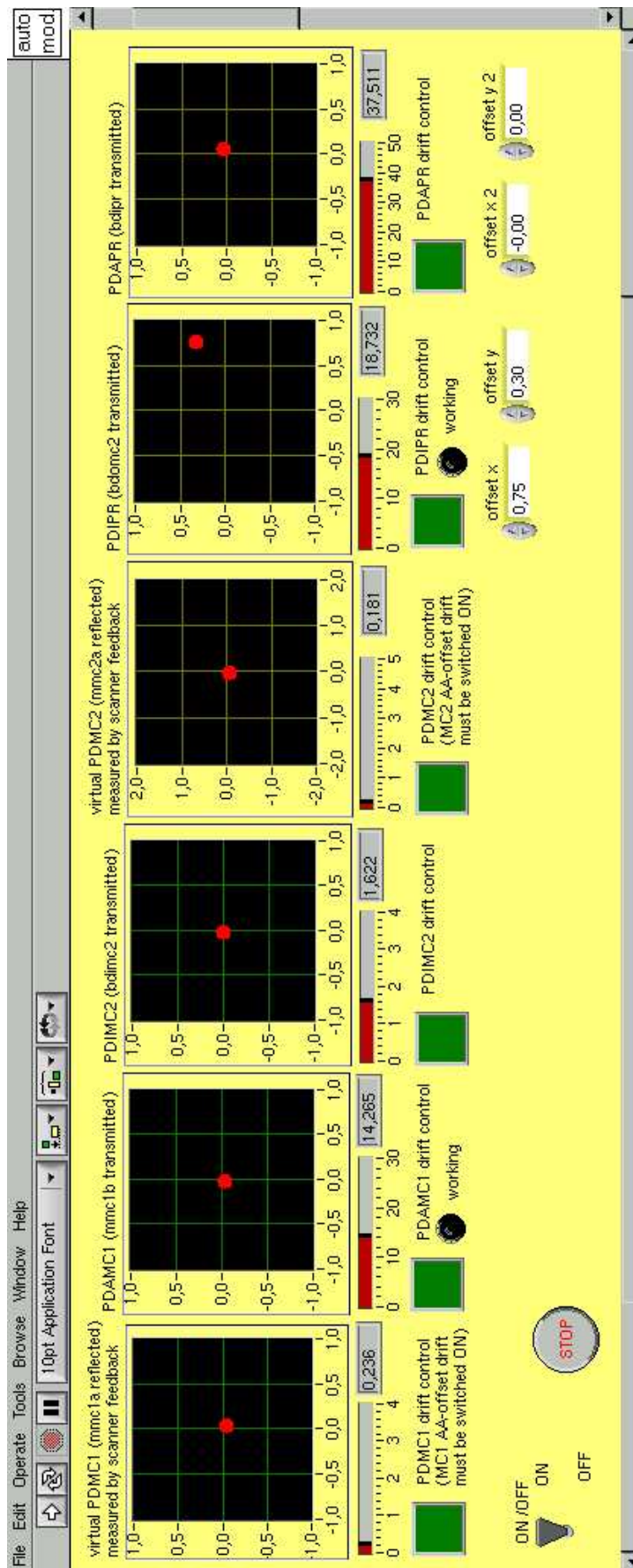


Figure C.5: Modecleaner spot position control VI panel.

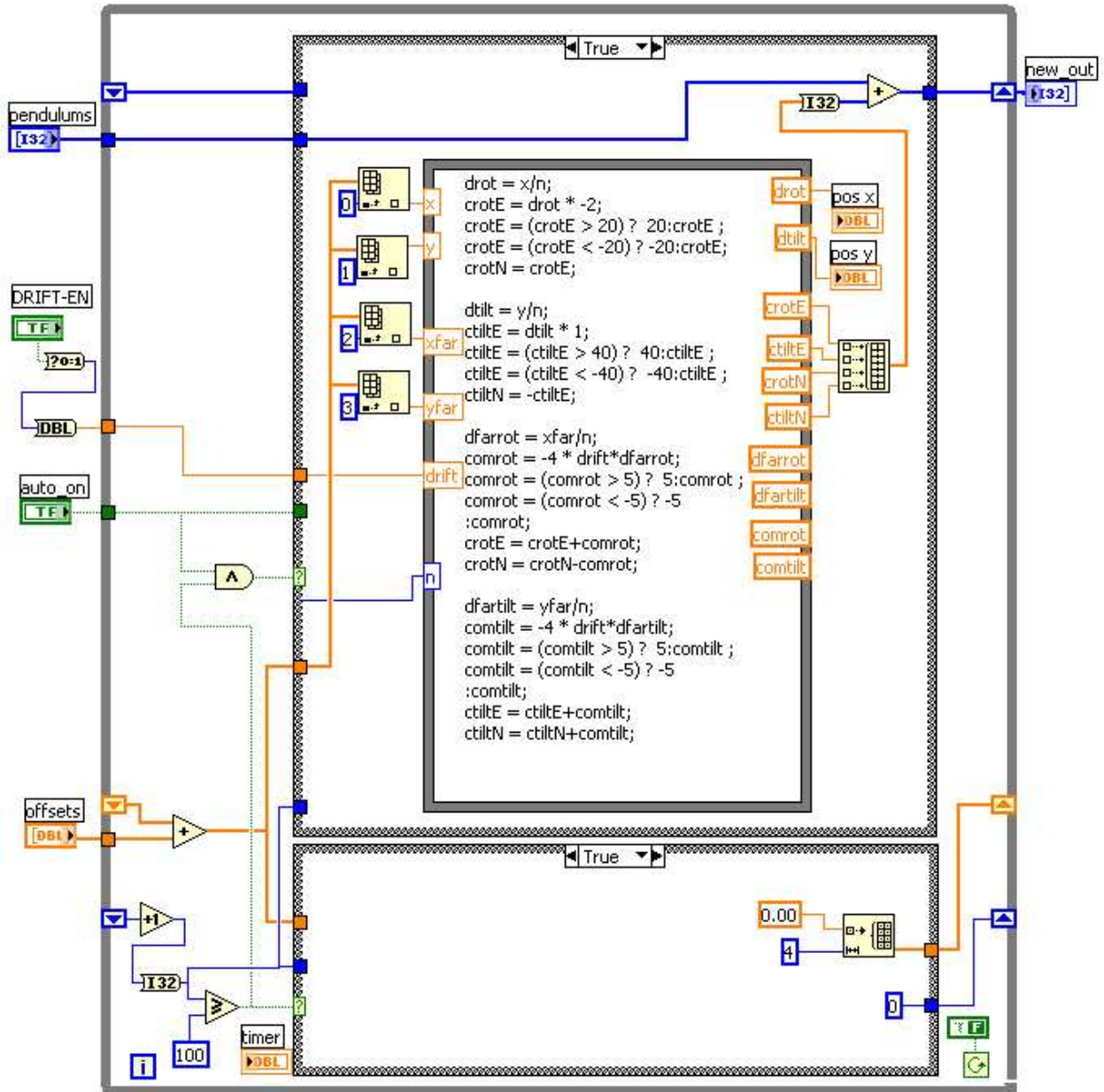


Figure C.6: Michelson drift control VI diagram.

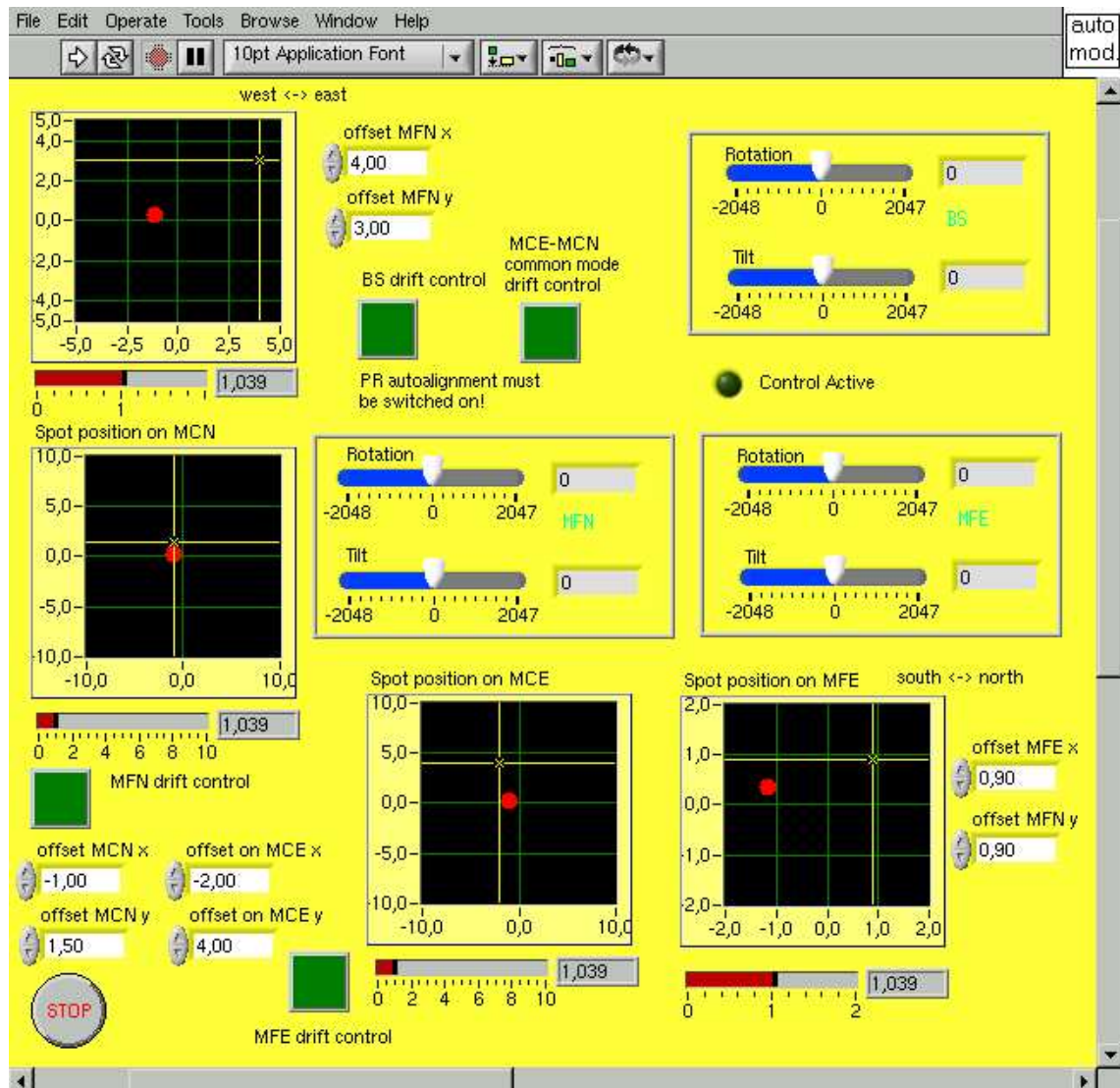
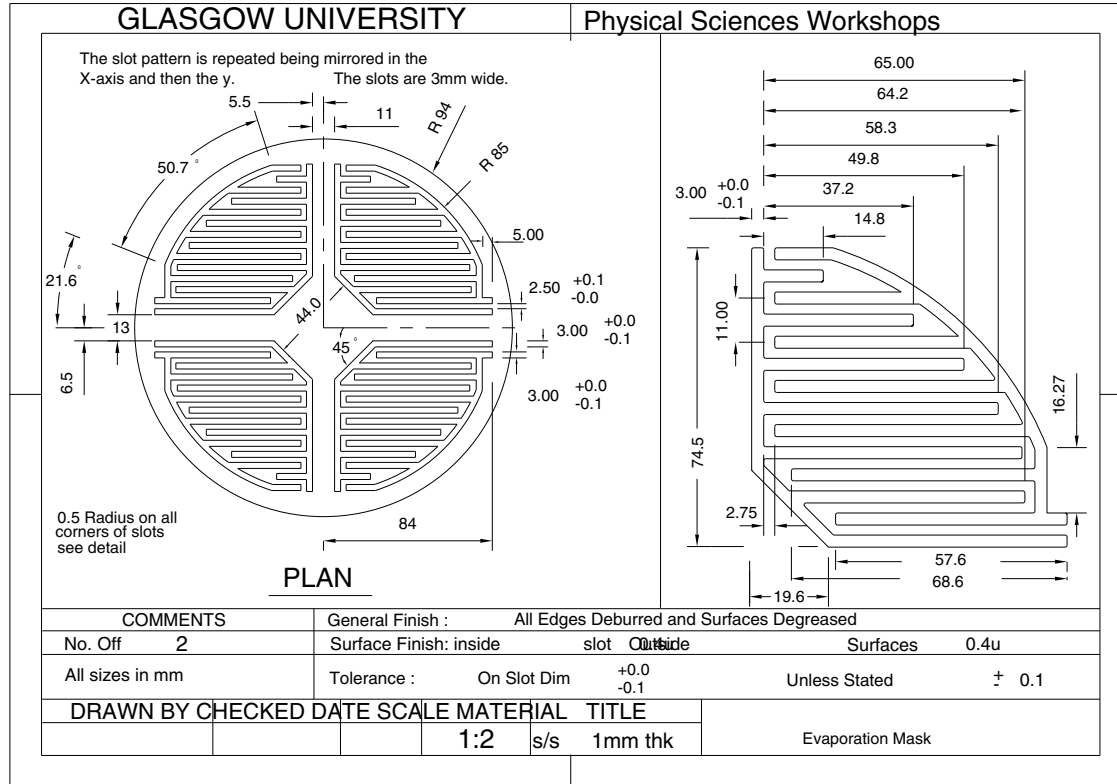


Figure C.7: Main interferometer spot position control VI panel.

Appendix D

ESD Design Drawing

Figure D.1: ESD design drawing.



Appendix E

Timetable

May		1999	MC1 DWS autoalignment.
January		2000	MC2 DWS autoalignment.
December		2000	'1200 m' experiments.
January		2001	DWS autoalignment for 1200 m cavity.
July	20,	2001	First fringes from Michelson interferometer.
September		2001	Michelson 'Mid fringe' lock with IM feedback only.
October	25,	2001	Power-recycled Michelson lock for > 1 minute.
November	2,	2001	Michelson 'Mid fringe' lock with ESD only.
December	20,	2001	Locking Michelson with PR & split feedback for > 10 minutes.
December	28,	2001	Start of 'E7' engineering run (17 days).
January		2002	Michelson DWS autoalignment.
June		2002	Complete autoalignment for all suspended mirrors.
July	26,	2002	First uninterrupted lock of the Michelson with PR over night.
August	23,	2002	Start of 'S1' data run (17 days).
November	15,	2002	First lock of largely detuned dual recycling.
December	23,	2002	Monolithic suspension of BS , MCE , and MCn finished.
March		2003	Locking largely detuned dual recycling with monolithic suspension for BS , MCE , MCn , MFe , and MFn .

Bibliography

- [ams⁺02] A. Freise, M.M. Casey, S. Gossler, H. Grote, G. Heinzel, H. Lück, D.I. Robertson, K.A. Strain, H. Ward, B. Willke, J. Hough, and K. Danzmann. Performance of a 1200 m long suspended fabry-perot cavity. *Class. Quantum Grav.*, 19:1389–1397, 2002.
- [Bar97] Andreas Barthel. Abstimmbares Signal-Recycling mit externer Modulation. Master’s thesis, Universität Hannover, Institut für Atom- und Molekülphysik, 1997.
- [Bea02] B.W. Barr and G. Cagnoli et al. Silica research in glasgow. *Class. Quantum Grav.*, 19:1655–1662, 2002.
- [Bon95] Kai Bongs. Automatische Gain-Kontrolle für Fabry-Perot-Resonatoren mit variablen Verlusten. Master’s thesis, Universität Hannover, Institut für Atom- und Molekülphysik, 1995.
- [Bro99] Sascha Brozek. *Frequenzstabilisierung eines ND:Yag-Hochleistungs-Laser-Systems für den Gravitationswellendetektor GEO 600*. PhD thesis, Universität Hannover, Institut für Atom- und Molekülphysik, 1999.
- [Cag02] G. Cagnoli. Personal communication, 2002.
- [CNSH01] D.A. Clubley, G.P. Newton, K.D. Skeldon, and J. Hough. Calibration of the Glasgow 10 m prototype laser interferometric gravitational wave detector using photon pressure. *Phys. Lett. A*, 283:85–88, 2001.
- [CWR00] Morag M. Casey, Harry Ward, and David I. Robertson. Computer monitoring and control of the GEO 600 gravitational wave detector. *Rev. Sci. Instr.*, 71:3910–3917, 2000.
- [DC83] R. W. P. Drever and Colleagues. Gravitational wave detectors using laser interferometers and optical cavities. Proc. of the NATO ASI Quantum Optics and Experimental General Relativity, Bad Windsheim 1981. Quantum Optics, Experimental Gravity and Measurement Theory, Plenum (New York), 1983.
- [DHK⁺83] R. W. P. Drever, J. L. Hall, F. V. Kowalski, J. Hough, G. M. Ford, and A. J. Munley. Laser phase and frequency stabilisation using an optical resonator. *Appl. Phys. B*, 31:97–105, 1983.

- [DLR⁺94] K. Danzmann, H. Lück, A. Rüdiger, R. Schilling, M. Schrempel, W. Winkler, J. Hough, G. P. Newton, N. A. Robertson, H. Ward, A. M. Campbell, J. E. Logan, D. I. Robertson, K. A. Strain, J. R. J. Bennett, V. Kose, M. Kühne, B. F. Schutz, D. Nicholson, J. Shuttleworth, H. Welling, P. Aufmuth, R. Rinkleff, A. Tünnermann, and B. Willke. *GEO 600 – Proposal for a 600m laser-interferometric gravitational wave antenna*, volume 190 of *MPQ*. MPQ Garching, 1994.
- [FHS⁺00] A. Freise, G. Heinzel, K.A. Strain, J. Mizuno, K.D. Skeldon, H. Lück, B. Willke, W. Winkler, R. Schilling, A. Rüdiger, and K. Danzmann. Demonstration of detuned dual recycling at the Garching 30-m laser interferometer. *Phys. Lett. A*, 277:135–142, 2000.
- [FMS⁺98] Peter Fritschel, Nergis Mavalvala, David Shoemaker, Daniel Sigg, Michael Zucker, and Gabriela Gonzalez. Alignment of an interferometric gravitational wave detector. *Applied Optics*, 37:6734–6747, 1998.
- [Fre98] Andreas Freise. Ein neues Konzept für Signal - Recycling. Master's thesis, Universität Hannover, Institut für Atom- und Molekülphysik, 1998.
- [Fre02] Andreas Freise. Finesse: Frequency domain interferometer simulation software. *Internal note*, 2002.
- [Fre03a] Andreas Freise. Personal communication, 2003.
- [Fre03b] Andreas Freise. *The Next Generation of Interferometry: Multi-Frequency Optical Modelling, Control Concepts and Implementation*. PhD thesis, Max-Planck-Institut für Gravitationsphysik, February 2003.
- [GHF⁺02] H Grote, G Heinzel, A Freise, S Gossler, B Willke, H Lück, H Ward, M Casey, K A Strain, D Robertson, J Hough, and K Danzmann. The automatic alignment system of GEO 600. *Class. Quantum Grav.*, 19:1849–1855, 2002.
- [GHF⁺03] H Grote, G Heinzel, A Freise, S Gossler, B Willke, H Lück, H Ward, M Casey, K A Strain, D Robertson, J Hough, and K Danzmann. Automatic beam alignment for the modecleaner cavities of GEO 600. *Appl. Optics*, 2003. Submitted for publication.
- [Hei99a] Gerhard Heinzel. *Advanced optical techniques for laser-interferometric gravitational-wave detectors*. PhD thesis, Max-Planck-Institut für Quantenoptik, February 1999. Also available as MPQ report 243.
- [Hei99b] Gerhard Heinzel. LISO - Program for Linear Simulation and Optimization of analog electronic circuits. User manual, 1999.
- [HGH⁺03] M. Hewitson, H. Grote, G. Heinzel, K. A. Strain, H. Ward, and U. Weiland. Calibration of the Power-Recycled Gravitational Wave Detector GEO 600. *Rev. Sci. Instr.*, 2003. Accepted for publication.
- [HH89] P. Horowitz and W. Hill. *The art of electronics*. Cambridge University Press, 2. edition, 1989.

- [HRS⁺99] G. Heinzl, A. Rüdiger, R. Schilling, K. A. Strain, W. Winkler, J. Mizuno, and K. Danzmann. Automatic beam alignment in the Garching 30-m prototype of a laser-interferometric gravitational wave detector. *Opt. Comm.*, 160:321–334, 1999.
- [HSM⁺98] G. Heinzl, K.A. Strain, J. Mizuno, K.D. Skeldon, B. Willke, W. Winkler, R. Schilling, A. Rüdiger, and K. Danzmann. Experimental demonstration of a suspended dual recycling interferometer for gravitational wave detection. *Phys. Rev. Lett.*, 81:5493–5496, 1998.
- [JNSH02] O. Jennrich, G. Newton, K.D. Skeldon, and J. Hough. A high power photodetection system for use with laser interferometric gravitational wave detectors. *Opt. Communications*, 205:405–413, 2002.
- [Kl00] Patrick Klövekorn. Mounting unit report. Internal note, 2000.
- [Maa95] Dirk Maaß. Signal-Recycling mit Schnupp-Modulation. Master’s thesis, Universität Hannover, Institut für Atom- und Molekülphysik, 1995.
- [Mal03] Michaela Malec. Personal communication, 2003.
- [Mee88] Brian J. Meers. Recycling in laser-interferometric gravitational-wave detectors. *Phys. Rev. D*, 38(8):2317, 1988.
- [Mee89] B. J. Meers. The frequency response of interferometric gravitational wave detectors. *Phys. Lett. A*, 142:465–470, 1989.
- [MMRW94] Euan Morrison, Brian J. Meers, David I. Robertson, and Henry Ward. Automatic alignment of optical interferometers. *Applied Optics*, 33:5041–5049, 1994.
- [MS91] B. J. Meers and K. A. Strain. Wave-front distortion in laser-interferometric gravitational-wave detectors. *Phys. Rev. D*, 43(10):3117–3130, 1991.
- [MSS98] Nergis Mavalvala, Daniel Sigg, and David Shoemaker. Experimental test of an alignment-sensing scheme for a gravitational-wave interferometer. *Applied Optics*, 37:7743–7746, 1998.
- [MST02] V.P. Mitrofanov, N.A. Styazhkina, and K.V. Tokmakov. Test mass damping associated with electrostatic actuator. *Class. Quantum Grav.*, 19:2039–2043, 2002.
- [MW95] T. G. Masters and R. Widmer. *Free Oscillations: Frequencies and Attenuation. In Global Earth Physics: a handbook of physical constants.* T. J. Ahrens, 1995.
- [Nag01] S. Nagano. 12 W Injection-locked laser performance. Internal note, 2001.
- [Pli03] Michael Plissi. Personal communication, 2003.
- [Sau94] Peter R. Saulson. *Fundamentals of Interferometric Gravitational Wave Detectors.* World Scientific, 1994.
- [Sch81] R. Schilling. Introduced the control scheme required for power recycling to the Garching prototype, unpublished, 1981.

- [Sch88] L. Schnupp. Vortrag beim European Collaboration Meeting on Interferometric Detection of Gravitational Waves, Sorrent, 1988.
- [Sch02] R. Schilling. OptoCad, A Fortran 95 module for tracing Gaussian beams through an optical set-up, Version 0.74. Internal note, 2002.
- [Sei02] Frank Seifert. Entwicklung einer quantenrauschbegrenzten Leistungsstabilisierung für ein Präzisionslasersystem. Master's thesis, Universität Hannover, Institut für Atom- und Molekülphysik, 2002.
- [SM91] K. A. Strain and B. J. Meers. Experimental demonstration of dual recycling for interferometric gravitational-wave detectors. *Phys. Rev. Lett.*, 66(11):1391, 1991.
- [SMH⁺97] D. Schnier, J. Mizuno, G. Heinzel, H. Lück, A. Rüdiger, R. Schilling, M. Schrempel, W. Winkler, and K. Danzmann. Power-Recycling in the Garching 30-m prototype interferometer for gravitational-wave detection. *Phys. Lett. A*, 225:210–216, 1997.
- [Str02] Kenneth Strain. Electrostatic drives for GEO 600. Internal note, 2002.
- [TS93] U. Tietze and Ch. Schenk. *Halbleiter - Schaltungstechnik*. Springer Verlag, 10. edition, 1993.
- [vW91] L. v. Wangenheim. *Aktive Filter in RC- und SC- Technik*. Hüthig - Verlag, 1991.
- [WAA⁺02] B. Willke, P. Aufmuth, C. Aulbert, S. Babak, R. Balasubramanian, B.W. Barr, S. Berukoff, S. Bose, G. Cagnoli, M.M. Casey, D. Churches, D. Clubley, C.N. Colacino, D.R.M. Crooks, C. Cutler, K. Danzmann, R. Davies, R. Dupuis, E. Elliffe, C. Fallnich, A. Freise, S. Goßler, A. Grant, H. Grote, G. Heinzel, A. Heptonstall, M. Heurs, M. Hewitson, J. Hough, O. Jennrich, K. Kawabe, K. Kötter, V. Leonhardt, H. Lück, M. Malec, P.W. McNamara, S.A. McIntosh, K. Mossavi, S. Mohanty, S. Mukherjee, S. Nagano, G.P. Newton, B.J. Owen, D. Palmer, M.A. Papa, M.V. Plissi, V. Quetschke, D.I. Robertson, N.A. Robertson, S. Rowan, A. Rüdiger, B.S. Sathyaprakash, R. Schilling, B.F. Schutz, R. Senior, A.M. Sintes, K.D. Skeldon, P. Sneddon, F. Stief, K.A. Strain, I. Taylor, C.I. Torrie, A. Vecchio, H. Ward, U. Weiland, H. Welling, P. Williams, W. Winkler, G. Woan, and I. Zawischa. The GEO 600 gravitational wave detector. *Class. Quantum Grav.*, 19:1377–1387, 2002.
- [ZBk⁺02] I. Zawischa, M. Brendel, K. Danzmann, C. Fallnich, M. Heurs, S. Nagano, V. Quetschke, H. Welling, and B. Willke. The GEO 600 laser system. *Class. Quantum Grav.*, 19:1775–1781, 2002.

Acknowledgements

It is my pleasure to thank the many people who contributed to this work in the one or other way. I would like to thank Karsten Danzmann for his generous support and the opportunity to participate in the challenging search for gravitational waves. The working group he established in Hannover is a great place to do science.

The electronics developed for the autoalignment system is based on designs from Gerhard Heinzl, who is always a source of inspiring ideas and help. I enjoyed very much working ‘on the site’ with Ken Strain, who patiently shared his broad knowledge about GEO 600 and physics in general.

I thank Benno Willke for always fruitful discussions about GEO. The project would not be where it is now, without the large amount of administrative effort he did and does for the GEO team. I thank Roland Schilling, Walter Winkler, Albrecht Rüdiger and Keita Kawabe for sharing their broad experience of the field.

Working on the site of GEO 600 is a great experience which I had or have the pleasure to share with Andreas Freise, Harald Lück, Martin Hewitson, Stefan Goßler, Uta Weiland, Michaela Malec, Kasem Mossavi, Karsten Kötter and many others, too numerous to mention. I also would like to thank Walter Grass for organizing equipment and coffee and I thank Volker Leonhard for playing volleyball with me.

Andreas Weidner designed and built parts of the electronics for the whole GEO project. He provides excellent craftsmanship, as well as Heiko zur Mühlen and the institute workshop.

I thank Gerhard Heinzl, Benno Willke, Andreas Freise, Harald Lück, Martin Hewitson, Michaela Malec and Bettina Grote for proof-reading the manuscript. Of course all remaining errors are in my own responsibility.

Finally I thank my parents and also Dirk Ulrich and Ulrike Braemer for a lot of support during the time of writing the manuscript.

Curriculum vitae

Hartmut Grote
Tieckstr. 26a
30625 Hannover

Born on February 19, 1967 in Hemer, Germany
Marital status: not married

08. 1973 – 07. 1977 Grundschule Ihmert
08. 1977 – 07. 1983 Friedrich-Leopold-Woeste Gymnasium Hemer
08. 1983 – 07. 1986 Staatliche Höhere Berufsfachschule für
Fertigungstechnik und Elektrotechnik
07. 1986 Facharbeiterbrief (IHK) Informationselektronik,
Fachhochschulreife
08. 1986 – 07. 1988 Bismarckschule Hannover, Gymnasium
07. 1988 Allgemeine Hochschulreife
01. 1989 – 08. 1990 Compulsory civil service, Medizinische Hochschule Hannover
10. 1990 – 06. 1999 Diploma studies in Physics and Geology, University of Hannover
04. 1992 – 11. 1997 Employed at research workshop of the Med. Hochschule Hannover,
Electronic and software development
06. 1999 Physik-Diplom, University of Hannover
08. 1999 – 09. 2000 Scientific Assistant, Max-Planck-Institut für Quantenoptik, Garching
08. 1999 – 07. 2003 Doctoral studies, University of Hannover
10. 2000 – 07. 2003 Scientific Assistant, University of Hannover,
Institut für Atom- und Molekülphysik
- since 8. 2003 Researcher, Max-Planck-Institut für Gravitationsphysik,
Albert-Einstein-Institut, Teilinstitut Hannover

List of publications

- H. Grote: *Autoalignment am GEO 600 Modecleaner*, Masters theses, Universität Hannover, Institut für Atom- und Molekülphysik (June 1999)
- H. Grote, G. Heinzl, A. Freise, S. Goßler, B. Willke, H. Lück, H. Ward, M. Casey, K.A. Strain, D. Robertson, J. Hough and K. Danzmann: *The automatic alignment system of GEO 600* Class. Quantum Grav. **19 No 7** (7 April 2002) p 1849–1855
- H. Grote, G. Heinzl, A. Freise, S. Goßler, B. Willke, H. Lück, H. Ward, M. Casey, K.A. Strain, D. Robertson, J. Hough and K. Danzmann: *Alignment control of GEO 600* accepted for publication by Class. Quantum Grav.
- H. Grote, A. Freise, M. Malec, G. Heinzl, B. Willke, H. Lück, K.A. Strain, J. Hough and K. Danzmann: *Dual Recycling for GEO 600* accepted for publication by Class. Quantum Grav.
- H. Grote, G. Heinzl, A. Freise, S. Goßler, B. Willke, H. Lück, H. Ward, M.M. Casey, K.A. Strain, D. Robertson, J. Hough, and K. Danzmann: *Automatic beam alignment for the mode-cleaner cavities of GEO 600* submitted to Applied Optics
- M. Hewitson, H. Grote, G. Heinzl, K. A. Strain, H. Ward, and U. Weiland *Calibration of the Power-Recycled Gravitational Wave Detector GEO 600*, accepted for publication in Review of Scientific Instruments
- G. Heinzl, A. Freise, H. Grote, K. Strain and K. Danzmann: *Dual recycling for GEO 600* Class. Quantum Grav. **19 No 7** (7 April 2002) p 1547-1553
- S. Goßler et al. *The GEO 600 mode-cleaning and injection optics*, accepted for publication in Review of Scientific Instruments
- A. Freise, M.M. Casey, S. Goßler, H. Grote, G. Heinzl, H. Lück, D.I. Robertson, K.A. Strain, H. Ward, B. Willke, J. Hough and K. Danzmann: *Performance of a 1200 m long suspended Fabry-Perot cavity* Class. Quantum Grav. **19 No 7** (7 April 2002) p 1389-1397
- S. Goßler, M.M. Casey, A. Freise, H. Grote, H. Lück, P. McNamara, M.V. Plissi, D.I. Robertson, N.A. Robertson, K. Skeldon, K.A. Strain, C.I. Torrie, H. Ward, B. Willke, J. Hough and K. Danzmann: *The modecleaner system and suspension aspects of GEO 600* Class. Quantum Grav. **19 No 7** (7 April 2002) p 1835-1842
- K. Kötter, C. Aulbert, S. Babak, R. Balasubramanian, S. Berukoff, S. Bose, D. Churches, C.N. Colacino, C. Cutler, K. Danzmann, R. Davies, R. Dupuis, A. Freise, H. Grote, G. Heinzl, M. Hewitson, J. Hough, H. Lück, M. Malec, S.D. Mohanty, S. Mukherjee, S. Nagano, M.A. Papa, D. Robertson, B.S. Sathyaprakash, B.F. Schutz, A.M. Sintes, K.A. Strain, I.J. Taylor, A. Vecchio, H. Ward, U. Weiland, B. Willke and G. Woan: *Data acquisition and detector characterization of GEO600* Class. Quantum Grav. **19 No 7** (7 April 2002) p 1399-1407
- B. Willke, P. Aufmuth, C. Aulbert, S. Babak, R. Balasubramanian, B.W. Barr, S. Berukoff, S. Bose, G. Cagnoli, M.M. Casey, D. Churches, D. Clubley, C.N. Colacino, D.R.M. Crooks, C. Cutler, K. Danzmann, R. Davies, R. Dupuis, E. Elliffe, C. Fallnich, A. Freise, S. Goßler,

A. Grant, H. Grote, G. Heinzl, A. Heptonstall, M. Heurs, M. Hewitson, J. Hough, O. Jennrich, K. Kawabe, K. Kötter, V. Leonhardt, H. Lück, M. Malec, P.W. McNamara, S.A. McIntosh, K. Mossavi, S. Mohanty, S. Mukherjee, S. Nagano, G.P. Newton, B.J. Owen, D. Palmer, M.A. Papa, M.V. Plissi, V. Quetschke, D.I. Robertson, N.A. Robertson, S. Rowan, A. Rüdiger, B.S. Sathyaprakash, R. Schilling, B.F. Schutz, R. Senior, A.M. Sintes, K.D. Skeldon, P. Sneddon, F. Stief, K.A. Strain, I. Taylor, C.I. Torrie, A. Vecchio, H. Ward, U. Weiland, H. Welling, P. Williams, W. Winkler, G. Woan and I. Zawischa: *The GEO 600 gravitational wave detector* Class. Quantum Grav. **19 No 7** (7 April 2002) p 1377-1387

B.W. Barr, G. Cagnoli, M.M. Casey, D. Clubley, D.R.M. Crooks, K. Danzmann, E.J. Elliffe, S. Goßler, A. Grant, H. Grote, A. Heptonstall, J. Hough, O. Jennrich, H. Lück, S.A. McIntosh, G.P. Newton, D.A. Palmer, M.V. Plissi, D.I. Robertson, N.A. Robertson, S. Rowan, K.D. Skeldon, P. Sneddon, K.A. Strain, C.I. Torrie, H. Ward, P.A. Willems, B. Willke and W. Winkler: *Silica research in Glasgow* Class. Quantum Grav. **19 No 7** (7 April 2002) p 1655-1662